Proceedings of the 6th International Colloquium on Nonlinear Dynamics and Control of Deep Drilling Systems

Editors:

Thiago G. Ritto, Universidade Federal do Rio de Janeiro (Brazil)

Daniel A. Castello, Universidade Federal do Rio de Janeiro (Brazil)

Balakumar Balachandran, University of Maryland, College Park, MD (USA)

Emmanuel Detournay, University of Minnesota, Minneapolis, MN (USA)

Nathan van de Wouw, Eindhoven University of Technology, Eindhoven (Netherlands)

GROUP PICTURE

Event webpage: https://eventos.abcm.org.br/dcds2024/

Contents

Foreword

The Sixth International Colloquium on Nonlinear Dynamics and Control of Deep Drilling Systems was held at the Federal University of Rio de Janeiro (UFRJ), Centro de Tecnologia, Cidade Universitária, Brazil. This meeting followed previous meetings, which were held at the University of Maryland, College Park, MD (2022), Preikestolen, Norway (2018), the University of Minnesota, Minneapolis, MN, USA (2014), the Eindhoven University of Technology, Eindhoven, the Netherlands (2012), and the University of Liège, Liège, Belgium (2009). This is the first time that this colloquium was held in South America.

The total number of participants was about 50 and the colloquium featured one keynote lecture and eighteen invited talks, out of which one talk was given virtually. About 45% of the participants were from the Industry and 55% from Academia. In addition, 70% of the participants were from Brazil and the other 30% from other countries (US, the Netherlands, UK, France, Iran, Singapore, Slovakia). Furthermore, 20% of the participants were students (undergrad, masters, PhD) and 80% of the participants were engineers, researchers, and faculty members.

There was a visit to the Laboratory of Acoustic and Vibration of the Department of Mechanical Engineering at UFRJ on the first day of the event. A drill string test rig experiment was shown, in which a slender bar was driven by an electrical motor at the top. At the bottom, a platform is lifted with a sample of material that is drilled by a bit that is attached at the bottom of the slender bar. Stick-slip phenomenon was demonstrated.

On the second day of the colloquium, a Panel was organized to discuss the "Challenges in Deep Drilling Dynamics Research." Ashley Johnson (SLB), Gregory Payette (ExxonMobil) and Roman Shor (Texas A&M) gave their perspectives on the subject, and brought some specific points to be addressed.

To meet the growing demands in drilling practices, further progress in this field will need collaborative efforts from various research communities, including computational sciences, dynamical systems, nonlinear structural vibrations, geomechanics, drilling technology, and control theory. Additionally, these advancements will require active partnerships between Academia and Industry.

This colloquium facilitated a lively exchange of ideas among participants from diverse backgrounds, all interested in the scientific challenges posed by this critical engineering application.

We would like to thank ABCM (Brazilian Association of Mechanical Sciences and Engineering) for promoting the colloquium, and acknowledge the support of the Mechanical Engineering Department, the Polytechnical School, COPPE, and the Technological Park of the Federal University of Rio de Janeiro. We would also like to thank the following companies that sponsored the event: Tomax, SLB, Halliburton, and ExxonMobil, as well as the Brazilian agencies: FAPERJ, CAPES, and CNPQ.

For citation purposes, for instance of the first paper, please use:

```
@inproceedings{Detournay2024,
author = {E. Detournay},
title = {Insights into Mechanics of Drilling},
booktitle = {Proceeding of the 6th International Colloquium on
Nonlinear Dynamics and Control of Deep Drilling Systems},
year = {2024},
address = {Rio de Janeiro, Brazil},
month = {July},
url = {https://eventos.abcm.org.br/dcds2024/proceedings/}}
```

The organizers hope this meeting will spark new collaborations to tackle future challenges in deep drilling systems.

Rio de Janeiro, 3rd July, 2024

T. G. Ritto, Universidade Federal do Rio de Janeiro, Rio de Janeiro, Brazil
D. A. Castello, Universidade Federal do Rio de Janeiro, Rio de Janeiro, Brazil
B. Balachandran, University of Maryland, College Park, MD, USA
E. Detournay, University of Minnesota, Minneapolis, MN, USA
N. van de Wouw, Eindhoven University of Technology, Eindhoven, the Netherlands

Colloquium Program

MONDAY JULY 1ST, 2024

13:30 – **Opening**

13:40 – 14:40 – **Keynote** (1 presentation)
"Insights into Mechanics of Drilling". Speaker: Prof. Emmanuel Detournay (University of Minnesota – USA)

14:40 – 15:40 – **Technical Session 1** (2 presentations)
"Recent advances in Drilling Optimization using Model-Based design and Rock Formation Logs: Brazilian Pre-Salt Case Studies". Speaker: Romulo Aguiar (SLB – Brazil)

"A PDE-ODE Model For The Regenerative Effect In Lateral Cutting: From Milling To Bit Whirls". Speaker: Kaidong Chen (Eindhoven University of Technology – Netherlands)

15:40 – 16:10 – **Coffee Break 1**

16:10 – 17:00 – **Laboratory visit**

TUESDAY JULY 2ND, 2024

8:30 – 9:30 – **Panel**
"Challenges in Deep Drilling Dynamics Research", with panelists: – Ashley Johnson (SLB – England) – Gregory Payette (ExxonMobil – USA) – Prof. Roman J. Shor (Texas A&M University – USA)

9:30 – 10:00 – **Coffee Break 2**

10:00 – 12:00 – **Technical Session 2** (4 presentations)

WEDNESDAY JULY 3RD, 2024

8:30 – 10:00 – **Technical Session 5** (3 presentations)
"Model-Based Drilling Performance Analysis of a Downhole Regulator". Speaker:
Prof. Nathan van de Wouw (Eindhoven University of Technology – Netherlands)

"On the robustness of deep drilling control techniques". Speaker: Prof. Marcelo
Trindade (Universidade de São Paulo – Brazil)

"Stick slip vibrations in drilling: modeling, estimation, avoidance". Speaker:
Dr. Jean Auriol (CNRS, Université Paris-Saclay – France)

10:00 – 10:30 – **Coffee Break 4**

10:30 – 12:30 – **Technical Session 6** (3 presentations)
*"Examples of Downhole Tools Lateral Dynamics Modeling in Frequency and
Time Domain"*. Speaker: Mohamed Mahjoub (DrillScan – France)

"Nonlinear Modeling of 3D Borehole Propagation in Directional Drilling". Speaker:
He Zhang (Halliburton – Singapore)

"Distributed drilling system analysis: a time-delay system approach". Speaker:
Dr. Shabnam Tashakori (Shiraz University of Technology – Iran)

Insights into Mechanics of Drilling

Emmanuel Detournay – University of Minnesota USA

Insights into Mechanics of Drilling

Emmanuel Detournay[1]

[1]Department of Civil, Environmental, & Geo- Engineering, University of Minnesota

Abstract: This review outlines the research in drilling mechanics by the author and his collaborators on formulating rate-independent bit/rock interface laws, modeling directional drilling, and analyzing the root cause of stick-slip vibrations in deep drilling systems.

Keywords: Bit/rock interface law, directional drilling, sick-slip oscillations

INTRODUCTION

Three topics in drilling mechanics researched by the author and his collaborators are outlined in this document, namely: (1) rate-independent bit/rock interface laws for drag (PDC) bits; (2) a model for directional drilling with a push-the-bit rotary steerable system; and (3) models to analyze the stability of deep drilling systems and simulate the development of stick-slip limit cycles.

BIT/ROCK INTERFACE LAWS

The form of the bit/rock interface laws are specific to the bit type, since the mechanisms of rock destruction and the modes of interaction are particular to each kind of bits — drag (PDC), roller-cone, and impregnated-diamond (ID) bits – used in rotary drilling. Furthermore, the coefficients of these laws embody aspects of the bit design, the bit bluntness, and also the strength properties of the rock. The interface laws for PDC bits are outlined in the following, as the bit/rock interaction for these bits is now well understood. We restrict consideration to the normal mode of bit-rock interaction, when the bit is drilling straight ahead with the bit velocity parallel to its axis of revolution and without any angular motion other than a rotation around its axis of symmetry (Detournay and Defourny, 1992; Detournay *et al.*, 2008). However, the most general mode of bit-rock interaction (in particular relevant for directional drilling) is characterized also by a lateral and an angular component, in addition to an axial component (Perneder *et al.*, 2012).

The drilling response model for the normal mode consists of a set of relationships between four quantities: the weight-on-bit W, the torque-on-bit T, the rate of penetration V, and the angular velocity Ω. The kinematic variables V and Ω are conjugated to the dynamic variables W and T, respectively. Provided that the state variables are averaged over at least one revolution, the laws that relate the dynamic to the kinematic variables can be expressed as $W = W(V, \Omega)$ and $T = T(V, \Omega)$, meaning that the forces on the bit, W and T, depend only on the instantaneous (but suitably time-averaged) velocities, V and Ω. However, if the processes that are taking place at the interface between the bit and the rock are rate-independent, the drilling response can be described by relations involving only three quantities: W, T, and the ratio V/Ω, i.e., $W = \tilde{W}(V/\Omega)$ and $W = \tilde{W}(V/\Omega)$. The ratio V/Ω is actually proportional to the depth of cut per revolution $d = 2\pi V/\Omega$.

There is strong experimental evidence, based on single cutter and drilling tests conducted under kinematic control, that the interface laws are indeed rate-independent. The stiff kinematic control virtually suppresses any vibrations during cutting or drilling. Hence, the decrease of torque T with angular velocity Ω that is often observed in field and laboratory experiments is likely a consequence of the axial vibrations experienced by the drill bit during drilling, with the apparent rate effects actually functions of the dynamical characteristics of the drilling system.

After scaling the weight on bit and the torque on bit to remove dependence on the bit dimension, the bit/rock interface laws take the general form $w = \tilde{w}(d)$ and $t = \tilde{t}(d)$, where $w = W/a$ and $t = 2T/a^2$, with a denoting the bit radius. The laws expressed by the functions $\tilde{w}(d)$ and $\tilde{t}(d)$ embed the bit design, its state of wear, the rock being drilled, and the bottom-hole pressure environment. It is also useful to introduce the following quantities: the specific energy $E = t/d$ and the drilling strength $S = w/d$. Both quantities have the dimension of a stress or equivalently of energy per volume. The specific energy E represents the energy spent to drill a unit volume of rock.

The PDC bit/rock interaction is actually a combination of cutting and frictional contact. The weight w and torque t and can thus be decomposed in terms of cutting (w_c, t_c) and frictional contact (w_f, t_f) components: $w = w_c + w_f$ and $t = t_c + t_f$. The cutting components (w_c, t_c) of the weight and torque and on bit are proportional to the depth of cut d, according to experimental results from single cutter tests and laboratory drilling tests; i.e, $t_c = \varepsilon d$ and $w_c = \zeta \varepsilon d$, where ε is the intrinsic specific energy, a quantity that quantifies the complex process of destruction and that essentially reflects the strength of the rock and the downhole pressure (Detournay and Atkinson, 2000). At atmospheric pressure, ε is about

equal to the unconfined compressive strength (UCS) of the rock (Richard *et al.*, 2012) and ζ is a number in the narrow range (0.5 $\sim$ 0.8) that characterizes the force inclination on the cutting face of the PDC cutters.

The contact components (w_f, t_f) of the weight and torque on bit have a complex dependence on the depth of cut d. Three phases appear to exist with increasing d, corresponding respectively to an increase of the contact forces, a saturation, and finally another increase of the contact forces associated to poor cleaning. It is conjectured that the increase of the contact force in phase I is predominantly due to a geometrical effect, as the two contacting surfaces are generally not conforming. Change in the depth of cut d indeed affects the angle between the two contacting surfaces thus causing not only a variation of the actual contact area but also a change in the contact pressure (Zhou and Detournay, 2014). In phase II $w_f = w_{f*}$, the contact forces are fully mobilized (Detournay *et al.*, 2008). Beyond a critical value of the depth of cut per revolution d (function of the bit bluntness), the contact forces do not increase anymore because the normal contact stress has reached a maximum value σ, and the actual contact area has attained a limiting value that characterizes the bit bluntness. This drilling regime is thus defined by $w_f = w_{f*}$, with the consequence that any increase of the weight w must necessarily be translated as an increase of the cutting component w_c. In phase II, the bit behaves incrementally as a sharp bit. Finally in phase III, the contact surface increases, through pile-up of sheared rock material between the bit and the rock, caused by poor cleaning (the production of cutting exceeds what can be removed by the flow of mud). Because of this increase of the contact area, w_f becomes larger than w_{f*}.
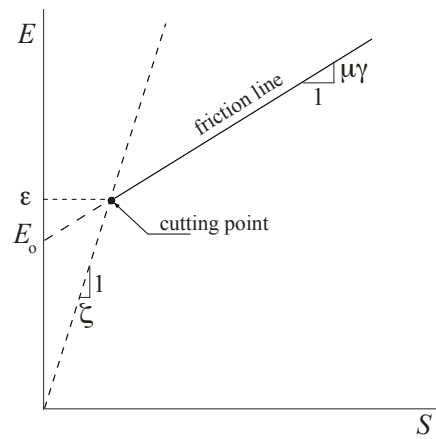
Figure 1 – E-S Diagram for PDC bits.

Irrespective of their magnitude, the frictional contact components (w_f, t_f) are constrained by the frictional relation $t_f = \mu \gamma w_f$, where μ is the coefficient of friction at the wear flat/rock interface and γ a bit constant that encapsulates the influence of the orientation and distribution of the contact forces, which is strongly influenced by the location and orientation of the cutters on the bit (Detournay and Defourny, 1992). This frictional relation together with the proportionality between the cutting components (w_c, t_c) and the depth of cut d leads to the existence of a linear constraint on the response of PDC bits between w, t, and d, which must be met irrespective of the state of wear of the bit and the magnitude of the contact forces. This linear constraint can be written as $E = E_o + \mu \gamma S$, with $E_o = (1 - \mu \gamma \zeta) \varepsilon$. This equation is represented by the friction line of slope $\mu \gamma$ in the $E - S$ diagram (see Fig. 1). In this representation, E_o is simply the intercept of the friction line with the E-axis. The cutting point, characterized by $E = \varepsilon$ and $S = \zeta \varepsilon$, corresponds to an ideally efficient drilling process, where all the energy provided to the bit is transferred into the cutting process. The cutting point is at the intersection of the friction line with the cutting locus, the line passing through the origin of the plane and inclined by ζ^{-1} to the S-axis. Admissible states of the drilling response of a PDC bit in the $E - S$ diagram are represented by all the points on the friction line, which lies to the right of (and above) the cutting point. The drilling efficiency η, i.e., the fraction of the energy provided to the bit that is used to fragment the rock, is thus naturally defined as $\eta = \varepsilon / E$. In contrast to the intrinsic specific energy ε (which represents the energy required to remove a unit volume of rock by an ideally sharp bit), the specific energy E depends not only on the wear state of the bit, but also on the depth of cut. The drilling response of a PDC bit in a given formation is expected to map on the friction line (with slope $\mu \gamma$) in the $E - S$ diagram. The bit/rock interface laws for PDC bits is extended to layered rocks by Aribowo *et al.* (2022)

DIRECTIONAL DRILLING

Drilling deep boreholes that weave complex trajectories in the subsurface has been made possible with the development of downhole tools that steer the bit, in particular the emergence of rotary steerable systems (RSS) in the late 1990s. These servo-controlled downhole robots, mounted on the bottom-hole assembly (BHA) behind the bit, steer the bit by either

applying a force on the borehole wall or by tilting the bit.

Studies of this dynamical system are motivated by engineering issues, which include: defining criteria of bit selection; designing the BHA to increase, maintain, or decrease the borehole inclination with or without the presence of a RSS; preventing borehole spiraling, an expression of self-excited oscillations triggered by a directional instability of the drilling system; or devising an appropriate controller for the RSS with the objective of tracking a predefined well path.

A drilling structure in its simplest abstraction is an extremely slender elastic body constrained to deform inside the borehole, see Figure 2a. It is subject to gravity, hydraulic forces associated with the flow of drilling mud, imposed forces at the rig and at the RSS, a force and a moment at the bit, and reaction forces at its contacts with the borehole. The directional propagation of the borehole depends on the force and moment at the bit; they are affected not only by the action of the RSS but also by the deformed configuration of the BHA, which is constrained by the stabilizers to espouse the existing borehole. Thus, the propagation of the borehole is governed by the interaction between a geometrical object —the wellbore, and a mechanical object —the drilling structure.
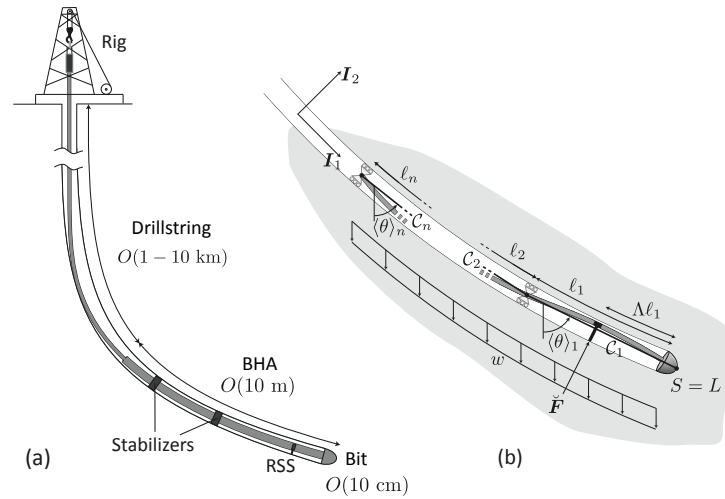
Figure 2 – (a) Typical rotary drilling system. (b) Model of the BHA.

The directional drilling model is formulated at an intermediate scale corresponding to the bottom part of the BHA, which is equipped with a bit, n stabilizers, and a push-the-bit RSS located between the bit and the first stabilizer (Fig. 2a). At this intermediate scale, which is —typically of order $O(10 \sim 100)$ m, the propagating borehole can be described as an evolving curve (restricted here to belong to a vertical plan) and the BHA is a slender elastic object subject to external forces and constrained by the stabilizers to conform to the borehole geometry. The modeled BHA section can be viewed as a Euler-Bernoulli beam, with the influence of the drillstring replaced by an assumed known force acting above the nth stabilizer and the complex interaction between the bit and the rock subsumed into boundary conditions to the beam equations.

The mathematical model is formulated from considerations involving (a) a bit/rock interaction law that relates the force and moment on the bit to its penetration into the rock; (b) kinematic relationships that describe the local borehole geometry from the bit motion; and (c) a beam model of the bottom-hole assembly (BHA) that expresses the force and moment at the bit as functions of both the loads applied on the BHA and the geometrical constraints imposed by the stabilizers that center the BHA in the borehole (Perneder *et al.*, 2017; Shakib *et al.*, 2019). The coupling between the model components leads to the formulation of a delay differential equation that governs the evolution of the borehole inclination, with spatial delays corresponding to the positions of the stabilizers behind the bit. The drilling response at a length scale corresponding to these delays is affected by the geometric feedback provided by the stabilizers that force the BHA to conform locally to the borehole geometry. At a length scale sufficiently large compared to the delays, the propagating borehole follows a trajectory characterized by a quasi-stationary curvature, which ultimately evolves towards a constant inclination equilibrium solution if it exists (Perneder and Detournay, 2013b,a). The trajectory is sometimes counterintuitive, with the borehole tending to steer opposite to that intended with the steering tool. Moreover, under certain conditions, which depend on the BHA configuration, on the design and bluntness of the bit, and on the rock, perturbations in the borehole trajectory that are sensed by the stabilizers are amplified progressively at the bit, until a limit cycle characterized by finite oscillations is reached (Perneder *et al.*, 2017; Shakib *et al.*, 2019), see Fig. 3. Both the directional stability of the system and the counter-intuitive behaviors can be related to a key dimensionless group that can be interpreted as the ratio of a pseudo-stiffness characterizing the bit/rock interaction and the bending stiffness of the BHA (Marck *et al.*, 2014; Marck and Detournay, 2016b,a)
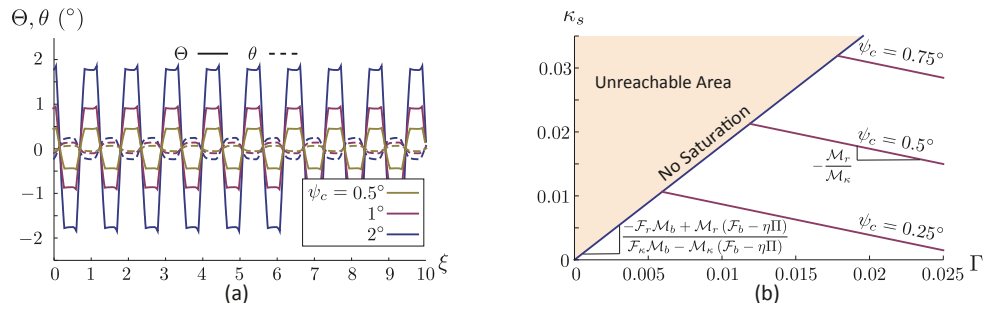
Figure 3 – Limit cycle for different saturation values of the bit tilt ($\psi_c = 0.5°$, $1°$, $2°$).

STICK-SLIP OSCILLATIONS

With the wide application of PDC bits in deep well drilling, the drillstring is observed to permanently experience self-excited torsional vibrations due to the high compliance of the drillstring and the regenerative nature of the rock cutting process. These torsional vibrations often degenerate into stick-slips, characterized by an alternating stick phase with the bit at rest for a period of time and a slip phase with the peak value of the bit angular velocity more than twice the surface imposed rotary speed. Torsional stick-slips can cause bit damage, premature failure of drillstring components, difficulties in steering the bit for directional drilling, eventually resulting in increased drilling costs.

It has been established that the driving mechanism for torsional stick-slips lays in the bit-rock interaction in vertical or steeply inclined wells. Observations from early field and laboratory measurements have revealed that the reactive torque-on-bit (TOB) reduces as the bit angular velocity increases during torsional stick-slips events. This falling characteristic of the TOB, referred to as the velocity-weakening law, was regarded as an inherent frictional characteristic of PDC bits and was widely accepted as the root cause of the torsional stick-slips. However, the rate-dependent interface law is not supported by results of kinematically-controlled single cutter experiments. Indeed, extensive research on rock cutting with a PDC cutter has provided compelling evidence that the cutter velocity ranging from cm/s to m/s has a negligible effect on the rock removal as well as on the magnitude of the cutting forces.
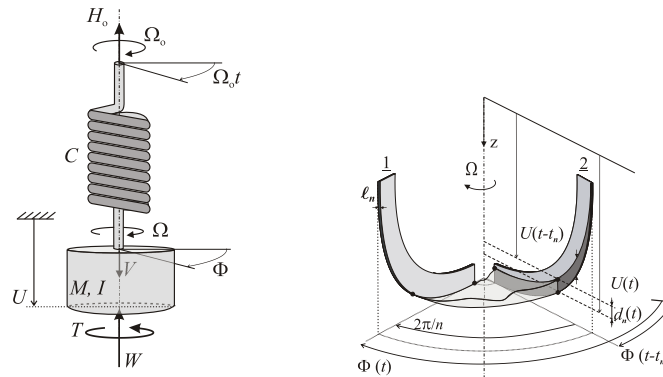
Figure 4 – RGD model.

The original discrete drillstring model (referred to as the RGD model) that integrates the rate-independent law described above only has two degrees of freedom (DOFs). They capture the axial and torsional motions of the BHA, which is viewed as a rigid body connected to the rig by a torsional spring (Richard *et al.*, 2004, 2007). Moreover, the RGD model considers an idealized drag bit with several identical blades distributed symmetrically around the bit axis of revolution. The cutting components of W and T are formulated to be proportional to the depth of cut, a state variable that is a function of the current and a delayed axial position of the bit, whereas the frictional components are associated with a set-valued function of the bit axial velocity, resulting in a nonlinear boundary condition. In view of the regenerative nature of the cutting process, the time delay involved in modeling the depth of cut depends on the bit torsional motion. Due to the existence of torsional vibrations, the delay is not constant but rather state-dependent. This introduces an additional coupling between the bit axial and torsional vibrations. A system of state-dependent delay differential equations (SDDDEs) is thus formulated to describe the bit axial and torsional dynamics. Numerical simulations with the RGD model reveal that the averaged velocity-weakening effect is a consequence rather than a root cause of the torsional stick-slips (Richard *et al.*, 2007; Germay *et al.*, 2009b). Influence of the bit design on stability is discussed by Tian *et al.* (2020).
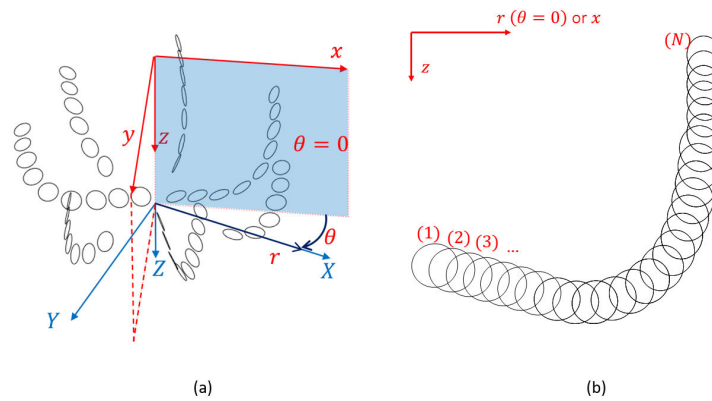
Figure 5 – Cutter layout on a PDC bit.

An integrated model to analyze self-excited axial and torsional vibrations in rotary drilling systems using realistic PDC bits is then described (Zhang *et al.*, 2024). The model combines a multi-degree-of-freedom (MDOF) drillstring representation (Germay *et al.*, 2009a; Zhang and Detournay, 2020, 2022) with a detailed PDC bit-rock interaction model (Tian and Detournay, 2021; Tian *et al.*, 2022) that accounts for the cutter layouts, see Fig. 5. The bit-rock interaction is described by rate-independent laws for reactive force and torque, encompassing cutting and frictional contact at the cutter face and wear flat. The regenerative rock cutting introduces numerous state-dependent delays due to complex cutter layout of the bit, while the unilateral nature of frictional contact is formulated as a nonlinear boundary condition. The state-dependent delays are transformed into constant angular offsets prescribed by the bit design by introducing a bit trajectory function whose evolution is governed by a partial differential equation (PDE). This PDE is coupled with the drillstring dynamics described by ordinary differential equations (ODEs)(Zhang and Detournay, 2020). The Galerkin method with Chebyshev polynomials transforms the set of coupled PDE-ODEs into a system of ODEs. This approach bypasses the need to search for multiple delays at each time step, allowing implementation of this integrated rock-bit-drillstring model. Simulation results replicate field observed torque-on-bit (TOB) effects including velocity-weakening and hysteresis due to torsional stick-slips, attributing them to cutting depth variation rather than downhole friction. Preliminary findings regarding the influence of bit design on torsional stick-slips align with field drilling practices. The results of parametric study correspond to field test observations, enabling analysis of bit design, drillstring configuration, and drilling parameters on self-excited torsional stick-slips (Zhang *et al.*, 2024).

ACKNOWLEDGMENTS

REFERENCES

Aribowo, A.G., Wildemans, R., Detournay, E. and van de Wouw, N., 2022. "Drag bit/rock interface laws for the transition between two layers". *International Journal of Rock Mechanics and Mining Sciences*, Vol. 150, p. 104980. doi:https://doi.org/10.1016/j.ijrmms.2021.104980.

Detournay, E. and Atkinson, C., 2000. "Influence of pore pressure on the drilling response in low-permeability shear-dilatant rocks". *International Journal of Rock Mechanics and Mining Sciences*, Vol. 37, No. 7, pp. 1091–1101. ISSN 1365-1609. doi:10.1016/S1365-1609(00)00050-2.

Detournay, E. and Defourny, P., 1992. "A phenomenological model of the drilling action of drag bits". *International Journal of Rock Mechanics and Mining Sciences*, Vol. 29, No. 1, pp. 13–23.

Detournay, E., Richard, T. and Shepherd, M., 2008. "Drilling response of drag bits: Theory and experiment". *International Journal of Rock Mechanics and Mining Sciences*, Vol. 45, No. 8, pp. 1347–1360. doi:10.1016/j.ijrmms.2008.01.010.

Germay, C., Denoël, V. and Detournay, E., 2009a. "Multiple mode analysis of the self-excited vibrations of rotary drilling systems". *Journal of Sound and Vibration*, Vol. 325, pp. 362–381. doi:10.1016/j.jsv.2009.03.017.

Germay, C., van de Wouw, N., Nijmeijer, H. and Sepulchre, R., 2009b. "Nonlinear drillstring dynamics analysis". *SIAM Journal On Applied Dynamical Systems*, Vol. 8, pp. 527–553. doi:10.1137/060675848.

Marck, J. and Detournay, E., 2016a. "Influence of Rotary-Steerable-System Design on Borehole Spiraling". *SPE Journal*, Vol. 21, No. 01, pp. 293–302. ISSN 1086-055X. doi:10.2118/174554-PA.

Marck, J., Detournay, E., Kuesters, A. and Wingate, J., 2014. "Analysis of Spiraled-Borehole Data by Use of a Novel Directional-Drilling Model". *SPE Drilling & Completion*, Vol. 29, No. 03, pp. 267–278. ISSN 1064-6671. doi: 10.2118/167992-PA.

Marck, J. and Detournay, E., 2016b. "Spiraled Boreholes: An Expression of 3D Directional Instability of Drilling Systems". *SPE Journal*, Vol. 21, No. 02, pp. 434–448. ISSN 1086-055X. doi:10.2118/173156-PA.

Perneder, L. and Detournay, E., 2013a. "Equilibrium inclinations of straight boreholes". *SPE Journal*, Vol. 18, No. 03, pp. 395–405.

Perneder, L. and Detournay, E., 2013b. "Steady-state solutions of a propagating borehole". *International Journal of Solids and Structures*, Vol. 50, No. 9, pp. 1226–1240. doi:https://doi.org/10.1016/j.ijsolstr.2012.12.011.

Perneder, L., Detournay, E. and Downton, G., 2012. "Bit/rock interface laws in directional drilling". *International Journal of Rock Mechanics and Mining Sciences*, Vol. 51, pp. 81–90. doi:https://doi.org/10.1016/j.ijrmms.2012.01.008.

Perneder, L., Marck, J. and Detournay, E., 2017. "A model of planar borehole propagation". *SIAM Journal on Applied Mathematics*, Vol. 77, No. 4, pp. 1089–1114. doi:10.1137/16M1094518.

Richard, T., Dagrain, F., Poyol, E. and Detournay, E., 2012. "Rock strength determination from scratch tests". *Engineering Geology*, Vol. 147-148, pp. 91–100. doi:10.1016/j.enggeo.2012.07.011.

Richard, T., Germay, C. and Detournay, E., 2004. "Self-excited stick-slip oscillations of drill bits". *Comptes Rendus Mecanique*, Vol. 332, No. 8, pp. 619–626. ISSN 1631-0721. doi:10.1016/j.crme.2004.01.016.

Richard, T., Germay, C. and Detournay, E., 2007. "A simplified model to explore the root cause of stick-slip vibrations in drilling systems with drag bits". *Journal of Sound and Vibration*, Vol. 305, No. 3, pp. 432–456. ISSN 0022-460X. doi:10.1016/j.jsv.2007.04.015.

Shakib, M.F., Detournay, E. and van de Wouw, N., 2019. "Nonlinear dynamic modeling and analysis of borehole propagation for directional drilling". *International Journal of Non-Linear Mechanics*, Vol. 113, pp. 178–201. doi: https://doi.org/10.1016/j.ijnonlinmec.2019.01.014.

Tian, K. and Detournay, E., 2021. "Influence of PDC bit cutter layout on stick–slip vibrations of deep drilling systems". *Journal of Petroleum Science and Engineering*, Vol. 206, p. 109005. doi:https://doi.org/10.1016/j.petrol.2021.109005.

Tian, K., Detournay, E. and Zhang, H., 2022. "An Alternative Formulation for Modeling Self-Excited Vibrations of Drillstring With Polycrystalline Diamond Compact Bits". *Journal of Computational and Nonlinear Dynamics*, Vol. 17, No. 5, p. 051002. ISSN 1555-1415. doi:10.1115/1.4053407.

Tian, K., Ganesh, R. and Detournay, E., 2020. "Influence of bit design on the stability of a rotary drilling system". *Nonlinear Dynamics*, pp. 1–25.

Zhang, H. and Detournay, E., 2020. "An alternative formulation for modeling self-excited oscillations of rotary drilling systems". *Journal of Sound and Vibration*, Vol. 474, p. 115241.

Zhang, H. and Detournay, E., 2022. "A high-dimensional model to study the self-excited oscillations of rotary drilling systems". *Communications in Nonlinear Science and Numerical Simulation*, Vol. 112, p. 106549. doi: https://doi.org/10.1016/j.cnsns.2022.106549.

Zhang, H., Tian, K. and Detournay, E., 2024. "A high-fidelity model for nonlinear self-excited oscillations in rotary drilling systems". *Journal of Sound and Vibration*, Vol. 573, p. 118193. doi:https://doi.org/10.1016/j.jsv.2023.118193.

Zhou, Y. and Detournay, E., 2014. "Analysis of the contact forces on a blunt pdc bit". In *48th US Rock Mechanics/Geomechanics Symposium held in Minneapolis, MN, USA, 1-4 June 2014*. ARMA 14-7351.

RESPONSIBILITY NOTICE

The author is the only one responsible for the printed material included in this paper.

Recent advances in Drilling Optimization using Model-Based design and Rock Formation Logs: Brazilian Pre-Salt Case Studies

Romulo R. Aguiar – SLB (Brazil)

Recent advances in Drilling Optimization using Model-Based design and Rock Formation Logs: Brazilian Pre-Salt Case Studies

Romulo Aguiar [1]

[1] SLB. Av. Republica do Chile, 330 - 18o andar, Torre Oeste - Ventura, 20031-170 Rio de Janeiro, Brazil

Abstract: After 15 years of Brazilian presalt exploration and development, the carbonate reservoirs continue to pose drilling challenges, leading to unwanted bottomhole assembly (BHA) trips due to severe shock and vibration, low rates of penetration (ROP), and premature drill-bit cutting structure damage. Today, industry efforts to improve the performance in the Brazilian presalt carbonates are driven by trial and error, which is very costly in the ultradeepwater drilling environment. The adoption of a collaborative mindset between SLB and operators with the desire to bring about a step change in drilling efficiency on the Brazilian presalt cluster enabled a systematic learning framework to capture, evaluate, and reuse knowledge from drilling dynamics, geological, and petrophysical aspects. The innovation of these efforts is the implementation of an improved, fully digital bit/ BHA design workflow, integrating a calibrated 4D dynamic Finite-Element simulation model and petrotechnical expertise from drilling engineering, geomechanics, geology, and petrophysics groups to continue to push the drilling performance envelope in the challenging Brazilian presalt application. More recently, a case study of the successful use of an acoustic logging-while-drilling (LWD) borehole image log for drilling optimization is also presented. The ultrasonic image was acquired at high-resolution (0.2 in.), displaying clear rock formation textural and hardness variations. These contrasts are the key for understanding and simulation of drill bit-rock interaction; therefore, using the high-resolution LWD borehole image log has the potential to optimize and reduce uncertainty in the operators' drilling development campaigns.

Keywords: drilling optimization, mode-based design, rock properties, formation evaluation

INTRODUCTION

The presalt reserves offshore Brazil currently drilled with various types of drill bits have proven to be a challenging environment. Consisting mainly of centimetric to metric cycles of laminites-spherulites-shrubs from an alkaline shallow-lake setting (Wright and Barnett 2015), such a heterogeneous formation can produce high-lateral vibration and stick/slip levels in the drilling system, leading to drill-bit cutter damage, BHA tool failure, well deviation, low ROP, nonproductive time, and increased drilling costs. Generally, in the reservoir intervals, operators encounter ring-out (RO) dull characteristics on the shoulder of the bit or core-out on the cone area, usually related to drilling dynamics. A huge challenge today is to reach the section total depth in a complex presalt interval during a single run with good overall ROP. Historically, polycrystalline diamond compact (PDC) bits have not performed well in hard and abrasion-prone applications within heterogeneous formations. With continuing advances in cutter technology and improved bit stability, these bits have increased their marketshare worldwide. Therefore, it is essential for the industry to create a differentiating cutting action to increase penetration rates and extend bit life to further reduce drilling costs.

The variability of performances for the same drilling system remains high, and this is primarily linked to the heterogeneity and nonuniform nature of these carbonates as explained previously, incremented by occurrences of silicates and volcanics. While some layers are homogeneous with low variance of rock properties, others are highly heterogeneous and laminated. The optimal drilling parameters for one layer might not be appropriate for another and could even be destructive for the bit and the entire drilling system, not to mention that worn or broken inserts present variations in the overall bit behavior. A good characterization and understanding of each of these zones, in addition to their occurrence and possible thickness, would be beneficial for drilling optimization.

Thus far, industry efforts to improve the drilling performance in the Brazilian presalt carbonates have been driven by a costly trial and error approach in the ultradeepwater drilling environment. To avoid such approach, it is key to have a dynamic modeling system platform with the objective to identify solutions that improve drilling performance by minimizing drill string vibrations, optimizing drilling systems and recommend best drilling practices for a given environment. In previous works (Aguiar et al. 2016, Aguiar et al. 2019, Aguiar et al. 2022), a workflow was developed for a systematic drilling system optimization. The workflow consists of the following steps.

Stratigraphic Zonation for Drillability. Stratigraphic zonation is the process of defining groups of rocks with similar drillability characteristics. Similar approaches to this process have been applied in other fields of the petroleum industry, including rock typing and well log clustering, generally for reservoir identification and characterization (Hbaieb et al 2012). For the present work, two formations are considered with similar drillability if they exhibit similar performances in terms of ROP, vibration signature, and bit grading when drilled with similar drilling systems and operating parameters (Aguiar et al. 2016).

Advanced 4D Dynamic Drilling Simulation Software and the Virtual pre-Presalt Rock. An advanced 4D transient drillstring dynamics modeling package was used to design the drill-bit cutting structure, predict the drilling dynamics of the bit, and plan the BHA and drilling parameters. In this package, cutting structure rock interaction is captured through laboratory testing. Formation samples of various types were gathered and analyzed at a drilling laboratory in Houston, Texas (Aslaksen et al. 2006). Indentation and scraping tests were conducted under confining pressure to obtain accurate cutter rock response in conditions similar to downhole conditions. Rock files were then generated for each rock sample, which contained the testing results at various backrake angles, siderake angles, and bevel sizes.

This transient drillstring dynamics package requires the following input: rock properties, cutting structure design details, BHA components, formation characteristics (heterogeneous, anisotropy, and orientation), well trajectory, casing schematic, and borehole geometry (Compton et al. 2010; Aslaksen et al. 2006). The drillstring dynamics package can be used to model and evaluate drillstring stability, steerability, efficiency, and wellbore quality. In fact, the model has many applications, such as bit design and selection, BHA design, drilling parameters optimization, and post-run validation and analysis based on field data.

Coupled with the detailed cutting structure model of the bit, the transient dynamics analysis is able to accurately capture the excitation forces at the cutting elements and evaluate their influence on the drillstring dynamic response. Compared with other transient analysis types, transient analysis containing the cutting structure generates a high-fidelity model. This model yields the most accurate drillstring mechanics prediction available, in spite of the cost of computation time (Wang et al. 2014).

Fully Digital Bit Design Workflow. Commonly used for drill-bit selection, BHA optimization, and drilling parameters recommendations, the 4D simulation software was used in an innovative way for developing a new 12 ¼-in. bit design. Based on a calibrated model, supported by drilling data, wireline, and mud logging (Aguiar et al. 2019), all design interactions were tested inside of the 4D simulation software, simulating field conditions (rock formation, BHA, borehole, right heave, etc.). For such an accomplishment, a multidisciplinary approach was used. This effort made use of the service provider's bit designer, bits product engineer, a geologist, a petrophysicist, a modeling and simulation engineer, and the operator's engineering team. All of the simulation results were compared with the current drill bits being used in the field. The goal of this effort was to have the next bit design provide a step change in drilling performance.

RECENT DEVELOPMENTS: FIRST CASE STUDY, PETROBRAS BUZIOS FIELD

This work shows two recent project developments with different operators drilling Brazilian pre-salt reservoirs in Santos basin. The first work is with Petrobras drilling in Buzios field, located approximately 180 km off the Brazilian coast with the reservoir more than 5000-m deep (underground), the field currently has four stationary production units operating at about 2000 m of water depth. With excellent quality reservoirs to 480-m thick and 60 drilled wells, Búzios contains the largest volume of oil and gas in deep waters in the world. With a total daily production of 687,000 BOE consisting of 551,800 BOPD and 21.5 million m3/D, according to the June 2021 ANP (Brazilian National Petroleum Agency) bulletin. The Búzios field is an undeniable example of the enormous potential of the assets in the Brazilian presalt.

As part of the Búzios field exploratory and development campaigns in the Santos basin offshore Brazil, the operator's objective was to minimize drilling costs by eliminating unplanned trips into the wells. Accordingly, development of application-specific bit designs was required to optimize drilling efficiency in the wells with the goal of drilling the entire reservoir section in a single bit run. These specific bit designs were planned to challenge the various carbonate complexities within the field.

Project developments were divided in two parts as follows:

1.   For the 12 ¼-in. borehole section, the bit design development followed an innovative full-digital cycle. After completing the stratigraphic zonation, calibrated 4D drilling dynamics software was used to identify the virtual presalt carbonate rocks in the Buzios field. As a result, it was possible to perform a full drill-bit design cycle in the new digital workflow.

2.   For the 8 ½-in. borehole section, there was insufficient time to perform the full digital development as was performed for the 12 ¼-in. section. Instead, a more standard bit selection process took place. Due to the technology enablers, especially the presalt virtual rock and the 4D drilling dynamics simulation software, it was possible to select a bit from a current catalog of best fit-for-purpose drill bits for the application.

For the 12¼-in. section, the operator selected the field test well based on the reservoir carbonate complexity. The challenge in this section was to increase average ROP and ensure drill-bit durability to successfully drill the presalt carbonates of the Barra Velha and Itapema formations. A comprehensive prejob study was performed, which included formation evaluation analysis of offset wells, stratigraphic zonation applied in the offset wells to estimate which drill zones to be drilled, and 4D dynamic drilling simulation to recommend best drilling parameters for each drill zone.

As of result, we were able to drill the entire presalt carbonate reservoir section in one bit run, drilling 327 m with an effective ROP of 10.1 m/h (average ROP of 9.8 m/h). Compared with the offset wells, this bit run offered an 89% improvement in drilled footage and 136% ROP (Fig. 1). The bit was pulled out of the hole and showed low-cutting structure wear after drilling the 327 m of the presalt carbonates. The overall surface torque and drilling dynamics (shock and vibration levels at the BHA) were significantly lower when compared with offset runs.
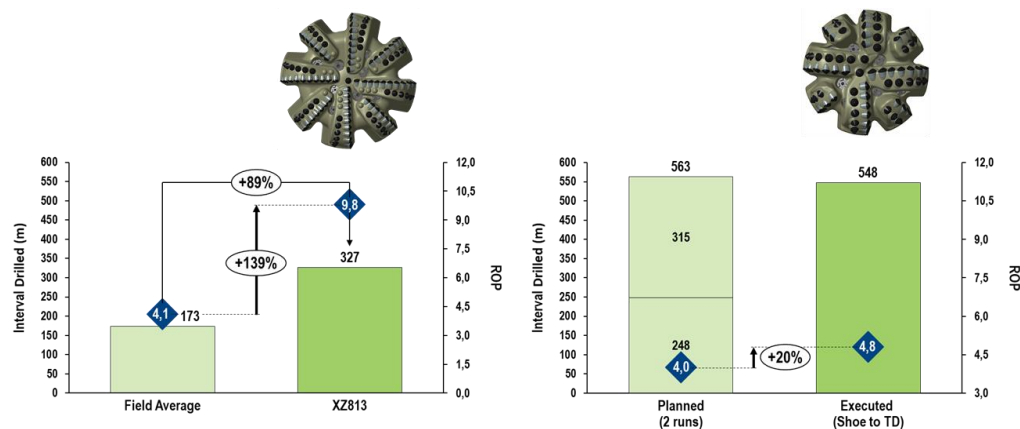

Fig. 1—Performance results in 12¼- in. section and 8½-in. section.

One important fact was observed when comparing the 4D dynamic drilling simulation results performed in the prejob with the field data. When comparing in what way drilling parameters (weight on bit and surface RPM) affect surface torque, ROP, and shock and vibration levels at the measurement-while-drilling and logging-while-drilling tools, there is very good agreement between prejob simulation predictions and the field data. This digital workflow made it possible to predict the drilling performance. It was even possible to predict cutting structure degradation using the calibrated 4D dynamic drilling simulation.

For the 8½-in. section, after selecting the bit, based on the calibrated rock formation inside the 4D drilling dynamics software, the results of the first well drilled exceeded operator expectations. The entire section was drilled in one bit run, whereas two bit runs were planned (Fig. 1). The bit drilled 548 m in this section with higher ROP than expected. This run represented a 23% reduction in rig hours, setting a new benchmark for the field and saving the operator significant time and costs. Combining the 12¼-in. and 8½in. bit run results, nine drilling runs followed using the improved workflow. The drilling runs averaged 300 m with a 6.5 m/h ROP, and two runs achieved double-digit ROP. These results represent a step change in drilling performance when compared with the offset wells drilled earlier not using this new digital workflow. Also, this performance improvement has not been matched in other blocks where the workflow was not applied.

RECENT DEVELOPMENTS: SECOND CASE STUDY, TOTALENERGIES LAPA FIELD

The Lapa field is a pre-salt field located in the Santos Basin, 300 km off the coast and in deep water depths of 2100 to 2200 m. The northeast field area development consists of two phases. A total of six wells were drilled in Phase 1 and four wells to be drilled in Phase 2 by the operator, of which two are producers and two are injectors.

The Brazilian pre-salt main reservoirs of the Santos Basin are within the Barra Velha formation, interpreted as alkaline shallow-lake deposits formed during the Gondwana rift phase (Aptian). Variance in paleo morphology and water composition are the drivers of faciological diversity on this lacustrine setting. This rich faciological assembly is composed of cyclic lithologies, such as buildups, spherulites, and laminites. The cyclic facies can appear in situ or reworked in the form of grainstones, rudstones, and wackstones. These facies also commonly present a strong diagenetical overprint from karstification, silicification, and dolomitization processes, which not only impact reservoir quality but can heavily create drilling challenges.

In previous works (Aguiar et al. 2016, Aguiar et al. 2019, Aguiar et al. 2022), a workflow was developed for a systematic drilling system optimization, as described. Initially, the calibrated model, validated on another pre-salt block (Aguiar et al. 2022), was used as a first approach in the Lapa field campaign. As a result, the model did not reproduce the actual field conditions, which shows the high level of heterogeneity of the pre-salt carbonate reservoirs in the Santos Basin. Therefore, the workflow had to be reset for this campaign. This is a possible indication that in some way, standard logs are not presenting the entire picture, which led to work presented.

High-Definition Borehole Imaging Tool

The work presented in this paper makes use of a new high-definition borehole image technology (Maeso et al. 2018). The logging tool adds 15 ft of sub to the drilling BHA and contains four sensors orthogonal to each other to acquire

ultrasonic images at two central frequencies in any type of mud. There are two electromagnetic sensors as well to acquire apparent resistivity images in oil-based mud; however, these sensors were not deployed for this campaign because the wells were drilled with water-based mud. The use of wireline and logging-while-drilling (LWD) advanced formation evaluation logs for additional reservoir characterization is a new approach, not fully explored in the industry. Also, the use of image logs to help be familiar with the challenges in the drilling operation is a new topic, at least to the authors of papers in recent literature. The high-resolution image data provide textural and hardness information, essential to the analysis of the formation's mechanical behaviour during drilling. By providing a more reliable model, the present study unlocks a spectrum of solutions beyond reservoir characterization, which will impact well planning, BHA, bit design, and ROP prediction.

The case study presented involves drilling the reservoir section in Phase 2 of the Lapa field development campaign. As mentioned previously, a total of four wells were drilled in Phase 2 by the operator, two being producers and two as injectors. Although in all of the wells, the service company was able to drill the entire reservoir section in single-bit runs, the bit became dull in all four wells, different from the typical pre-salt reservoir section drilling in other Santos Basin blocks. Generally, in the reservoir intervals, operators encounter ring-out dullness characteristics on the shoulder of the bit or core-out on the cone area, usually related to drilling dynamics. Fig. 2 shows a comparison between typical bit dullness used in the reservoir section and a dull bit used to drill the last well in the Lapa Phase 2.

(a) (b)

Fig. 2—Comparison of (a) typical dull bit used in the reservoir section, and (b) dull bit used to drill the last well in Lapa Phase 2.

Using as example the last run, in terms of drilling dynamics, the run showed low levels of shock and vibration. Examining the ROP, there appears to be two major intervals; i.e., the first interval with constant, low ROP (approximately the first 50 m) and a second interval where the ROP is higher and also presents higher variation.

When observing the mechanical specific energy (MSE) (Teale 1965), additional comprehensive drill zones are observed. Contained in the first ROP interval (first 50 m drilled) are intervals A and B as shown in Fig. 5. Interval A contains the first 30 m, with the highest levels of MSE in the entire drilled section. The following interval B consists of the following 20 m, showing a decrease in MSE. The following interval C, which is the final 80 m contains the lowest levels of MSE and lower variation of MSE. The last interval consists of the last 20 m drilled and shows similar behavior as in Interval B.

Formation Evaluation Analysis Using the High-Definition Borehole Imaging Tool. The high-resolution acoustic image log was interpreted using an unsupervised textural clustering method (dos Santos et al. 2022) and tensorboard (Abadi et al. 2015). The interpretation module divides the borehole image vertically in intervals of 180 pixels with an overlap of 75% between each subsampled image. The module first extracts 11 first- and second-order statistic properties, and then applies the t-distributed Stochastic Neighbor Embedding method, which generates a 3D similarity plot. Each cluster presents a variety of features such as dip angle, thickness, and acoustic impedance (associated with mineralogy). There are two main groups of clusters, including:

• Lower dips, thin-to-medium laminated with varied acoustic impedance, concentrated on the upper interval and the very bottom indicated in shades of green. This group consists of the MSE intervals A, B, and D (see Fig. 3).

• Higher dips with changing stacking patterns, karstified zones, homogeneous mineralogy, distributed in the mid to bottom interval, indicated in shades of blue. This group overlaps with the MSE interval C (see Figs. 3).

Facies with higher acoustic impedance were associated with a low ROP and high MSE. The facies with greater acoustic impedance had greater ROP average and low MSE values. On the mid-bottom interval, the facies with the highest dissolution signatures (karsts), were also linked with abnormal ROP peaks.
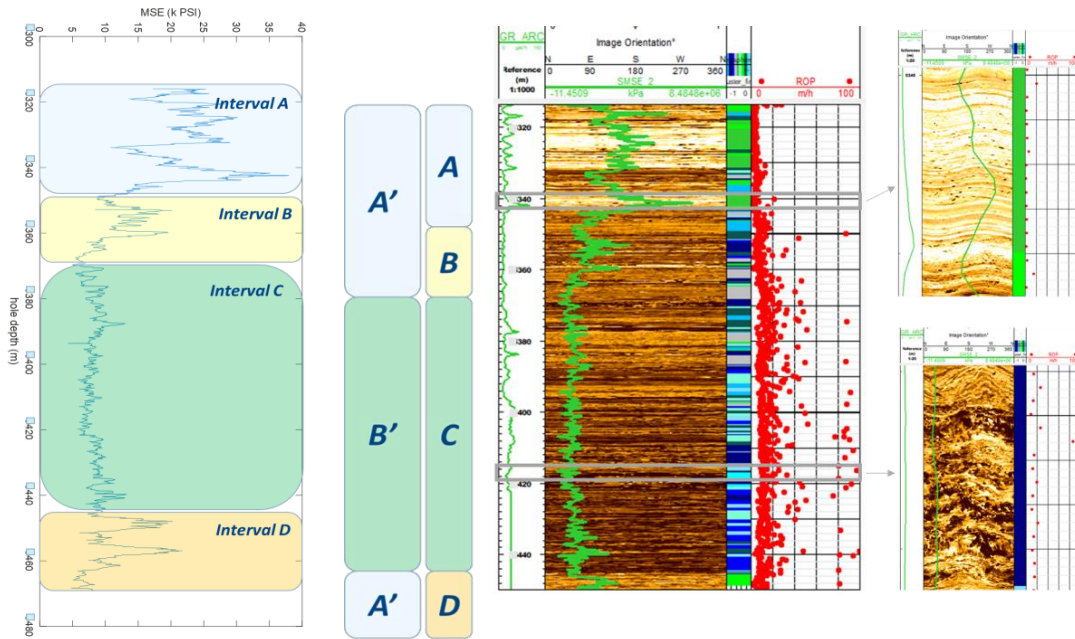
Fig. 3— LEFT: MSE drilling data along the borehole depth. RIGHT: reinterpreted zones (A' and B'), the MSE zones (A, B, C, and D), the depth track with gamma ray, the MSE and borehole image log, textural clusters, and the ROP. The image on the upper-right is an example of Group A' interval with low ROP; and on the bottom-right, an image with karsts and ROP peaks.

Even with the 4D drilling simulator reproducing field conditions, it is not yet possible to identify the root cause of the drillbit dullness. The next task is to use the high-definition borehole imaging tool logs aligned with the drilling data and investigate for unusual events that could lead to the final drillbit dullness condition. When drilling the interval B', as observed during the geological evaluation, field data shows several peaks in the ROP channel. The instantaneous ROP peaks vary between 40 and 90 m/hr, where the average ROP of the interval B' is approximately 15 m/hr (see Fig. 11). It is important to emphasize that the high-definition Borehole Imaging Tool is the only tool capable of observing such vugs. As shown in Fig. 4, there are no changes in other logs due to the presence of karsts.
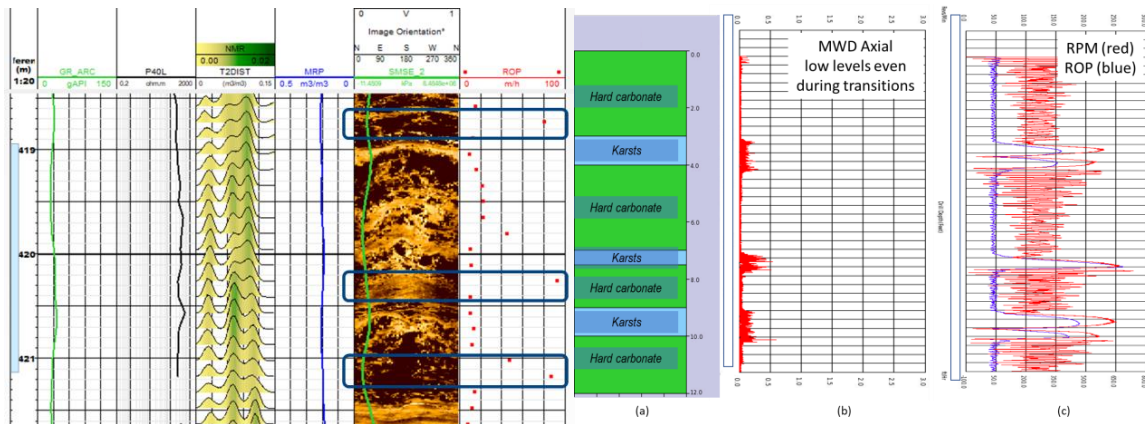
Fig. 4— LEFT: Correlating karsts and ROP peaks in Interval B'. Other logs do not show any changes when passing through the karst. RIGHT: Simulation of drilling through carbonate with karsts. (a) Rock diagram vs. depth; (b) MWD axial vibrations, (c) RPM and ROP.

Similar to what is observed in actual drilling conditions, there is a strong correlation between the ROP peaks and the presence of the karsts; thus, the 4D drilling simulator captures the same phenomenon. Interesting to note, there is not a solid correlation between the ROP peaks and the axial vibration measured by the MWD tool. In fact, examining the drilling data shows there are no spikes in the MWD axial vibrations when drilling the karsts. Simulation results show that such a small drilling break do not translate into a peak in the MWD axial vibration. Therefore, the simulation results match the observation on the image logs and drilling data. Because there is a certain level of confidence that the 4D drilling simulator reproduces the field conditions when drilling the karsts, the next task is to observe what takes place with the drill-bit cutters when drilling in such interbedded scenarios. The main results of this analysis are shown in Fig. 5.
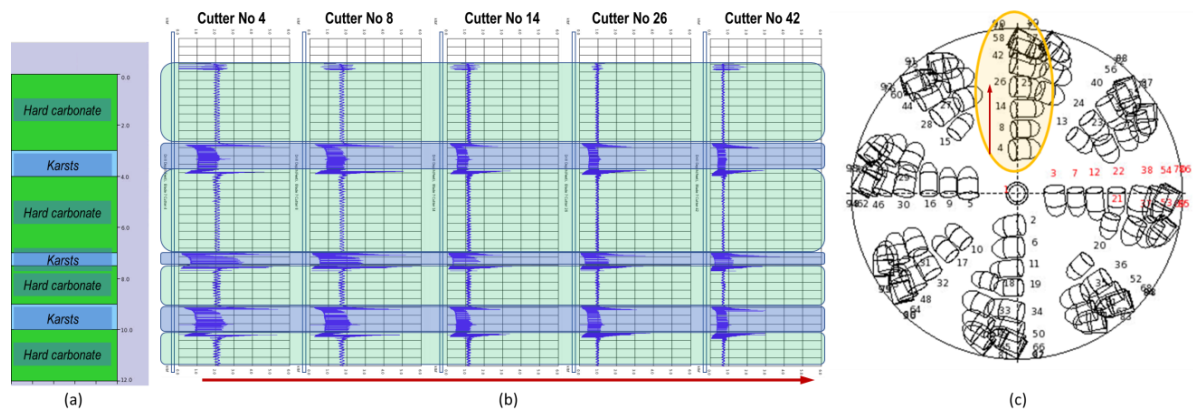
Fig. 5—Simulation of drilling through carbonate with karsts. (a) Rock diagram vs. depth; (b) normal force over depth of cutters #4, #8, #14, #26, and #42; (c) drill bit image showing cutter numbers and locations.

Fig. 5 shows the results from the 4D drilling simulator when drilling in a transitional scenario. The charts shown are the bit cutter normal force in addition to one of the drill-bit blades. Cutter number 4 (far left) is the innermost cutter of that blade, whereas cutter number 42 (far right) is in the middle of the blade. As shown, when drilling through the karsts, there is a peak in the cutter normal force. Also, the highest values of the peaks are related to the cutters located in the inner portion of the blade (cutters number 4, number 8, and number 14). The normal force is responsible for chipping and separation of the cutters. Therefore, it is fair to say in terms of the drill-bit normal force, the drill-bit cone area has the highest peaks. This observation is in line with drill-bit dullness (Fig. 2(a)), where highest dullness is at the cone.

Comprehending the underlying root causes for the low drilling efficiency is important to obtaining the solution delivery. It is essential to identify the cutter failure mechanism while drilling through complex hard and impact-prone lithologies, such as the pre-salt reservoir, and propose customized solutions to alleviate the damage. While drilling though the karsts, such a challenging formation can produce drilling breaks that lead to premature PDC cutter damage, unbalanced cutting structure workload, and eventually costly unwanted BHA trip. As of today, it is a challenge to predict what is happening downhole; thus, it is of the utmost importance to use a virtual calibrated formation plan, which can better reproduce the actual drilling conditions to create a suitable cutting structure.

To design a new cutting structure for this application, two approaches were selected. The first approach is to replace the flat PDC cutters with 3D cutters. The second approach is to apply drill-bit design features and evaluate different design concepts using the 4D dynamic drilling simulator. Both approaches aimed to improve cutting structure durability against cutter impact damage, by enhancing cutter resistance to tangential loads as well as reducing the cutter normal forces. To prevent premature failure and to optimize drilling efficiency, a novel eight-bladed, 13-mm cutter drill bit was designed and optimized specifically for this pre-salt application using a virtual calibrated formation plan. The goal was to improve the cutting structure durability, mainly on the cone and nose areas, to prolong cutting structure sharpness, and to yield superior overall ROP. These goals were achieved by examining how the new design compared with the baseline in the calibrated model to ensure that the changes being made resulted in less drill-bit cutter normal forces to allow for smoother drilling and in turn, prolong the cutting structure life (Fig. 6).
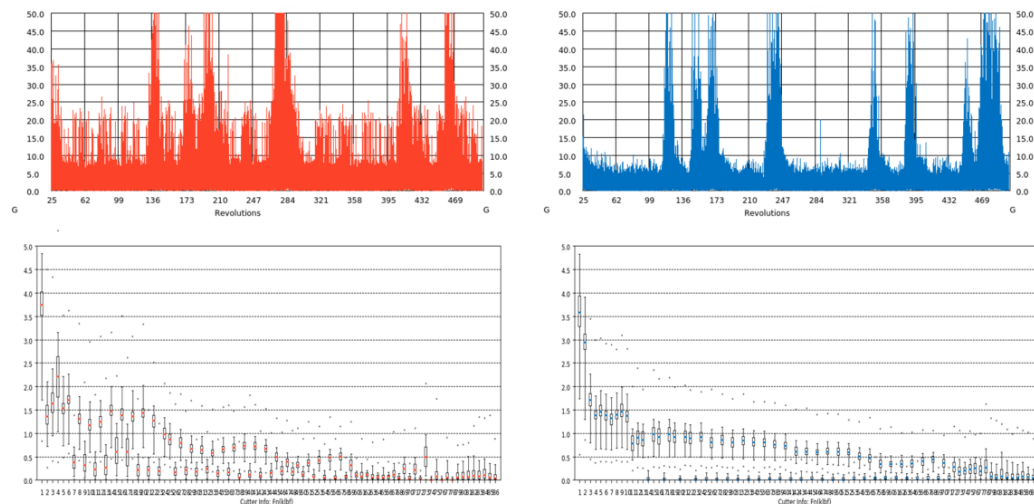
Fig. 6—Dynamic simulation results showing a more stable behavior from the new-concept PDC drill-bit design compared with the reference PDC drill bit.

CONCLUDING REMARKS

On the first case study, this paper has presented the implementation of an improved, fully digital bit design workflow. The workflow integrates a calibrated 4D dynamic simulation model and petrotechnical expertise from drilling engineering, geomechanics, geology, and petrophysics groups to continue to push the drilling performance envelope in the challenging Brazilian presalt exploration and development. In a collaboration between different engineering teams, decisions included selecting a specific design features of the drill bit. The features, which encompassed cutters selection, cutting structure layout to the blade top features, were made inside the 4D dynamic simulation software. The results were tested in the presalt virtual rock, under the actual drilling conditions.

This system engineering workflow highlighted the integration efforts between multidisciplinary teams, leading to success in different borehole sizes when drilling the carbonate reservoirs in this challenging Brazilian presalt interval. In the 12¼-in. borehole, an innovative bit design produced an 89% improvement in footage drilled and 136% improvement in ROP compared with the field average. In the 8½-in. borehole, a thorough investigation of current available drill bits led to a customized bit selection, resulting in one-bit run interval to reach section total depth.

On the second case study, this paper has presented the implementation of an improved, digital bit design workflow based on high-resolution borehole image logs. The workflow integrates a calibrated 4D dynamic simulation model and petrotechnical expertise from drilling engineering, geomechanics, geology, and petrophysics groups. The combination of the improved workflow and petrotechnical expertise have improved the drilling performance envelope in the challenging Brazilian pre-salt exploration and development. The textural and faciological grouping was translated into rock files for the in-house 4D dynamic drilling simulator. The rock files are digital representations of the rock in the drilling simulation software. This software can reproduce laminations, beddings, pores, nodules, and hardness, features that are best described by the borehole images. The high-resolution image data provided textural and hardness information, essential to the analysis of the formation's mechanical behavior during drilling. By providing more reliable modelling than previously available, this study has unlocked a spectrum of solutions beyond reservoir characterization, which will impact well planning, BHA and bit design, and ROP prediction.

ACKNOWLEDGMENTS

REFERENCES

Abadi, M., Agarwal, A., Barham, P. et al. 2015. TensorFlow: Large-Scale Machine Learning on Heterogeneous Distributed Systems. Download available from tensorflow.org.

Aguiar, R.R., Hbaieb, S., Azar, M. et al. 2016. Optimization of the PDC/ CDE Hybrid Cutting Structure Developed to Drill the Pre-salt Carbonates Reservoirs Offshore Brazil. Paper presented at the Rio Oil & Gas Expo and Conference, Rio de Janeiro, Brazil, 24–27 October. IBP1296_16.

Aguiar, R.R., Tocantins, J.P., Marquinez, V. et al. 2019. Drilling Optimization Using Model-Based Design and Stratigraphic Zonation: Successful Application in Brazilian Deep Water Pre-Salt Carbonate. Paper presented at the SPE ATCE, Alberta, Calgary, Canada, 30 September–2 October. SPE-196057-MS. https://doi.org/10.2118/196057-MS.

Aguiar, R.R, Lima, L, et al. 2023. Using LWD Borehole Image interpretation for Drilling Optimization: A Brazilian Pre-Salt Case Study. Presented at the Offshore Technology Conference, May 1-4. OTC-32549-MS.

Aslaksen, H., Annand, M., Duncan, R. et al. 2006. Integrated FEA Modeling Offers System Approach to Drillstring Optimization. Paper presented at the SPE/IADC Drilling Conference, Miami Beach, FL, 21–23 February. IADC/SPE 99018-MS.

Compton, M., Verano, F., Nelson, G. et al. 2010. Managing Downhole Vibrations for Hole-Enlargement-While-Drilling in Deepwater Environment: A Proven Approach Utilizing Drillstring Dynamics Model. Paper presented at the SPE Latin American & Caribbean Petroleum Engineering Conference. Lima, Peru, 1–3 December. SPE 139234-MS. https://doi.org/10.2118/139234-MS.

dos Santos, L. L. A., Bize-Forest, N., da Fraga Carneiro, G. et al. 2022. Unsupervised Facies Pattern Recognition of Brazilian Pre-Salt Carbonates Borehole Images. Presented at the SPWLA 63rd Annual Logging Symposium, Stavanger, Norway, 11–15 June. SPWLA-2022-0129. https://doi.org/10.30632/SPWLA-2022-0129.

Hbaieb, S., Pirovolou, D., Fonseca, C. Et al. 2012. Stratigraphic Zonation Applied for Drillability - Motivation and Proposed Workflow. Paper presented at the Rio Oil & Gas Expo and Conference, Rio de Janeiro, Brazil. IBP17325_12.

Maeso, C., Legendre, E., Hori, H. et al. 2018. Field Test Results of a High Resolution, Dual Physics Logging-While-Drilling Imaging Tool in Oil Base Mud Presented at SPWLA 59th Annual Logging Symposium, London, UK, 2–6 June. SPWLA-2018-U.

Orban, N., Gark, S., Shaldaev, M. et al. 2021. Assessment of new high-definition borehole imaging while drilling technology: learning from the pre-salt carbonates of Brazil. Presented at the SPWLA 62nd Annual Logging Symposium, Virtual event, 17–20 May. SPWLA-2021-0050; https://doi.org/1030632/SPWLA-2021-0050.

Teale, R. 1965. The Concept of Specific Energy in Rock Drilling. Intl. J. Rock Mech. Mining Sci. 2 (1): 57–73.

Wang, Y., Shen, Y., Charter, M. et al.2014. High Frequency Vibration Measurement Coupled with Time-Based Dynamic Simulations: New System to Predict/Solve Instability Issues. Paper presented at the SPE Annual Technical Conference and Exhibition. Amsterdam, The Netherland, 27–29 October. SPE 170708-MS. https://doi.org/20.2118/170708-MS.

Wright, V. and Barnett, A. 2015. An abiotic model for the development of textures in some South Atlantic early Cretaceous lacustrine carbonates. Geological Society, London, Special Publications, 418 (2012): 1–11.

RESPONSIBILITY NOTICE

The authors are the only responsible for the printed material included in this paper.

A PDE-ODE Model For The Regenerative Effect In Lateral Cutting Processes: From Milling To Bit Whirl

Kaidong Chen – Eindhoven University of Technology (Netherlands)
Emmanuel Detournay – University of Minnesota (USA)
Nathan van de Wouw – Eindhoven University of Technology (Netherlands)

A PDE-ODE Model For The Regenerative Effect In Lateral Cutting Processes: From Milling To Bit Whirl

Kaidong Chen[1], Emmanuel Detournay[2], and Nathan van de Wouw[1]

[1] Department of Mechanical Engineering, Eindhoven University of Technology, P.O.Box 513, 5600MB Eindhoven, The Netherlands

[2] Department of Civil, Environmental and Geo-Engineering, University of Minnesota, Minneapolis, MN 55455, USA

Abstract: The regenerative effect refers to the dependance of the depth of material removed by a cutter on the motion history of the cutting tool. This phenomenon, which exists in various machining processes, as well as in deep drilling to access earth resources, is recognized as a root cause of harmful vibrations in these operations. Here we introduce a model in terms of a partial differential equation (PDE) to compute the regenerative chip thickness in the milling process. By combining this PDE model with an ordinary differential equation (ODE) describing the tool dynamics, a system of PDE-ODE equations to model the self-excited vibrations of a milling tool is formulated. It is proved analytically that the proposed PDE-ODE model can be simplified to the classical delay differential equation (DDE) model. From this perspective, the DDE model is more efficient in specific (though common) scenarios while the PDE-ODE model can be more accurate in extreme scenarios, such as in the case of large axial depth of cut. This paper concludes with a brief discussion on how to extend the proposed model PDE-ODE model to the bit whirl problems in drilling industry.

Keywords: Milling, Regenerative Effects, PDE-ODE, Drilling, Bit Whirl

INTRODUCTION

Removing material from a solid body using a tool equipped with multiple cutters is a common operation in multiple machining processes, such as turning (Wahi and Chatterjee, 2008), milling (Chen *et al.*, 2024), and drilling (Roukema and Altintas, 2006), as well as in deep drilling to access earth resources (Zhang *et al.*, 2023). In all these processes, the cutters interact with a solid material surface previously machined by the same cutting tool. As a result, the amount of material removed by the cutters, also known as depth of cut or chip thickness, strongly depends on the history of the motion of the cutting tool. This dependence is referred to as the regenerative effect (Stepan *et al.*, 2004). The chip thickness further affects the cutting force on the tool, which in turn affects the motion of the cutting tool through tool dynamics. As illustrated in Figure 1, a loop of self-excited vibration is formed, which is recognized as a root cause of the harmful oscillations in these processes (Richard *et al.*, 2007; Stepan *et al.*, 2004).
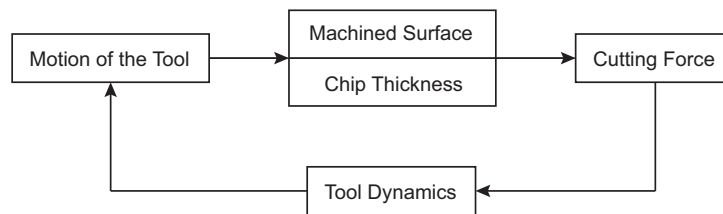
Figure 1 – Loop of self-excited vibration in regenerative machining processes.

Conventional models compute the regenerative depth of cut using the current (at time t) and previous (at time $t - \tau$) positions of the center of the tool, leading to the formulation of a delay differential equation (DDE) (Richard *et al.*, 2007; Stepan *et al.*, 2004). Here τ is the time delay. However, the classical DDE formulation is invalid when the tool is cutting the outer region of the workpiece (for example, when $t < \tau$), or for large-amplitude tool vibrations leading to fly-over (Niu *et al.*, 2021), or when multiple regenerative effects (Wahi and Chatterjee, 2008) occur. Targeting these limitations, recent efforts have led to the formulation of an alternative approach, where the regenerative depth of cut is determined through a partial differential equation (PDE) model governing the evolution of the machined surface (Wahi and Chatterjee, 2008; Zhang *et al.*, 2023). However, these models are not applicable for lateral cutting processes such as milling (Chen *et al.*, 2024) and bit whirl in drilling (Kovalyshen, 2013).

This abstract first introduces a PDE method (Chen *et al.*, 2022) to compute the regenerative chip thickness in the milling process. By combining this PDE model with an ordinary differential equation (ODE) describing the tool dynamics, a PDE-ODE system (Chen *et al.*, 2024) is then formulated to model the self-excited vibrations of a milling tool. It is proven that the PDE-ODE and the DDE approaches are equivalent under specific assumptions. Utilizing the boundary conditions

implied by these assumptions, the PDE of the PDE-ODE system is solved analytically and the PDE-ODE formulation is accordingly transformed to a DDE. From this perspective, DDE models can be viewed as a simplifying approximation of the PDE-ODE model. As a result, the DDE model is more computationally efficient than the PDE-ODE model in specific (though common) scenarios but can be less accurate in extreme cases. Finally, the extension of the proposed PDE-ODE model to simulate bit whirling in the drilling industry is briefly discussed.

CHIP THICKNESS COMPUTATION USING PDE METHOD

Surface Function

As illustrated in Figure 2(a), the evolving geometry of the machined surface around the mill can be described by the surface function $r(\theta, t)$. This function expresses that the distance r between the center of the tool O and an arbitrary surface point P is a function of the orientation θ of point P and time t. Here θ is the angle between line $\overline{OP}$ and the y-axis of the bit frame (x, y). For the sake of simplicity, the y-axis is aligned with an arbitrary cutter and the x-axis is set orthogonal to this cutter. This reference cutter is numbered as cutter 1 and the other cutters are sequentially numbered clockwise. Using this surface function, the depth of cut ahead of cutter i ($i = 1, 2, \ldots, N$ with N denoting the total number of the cutters) can be computed according to (Chen *et al.*, 2022):

$$h_i = \max \left\{ 0, R - r \left(\theta_i^+, t \right) \right\}, \qquad i = 1, 2, \ldots, N, \tag{1}$$

where R is the distance between the center of the tool and the edge of the cutter, θ_i is the direction of cutter i with respect to the y-axis. Notation $r\left(\theta_i^+, t\right)$ is used to denote the right limit of function $r(\theta, t)$ at $\theta = \theta_i$, which represents the distance between the center of the tool and the surface ahead of cutter i. It is noted that throughout this abstract, we only consider full radial immersion milling.
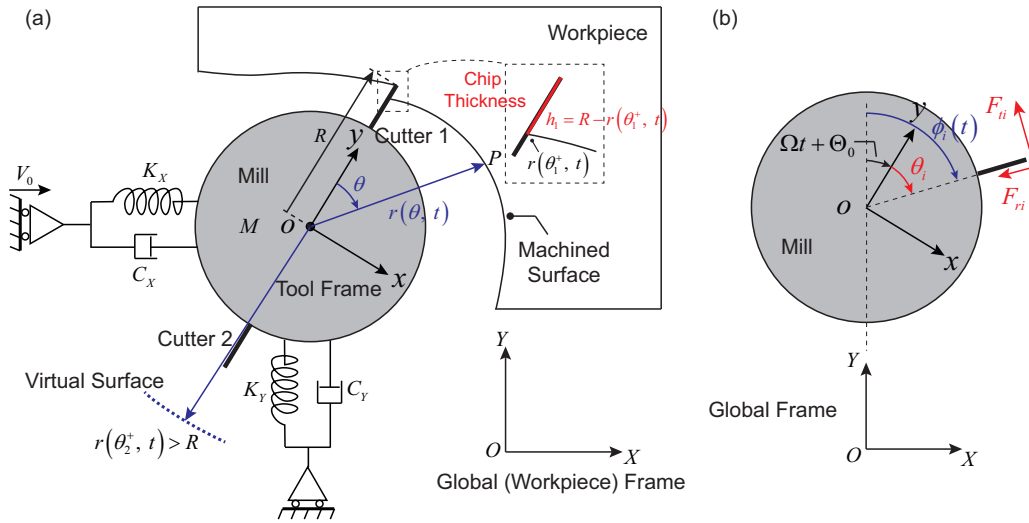
Figure 2 – (a) The mass–spring–damper model of the milling tool/machine dynamics. (b) Coordinate transformation of the cutting force at the cutter. Adopted from (Chen *et al.*, 2024).

PDE Governing the Evolution of the Surface Function

According to Chen *et al.* (2022), the evolution of the surface function around the tool is governed by a conservation law with a source term:

$$\frac{\partial r}{\partial t} + \frac{\partial f}{\partial \theta} = \psi \tag{2}$$

with

$$f(r, \theta, t) = -\Omega r - V_t \ln(r), \quad \psi(r, \theta, t) = V_r \left[\ln(r) - 1\right]. \tag{3}$$

For an arbitrary surface point P, term $V_r = V \sin(\theta + \Omega t + \Theta_0 + \Phi)$ is the radial component of the velocity of the center of the mill along line $\overline{OP}$, while $V_t = V \cos(\theta + \Omega t + \Theta_0 + \Phi))$ is the tangential component vertical to line $\overline{OP}$. Here, Ω is the spindle speed of the mill, V is the magnitude of the tool center measured in the global frame (X, Y), Φ is the direction of the velocity with respect to the X-axis, and Θ_0 is the initial angle between the bit frame (x, y) and the global frame (X, Y) at $t = 0$.

Conditions at Cutters

According to Chen *et al.* (2022), the material removal process at cutter *i* is described by:

$$r\left(\theta_i^-, t\right) = \max\left\{r\left(\theta_i^+, t\right), R\right\}, \qquad i = 1, 2, \ldots, N, \tag{4}$$

where $r\left(\theta_i^-, t\right)$ is the left limit of function $r(\theta, t)$ at $\theta = \theta_i$; it represents the distance between the center of the tool and the machined surface just created by cutter *i*. Equation (4) is a general expression of two cutting scenarios: (i) normal cutting $(R > r\left(\theta_i^+, t\right))$ where a new material surface is created by the cutter with Eq. (4) accordingly becoming $r\left(\theta_i^-, t\right) = R$; (ii) fly-over $(R \leq r\left(\theta_i^+, t\right))$ where the material surface remains continuous and Eq. (4) becomes $r\left(\theta_i^-, t\right) = r\left(\theta_i^+, t\right)$.

As mentioned earlier, Cutter 1 is aligned with the *y*-axis ($\theta_1 = 0$). For $\theta \in [0, 2\pi]$, the boundary value of the surface function can be alternatively expressed as: $r(0, t) = r(\theta_1^+, t)$ and $r(2\pi, t) = r(\theta_1^-, t)$. Therefore, the material removal condition (4) also serves as the boundary condition of the PDE (2) when $i = 1$.

Equations (2) - (4) form a PDE system governing the evolution of the surface function. By solving this PDE, the chip thickness ahead of a cutter is readily determined through Eq. (1).

PDE-ODE MODEL FOR SELF-EXCITED VIBRATION IN MILLING

Tool Dynamics

As illustrated in Figure 2 (a), the dynamics of the milling tool is modeled by a mass-spring-damper system (Faassen *et al.*, 2006):

$$M_X\ddot{X}_T + C_X\left(\dot{X}_T - V_0\right) + K_X\left(X_T - V_0 t\right) = F_X$$
$$M_Y\ddot{Y}_T + C_Y\dot{Y}_T + K_Y Y_T = F_Y, \tag{5}$$

where $X_T(t)$ and $Y_T(t)$ are the coordinates of the tool center in the global frame (X, Y), V_0 is the prescribed velocity of the center of the tool along the *X*-axis, and M_I, C_I, and K_I are the mass, damper, and stiffness parameters along I ($I = X, Y$) direction. Terms $F_X = \sum_{i=1}^{N} F_{Xi}$ and $F_Y = \sum_{i=1}^{N} F_{Yi}$ are the total cutting forces along *X*- and *Y*- directions. Here F_{Xi} and F_{Yi} are cutting force components of cutter *i*, which are determined through a coordinate transformation from the cutter frame to the global frame, see Figure 2 (b):

$$\begin{bmatrix} F_{Xi} \\ F_{Yi} \end{bmatrix} = \begin{bmatrix} -\cos\phi_i(t) & -\sin\phi_i(t) \\ \sin\phi_i(t) & -\cos\phi_i(t) \end{bmatrix} \begin{bmatrix} F_{ti} \\ F_{ri} \end{bmatrix}, \tag{6}$$

where $\phi_i(t) = \theta_i + \Omega t + \Theta_0$ is the direction of cutter *i* with respect to the *Y*-axis, and F_{ti} and F_{ri} are the tangential and radial cutting force components on cutter *i* (Chen *et al.*, 2024):

$$F_{ti} = K_t a_p h_i^\beta(t), \qquad F_{ri} = K_r a_p h_i^\beta(t), \qquad i = 1, 2, \ldots, N, \tag{7}$$

where K_t, K_r, and $0 \leq \beta \leq 1$ are cutting parameters, and a_p is the axial depth of cut (Chen *et al.*, 2024).

PDE-ODE Formulation

The ODE system (5) - (7) governing tool dynamics and the PDE system (1) - (4) governing the evolution of the machined surface around the mill are coupled following the logic illustrated in Figure 1, and a PDE-ODE system describing the self-excited vibration of a milling tool is correspondingly formulated, see Figure. 3(a). It is noted that the magnitude and direction of the velocity of the center of the tool are determined from $V = \sqrt{\dot{X}_T^2 + \dot{Y}_T^2}$ and $\tan\Phi = \dot{Y}/\dot{X}$.

COMPARISON BETWEEN PDE-ODE AND DDE MODELS

Figure 3(b) illustrates the formulation of a DDE model (Faassen *et al.*, 2006). Comparing Figure 3 (a) and (b), the DDE and PDE-ODE models have two main differences.

First, the DDE model compute the chip thickness using a different formula:

$$\bar{h}_i(t) = \sin\phi_i(t)\left[X_T(t) - X_T(t - \tau)\right] + \cos\phi_i(t)\left[Y_T(t) - Y_T(t - \tau)\right] + R - R\cos\left(\Omega\tau - \bar{\theta}\right), \tag{8}$$

where $\bar{\theta} = 2\pi/N$ is the angle between neighboring cutters, and $\tau = \frac{\bar{\tau}\bar{\theta}r}{f_z\cos\phi_i(t) + \bar{\theta}r}$ is the time delay. Here $\bar{\tau} = \bar{\theta}/\Omega$ and $f_z = \frac{2\pi V_0}{N\Omega}$ is the feed per tooth.

Second, the DDE model adds an additional function $g_i(\phi_i(t))$ to the cutting force components:

$$F_{ti} = K_t a_p \bar{h}_i^\beta(t) g_i(\phi_i(t)), \qquad F_{ri} = K_r a_p \bar{h}_i^\beta(t) g_i(\phi_i(t)), \qquad i = 1, 2, \ldots, N \tag{9}$$

(a)

PDE of the Evolution of Machined Surface

$$f = -\Omega r - V_t \ln(r) \qquad \frac{\partial r}{\partial t} + \frac{\partial f}{\partial \theta} = \psi$$
$$\psi = V_r \left[\ln(r) - 1 \right]$$

Chip Thickness $\quad h_i = \max\left\{ 0, R - r\left(\theta_i^+, t\right) \right\}$

Motion of the Tool

$$V_r = V \sin\left(\theta + \Omega t + \Theta_0 + \Phi\right)$$
$$V_t = V \cos\left(\theta + \Omega t + \Theta_0 + \Phi\right)$$
$$V = \sqrt{\dot{X}_T^2 + \dot{Y}_T^2}$$
$$\tan\Phi = \dot{Y}_T / \dot{X}_T$$

Cutting Force

$$F_{ti} = K_t a_p h_i^\beta(t) \qquad F_{ri} = K_r a_p h_i^\beta(t)$$
$$\begin{bmatrix} F_{Xi} \\ F_{Yi} \end{bmatrix} = \begin{bmatrix} -\cos\phi_i(t) & -\sin\phi_i(t) \\ \sin\phi_i(t) & -\cos\phi_i(t) \end{bmatrix} \begin{bmatrix} F_{ti} \\ F_{ri} \end{bmatrix}$$
$$F_X = \sum_{i=1}^N F_{Xi} \qquad F_Y = \sum_{i=1}^N F_{Yi}$$

ODE of Tool Dynamics

$$M_X \ddot{X}_T + C_X\left(\dot{X}_T - V_0\right) + K_X\left(X_T - V_0 t\right) = F_X$$
$$M_Y \ddot{Y}_T + C_Y \dot{Y}_T + K_Y Y_T = F_Y$$

(b)

Chip Thickness

$$\bar{h}_i(t) = \sin\phi_i(t)\left[X_T(t) - X_T(t - \tau) \right]$$
$$+ \cos\phi_i(t)\left[Y_T(t) - Y_T(t - \tau) \right]$$
$$+ R - R\cos\left(\Omega\tau - \bar{\theta}\right)$$

$$\bar{\tau} = \frac{\bar{\theta}}{\Omega} \qquad \tau = \frac{\bar{\tau}\bar{\theta}R}{f_z \cos\phi_i(t) + \bar{\theta}R}$$

Motion of the Tool

$$X_T(t) \quad Y_T(t)$$
$$\phi_i(t) = \theta_i + \Omega t + \Theta_0$$
$$f_z = \frac{2\pi V_0}{N\Omega} \quad \bar{\theta} = \frac{2\pi}{N}$$

Cutting Force

$$F_{ti} = K_t a_p \bar{h}_i^\beta(t) g\left(\phi_i(t)\right)$$
$$F_{ri} = K_r a_p \bar{h}_i^\beta(t) g\left(\phi_i(t)\right)$$
$$\begin{bmatrix} F_{Xi} \\ F_{Yi} \end{bmatrix} = \begin{bmatrix} -\cos\phi_i(t) & -\sin\phi_i(t) \\ \sin\phi_i(t) & -\cos\phi_i(t) \end{bmatrix} \begin{bmatrix} F_{ti} \\ F_{ri} \end{bmatrix}$$
$$F_X = \sum_{i=1}^N F_{Xi} \qquad F_Y = \sum_{i=1}^N F_{Yi}$$

ODE of Tool Dynamics

$$M_X \ddot{X}_T + C_X\left(\dot{X}_T - V_0\right) + K_X\left(X_T - V_0 t\right) = F_X$$
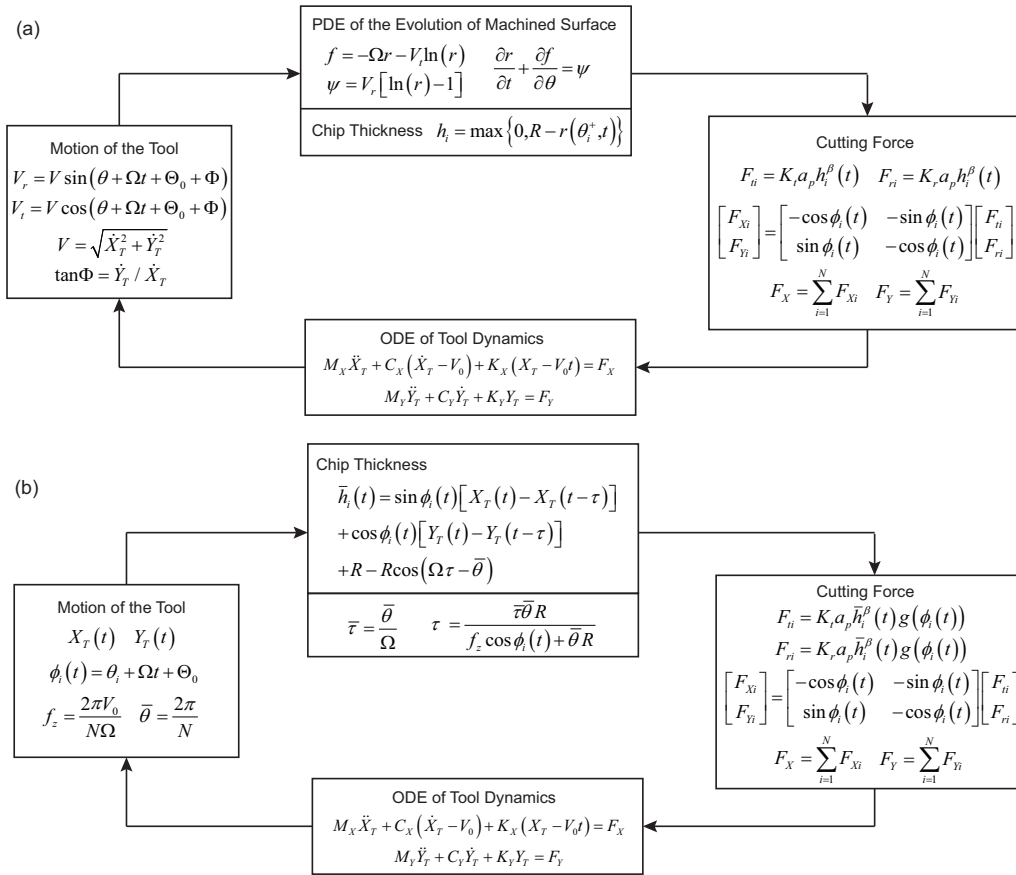$$M_Y \ddot{Y}_T + C_Y \dot{Y}_T + K_Y Y_T = F_Y$$

Figure 3 – (a) The PDE-ODE system describing the self-excited vibration of a milling tool. (b) The DDE model describing the self-excited vibration of a milling tool.

with

$$g_i\left(\phi_i(t)\right) = \begin{cases} 1, & \phi_s \le \phi_i(t) \le \phi_e \\ 0, & \text{otherwise}. \end{cases} \tag{10}$$

where ϕ_s and ϕ_e are the entry and exit angles (Faassen *et al.*, 2006).

In this section, we will prove that the PDE-ODE model can be simplified to a DDE model (Faassen *et al.*, 2006) under the following three assumptions.

Assumption 1: The machined surface interacting with cutter i is created by the neighboring previous cutter $i+1$ and there is no fly-over (Niu *et al.*, 2021), see Figure 4.

Assumption 2: The early-stage behavior when the tool cuts the outer boundary of the workpiece (Chen *et al.*, 2022, 2024) is not considered.

Assumption 3: The prescribed motion of the tool, translational motion with a constant velocity V along X-direction, plays a dominant role in the calculation of time delay and entry and exit angles.

As illustrated in Figure 4, by assuming that the material surface ahead of cutter i is created previously by the neighboring cutter $i+1$ (Assumption 1), we only need to consider the material surface between these two cutters. As a result, the range of θ is reduced from $\theta \in [0, 2\pi]$ to $\theta \in [\theta_i, \theta_{i+1}]$, and a new boundary condition need to be accordingly defined at $\theta = \theta_{i+1}$. When there is no fly-over, cutter $i+1$ is always in the cutting mode ($R > r\left(\theta_{i+1}^+, t\right)$), thus the boundary condition at $\theta = \theta_{i+1}$ is obtained from Eq. (4): $r\left(\theta_{i+1}^-, t\right) = R$. According to Assumption 2, the influence of the initial condition is ignored and the PDE (2) is solved using the boundary condition at $\theta = \theta_{i+1}$. In summary, a simplified PDE system is obtained:

$$\frac{\partial r}{\partial t} - \left[\Omega + \frac{V \cos\left(\phi(t) + \Phi\right)}{r(\theta, t)} \right] \frac{\partial r}{\partial \theta} = -V \sin\left(\phi(t) + \Phi\right), \quad \theta \in [\theta_i, \theta_{i+1}], \quad r\left(\theta_{i+1}^-, t\right) = R. \tag{11}$$

Here we substitute Eq. (3) into Eq. (2) and define $\phi(t) = \theta + \Omega t + \Theta_0$. Equation (11) has the following solution:

$$r(\theta, t) = R\cos\left(\Omega\tau + \theta - \theta_{i+1}\right) - \sin\phi(t)\left[X_T(t) - X_T(t - \tau) \right] - \cos\phi(t)\left[Y_T(t) - Y_T(t - \tau) \right], \tag{12}$$
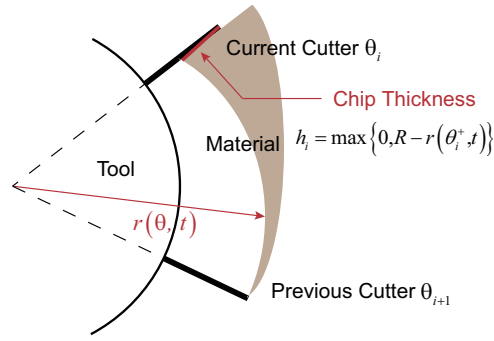
Figure 4 – Surface function between two neighboring cutters.

where τ is the minimum positive value satisfying:

$$R\sin\left(\Omega\tau + \theta - \theta_{i+1}\right) + \cos\phi\left(t\right)\left[X_T\left(t\right) - X_T\left(t - \tau\right)\right] - \sin\phi\left(t\right)\left[Y_T\left(t\right) - Y_T\left(t - \tau\right)\right] = 0. \tag{13}$$

Substitute Eq. (13) into Eq. (1), and rewrite the maximum function into an alternative form, we obtain:

$$h_i = \max\left\{0, R - r\left(\theta_i^+, t\right)\right\} = \max\left\{0, \bar{h}_i\left(t\right)\right\} = \bar{h}_i\left(t\right)g_i\left[\bar{h}_i\left(t\right)\right], \qquad i = 1, 2, \ldots, N, \tag{14}$$

where $\bar{h}_i\left(t\right)$ is exactly the chip thickness formula introduced in the DDE model (Faassen *et al.*, 2006), and function $g_i\left[\bar{h}_i\left(t\right)\right]$ is defined as:

$$g_i\left[\bar{h}_i\left(t\right)\right] = \begin{cases} 1, & \bar{h}_i\left(t\right) > 0 \\ 0, & \text{otherwise}. \end{cases} \tag{15}$$

The period when $\bar{h}_i\left(t\right) > 0$ can also be determined using the entry (ϕ_s) and exit (ϕ_e) angles. In other words, the chip thickness ahead of cutter i is positive when its orientation with respect to the Y-axis, $\phi_i\left(t\right) = \theta_i + \Omega t + \Theta_0$, is in the range $\phi_s \leq \phi_i\left(t\right) \leq \phi_e$. The entry and exit angles can be determined by solving the equation $\bar{h}_i\left(t\right) = 0$. Here we assumes that prescribed motion of the mill plays the dominant role (Assumption 3), i.e., $X_T\left(t\right) \approx V_0 t$ and $Y_T\left(t\right) \approx 0$, the following approximated entry and exit angles are obtained:

$$\phi_s \approx -\frac{\bar{\theta}f_z}{2\left(f_z + \bar{\theta}R\right)}, \qquad \phi_e \approx \pi - \frac{\bar{\theta}f_z}{2\left(f_z + \bar{\theta}R\right)}, \tag{16}$$

which are the same entry and exit angles derived in the DDE model (Faassen *et al.*, 2006). Using these two angles, the function $g_i\left[\bar{h}_i\left(t\right)\right]$ can be rewritten as a function of $\phi_i\left(t\right)$, i.e., the $g_i\left(\phi_i\left(t\right)\right)$ function in Eq. (10).

Substitute Eq. (14) into (7), we obtain exactly the same cutting force formula (9) in the DDE model. Here the identity $g_i^\beta\left(\phi_i\left(t\right)\right) = g_i\left(\phi_i\left(t\right)\right)$ ($\beta > 0$) is used. Until now, we obtain a DDE model from the PDE-ODE model using three simplifying assumptions. In other words, the DDE model can be viewed as a simplified formulation of the PDE-ODE model. From this perspective, the DDE model is computationally more efficient in specific, though common, scenarios, because the PDE is solved analytically under simplifying assumptions and the numerical simulation of the PDE is avoided. However, the PDE-ODE model can be more accurate when these simplifying assumptions are invalid.

This conclusion is further confirmed by numerical simulations. As illustrated in Figure 5, the DDE model ignores the transient tool behavior at early stage ($t \in [0, 0.01]$s), which is naturally captured by the PDE-ODE model. This is because Assumption 1 is invalid, and the initial condition needs to be considered when the tool is cutting the outer region of the workpiece. More details of this example are provided in (Chen *et al.*, 2024).
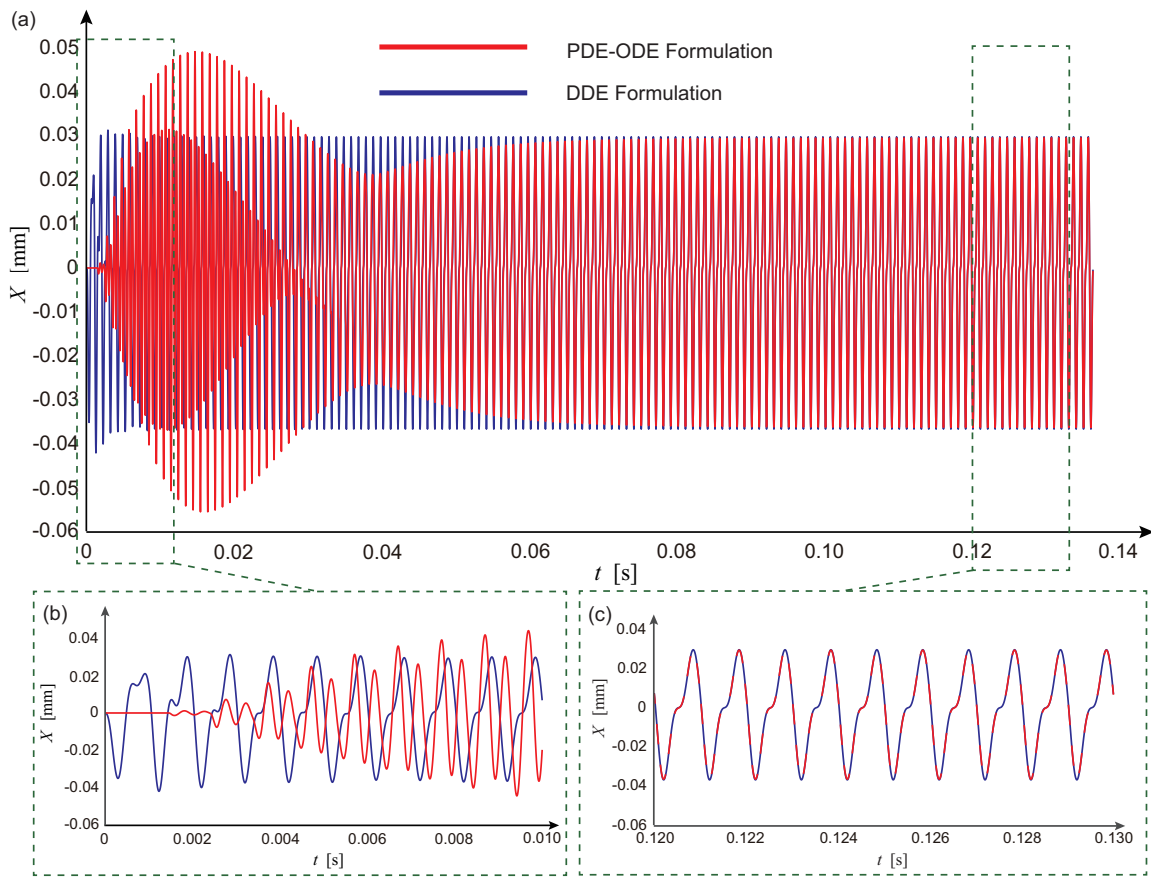
Figure 5 – (a) Tool center vibration in the X-direction : (b) simulation results from t=0 to t=0.01s, and (c) simulation results from t=0.12 to t=0.13s. Adopted from (Chen *et al.*, 2024)

OUTLOOK TOWARDS PDE-ODE MODEL FOR BIT WHIRL
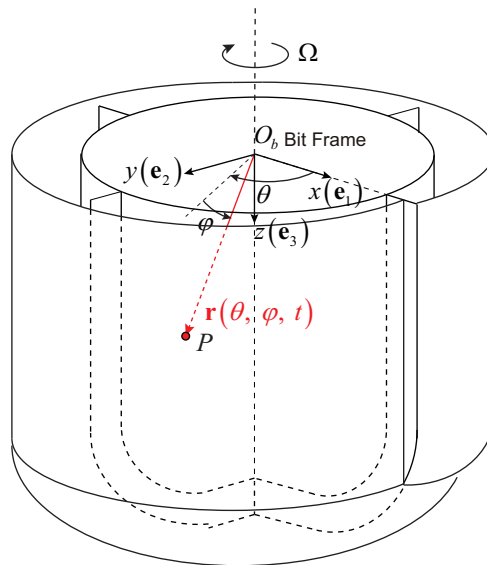
Figure 6 – Surface function in drilling.

In the milling process and in bit whirl in drilling (Kovalyshen, 2013), the cutting tools are moving laterally. From this perspective, the proposed PDE method can be extended to describe the evolution of the bottom hole surface when

bit whirling occurs. As illustrated in Figure 6, the concept of surface function can be extended to the drilling process, describing the distance between an arbitrary point P on the rock surface and a reference point O_b on the bit. Given the fact that the bit is moving along its central axis and has more complex design, the surface function is extended from two-dimensional $r(\theta, t)$ in milling to three-dimensional $r(\theta, \varphi, t)$. Herein, φ is the angle between line O_bP and $x - y$ plane. Similar to the PDE (2), the evolution of the extended surface function $r(\theta, \varphi, t)$ is also governed by a conservation law with a source term:

$$\frac{\partial r(\theta, \varphi, t)}{\partial t} + \frac{\partial f(\theta, \varphi, t)}{\partial \theta} + \frac{\partial g(\theta, \varphi, t)}{\partial \varphi} = \psi(\theta, \varphi, t),$$ (17)

where $f(\theta, \varphi, t)$, $g(\theta, \varphi, t)$, and $\psi(\theta, \varphi, t)$ are all functions of the motion of point O_b. Following the logic illustrated in Figure 1, the PDE (17) can then be coupled with ODEs describing bit dynamics (Richard *et al.*, 2007; Kovalyshen, 2013), thus a PDE-ODE system describing bit whirl can be formulated. Detailing such model is subject to future work.

ACKNOWLEDGMENTS

REFERENCES

Chen, K., Zhang, H., van de Wouw, N. and Detournay, E., 2022. "An alternative approach to compute chip thickness in milling". *Journal of Manufacturing Science and Engineering*, Vol. 144, No. 11, p. 111006.

Chen, K., Zhang, H., van de Wouw, N. and Detournay, E., 2024. "An alternative approach to model the dynamics of a milling tool". *Journal of Sound and Vibration*, Vol. 569, p. 117940.

Faassen, R.P.H., van de Wouw, N., Nijmeijer, H. and Oosterling, J.A.J., 2006. "An Improved Tool Path Model Including Periodic Delay for Chatter Prediction in Milling". *Journal of Computational and Nonlinear Dynamics*, Vol. 2, No. 2, pp. 167–179. doi:10.1115/1.2447465.

Kovalyshen, Y., 2013. "A simple model of bit whirl for deep drilling applications". *Journal of Sound and Vibration*, Vol. 332, No. 24, pp. 6321–6334.

Niu, J., Jia, J., Wang, R., Xu, J., Sun, Y. and Guo, D., 2021. "State dependent regenerative stability and surface location error in peripheral milling of thin-walled parts". *International Journal of Mechanical Sciences*, Vol. 196, p. 106294.

Richard, T., Germay, C. and Detournay, E., 2007. "A simplified model to explore the root cause of stick-slip vibrations in drilling systems with drag bits". *Journal of sound and vibration*, Vol. 305, No. 3, pp. 432–456.

Roukema, J.C. and Altintas, Y., 2006. "Time domain simulation of torsional–axial vibrations in drilling". *International Journal of Machine Tools and Manufacture*, Vol. 46, No. 15, pp. 2073–s2085.

Stepan, G., Szalai, R., Mann, B.P., Bayly, P.V., Insperger, T., Gradisek, J. and Govekar, E., 2004. "Nonlinear dynamics of high-speed milling–analyses, numerics, and experiments". *Journal of Vibration and Acoustics*, Vol. 127, No. 2, pp. 197–203.

Wahi, P. and Chatterjee, A., 2008. "Self-interrupted regenerative metal cutting in turning". *International Journal of Non-Linear Mechanics*, Vol. 43, No. 2, pp. 111–123.

Zhang, H., Tian, K. and Detournay, E., 2023. "A high-fidelity model for nonlinear self-excited oscillations in rotary drilling system". *Journal of Sound and Vibration*, p. 118193.

RESPONSIBILITY NOTICE

The authors are the only responsible for the printed material included in this paper.

Innovative Downhole Anchoring and Drive System Reduces Drilling Dysfunction and Enables Autonomous Reeled Drilling

Liam Lines – GA Drilling (USA)
John Wisinger – GA Drilling (USA) William Murray
Matus Gajdos – GA Drilling (Slovakia)
Mark Webb – GA Drilling (UK)
Graham Watson – GA Drilling (UK)

Innovative Downhole Anchoring and Drive System Reduces Drilling Dysfunction and Enables Autonomous Reeled Drilling

Liam Lines [1], John Wisinger [1], William Murray [1], Matus Gajdos [2], Mark Webb [3], and Graham Watson [3]

[1] GA Drilling, LLC, 4201 Main St, Ste. 200 – 189, Houston, TX 77002, United States

[2] GA Drilling, a. s., Headquarters – Technology Center, Vápenka 4, 841 07 Bratislava, Slovakia

[3] GA Drilling Ltd., Broad Quay House, Prince Street, BS1 4DJ Bristol, United Kingdom

Abstract: This paper outlines an innovative Downhole Anchoring and Drive System that offers significant reduction in well construction cost through elimination of downhole drilling dysfunction, closed loop optimization of drilling parameters and the ability to extend well length through application of downhole thrust to the drill bit. This paper also shows how this system is a critical enabler of an Autonomous Reeled Drilling System allowing large diameter wellbores to be drilled in hard rock with coiled tubing, promising an even larger reduction in well construction cost, especially for offshore deepwater applications.

Keywords: downhole anchoring, reeled drilling, coiled tubing, hard rock drilling, offshore.

INTRODUCTION

An innovative Downhole Anchoring and Drive (DAD) system is under development that will significantly reduce well construction cost through elimination of downhole drilling dysfunction and, through application of significant and optimized downhole thrust force to the drill bit, allow faster and/or longer wells to be drilled than currently possible with today's conventional technologies.

What follows is an overview of the problems typically encountered while drilling hard rock, what the DAD system is and how it eliminates these problems and ultimately how it is a key enabler to future Autonomous Reeled Drilling Systems.

DRILLING DYSFUNCTION

Drilling dysfunctions consume significant amounts of energy that could otherwise be used to drill rock faster. They take many forms but ultimately increase drilling cost and risk through elevated downhole tool wear and damage, reduced Rate of Penetration (ROP), increased number of trips in and out of hole and potentially, in the case of lost in hole event, the loss of a well.

A typical example of dysfunction is torsional vibration – large fluctuations, usually periodic, in drill bit rotation rate despite constant rotation rate at surface. Lines (2016) outlined the many forms of this that occur in drilling operations, their cause and consequence but namely the result is premature wear and damage to drill bits and a reduction in ROP. See Figure 1 for examples of the three main types (Figure 1(a)-Figure 1(c)).
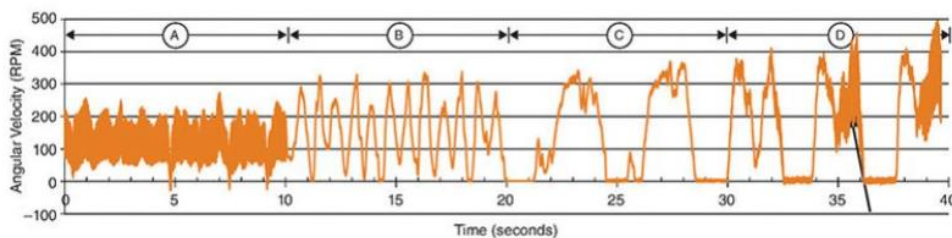
Figure 1 – drill bit RPM vs time plot showing various modes of torsional vibration – a) high frequency torsional oscillation, b) low frequency torsional oscillation, c) full stick slip, d) combined low frequency torsional oscillations, stick slip and high frequency torsional oscillations (Lines, 2016)

Torsional vibration ultimately stems from the inverse relationship between drilling torque and rotation speed of the now ubiquitous PDC drill bit, see Figure 2. This results in negative damping and a tendency for the rotary speed of the drill bit (and the drillstring connected to it) to oscillate when perturbed (Richard, 2007).
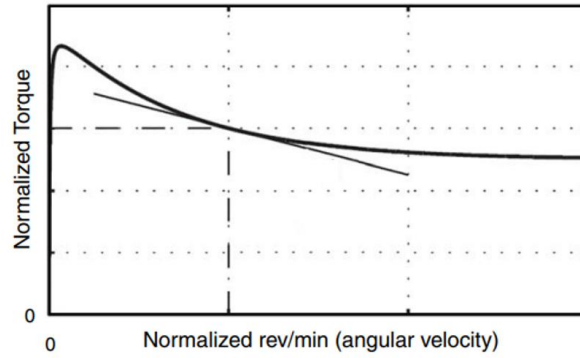
Figure 2. Velocity dependent PDC drill bit torque (Hohl, 2015)

Another example of dynamic dysfunction is lateral vibration whereby the lateral stabilization of the drilling assembly and/or the engagement of the drill bit with the rock (a large component of drill bit lateral stability is the result of PDC cutter force balancing that relies on sufficient cutter engagement with the rock face) is insufficient to constrain lateral force instability or acceleration of the drill bit or other components within the drilling assembly. Not only can this form of dysfunction result in damage to downhole tools, but it can also cause significant irregularity in wellbore path (tortuosity) that can then result in poor weight transfer to the drill bit (and further lateral vibration issues) as drilling progresses (Dupriest, 2013). Two common types of lateral vibration are forward whirl – typically occurs with limber drillpipe/collars that precess in the same direction and similar frequency to drillstring rotation - and backward whirl – typically occurs on drill bit and stabilizers whereby the rotation of the component within the wellbore is in the opposite direction to drillstring/bit rotation and at much higher frequency (Stroud, 2011). Both result in high impact shock and vibration damage along with rapid accumulation of bending fatigue (especially in the case of backward whirl).

Dynamic stability plots show the relationship of the above dysfunctions to drilling parameters (Figure 3). For maximum performance it's desirable to work towards the upper right of the stability plot using the highest WOB along with the highest RPM while avoiding adverse dynamics – staying in the optimum zone. Watson (2013) confirmed through fundamental cutter testing that PDC drill bit ROP and life is maximized in hard rock by drilling at high WOBs.
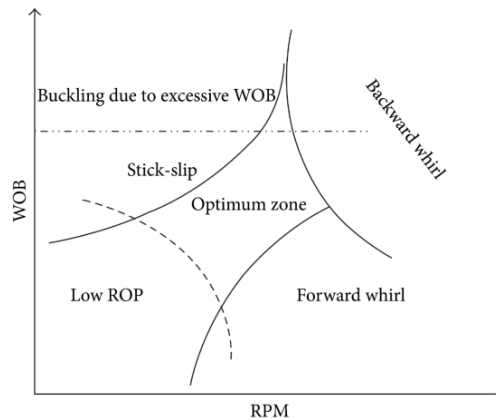
Figure 3: Typical stability diagram for drilling (Wu, et al. 2010)

Mitigation and avoidance of dysfunction is challenging. Typically, the cause of the dysfunction is at the bottom end of the drilling assembly (for instance the PDC drill bit) whereas the control and actuation system is many kilometers away on the top side. This results in a severely underactuated drilling system that can be very challenging to control (Krstic, 2022 & Auriol, 2022).

Figure 4 shows a drillstring drag analysis for the longest 3D granite well drilled in Thailand (Thai, 2022). This well reached a Total Depth (TD) of 6768m with a circa 3500m horizontal section. The cumulative drag at TD at 0rpm (sliding) was predicted at 185,200lbs with approximately 25lb/m rate of increase in the horizontal section. The DAD system can apply approximately up to 60,000lbs of extra WOB in this hole size. In this well that would have resulted in an extra 2400m or 77% more horizontal footage before the same drillstring drag and levels of buckling would have been encountered.
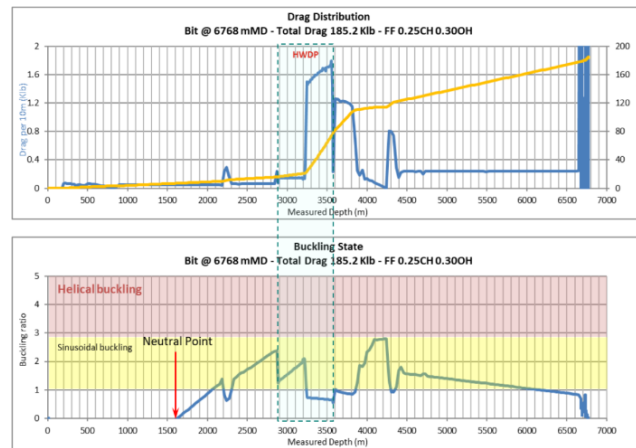

Figure 4: Drag Plot for Long Granite Well in Thailand (Thai, 2022)

What if the control and actuation system responsible for the drilling process was placed downhole in proximity (within 30m) of the source of instability e.g. the drill bit? What if it could apply significant and controlled downhole WOB to counteract the inverse bit torque to rotary speed relationship / negative damping and keep the drill bit cutters consistently engaged with the rock face to improve lateral stability and cutter life? What if this system could apply significant WOB downhole directly to the drill bit to eliminate drillstring buckling and maximize reach? What if this system could also autonomously adjust parameters, for instance WOB, and instantly see in high fidelity the impact on ROP and vibration severity……the answer is a more efficient drilling system that can drill both further and faster than the incumbent technology and ultimately reduces well construction cost and risk. This is what the DAD system offers the global drilling industry.

The DAD system is positioned within the bottom hole assembly (BHA) and contains hydraulically actuated gripping elements that anchor the BHA to the borehole wall and allow torsional and/or axial load to be reacted directly into the borehole wall rather than conveyed many kms above. The system contains a hydraulic thrusting unit that can apply significant and controlled thrust to the drill bit to both drill faster and actively reduce drilling dysfunction. The drilling process is controlled from the bottom of the hole with real-time sensor feedback to aid in optimization and includes many of the control modes that Drillers are accustomed to with the latest surface based Automatic Drillers (ROP, WOB, Torque etc.).

The resulting stability plot with DAD system in the BHA can be seen in Figure 5. The threshold for buckling has shifted upwards resulting from the ability of the DAD system to apply WOB downhole and require less compression in the drillstring above (compression causes buckling). The stability resulting from local gripping of the wellbore has eliminated forward whirl and the ability to increase WOB and drill bit cutter engagement with the rock reduces the tendency to backward whirl. Ultimately this extends the optimum zone, allowing higher WOBs and higher RPMs to be used, resulting in faster ROPs with less occurrences of damaging dynamics and adverse PDC cutter wear.
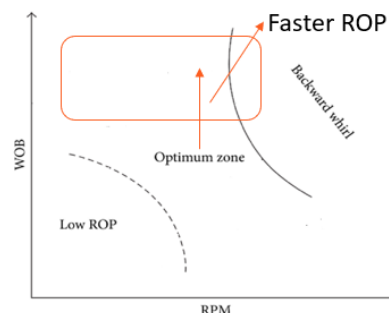

Figure 5 – Modified stability plot showing impact of DAD System

In addition to optimization of the drilling process through proximity of the DAD system to the drill bit and its advanced control and actuation system, its ability to react torque and axial force into the formation is a critical enabler for drilling large diameter, hard rock wells with reeled pipe and/or coiled tubing. Coiled tubing is typically used for small diameter, low cost well intervention and workover operations which require low torque and pull/weight capacity (compared to conventional jointed pipe in drilling applications). The ability to drill large hole diameter holes through hard rock with coiled tubing offers immense cost savings over conventional jointed pipe operations:

- **Smaller, lower cost drilling rig** due to reduced derrick capacity and tubular handling requirements

- **Faster drilling and tripping times** due to not needing to make/break rotary connections and pick-up/ rack-back pipe (typically 3-4x the tripping speed compared to conventional jointed pipe)

- **Improved well control** through ability to continuously circulate while tripping in/out of hole.

- **Reduced workplace hazards** due to elimination of rotary shouldered connections made/break on the rig floor.

- **Improved command and control** of the downhole tools through continuous data link to surface via wireline.

AUTONOMOUS REELED DRILLING SYSTEM

A schematic overview of the Autonomous Reeled Drilling System with the DAD system can be seen in Figure 6.
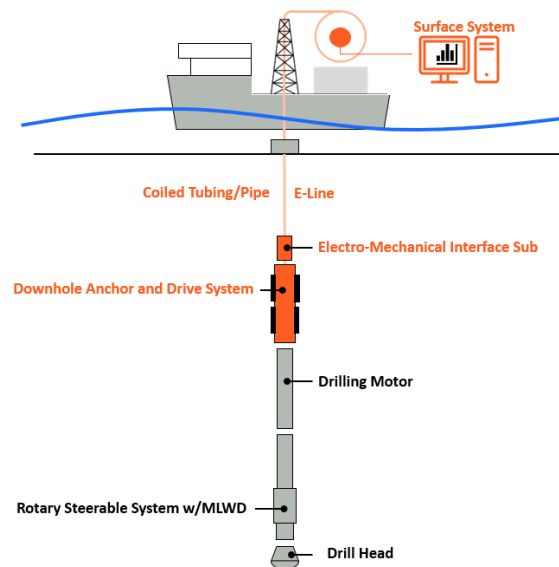
Figure 6 - main components of Autonomous Reeled Drilling Solution. Orange indicates new system components; grey are industry standard off-the-shelf components.

The components of the Autonomous Reeled Drilling System are as follows:

- **Drill Bit** – conventional PDC, roller cone or alternative rock destruction methods e.g. plasma.

- **Directional Drilling Assembly** – allows steering of wellbore along with navigational and petrophysical logging measurements. Pictured with Rotary Steerable System (RSS)

- **Drilling Motor** – converts hydraulic energy in drilling fluid into mechanical energy for rotating the drilling assembly.

- **DAD System** – The anchoring system reacts the drilling motor torque into the formation to avoid damage and twist of the coiled tubing string. The 700 series DAD can react the stall torque of the heaviest duty 7-in OD drilling motors (for drilling 8.5in to 8.75in nominal hole size)

- **Coiled Tubing Interface** – electromechanical connection of DAD system and BHA to coil tubing.

- **Coiled Tubing** – customized coil tubing with improved fatigue properties and mechanical/hydraulic capacities

- **E-Line** – provides power and communications conduit between surface and downhole tools.

- **Rig** – standard CT/intervention rig or vessel. Shown here utilizing a light well intervention vessel to reduce the cost of deepwater drilling.
- **Surface System** – allows data visualization and bi-directional communications and control of DAD system. Also possible to receive MWD and LWD data.

DAD SYSTEM TEST AND DEVELOPMENT UPDATE

The predecessor to the DAD system focused on mechanically isolating the drill bit from the 'spring' of the drillstring to provide a rigid torsional anchor point above the drill bit to react the torque output from the drilling motor/ drill bit and allow maximum weight to be applied without triggering stick/slip – stick/slip is a major cause of drill bit damage that limits hard rock drilling performance. The Concept Prototype (CP) utilized hydraulic oil to energize gripper pistons. The gripper pistons extended to grip the wellbore wall and transmit torque. The tool comprised two anchoring units connected via a closed hydraulic circuit. This hydraulic circuit synchronized the movement of the two anchors such that while one was gripping the wellbore the other unit was resetting position such that it could take over from the gripping unit when it reached the end of its travel. The target was to continuously react torque to the formation via the grippers up to the maximum ROP – 70ft/hr. for the CP.

The CP tool had no means of applying thrust to the drill bit and relied on it being applied by conventional means – heavy weight or drill collars in the BHA and the Driller controlling hookload/ slack off weight to apply force to the drill bit. This CP was tested at the facility of a major drilling contractor in Houston, Texas and drilled a shallow cased hole filled with cement. The specifics of the test and results are described in Gajdos (2024). The CP can be seen in Figure 7. The shake down test was successfully concluded with two main achievements:

- The CP tool reliably gripped the wellbore while drilling and the movement of the two anchoring units were sufficiently synchronized (via the closed hydraulic circuit connecting them) to ensure continuous gripping during the test. The CP achieved the required 70 ft/hr with testing not able to reach the maximum limit of the tool´s capability.

- Downhole drilling dynamics subs located above and below the downhole motor detected vibrations reduced by up to 35% when compared to drilling without the CP in the drillstring.

Figure 7 – CP suspended in derrick during drilling tests at drilling contractor facility, Houston, TX

A requirement for the original anchoring concept was for a purely hydro-mechanical tool with no electrical or electronic systems. This resulted from the desire for ultra-high temperature operations (350degC) for geothermal applications. As a drive to facilitate creation of an Autonomous Reeled Drilling System, along with the aim to simplify the hydromechanical controls and modularize the design, it was decided to 'electrify' the anchoring tool with the addition of electronic actuation and control and, at the same time, add extra capabilities such as application of controlled axial thrust/ WOB to the drilling assembly and implementation of autonomous control loops similar to those in today´s cutting edge automated drilling systems – these enhancements resulted in the DAD system as shown in Figure 8.

A summary of the enhancements of the DAD system over the CP tested at the drilling contractor's facility in Houston:

- Incorporates electronic/electrical control and actuation system to allow enhanced active control mechanisms to optimize the drilling process and reduce dysfunction.

- Allows the drillstring to be rotated through the anchors to minimize drillstring drag and allow use of conventional directional drilling motors and processes (e.g. slide and rotate)

- Includes a comprehensive set of sensors and diagnostic data – e.g. pressure, torque, WOB, temperature, RPM, shock and vibration

- Utilizes pressurized drilling fluid to reduce tool complexity and cost and will follow a similar design ethos to the most commercially successful RSS tools.

- Includes axial push/pull capability which can be used to apply additional WOB to improve ROP through higher depth of cut and/or reduced drill string buckling/drag.

- Modular design allowing multiple anchors and thrusting units to be stacked in series should higher forces be required.

- Utilizes a common electrical architecture that facilitates power and communications exchange between multiple modules and other third-party tools in the BHA creating the potential for a true integrated and autonomous drilling system.
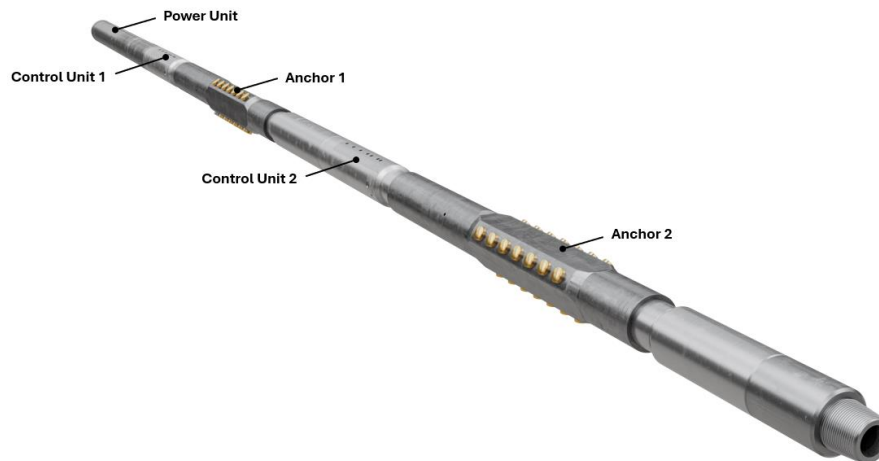
Figure 8: Visualization of the next version of Downhole Anchoring and Drive (DAD) system

The DAD System has two main tool configurations:

- **Axial anchoring only** - allows the central shaft to rotate through the anchoring modules and for true "plug and play" into conventional bent motors and jointed pipe applications without the need for extra tools in the drillstring. The system utilizes modulation of axial thrust to mitigate stick/slip (and other dysfunctions).

- **Axial and Torsional anchoring** – Torsionally locks the central shaft running through the system to the anchors such that when the anchors engage the borehole wall the drillstring above the DAD system cannot be rotated. Drilling motor torque reacts into the borehole wall (via the anchors) rather than into the drillstring. Allows high torque and extended reach drilling with coil tubing.

The DAD system comes equipped with the following control modes:

- **ROP Mode** – utilizes anchor traverse speed to control ROP allowing for much more consistent drilling and eliminates common dysfunctions (e.g. axial stick/slip) and well control issues.

- **Bit Torque Mode** – utilize torque feedback to stabilize drilling torque to significantly improving motor and drill bit life and allows motors to be ran closer to maximum power (faster ROP) without risk of damage

- **WOB Mode** – utilizes feedback from WOB sensor to control axial thrust to stabilize WOB for a more consistent drilling process.

The commercial tool is undergoing development and testing for planned deployments towards the end of 2025.

CONCLUDING REMARKS

The paper describes the innovative new Downhole Anchoring and Drive System originally proposed for hard rock drilling in geothermal applications, but with significant synergies for oil & gas drilling and as the critical enabler of an offshore Autonomous Reeled Drilling System. Typical forms of drilling dysfunction are discussed along with the ability of the DAD system to mitigate these along with its ability to extend drilling distances through the application of downhole thrust. The DAD system will be commercially deployed in 2025 for geothermal applications and a project is underway with a major oil company to develop and commercialize the Autonomous Reeled Drilling System for offshore deepwater.

REFERENCES

Auriol, J., Boussaada, I., Shor, R., Mounier, Hugues., Niculescu, Silviu-Iulian., 2022. "Comparing Advanced Control Strategies to Eliminate Stick-Slip Oscillations in Drillstrings", IEEE Access volume 10, pp. 10949-10969, 2022, doi: 10.1109/ACCESS.2022.3144644.

Dupriest, F. 2017, "Thus, The Lowly Stabilizer", Presentation Given at International Association of Directional Drilling, July Meeting, 2013

Dupriest, F. and Noynaert, S., 2022, "Drilling Practices and Workflows for Geothermal Operations", Proceedings of the IADC/SPE International Drilling Conference and Exhibition, Galveston, Texas, USA. https://doi.org/10.2118/208798-MS.

Thomas Richard, Christophe Germay, Emmanuel Detournay, 2007, "A simplified model to explore the root cause of stick–slip vibrations in drilling systems with drag bits", Journal of Sound and Vibration, Volume 305, Issue 3, 2007, Pages 432-456, ISSN 0022-460X, https://doi.org/10.1016/j.jsv.2007.04.015.

Gajdoš, M., Watson, G., Webb, M., Glover, D., Krištofič, T., Kočiš, I., Lines, L., Murray, W., Codazzi, D. and Jeffryes, B., 2024, "Progress in Development and Testing of Anchoring Technology for Hard and Abrasive Drilling Conditions", Proceedings of the Stanford Geothermal Workshop 2024, Stanford University, USA.

Hohl, A., Tergeist, M., Oueslati, H. et al. 2015. Derivation and Experimental Validation of an Analytical Criterion for the Identification of Self-Excited Modes in Drilling Systems. J Sound Vib 342: 290–302. https://doi.org/10.1016/j.jsv.2015.01.002.

Krstic, M., 2022 "Control of Drill String and Flow Instabilities by PDE Backstepping" Proceedings of the Fifth International Colloquium on Nonlinear Dynamics and Control of Deep Drilling Systems, pp. 13-14, University of Maryland, USA.

Lines, L., 2016, "Technology Update: A Holistic Approach to Controlling Torsional Dynamics in the Drillstring." *J Pet Technol* 68 (2016): 20–23. doi: https://doi.org/10.2118/1016-0020-JPT

Stroud, D. R., Lines, L. A., and D. J. Minett-Smith., 2011, "Analytical and Experimental Backward Whirl Simulations for Rotary Steerable Bottom Hole Assemblies." Paper presented at the SPE/IADC Drilling Conference and Exhibition, Amsterdam, The Netherlands, March 2011. doi: https://doi.org/10.2118/140011-MS

Thai, L., Nguyen, N., Blackwell, G., and Minh D., 2022, "Longest 3D Horizontal Granitic Basement Section Record Drilled in Vietnam Using Friction Reduction Technology and Real-Time Torque & Drag Management." Paper presented at the IADC/SPE Asia Pacific Drilling Technology Conference and Exhibition, Bangkok, Thailand. doi: https://doi.org/10.2118/209915-MS.

Watson. G., 2013, "Effect of Drilling Parameters on PDC Cutter Wear", Hard Rock Drilling Workshop, International Research Institute of Stavanger (2013).

Wu, S. X, Paez, L., Partin, U. Agnihotri, M., 2010, "Decoupling stick-slip and whirl to achieve breakthrough in drilling performance," Proceedings of the IADC/SPE Drilling Conference and Exhibition, pp. 966–978, New Orleans, USA. https://doi.org/10.2118/128767-MS.

RESPONSIBILITY NOTICE

The authors are only responsible for the printed material included in this paper.

Optimizing Drilling Strategies for Deep Wells in Complex Interbedded Formations: Addressing Drill String Stress, BHA Tool Failure, and Performance Enhancement

Adriano Passos – Petrobras (Brazil)
Flank Lima – Petrobras (Brazil)
Guilherme Britto – Petrobras (Brazil)
José R. B. Moura Filho – Petrobras (Brazil)
Márcio Francisco – Petrobras (Brazil)
Reinaldo Tomita – Petrobras (Brazil)

Optimizing Drilling Strategies for Deep Wells in Complex Interbedded Formations: Addressing Drill String Stress, BHA Tool Failure, and Performance Enhancement

Adriano Passos, Flank Lima, Guilherme Britto, José Brígido, Márcio Francisco, Reinaldo Tomita

[1] Petrobras - Edifício Senado. Rua Henrique Valadares, 28. Rio de Janeiro - RJ, CEP 20231-030

Abstract: This paper addresses the analysis of drill string failure during the big hole section drilling, aboarding the drill string stresses involved in this process. The objective is to understand the main causes and identify possible solutions to minimize drill string failure occurrences. Based on these analyses, recommendations are proposed to improve drilling practices, aiming to prevent or mitigate the risks of drill string failure during big hole section drilling. The obtained results contribute to the advancement of knowledge in this field and can be applied in the planning and execution of future big hole drilling projects, with the goal of enhancing safety and efficiency in this stage of the oil and gas exploration process.

Keywords: string, failure, drilling, big hole section.

INTRODUCTION

Drilling deep wells with larger bits in complex formations consisting of shale, mudstone, marl, limestone, diamictite, and sandstone, located in different sections, presents a challenge due to the stress on the drill string. Tool failure, bit wear, and drill string breakage are the main issues in this drilling scenario.

The mechanical conditions of the well, particularly the dimensions of the wellbore, greatly impact the difficulties encountered during drilling. The selection of the appropriate bit type, bottom hole assembly (BHA), and drill string is crucial in determining the drilling dynamics. Additionally, rig equipment such as the top-drive, heave compensation system, and vibration control systems like stick-slip mitigators and automatic drilling parameter control systems are necessary to facilitate drilling under severe conditions.

This article aims to examine the events that took place in wells drilled under these challenging circumstances, as well as compare different BHA solutions and drilling parameters used, with the goal of reducing vibration levels and enhancing performance in offshore well construction.

DRILLING WELLS IN LARGE HOLE DIAMETERS

The drilling of the initial phases of pre-salt wells is still a major challenge for drilling operations, either due to the large diameters of the drill bits and casings or due to the geological characteristics of the region. As mentioned by Tomita et al, the number of well phases is defined to be able to reach, in the riserless phase, the necessary depth to set the surface casing shoe and have enough formation strength to allow drilling of the salt section. This strategy generates two as shown in the Figure 1 below:
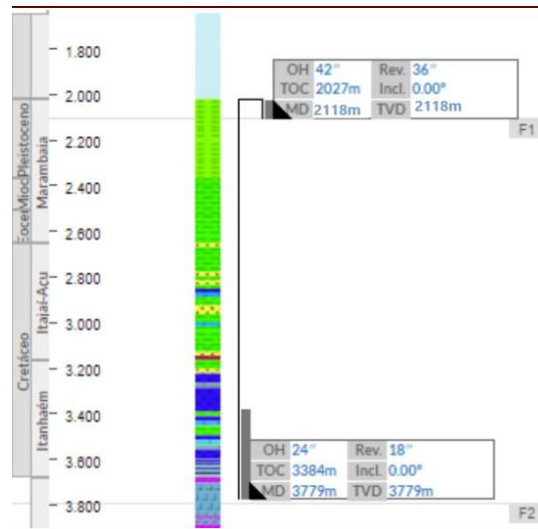
Figure 1 – Well Schematic

Strategies for BHA, fluids, drilling parameters, drill bit technology, drilling string size, evaluating drilling rig equipment and capabilities, such as top drive and heave compensator, for example, have a significant impact on the final drilling outcome.

## Bottom Hole Assembly (BHA) Strategy

The definition of the Bottom Hole Assembly (BHA) depends on the drilling goals and the equipment available on the rigs. Historically, especially in the early 2000s, the available drill pipe was 5" with NC 50 connections, which had a drilling torque of around 29Klbs.ft, leading to the use of downhole motors to compensate for the drilling string's fragility. With the introduction of new drilling strings, such as 5 ½" or 5 7/8", which have higher torque capacity, the BHAs were modified to be stabilizers, meaning they no longer have a power section.

Stabilized BHAs brought greater performance and increased drilling rates; however, they also resulted in higher levels of vibration and column break events. In Figure 2, we have a schematic of the drilling BHA for these large-diameter post-salt sections:

COMPONENT DATA								
Item #	Description	OD (in)	ID (in)	Gauge (in)	Weight (ppf)	Top Connection	Length (m)	Total (m)
1	Broca Kymera	11.000	3.000	24.000	573.78	P 7 5/8" REG	0.708	0.708
2	Near Bit Stabilizer	9.500	3.000	23.875	192.45	B 7 5/8 REG	2.670	3.378
3	9 1/2'' Short Drill Collar	9.500	3.000		211.68	B 7 5/8" REG	4.570	7.948
4	Integral Blade Stabilizer – 23 3/4"	9.500	3.000	23.750	217.48	B 7 5/8" REG	2.740	10.688
5	9 1/2'' Contingency Sub	9.500	3.000		217.48	B 7 5/8" REG	1.050	11.738
6	9 1/2'' DrillDOC	9.500	2.370		210.30	B 7 5/8" REG	2.660	14.398
7	9 1/2'' DM Collar	9.500	4.125		208.40	B 7 5/8" REG	2.780	17.178
8	9 1/2'' DGR Collar	9.500	2.375		201.70	B 7 5/8" REG	2.020	19.198
9	9 1/2'' EWR-P4D Collar	9.500	2.375		212.00	B 7 5/8" REG	3.727	22.925
10	9 1/2'' PWD	9.500	2.375		213.20	B 7 5/8" REG	1.310	24.235
11	9 1/2'' HCIM Collar	9.500	2.375		212.70	B 7 5/8" REG	2.330	26.565
12	In Line Stab (ILS) – 23 7/8"	9.500	3.000	23.750	192.45	B 7 5/8" REG	1.500	28.065
13	9 1/2'' Pulser	9.500	2.750		197.60	B 7 5/8" REG	4.790	32.855
14	Filter Sub	9.500	3.250		217.48	B 7 5/8" REG	1.450	34.305
15	Float Sub (Flapper Non Ported AF)	9.500	3.250		142.83	B 7 5/8" REG	0.914	35.220
16	Integral Blade Stabilizer – 23 3/4"	9.500	3.000	23.750	217.00	B 7 5/8" REG	2.800	38.020
17	7x 9 1/2" Drill Collar	9.500	3.000		216.94	B 7 5/8" REG	65.000	103.020
18	Drilling Jar	9.620	3.000		186.67	B 7 5/8" REG	6.858	109.878
19	2x 9 1/2" Drill Collar	9.500	3.000		216.94	B 7 5/8" REG	18.400	128.278
20	X-Over Sub	8.000	2.875		147.00	B 6 5/8" REG	1.000	129.278
21	8x 8" Drill Collar	8.000	3.125		146.85	B 6 5/8" REG	74.370	203.648
22	X-Over Sub	8.000	3.240		142.83	XT57	1.000	204.648
23	12x 5 7/8" HWDP	5.875	4.000		54.64	XT57	113.400	318.048
24	5 7/8" Drill Pipe S135	5.875	5.045		29.11	XT57	3475.952	3794.000
							Total:	3794

Figure 2 – 24" BHA Components

In this 24" BHA for drilling through the post-salt and entering 150m into the salt, we see a much more robust drilling string with 5 7/8" drill pipe and XT57 connections (e.g., NOV), which have a torque limit close to 56Klbs.ft. Figure 3 below provides a more detailed overview of the tension and torque capacities of the 5 7/8" drill pipe with XT57 connection:

Figure 3 - Torque-Tension Graph XT-57
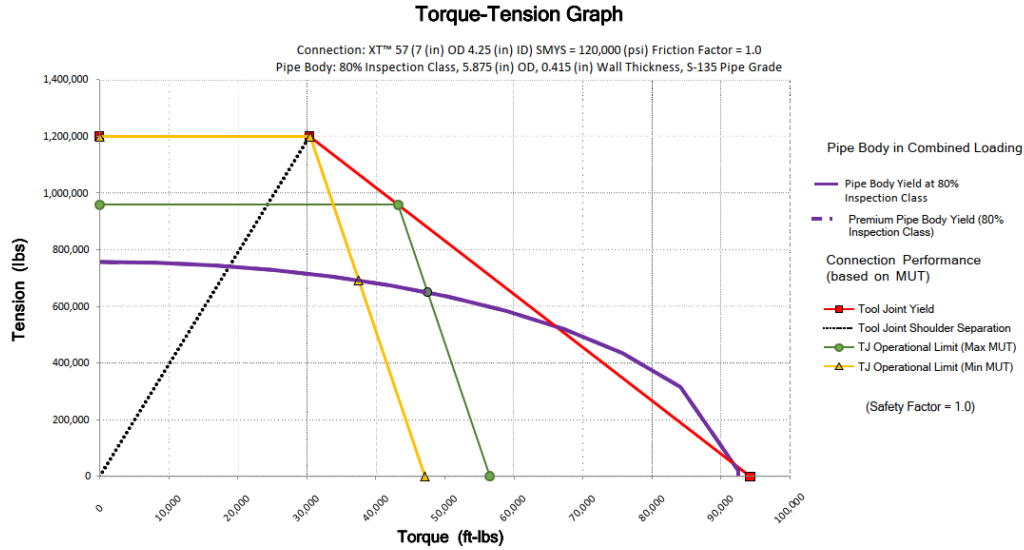
Simulations and Operational Limits

Due to the BHA and the well's schematic design, a series of analyses are performed to assess the column's stress and operational limits. Currently, our simulators cannot clearly and accurately capture the dynamic drilling conditions, making it difficult to predict and analyze column failure events. The most common simulations are able to capture the limits of forces and loads, as shown in Figure 4 below:

Mechanical Limitations

Overpull Margin during a Tripping Out operation	134.2 kip	using	80.00% of yield
Minimum Weight on Bit to Sinusoidal Buckle during a rotating on bottom operation	57.8 kip	at	3776.82 m
Minimum Weight on Bit to Helical Buckle during a rotating on bottom operation	77.5 kip	at	3776.82 m
Pick-Up Drag	24.2 kip		
Slack-Off Drag	21.8 kip		

Load Summary

Load Condition	Stress Failure			Buckling Limits			Torque Failure	Torque at the Rotary Table (ft-lbf)	Total Windup with Bit Torque (revs)	Total Windup without Bit Torque (revs)	Measured Weight (kip)	Total Stretch (m)	Axial Stress = 0		Neutral Point Distance from surface (m)	Neutral Point Distance from Bit (m)
	Fatigue	90% Yield	100% Yield	Sinusoidal	Helical	Lockup							Distance from Surface (m)	Distance from Bit (m)		
Tripping In								0.0	0.0	0.0	608.7	3.27	3589.35	204.65	3794.00	0.00
Tripping Out								0.0	0.0	0.0	654.7	3.82	3589.35	204.65	3794.00	0.00
Rotating On Bottom								28821.6	11.5	1.9	580.5	2.74	3587.30	206.70	3710.54	83.46
Rotating Off Bottom								7026.3	2.3	2.3	630.5	3.53	3589.35	204.65	3794.00	0.00

Figure 4 - Mechanical Limitations and Load Summary 24-inch section

Simulations provide a good initial understanding for defining stabilizer positions, available weight below the drilling jar, and overpull limits. However, in current simulations, formation characteristics, especially formation washout, are not considered. The lack of understanding of the well's true mechanical condition creates a significant difference between the static simulation, performed during project planning, and the actual drilling conditions.

Changes in the well's mechanical conditions occur due to various reasons, such as interbedded formations, sand washout, and swelling of reactive formations, among others, which completely change the contact points between the drilling string and the wellbore walls. Figure 5 shows a force analysis, with special emphasis on the stabilizer and drill

bit positions represented by the red lines. A washout in that position will result in much greater displacement, causing more BHA failures and increasing the risk of failures.
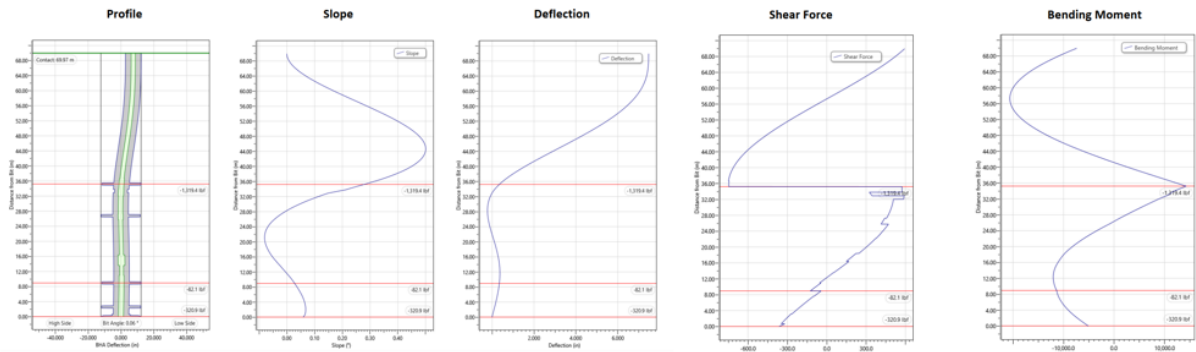
Figure 5 – BHA stress Analysis – 24-inch Section

Rig Equipment and Systems

Drilling rigs and their facilities and equipment are crucial in achieving performance goals, reducing well construction time, and eliminating BHA failures or breaks. The characteristics of the top drive, heave compensator, and systems like Auto-Drill and Soft-Speed, provided by companies such as NOV, are the main features of the drilling rig that impact drilling performance.

The Auto-Drill system works in conjunction with the rig's compensation system and aims to maintain a constant weight on bit (WOB) during drilling. The Auto-Drill control system acts as a fine adjustment of the rig's compensators. In Figure 6, the WOB variation and the heave compensator behavior in systems with and without automatic drilling control or Auto-Drill can be observed:

Figure 6 - Active compensation system + Auto Driller

Another rig features with a significant impact on drilling are control systems for top drive torque and speed. SoftSpeed (NOV) or SoftTorque (HMH) helps reduce torsional forces and vibrations during drilling. For this system to work effectively, the BHA and drilling string characteristics must be correctly registered in the system. In Figure 7, we can see the torque and rotation behavior of the top drive based on the status of the SoftTorque system being on or off:
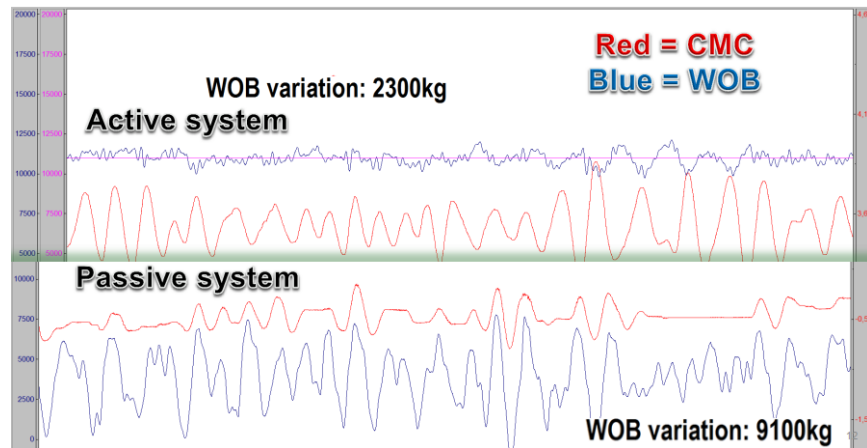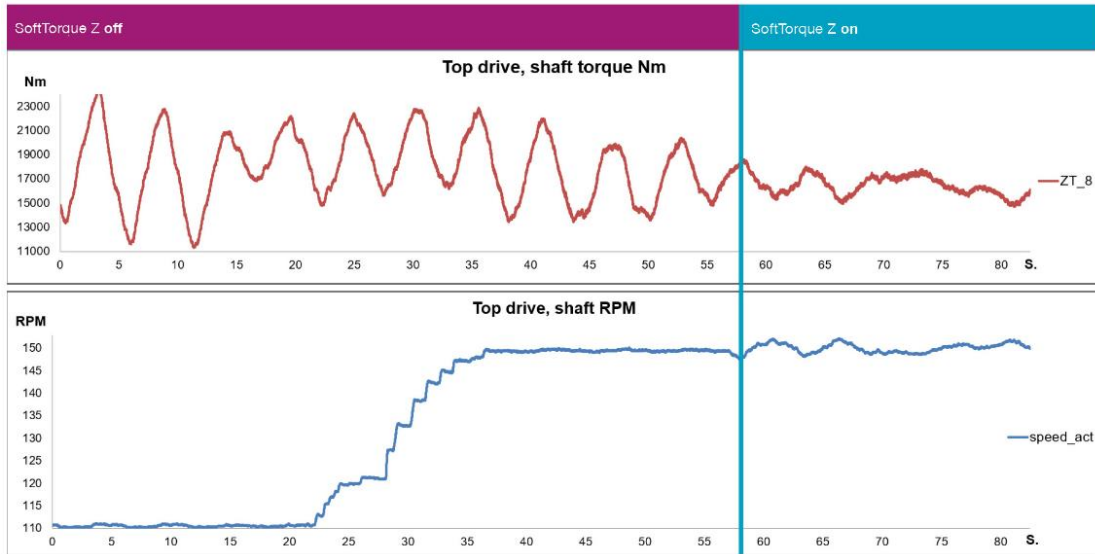

Figure 7 – SoftTorque performance

Drilling wells with these rig facilities, such as the WOB and torque/rotation control systems, enforce better drilling performance and reduces the number of column failures or BHA breaks. Figure 8 shows an improvement in performance and stabilization of torque and rotation parameters based on the operation of SoftTorque:

Data/Hora			PERFURAÇÃO			O	TAXA	PSB	COL	BR	Pres. (psi)		VAZ	torq*10³	
INIC	FIM	Dia	INIC	FIM	INT	P	m/h	klbf	rpm	rpm	OFF	ON	gpm	OFF	ON
00:59	01:05		2.274	2.313	39	R	390,0	65	150	150	3800	3800	1250	4	27
01:18	01:31		2.313	2.352	39	R	180,0	65	150	150	3850	3850	1250	4	28
01:45	02:01		2.352	2.391	39	R	146,3	65	150	150	3850	3850	1250	4	30
02:11	02:29		2.391	2.430	39	R	130,0	65	150	150	3850	3850	1250	4	30
02:41	03:03		2.430	2.469	39	R	106,4	65	180	180	3850	3850	1250	4	32
03:13	03:34		2.469	2.508	39	R	111,4	65	180	180	3900	3900	1250	4	32
03:44	04:04		2.508	2.547	39	R	117,0	65	180	180	3900	3900	1250	4	32
04:15	04:44		2.547	2.586	39	R	80,7	65	180	180	3900	3900	1250	4	32
04:54	05:21		2.586	2.624	38	R	84,4	65	180	180	3900	3900	1250	4	32
05:32	06:04		2.624	2.663	39	R	73,1	65	180	180	3900	3900	1250	4	32
06:15	06:43		2.663	2.701	38	R	81,4	65	180	180	3900	3900	1250	4	32
06:53	07:28		2.701	2.740	39	R	66,9	65	180	180	3960	3960	1250	4	32
07:40	07:56		2.740	2.779	39	R	146,3	55	180	180	3960	3960	1250	4	32
08:06	08:25		2.779	2.818	39	R	123,2	60	180	180	4000	4000	1250	4	32
08:36	09:04		2.818	2.857	39	R	83,6	60	180	180	4000	4000	1250	4	32
09:13	09:28		2.857	2.896	39	R	156,0	60	180	180	4030	4030	1250	5	29
09:38	09:55		2.896	2.935	39	R	137,6	60	180	180	4100	4100	1250	5	31
10:05	10:27		2.935	2.974	39	R	106,4	60	180	180	4100	4100	1250	5	29
10:37	10:55		2.974	3.012	38	R	126,7	60	180	180	4100	4100	1250	5	32
11:05	11:29		3.012	3.052	40	R	100,0	60	180	180	4100	4100	1250	5	30
11:40	11:58		3.052	3.091	39	R	130,0	60	180	180	4100	4100	1250	5	32
12:10	12:28		3.091	3.130	39	R	130,0	60	180	180	4100	4100	1250	5	29
12:41	12:59		3.130	3.169	39	R	130,0	60	180	180	4100	4100	1250	5	31
13:09	13:31		3.169	3.207	38	R	103,6	60	180	180	4100	4100	1250	5	30
13:42	14:01		3.207	3.246	39	R	123,2	60	180	180	4100	4100	1250	5	32

Figure 8 – Soft torque actuation results

Case Study 1: Disconnection on WELL A's Drilling String

Drilling wells in large hole diameters and interbedded formations highlight the difference between studies conducted during planning, which involve static simulations, and the actual drilling process, where dynamic conditions often override all previous assessments.

During the drilling of the surface phase of **Well A** on the drillship, a disconnection of the drilling string was identified, later evaluated as an unscrewing of the drilling string connection. Figure 9 shows the monitored parameters at the exact moment of the disconnection.
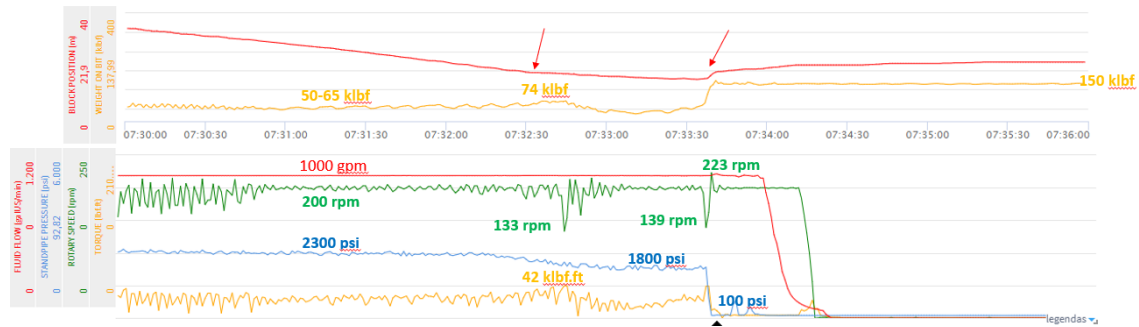

Figure 9 - Monitored Drilling Parameters

The drilling was being performed in a 26" hole size with a PDC drill bit, a similar stabilized BHA to the one illustrated in Figure 2, and a 5 7/8" 34.21 ppf V-150 drilling string. Through the analysis of parameters, later confirmed, the disconnection occurred in the connection between the first and second drill pipe stands above the BHA.

During the process of pulling the drilling string out of the hole and fishing operations for the fish stuck in the well, three more disconnections/unscrewing events were observed: an unscrewing of two drill pipe stands above the first unscrewing during the removal of the drilling string after the first event, a connection slightly above the BHA that was detorqued and had only three threads engaged, and an unscrewing of the connection between the Near Bit stabilizer and the DC. Figure 10 shows the pin from the second disconnection point, where the completely preserved threads and the fish from the Near Bit disconnection can be seen on the seafloor.

Figure 10 - The pin from the second disconnection point and the Near Bit with the drill bit on the seafloor

Despite being a section with easy-to-drill formations (mostly shales) and low vibration expectations, the drilling observed several events measured by the MWD sensors, mainly high levels of stick-slip (variations in column rotation), indicating at times variations between 0 and 400 rpm and rotations in the opposite direction of the drilling string. Figure 11 shows the vibration levels indicated by the sensors (columns 4 to 11) and the difference in results with SoftSpeed on and off.
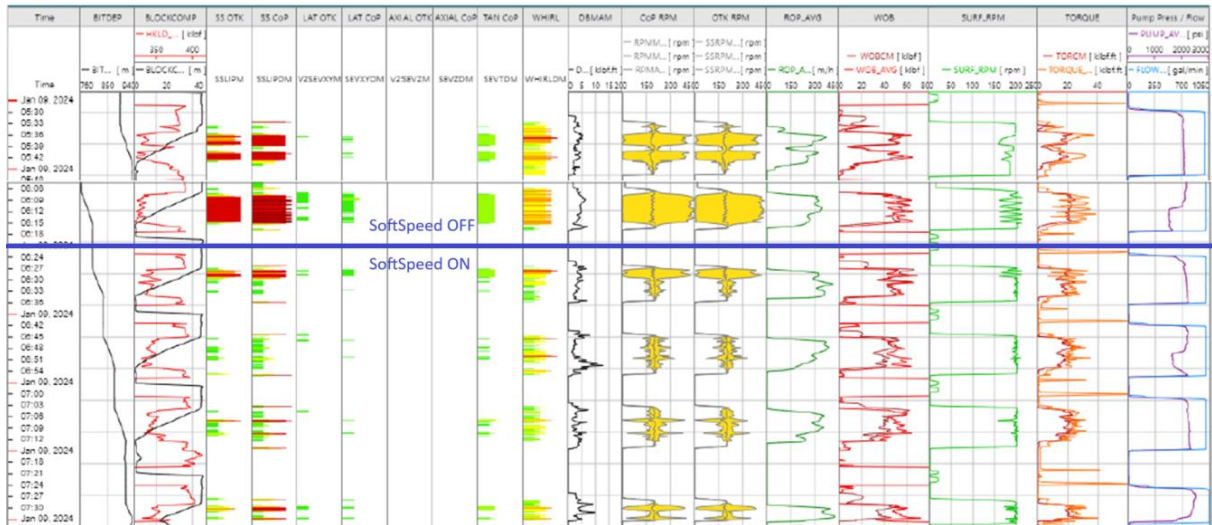
Figure 11 – Drilling Parameters with and without SoftSpeed

It is possible to observe the difference in rotation variations by comparing the MWD measurement data (columns 13 and 14, CoP RPM and OTK RPM) and the surface data, Top Drive (column 17, SURF_RPM). Just before turning on SoftSpeed, some indications in darker red can be seen in column 5, SS CoP, indicating vibration levels in which the MWD rotation would have been negative, opposite to the Top Drive rotation.

Other notable points that occurred during drilling were the occurrence of backward whirl events, indicated in red in column 11, WHIRLDM.

Case Study 2: Column Break in WELL B

In **Well B**, we had a slightly different scenario from the previous example, with the problem of breaking the pin connection between a short sub and a stabilizer (leaving a fish composed of drill bit, near bit stabilizer, and short sub), and subsequently, the problem of breaking the pin of the Drilling Jar when it was being connected to the rotary table. The figure below shows pictures of the disconnection points.

Figure 12 - On the right, the broken pin between the sub and stabilizer. In the left, the broken pin in the connection of the Drilling Jar.

In this case, the analysis points to fatigue failure in the elements, as high levels of vibration and stress (bending moment) were observed during drilling and tripping operations in the well. Figure 13 shows a summary of the parameters used and measured during the drilling of this well. The bending moment can be observed in the DBMAM column, lateral vibrations (LAT OTK and LAT CoP columns), and rotation vibration in the WHIRL column, with darker colors (red)

denoting high levels of the corresponding vibration. The breakage of the column occurred at the end of the data presented in Figure 13, the last column in the purple line, where there is a gradual drop in pump pressure until there is an abrupt decrease of 300 psi before reducing the flow rate (blue line).

Figure 13 – Drilling and Vibration parameters during Well A section

CONCLUDING REMARKS

Drilling in large diameters, especially in interbedded formations, is associated with high levels of stress and events such as column breaks, disconnections, and failures of electronic BHA tools. Therefore, several studies are conducted during the planning phase, including various torque and drag simulations.

These studies conducted during the planning phase are typically performed under static conditions, providing a good understanding of how the BHA behaves under standard conditions. However, during drilling, the boundary conditions change, such as the wellbore diameter due to washout and bit wear, completely altering the stress on the drilling string and rendering those previous simulations obsolete.

The application of maximum drilling parameters throughout the operation is another factor that should be considered in risk analysis to prevent column failures or breaks. The low frequency of downhole data is another factor that increases the risk of operational failures, as several events are not observed in real-time due to telemetry limitations.

The mechanical conditions of the drilling pipes and BHA tools, as well as the levels of maintenance and inspection, are aspects that are not well managed by operators. Information on fatigue cycles or tool utilization time is not readily available for evaluation, making it challenging to mitigate undesirable events through preventive actions such as tool rotation or replacement.

In summary, there is a significant knowledge gap between static simulations conducted by operators and service companies and the real and dynamic condition that occurs in the well. Reported events illustrate this knowledge gap and suggest several actions, as mentioned above, such as:

- Use of SoftTorque or SoftSpeed
- Implementation of AutoDrill or automatic control system for WOB and other drilling parameters
- Flow rate reduction to prevent washout
- Improvement in the frequency of data acquisition and transmission from the downhole
- Enhanced control and inspection of drilling columns and BHA tools
- Reduction of the drilling diameter
- Enhancement of simulation software solutions to include real well conditions.

REFERENCES

Tomita, R. A., dos Passos, A. G. L. G., de Resende, D. L., de Lima, F. M., Weidlich, M. C., and R. P. M. Moreira. "Drilling Practices, New Technologies and Well Integrity in Brazilian Pre-Salt Wells: A 15 Year Review and Performance Evolution." Paper presented at the Offshore Technology Conference, Houston, Texas, USA, May 2024. doi: https://doi.org/10.4043/35255-MS

Petti, Grant, Zheng, Nanjiu, and Srinivasa Koneti. "Impact of Top Drive Torque Limit on Downhole Vibration Failures of Rotary Shouldered Connections." Paper presented at the IADC/SPE International Drilling Conference and Exhibition, Galveston, Texas, USA, March 2022. doi: https://doi.org/10.2118/208677-MS

http://hmhw.com/wp-content/uploads/2023/05/Soft-Torque-Z.pdf

RESPONSIBILITY NOTICE

The authors are the only responsible for the printed material included in this paper.

Uncertain propagation in the thermo-mechanical coupled dynamic of a drill string model

Yuri B. S. Moralles – Universidade Federal do Rio de Janeiro (Brazil)
Daniel A. Castello – Universidade Federal do Rio de Janeiro (Brazil)
Thiago G. Ritto – Universidade Federal do Rio de Janeiro (Brazil)

Uncertain propagation in the thermo-mechanical coupled dynamic of a drill string model

Moralles Y.B.S.[1]**, Castello D.A.**[1]**, and Ritto T.G.**[1]

[1] Department of Mechanical Engineering, Universidade Federal do Rio de Janeiro (UFRJ), Rio de Janeiro, RJ, Brazil

Abstract: Thermal assisted drilling is a novel drilling technology, which is implemented in order to increase the process efficiency. However, this new method has some implications on drill string dynamic behavior, which are still unknown. In this paper, a 2-DOF drill string model regarding axial and torsional dynamics is considered based on an experimental assembly. Then, thermal effects are inserted in the dynamic problem by modeling the temperature dependence on the coupled nonlinear bit-rock interaction model. The thermal modeling gives axial and tangential forces varying along with the temperature of rock, and has a decreasing pattern based on experimental data found in the literature. As a final analysis, some bit-rock parameters were considered as correlated random variables, emulating the drilling operation through different rock types and the inner minerals for each rock specimen. The results show a nonlinear decreasing behavior in rock strength along temperature, which provides higher rate of penetration and lower efforts on the drill bit. It was also concluded that there are not significant changes on stick-slip occurrence regarding thermal effects. The uncertainty analysis has shown that rate of penetration is drastically affected by some rock parameters. In the other hand, torque and axial reactions are much less influenced and the angular speed has almost no influence from these parameters. Finally, thermal effects and uncertainty were considered to analyze rate of penetration on rock subjected to different temperatures.

Keywords: coupled dynamics, axial-torsional, drill-string, thermal assisted drilling, bit-rock interaction.

INTRODUCTION

Oil and gas remains one of the most abundant energy sources around the world. Although, the drilling process faces high costs, specially when it comes to drilling in hard dry rock formations. This kind of operation usually causes some issues like drill bit damage and low rate of penetration (Yang *et al.*, 2024).

Some recent researches brought up novel technologies in order to improve the entire drilling process regarding rate of penetration and costs. Some of these methods are: High Voltage Electrical Pulse Drilling and Flame Jet Drilling, both these technologies work based on the thermal spallation principle (Saksala *et al.*, 2021) (Zhu *et al.*, 2020). Rossi *et al.* (2020) proposed a model for the combination of rotary and flame jet technologies, usually called as Thermal Spalling Assisted Rotary Cutting (TSARC). Liu *et al.* (2021) developed some numerical models considering the granite and its heterogeneity provided by the mineral composition, and also found that the thermal phenomena decrease significantly the cutting forces.

Many scholars have observed the effects of TSARC on the rock breaking mechanisms and the efforts on the bit cutter, although there is a clear gap on research when it comes to the implications of TSARC on the entire drill string dynamics. The dynamic behavior of drill strings have been studied in the literature, specially because of some common vibration phenomena, which cause several damage to drilling equipment (Germay *et al.*, 2009).

The main aspect when it comes to drill string vibration is the bit-rock interaction model. This model gives force and torque function provided by the cutting process, which excites the drill string (Trindade and Sampaio, 2005). Detournay and Defourny (1992) proposed a model of axial-torsional coupling for the bit-rock interaction, considering cutting and friction torques and forces. Ritto *et al.* (2010) obtained numerical results for a finite elements model using axial-torsional bit-rock interaction model from Tucker and Wang (2003). Liu *et al.* (2014) considered a lumped parameters discrete model for a drilling operation using bit-rock interaction model from Detournay and Defourny (1992) to analyse the stability of a drilling operation. However, new models capable of incorporating the influence of thermal phenomena in the bit-rock interaction are needed. In the present work, Detournay and Defourny (1992) model will be used for a vertical drill string based on an experimental assembly, analyzing the thermal phenomena capable of modifying rock properties and thereby affecting the drilling motion. Thus, the dynamic response of the drill string in a TSARC operation will be analyzed.

Dynamic Model

For the present study, an experimental drilling assembly was the object of the dynamic problem, which is shown in Figure 1a. Lobo *et al.* (2020) has proposed a lumped parameters model for this case, as it is described in Figure 1b. Lobo also proposed the Equations 1, 2 and 3 for the drill string motion.

$$I\ddot{\theta}_{bit}(t) + c_t\dot{\theta}_{bit}(t) + k_t\theta_{bit}(t) = -T_b + c_t\Omega + k_t\Omega t \tag{1}$$

$$M\ddot{U}(t) = H_0 - Mg - W_b \tag{2}$$

$$H_0 = \bar{H}_0(1 + h\cos(\omega t)) \tag{3}$$

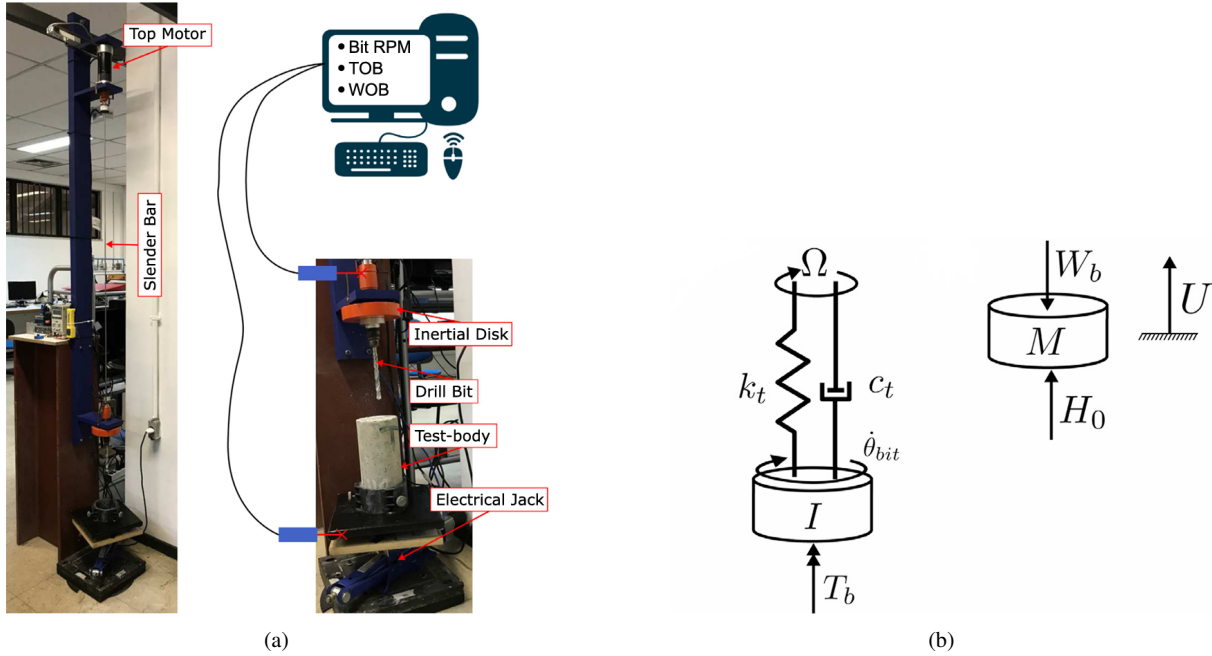(a)   (b)

Figure 1: (a) Experimental assembly and (b) Dynamic lumped parameters modeling (Lobo *et al.*, 2020).

METHODOLOGY

In this chapter, the bit-rock interaction model is proposed and discussed. Furthermore, it is considered the thermal effects in the drill string dynamics, as a model of temperature dependence on bit-rock interaction forces. In the end, The uncertainty quantification model is proposed.

Bit-rock interaction model

Axial-torsional coupled model from Detournay and Defourny (1992) describes torque on bit T_b and weight on bit W_b. Although, for both efforts, the response tends to infinity for low angular speeds, which makes integration operations more unstable. Therefore, a regularization function was proposed and implemented in T_b and W_b. The final bit-rock interaction model is showed in Equations 4, 5 and 6.

$$T_{bit} = \frac{1}{2}a^2\varepsilon\frac{2\pi\dot{u}(t)}{n_b\dot{\theta}(t)}Z^2(\dot{\theta}_{bit}) + \frac{1}{2}\mu\gamma a^2\sigma l Z(\dot{\theta}_{bit}) \tag{4}$$

$$W_{bit} = \varepsilon a\zeta\frac{2\pi\dot{u}(t)}{n_b\dot{\theta}(t)}Z(\dot{\theta}_{bit}) + \sigma al \tag{5}$$

$$Z(\dot{\theta}_{bit}) = \frac{\dot{\theta}_{bit}}{\sqrt{\dot{\theta}_{bit}^2 + e^2}} \tag{6}$$

The equations depends on angular speed $\dot{\theta}(t)$, axial velocity $\dot{u}(t)$ and some bit and rock parameters. $Z(\dot{\theta}_{bit})$ is the proposed regularization function depending on the angular speed and on a regularization parameter e. The torque and axial force behavior is shown in Figure 2
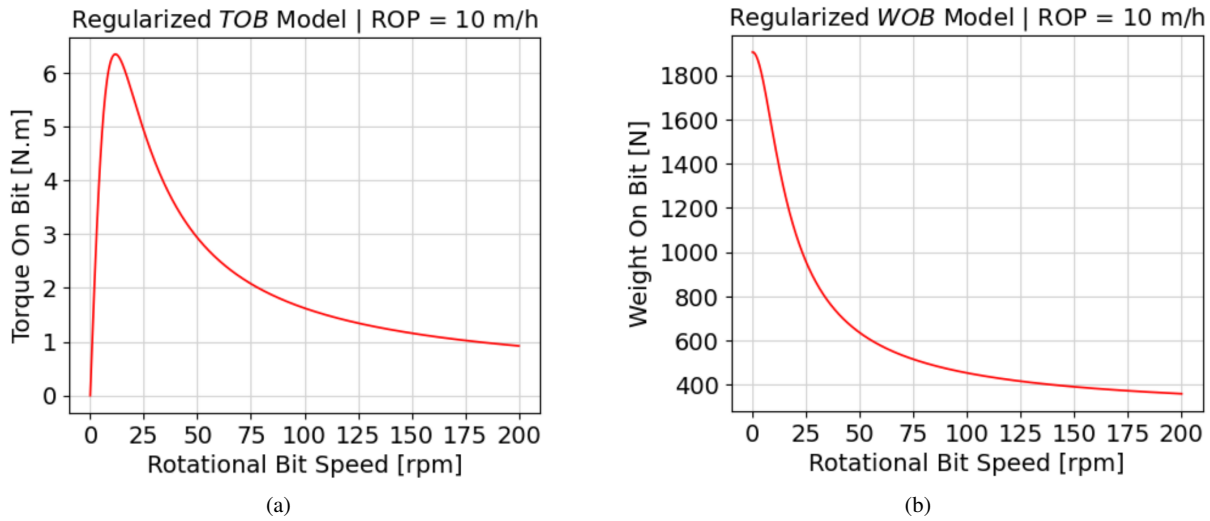
Figure 2: (a) Torque on bit response along angular speed with fixed rate of penetration and (b) weight on bit response along angular speed with fixed rate of penetration.

Model Calibration

In order to implement the bit-rock interaction model, several parameters must be obtained. There are the bit and rock parameters for the interaction model, the damping factor for the angular motion and the regularization parameter. Seven parameters from bit-rock interaction model and the damping factor for the angular motion.

A residual term was proposed regarding the comparison between experimental data from Lobo *et al.* (2020) and the computational model response. Therefore, angular speed, torque on bit and weight on bit were considered in the residual. An optimization method was used to obtain the set of parameters that minimize the residual term, in which $\hat{\psi}$ is the optimal vector of parameters, as it is shown in Equation **??**. The *PSO* parameters used were both population and sample size equals to 50.

Thermal Influence

Recent researches brought up the relation between temperature of rock and cutting forces on drilling process. Liu *et al.* (2021) got the variation of tangential and axial forces acting on the cutter along with different temperatures. It was observed that both forces decrease above 200°C. Therefore, it was proposed an exponential approximation to the literature data starting from 200°C, which is expressed in Equation 7. This equation has the parameters α and β, that had been estimated by Nelder-Mead method to fit the data curve.

$$F = \alpha e^{-\beta T} \tag{7}$$

Therefore, two factors were proposed to tangential and axial forces. These factors are equal to 1 at ambient temperature.

Uncertainty Quantification

The parameter ε was modeled as a Truncated Gaussian process, in order to represent the rock heterogeneity. Although, in drilling operations sometimes the drill bit goes through different layers made of different types of rock. Therefore, ε was modeled as a correlated random variable, to keep the variability around different regions for certain amounts of time.

An exponential the covariance function is considered. The standard deviation σ was defined as $\varepsilon_{mean}/3.5$ to keep the variation between the range observed in the literature (Liu *et al.*, 2014). The correlation factor L was defined as 0.5 to keep the value for a reasonable amount of time in each region.

RESULTS

First of all, the model calibration results have shown a reasonable approximation to experimental data, also having a similar behavior, as it is shown in Figure 3.

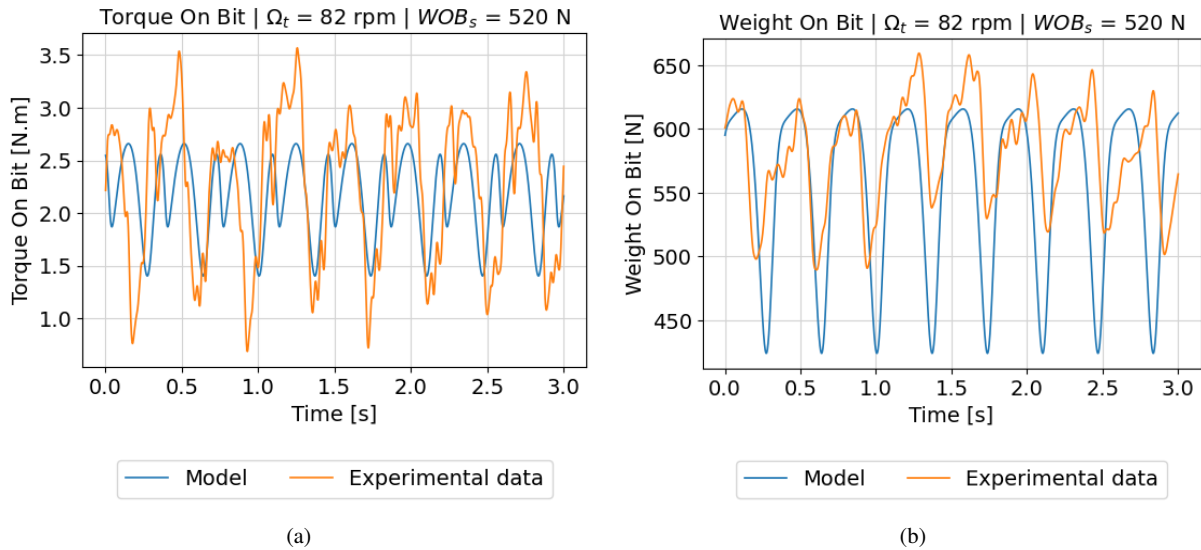(a)   (b)

Figure 3: (a) Comparison between calibrated model and experimental data for (a) torque on bit and (b) weight on bit.

Hence, implementing the thermal effects on bit-rock interaction model, different temperature scenarios were compared. An operational map varying the static weight on bit and top rotational speed with different temperatures have shown the potential of rock high temperatures on the rate of penetration increase, shown in Figure 4.

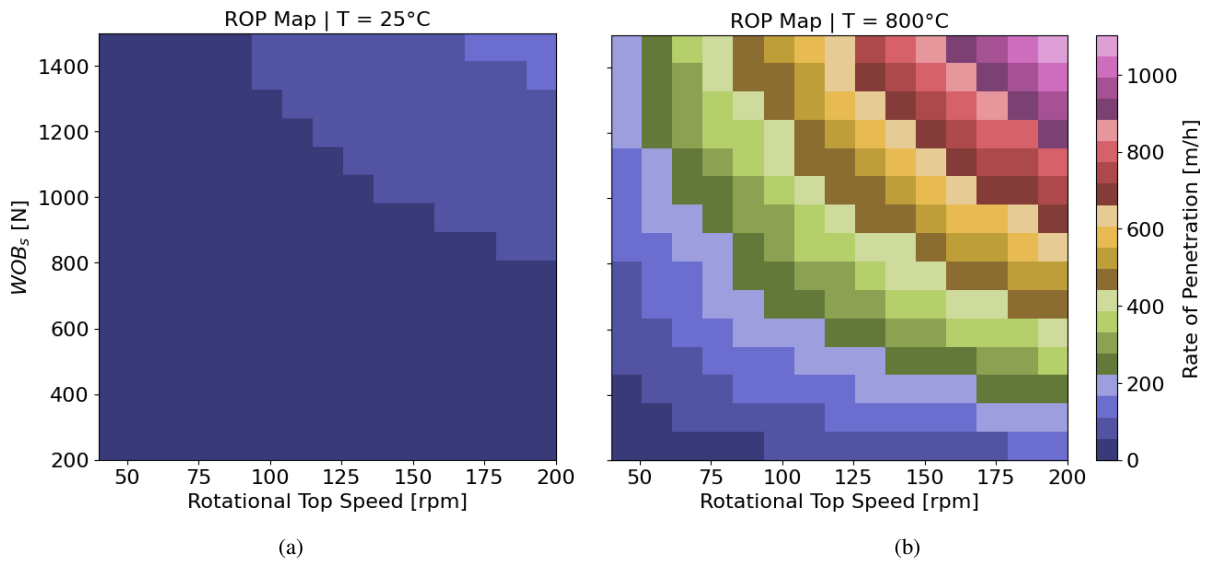(a)   (b)

Figure 4: Operational map of rate of penetration varying with static weight on bit and top angular speed, for (a) temperature equals to 25°C and (b) equals to 800°C.

It is worth noting that it is possible to see high rate of penetration in this case, considering that another aspects like drilling equipment and drill string mechanical limitations had not been analyzed in this work.

Then, the uncertainty was applied on the intrinsic specific energy of rock. It was noticed that the rate of penetration is the most affected response regarding the ε variability. Figure 5 shows the envelope of *ROP* response, without temperature effects.
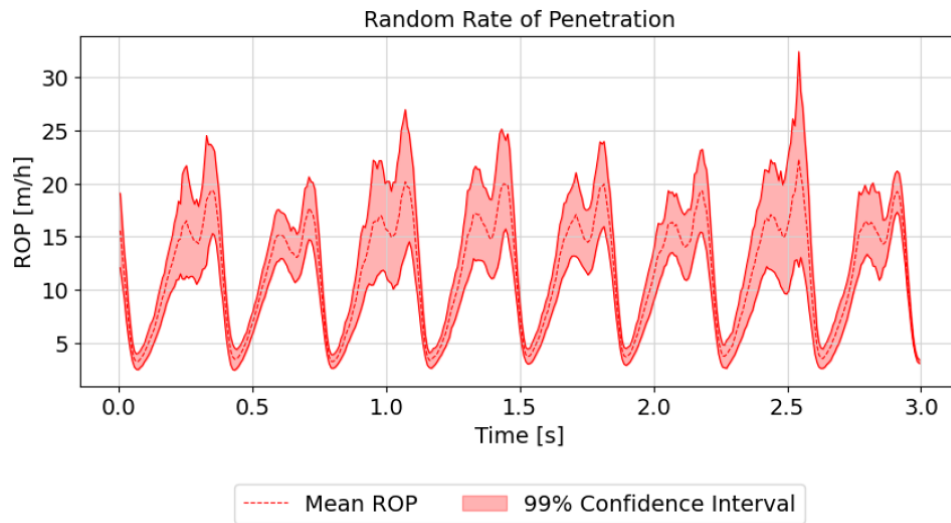
Figure 5: Rate of penetration response envelope with temperature equals to 25°C.

Finally, both thermal effects and uncertainty were considered together in order to visualize the *ROP* variation. Hence, the average *ROP* was calculated with different temperatures, from 25°C to 800°C, considering the correlated random ε, as it is shown in Figure 6. It was observed a larger envelope on higher temperatures.
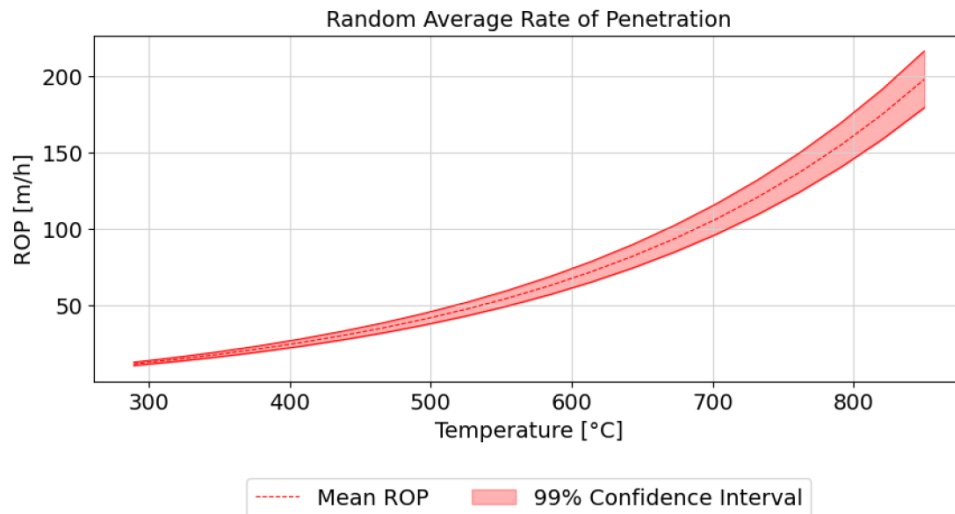

Figure 6: Average rate of penetration envelope varying with temperature.

CONCLUDING REMARKS

As conclusions we have: the model could approach experimental data with a reasonable accuracy; uncertainty on rock type has a significant role on rate of penetration. thermal effects have a high potential to increase rate of penetration.

REFERENCES

Detournay, E. and Defourny, P., 1992. "A phenomenological model for the drilling action of drag bits". In *International journal of rock mechanics and mining sciences & geomechanics abstracts*. Elsevier, Vol. 29, pp. 13–23.

Germay, C., Denoël, V. and Detournay, E., 2009. "Multiple mode analysis of the self-excited vibrations of rotary drilling systems". *Journal of Sound and Vibration*, Vol. 325, No. 1-2, pp. 362–381.

Liu, W., Zhu, X., Lv, Y. and Tong, H., 2021. "On the mechanism of thermally induced micro-cracking assisted rock cutting in hard formation". *Journal of Petroleum Science and Engineering*, Vol. 196, p. 107666.

Liu, X., Vlajic, N., Long, X., Meng, G. and Balachandran, B., 2014. "Coupled axial-torsional dynamics in rotary drilling with state-dependent delay: stability and control". *Nonlinear Dynamics*, Vol. 78, pp. 1891–1906.

Lobo, D., Ritto, T., Castello, D. and de Souza, M., 2020. "On the calibration of drill-string models based on hysteresis cycles data". *International Journal of Mechanical Sciences*, Vol. 177, p. 105578.

Ritto, T., Soize, C. and Sampaio, R., 2010. "Robust optimization of the rate of penetration of a drill-string using a stochastic nonlinear dynamical model". *Computational Mechanics*, Vol. 45, pp. 415–427.

Rossi, E., Jamali, S., Saar, M.O. and von Rohr, P.R., 2020. "Field test of a combined thermo-mechanical drilling technology. mode i: thermal spallation drilling". *Journal of Petroleum Science and Engineering*, Vol. 190, p. 107005.

Saksala, T., Kouhia, R., Mardoukhi, A. and Hokka, M., 2021. "Thermal jet drilling of granite rock: a numerical 3d finite-element study". *Philosophical Transactions of the Royal Society A*, Vol. 379, No. 2196, p. 20200128.

Trindade, M.A. and Sampaio, R., 2005. "Modeling of axial-torsional coupled vibrations of drillstrings". In *13th International Workshop on Dynamics and Control, Daimler–Chrysler Training Center, Wiesenteig, Germany, Shaker Verlag*.

Tucker, R.W. and Wang, C., 2003. "Torsional vibration control and cosserat dynamics of a drill-rig assembly". *Meccanica*, Vol. 38, pp. 145–161.

Yang, F., Liu, W., Zhu, X. and Xiang, C., 2024. "The rock-breaking mechanism of thermal spalling-assisted rock cutting by pdc cutter". *Rock Mechanics and Rock Engineering*, Vol. 57, No. 2, pp. 993–1012.

Zhu, X., Luo, Y. and Liu, W., 2020. "On the rock-breaking mechanism of plasma channel drilling technology". *Journal of Petroleum Science and Engineering*, Vol. 194, p. 107356.

RESPONSIBILITY NOTICE

The authors have total responsibility for the printed material included in this paper.

Nonlinear dynamics of smart drilling systems

Marcelo A. Savi – Universidade Federal do Rio de Janeiro (Brazil)

Nonlinear Dynamics of Smart Drilling Systems

Marcelo A. Savi[1]

[1] Universidade Federal do Rio de Janeiro, COPPE – Mechanical Engineering, Center for Nonlinear Mechanics.
 Email: savi@mecanica.coppe.ufrj.br

Abstract: Smart materials present multiphysics couplings that confer remarkable properties related to adaptive behavior. These characteristics are motivating engineering applications in different fields of human knowledge, including oil & gas industry. Several alternatives have been investigated employing distinct smart materials, characterized by different couplings. In this regard, it should be pointed out shape memory alloys, piezoelectric and magnetostrictive materials. This paper presents a collection of results of smart drilling systems emphasizing shape memory alloy couplers to mitigate drilling vibration; and piezoelectric mechanical energy harvester.

Keywords: Smart materials, shape memory alloys, piezoelectric, drilling, energy harvesting.

INTRODUCTION

Smart materials present multiphysics couplings connecting fields that usually are not connected. This includes the coupling between mechanical and non-mechanical fields that confers special kinds of behaviors. The multiphysics couplings confer adaptive characteristics that are induced by environmental changes. Smart materials can be considered a transdisciplinary subject since it involves at least two different physical domains. The classification and main definitions are related to the domains that are coupled and, in general, it is possible to consider physical domains as mechanical, magnetic, electrical, thermal, optical, and chemical. On this basis, several smart materials can be identified based on the coupled domains.

Piezoelectric materials present electromechanical coupling, which means that an applied mechanical strain induces an electric potential, or vice-versa. Magnetostrictive materials present magnetomechanical coupling, and therefore, a magnetic field induces a mechanical strain. Shape memory alloys present a thermomechanical coupling associated with phase transformations that can be induced either by mechanical strain/stress or by temperature. This kind of material can recover its shape, or it can vary its properties due to temperature variations. Variations of these materials include shape memory polymers that increase even more their applicability.

The choice of proper material for each application depends on many factors and two design drivers need to be highlighted (Lagoudas, 2008): the actuation energy density; and the actuation frequency of the material. Basically, this indicates that high frequencies are usually related to low forces, and vice-versa.

This paper presents some ideas related to the use of smart materials in drilling systems. Shape memory alloys and piezoelectric materials are discussed showing potential applications. Shape memory alloys are employed to build couplers that can mitigate critical vibration situations. On the other hand, piezoelectric materials are employed in mechanical energy harvesters useful to provide energy in remote areas.

SHAPE MEMORY ALLOYS

Shape memory alloys (SMAs) present a thermomechanical coupling in such a way that they have the ability of recover a previous shape when subjected to a proper thermomechanical loading process. When there is a restriction to the shape recovery, these alloys promote high restitution forces. The remarkable properties of SMAs are associated with solid phase transformations responsible for different thermomechanical behaviors of these alloys. Basically, two different phases are possible in SMAs: austenite and martensite. Austenitic phase is stable at high temperatures and stress-free state presenting a single variant. On the other hand, martensitic phase is stable at low temperature in a stress-free state, being related to numerous variants. Phase transformation may be induced either by stress or by temperature. When the martensite is induced by temperature, it is called twinned martensite, which has 24 variants that represent subtypes with different crystallographic orientations. The martensitic formation induced by stress tends to change these 24 variants of twinned martensite into only one variant, aligned with the stress direction, which is called detwinned martensite. Therefore, besides phase transformation, reorientation is another driving behavior of SMAs.

The macroscopic behavior of SMAs can be expressed by stress-strain-temperature (or force-displacement-temperature) curves. SMA thermomechanical behavior is complex being represented by different phenomena. Pseudoelasticity, shape memory effect, two-way shape memory effect, transformation induced plasticity are some examples of the thermomechanical behavior of SMAs. Typically, applications exploits both shape recovery, property changes due to phase transformations and hysteretic dissipation.

The modeling of SMA thermomechanical behavior is the objective of numerous research efforts, being a complex subject due to the phenomena involved. It is essentially a multiscale effort, and the constitutive modeling is related to

phenomenological features. Paiva & Savi (2006), Lagoudas (2008) and Cissé et al. (2016) presented general overviews of the SMA constitutive modeling, discussing the main models available in the literature. In general, the constitutive models are developed within the framework of the continuum mechanics, with a formulation guided by the second law of thermodynamics. An interesting alternative to describe the SMA macroscopic behavior is a geometric-based approach known as Preisach model (Alvares et al., 2024).

Among the available constitutive models there is one that is able to describe several SMA complex phenomena with flexibility. The constitutive model is developed within the framework of the generalized standard materials, being able to describe SMA behavior either in one-dimensional or three-dimensional media (Paiva et al., 2005; Oliveira et al., 2014; Oliveira et al., 2018; Dornelas et al., 2020, 2021). Among alternatives, it should be highlighted the model due to Lagoudas et al. (2012).

SMA Couplers

SMA high dissipative behavior due to hysteretic response can be exploited in drilling process in order to mitigate critical vibrations. Silva et al. (2021) proposed the use of SMA elements in drill-string couplers and the proof of concept of this idea can be shown by assuming a multi-degree of freedom torsional model using lumped parameters, described by the following equation,

$$M\ddot{\phi} + C\dot{\phi} + K\phi = T_r + T_b + T_s \tag{1}$$

where M is the mass matrix; K is the stiffness matrix; C is the proportional damping matrix; T_r is the rotary table torque vector; T_b is the torque on bit vector; T_s is the SMA coupler torque vector.

The description of the SMA coupler torque needs to consider a proper constitutive equation. A phenomenological model proposed by Lagoudas et al. (2012) is employed considering modifications proposed by Enemark et al. (2016). By assuming that τ is the shear stress; γ is the shear strain; γ_t is the phase transformation shear strain; β is the martensitic volume fraction, the following equations are written,

$$\tau = G_S(\gamma - \gamma_t) \tag{2}$$

$$\dot{\gamma}_t = \dot{\beta}\Lambda \tag{3}$$

where Λ is defined by employing hardening functions (Silva et al., 2021).

The total torque is defined by analyzing the coupler behavior, a typical torsional element that can be described by integrating dF, and using a proper SMA constitutive equation,

$$T_S = \int_{r_i}^{r_0} r \, dF = 2 \int_{r_i}^{r_0} G_S(\gamma - \gamma_t) \, \pi \, r^2 \, dr \tag{4}$$

By assuming that phase transformation is homogeneous in a cross-section of the element, it is possible to write the torque as follows,

$$T_S = \frac{G_S J_S}{r_0}(\gamma^* - \gamma_t) \tag{5}$$

where γ^* is the strain at a representative radius.

On this basis, the coupler hysteretic response tends to dissipate undesirable behaviors, promoting better conditions for the drill-string system. Figure 1 shows a comparison between the response of the drill-string system with SMA couplers and a reference response, without SMA, for different weight on bit values, W_b: 200, 275 and 350 kN. Note that hysteretic behavior tends to decrease vibration amplitudes, and this trend can be altered by either temperature or prestress. Therefore, it is possible to develop a proper design according to the operational conditions.
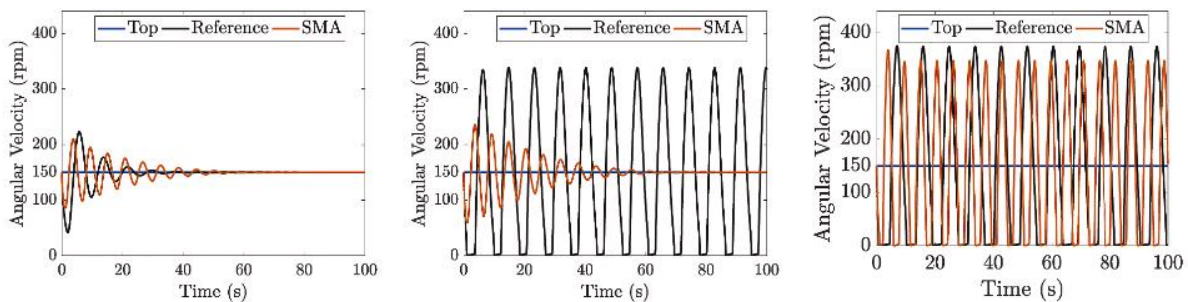
Figure 1 – Comparison between drill-string system with SMA couplers and a reference response, without SMA, for different weight on bit, W_b: 200, 275 and 350 kN.

PIEZOELECTRIC MATERIALS

Piezoelectric materials present electromechanical coupling and therefore, once an electrical field is applied, the material exhibits a mechanical deformation; on the other hand, when the material undergoes a mechanical load, an electrical potential is generated. This reciprocity enables this kind of material to be used either as sensors or actuators in smart structures.

Mechanical energy harvesting is critical to address energy challenges and recently, the necessity to provide energy to portable electronic devices increases even more its importance. Cableless installations and the need to avoid battery replacements are critical especially on advanced scenarios that include Internet of Things (IoT), smart cities and oil & gas industry. In this regard, energy harvesting has an increasing importance with the idea to capture the ambient energy surrounding and convert it into usable electrical energy.

The most common configuration of a mechanical energy harvester is a cantilever beam coupled to an electronic circuit by a piezoelectric element. This piezo-elastic device has a performance strictly related to the beam natural frequency, which means that it has satisfactory performance under resonant conditions. Since external sources are related to uncertainties, it is necessary to enhance energy harvesting capacity by different strategies.

Besides the development of proper design configurations, nonlinearities are essential for the enhancement of energy harvesting capacity. Multistability is the essential point for this purpose, which can be achieved by impacts, buckling and magnetic interactions. Monostable, bistable, tetrastable, pentastable systems are possible to be imagined. Magnetic interactions are the most common strategy to reach the desired multistability. On this basis, bistable systems are usually represented by Duffing-type systems, with cubic nonlinearities, and other polynomial approximations can be used to higher order cases. The classical nonlinear energy harvesting device can be described by a Duffing oscillator with cubic nonlinearity. By assuming a one-degree of freedom mechanical system, represented by displacement *u*, the following electromechanical equation of motion is presented by assuming that *v* is the voltage,

$$\ddot{u} + 2\xi\dot{u} + \alpha u + \delta u^3 - \chi v = \gamma \sin(\Omega t) \tag{1}$$

$$\kappa\dot{u} + \dot{v} + \varphi v = 0 \tag{2}$$

where ξ is the dissipation, α and δ characterize the Duffing-type restitution; χ is the electromechanical coupling; φ is an electrical property; and the external energy source is represented by a harmonic stimulus $\gamma \sin(\Omega t)$.

The development of novel nonlinear configurations is showing to be the solution for the design of enhanced energy harvesters. Costa & Savi (2024) proposed a novel nonlinear dual-beam structure with two sets of magnets and transducers (Figure 2). This design enables efficient utilization of unused space with unprecedented multistable characteristics, enhancing the overall functionality of this type of harvester (Costa et al., 2024).

The model for the dual-beam device can be related to a two-degrees of freedom Duffing oscillator that presents rich multistable characteristics. A comparison with the classical energy harvester composed by a bistable beam shows that the dual-beam presents better overall performance. Figure 3 shows a comparison between both systems for different external stimulus parameters: amplitude, γ; and frequency, Ω. The red color represents situations where the dual-beam performance exceeds the classical beam. It should be pointed out that the dual-beam better performance is the preponderant behavior, exceeding the classical devices except to the linear resonant condition.
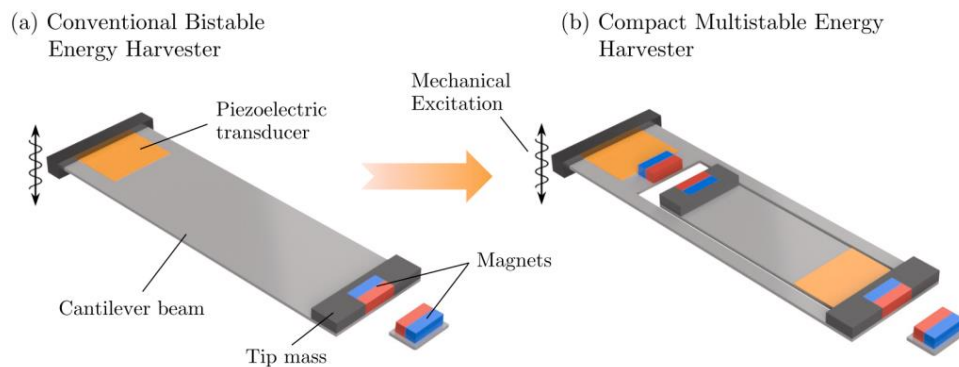

(a) Conventional Bistable Energy Harvester

(b) Compact Multistable Energy Harvester

Figure 2 – Classical energy harvester and the evolution of its design for a dual-beam.
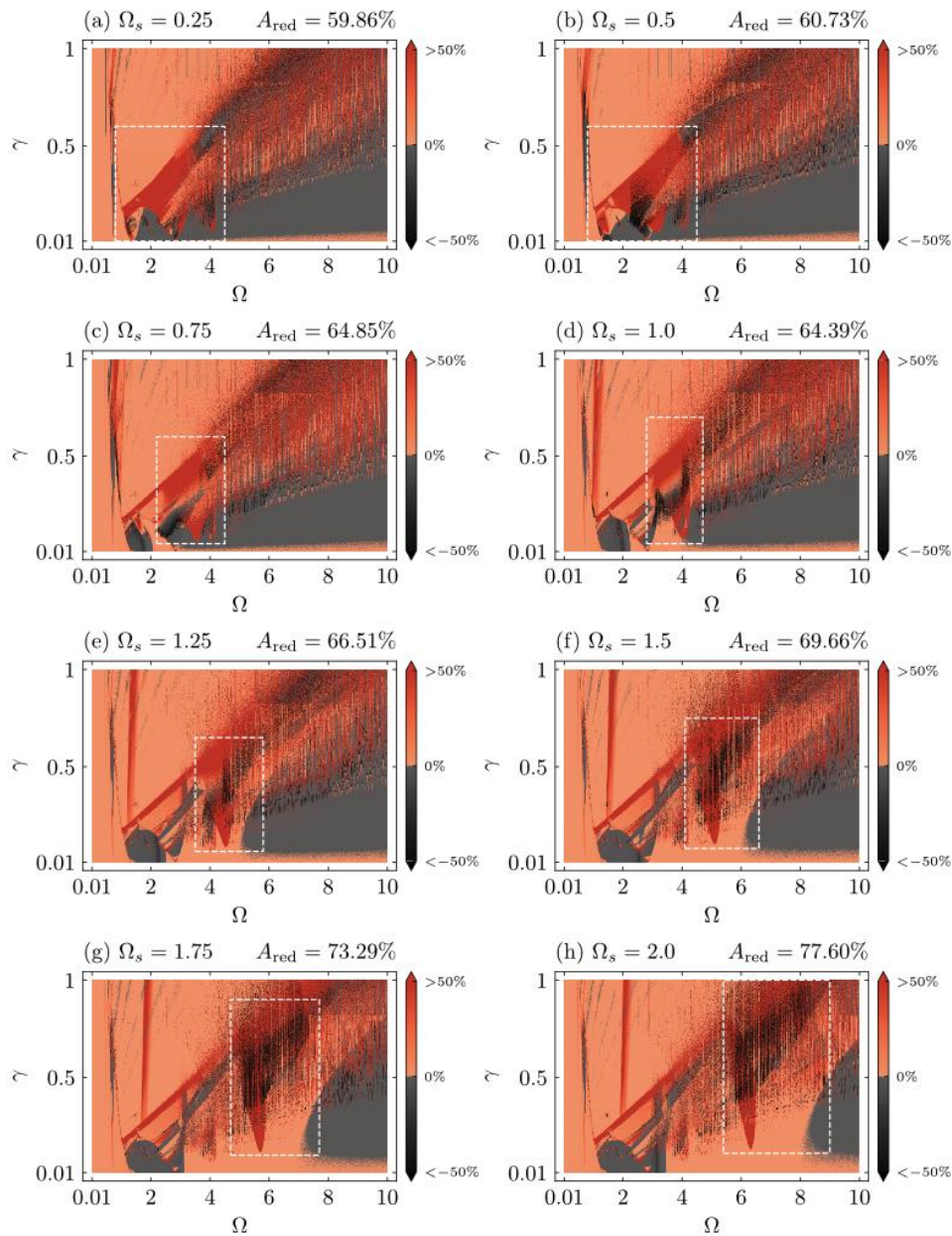

Figure 3 – Comparison of performance of the novel dual-beam design compared with the classical beam harvester: red means better performance of the dual-beam.

CONCLUDING REMARKS

This paper presents a general overview of smart systems and structures, especially with their application to oil & gas industry. A collection of results related to shape memory alloy and piezoelectric system are of special interest. SMA couplers for drilling system is discussed showing the idea to exploit hysteretic dissipation to mitigate vibration critical situations. Besides, piezoelectric mechanical energy harvesting is investigated, showing to be a feasible and interesting idea to provide energy in remote areas.

ACKNOWLEDGMENTS

a collaborator with whom we developed the idea of the SMA coupler. Besides, it is important to mention R.S. Silva and Luã G. Costa that worked on the selected subjects.

REFERENCES

T.Q. Alvares, V.M. Dornelas, S.A. Oliveira & M.A. Savi (2024), "Thermomechanical description of shape memory alloys using the Preisach model", Smart Materials and Structures, v.33, n.3, Article 035019.

C. Cisse, W. Zaki & T. B. Zineb (2016), "A review of constitutive models and modeling techniques for shape memory alloys", International Journal of Plasticity, v., pp.244–284.

L.G. Costa & M.A. Savi (2024), "Nonlinear dynamics of a compact and multistable mechanical energy harvester", International Journal of Mechanical Sciences, v.262, Article 108731.

L.G. Costa, L.L.S. Monteiro & M.A. Savi (2024), "Multistability investigation for improved performance in a compact nonlinear energy harvester", Journal of the Brazilian Society of Mechanical Sciences and Engineering, v.46, Article 212.

L.G. Costa, L.L.S. Monteiro, P.M.C.L. Pacheco & M.A. Savi (2021), "A parametric analysis of the nonlinear dynamics of bistable vibration-based piezoelectric energy harvesters", Journal of Intelligent Material Systems and Structures, v.32, n.7, pp.699-723.

V. M. Dornelas, S. A. de Oliveira, M. A. Savi, P. M. C. L. Pacheco & L. F. G. de Souza (2021), "Fatigue on shape memory alloys: experimental observations and constitutive modeling", International Journal of Solids and Structures, v.213, pp. 1–24.

V. M. Dornelas, S. A. de Oliveira & M. A. Savi (2020), "A macroscopic description of shape memory alloy functional fatigue", International Journal of Mechanical Sciences, v.170, Article 105345.

S. Enemark, M.A. Savi & I.F. Santos (2016), "Modelling, characterisation and uncertainties of stabilised pseudoelastic shape memory alloy helical springs", J. Intell. Mater. Syst. Struct, v.27, pp.2721–2743.

D. Lagoudas. "Shape memory alloys", Springer, 2008.

D. Lagoudas, D. Hartl, Y. Chemisky, L. Machado, P. Popov (2012). "Constitutive model for the numerical analysis of phase transformation in polycrystalline shape memory alloys", Int. J. Plasticity, v.32–33, pp.155–183

S.A. Oliveira, V.M. Dornelas, M.A. Savi, P.M.C.L. Pacheco & A. Paiva (2018), "A phenomenological description of shape memory alloy transformation induced plasticity", Meccanica, v.53, n.10, pp.2503-2523.

S.A. Oliveira, M.A. Savi & I.F. Santos (2014), "Uncertainty analysis of a one-dimensional constitutive model for shape memory alloy thermomechanical description", International Journal of Applied Mechanics, v.6, n.6, Article 1450067.

A. Paiva & M.A. Savi (2006), "An overview of constitutive models for shape memory alloys", Mathematical Problems in Engineering, v.2006, 056876.

A. Paiva, M.A. Savi, A.M.B. Braga & P.M.C.L. Pacheco (2005), "A constitutive model for shape memory alloys considering tensile-compressive asymmetry and plasticity", International Journal of Solids and Structures, v.42, pp.3439-3457.

R.S. Silva, T.G. Ritto & M.A. Savi (2021), "Shape memory alloy couplers applied for torsional vibration attenuation of drill-string systems", Journal of Petroleum Science and Engineering, v. 202, Article 108546.

RESPONSIBILITY NOTICE

Closing Pandora's Box: Characterizing and Mitigating High- Frequency Torsional Oscillation

Ashley Johnson – SLB (UK)
Dave Scott – SLB (UK)

Closing Pandora's Box: Characterizing and Mitigating High-Frequency Torsional Oscillation

Ashley Johnson[1] and Dave Scott[1]

[1]SLB Cambridge Research, High Cross, Madingley Rd., Cambridge, UK

High-frequency torsional oscillation (HFTO) is one of the most damaging drilling dysfunctions encountered today. In the drilling assemblies we have seen torsional waves with amplitudes of 3,500 lbf·ft at frequencies in excess of 350 Hz. The resultant damage from this dysfunction includes cracked drill collars, broken mechanical components, shattered electronics, twisted off bits, and shorted batteries.

We have developed experimental equipment to generate HFTO at a bit scale in laboratory testing. We show that the origin of the resonance is at the cutter rock contact and is driven by the elastic nature of the formation contact.

We show that at low speeds below a threshold level, the resonance is stable and sustained, growing as amplitude grows with speed. Above this threshold, the oscillation is not sustained. It will be triggered, grow in amplitude in a few milliseconds, but then be mitigated as quickly. We see high-amplitude bursts that will last less than 40 ms.

This new understanding can enable a step change in the mitigation of this most damaging dysfunction.

Keywords: drilling, dysfunction, HFTO, bits

INTRODUCTION

HFTO is one of the most damaging drilling dysfunctions we encounter in regular operations. With fundamental frequencies up to 400 Hz and amplitude as large as the mean drilling torque, the impact of fatigue is considerable. Although HFTO was first reported by Pastusek et al. (2007), it was after 2015 in unconventional wells where the first torsional fatigue cracks appeared in collars. These failures were mitigated by using larger outside diameter (OD) collars, but we now see other vibration- and strain-driven failures.

Attempts at mitigation using dampers or low friction contact points have been implemented, which bring some benefits but do not stop the problem.

It has been considered that the HFTO is driven by the bit, so understanding the characteristic of the cutting structure could present an opportunity to eliminate this dysfunction entirely.

We have developed a torsionally resonant system for our laboratory drilling machine to enable HFTO as required, which enables the direct comparison of different systems and separation of variables to make a scientific evaluation of the fundamental drivers behind HFTO.

HFTO

HFTO is a torsional oscillation of the lower bottomhole assembly (BHA). It is similar to stick-slip in that there are torsional standing waves along the drilling assembly; however, the fundamental frequency is in the range of 50 to 400 Hz, so the wavelength is shorter, typically in the range of 20 to 150 ft (6 to 50 m).

Using field data, Johnson et al. (2023) showed that the frequency was determined by the BHA. Notably, a node would be formed at the first torque discontinuity, either the high friction contact point or at the motor. Fig. 1 shows the frequency plotted against the distance from the bit for both rotary- and motor-driven assemblies together with the fit:

$$f = \frac{kv}{x} \tag{1}$$

where x is the distance to the first high-friction contact or the motor and $0.5 < k < 1$.
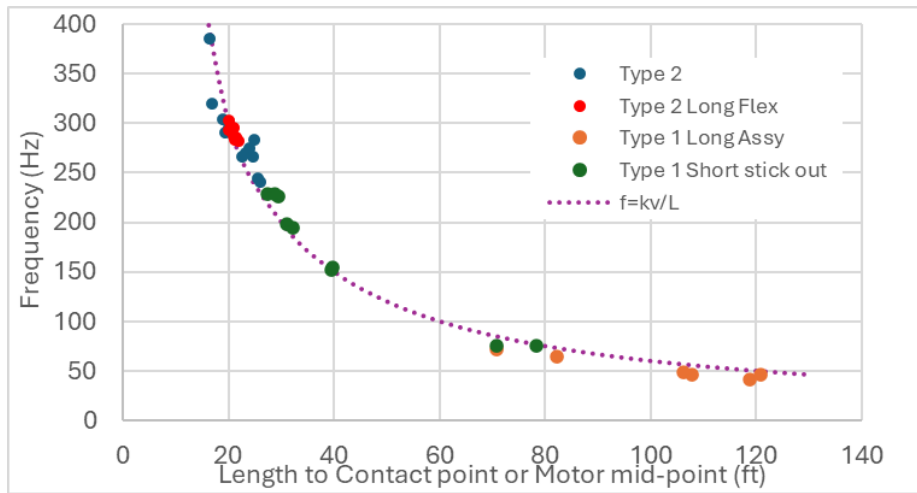
Fig. 1—Frequency of HFTO plotted against the length to the contact point or position of the node in the motor. Data are for runs in four geographical basins, motor-driven and nonmotor-driven assemblies and for 4.75-in. and 6.75-in. BHA sizes.

For continuous systems in torsional vibration, Prentis (1980) showed the velocity could be calculated from

$$v = \sqrt{\rho/C} \tag{2}$$

where ρ and C are the density and modulus of rigidity of the collar material. Using this estimate and equation 1, we find $k \sim 0.7$. The bit is neither a node (zero displacement) nor an antinode (zero torque variation). We can consider that the torque and displacement are coupled here. With this coupling, the bit is an ideal point to eliminate HFTO.

Another characteristic previously noted is the impact of collar speed on this dysfunction. Johnson et al. (2023) also reported how HFTO would be energized and attenuated though the period of stick-slip (Fig. 2). As the collar speed increased the amplitude grew, but would then drop at the highest collar speed. Although this phenomenon has been noted by a number of authors there is no clear understanding of it.
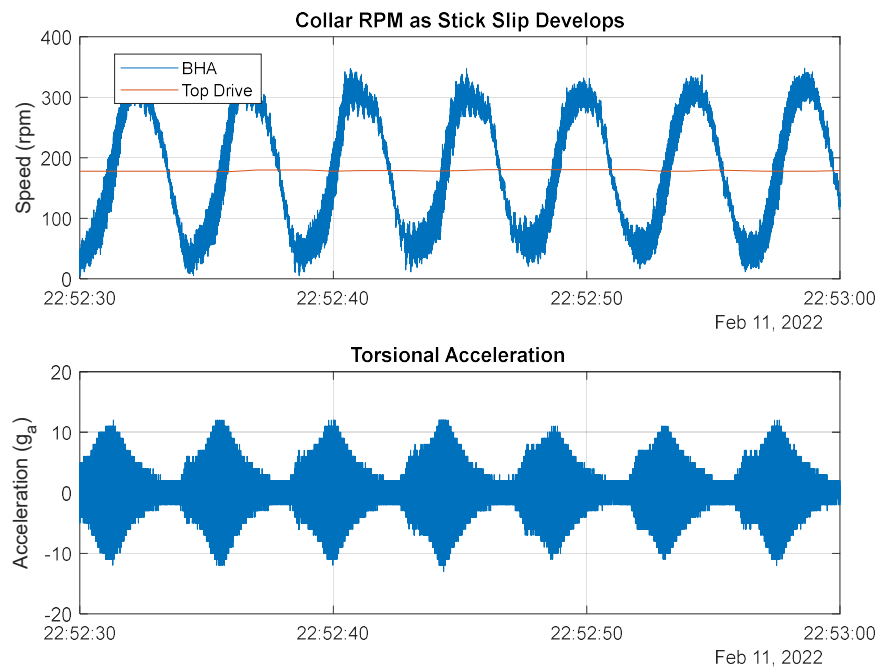

Fig. 2—Collar RPM (top) and torsional acceleration (lower) for a 30-s period of stick-slip recorded with a memory tool while drilling with a rotary assembly.

LABORATORY SCALE TESTING HFTO

It is evident that this dynamic is driven by the bit, but the actual triggers are not immediately clear. We launched a study to identify the fundamental driver of HFTO. As such, we needed to modify our large atmospheric drilling machine (LAM; Fig. 3) to generate HFTO, as well as make direct comparisons to non-HFTO conditions.

Various approaches have been taken to generate HFTO in a laboratory setting. Notably, Kueck et al. (2023) used a long drill collar to allow for the torsional compliance needed to generate good HFTO characterization at the bit. However, this approach would not have provided the flexibility required to enable with/without conditions for the desired HFTO comparison. Alternatively, Tipples et al. (2021) used a stiffer system but looked for HFTO at a very low level. This condition is appropriate for linear dynamic systems, but we wanted a direct comparison to the field system with appropriate levels of perturbation.

Fig. 3—LAM with the complaint HFTO-enabling shaft.

Building a facility with a long collar would be difficult and would be impossible to enable and disable HFTO when needed, so we used an alternative approach. To generate a resonance, we implemented the torsional equivalent of a mass spring resonance system. In linear systems, resonance is known with a frequency $f = \sqrt{s/m}$, where s and m are the stiffness and mass, respectively. By taking the same approach in the torsional domain, we built a torsional spring (compliant shaft in Fig. 4) designed with the bit polar moment of inertia to resonate in the range of 200 to 350 Hz.

In Fig. 4 we show the fast fourier transform (fft) of the measured drilling torque for two tests with the identical drilling conditions, bit, and rock except with a regular (conventional) collar and the compliant collar. The torsional resonance is evident in the window ~340 Hz for the compliant shaft system. With this we now have a system whereby we can energize HFTO as needed, and with the stiff shaft make a direct comparison to non resonance drilling.

It is noteworthy that the resonance at 85 Hz is driven by vibration from the gearbox and is the same amplitude regardless of the shaft configuration.
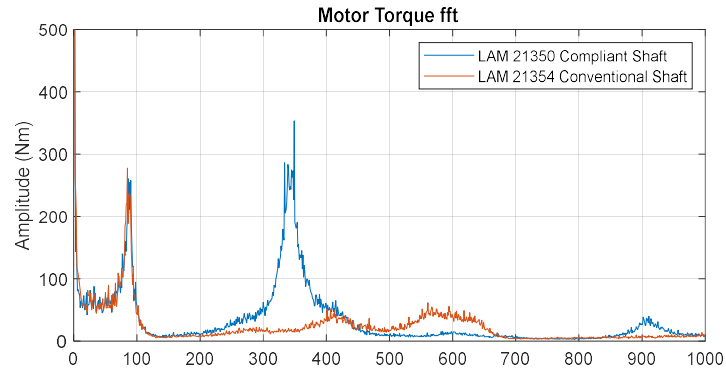
Fig. 4—fft of the drilling torque drilling a Rocharon Limestone with the same bit and drilling parameters but with a conventional and the compliant shaft. The resonance at 340 Hz is HFTO energized by resonance in the bit. The 85 Hz is caused by noise from the gearbox.

DRIVERS FOR HFTO

It had been postulated that HFTO was driven by drilling noise from the bit energizing a resonance in the mechanical drilling system. To test this hypothesis, we compare the amplitude of the HFTO drilling two different rocks (Lazonby, a 4,500-psi sandstone and Rocharon, a 24,000-psi limestone) both with and without HFTO. If HFTO was driven by bit noise, we could expect the relative amplitude of the HFTO for the two rocks would be similar to the relative amplitude of the drilling noise without resonance.

In Fig. 5 (left plot) we show the fft of the drilling torque for the two rocks. We see a similar amplitude for the perturbation at the 85-Hz gearbox resonance, but at the HFTO frequency it is almost an order of magnitude higher for the harder rock. However, for the test with the stiff shaft (right plot), the amplitude for the drilling noise is very similar over all frequencies.

Therefore, we must reject the hypothesis that the HFTO is driven by broadband drilling noise and consider that it is caused by a resonance in the actual bit-rock interaction (the cutter-rock interaction).
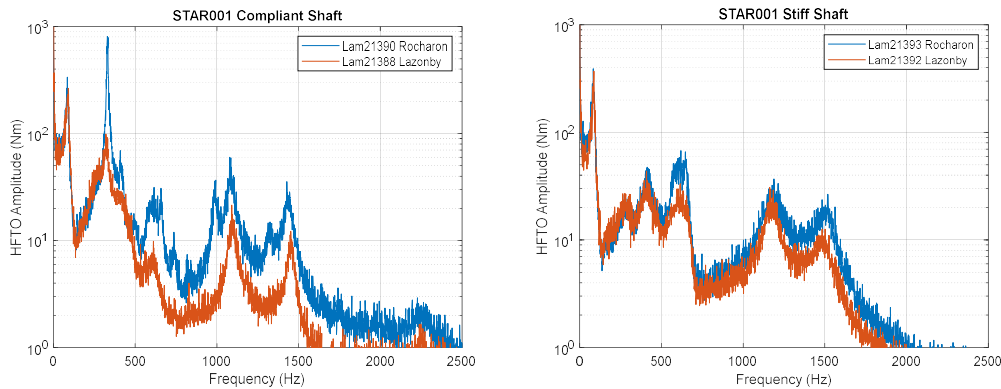
Fig. 5—fft of the drilling torque, with the compliant (HFTO) shaft and the stiff (non-HFTO) shaft on right drilling Rocharon Limestone (24,000 psi) and Lazonby Sandstone (4,500 psi) without HFTO drilling with the regular stiff shaft.

COLLAR SPEED

To characterize the impact of speed on the amplitude of the HFTO, we devised an experimental procedure to cycle the bit through a speed range. We accelerate the bit from stationary to 200 rpm, hold it, then drop it back to stationary. The period for this cycle is 6 seconds. We repeat this over several cycles. A dataset from one test is shown in Fig. 6. The speed is shown in the lower frame and is color coded. The HFTO amplitude is in the upper frame plotted against speed and color coded by the point in the speed cycle.

As the collar speed increases the amplitude of the HFTO also goes up, almost linearly with the rotation rate. As it crosses an upper threshold, around 100 rpm for this system, the amplitude of the HFTO drops rapidly, then continues at

this lower level to the maximum speed. The impact of the drop in speed is an almost exact reversal of the speed increase. The level remains low but jumps to the higher level at the same upper threshold speed.

In this plot we calculated the HFTO amplitude with an fft over a 0.1-second window. This is effective but will smear out events that occur more rapidly. In Fig. 7, we show a time series of the bit speed, the drilling torque, and the HFTO amplitude from an fft over 0.016 seconds. Here we see a 2-second interval with the bit accelerating from +20 rpm to 200 rpm. We see the amplitude of the HFTO increase, then at around 100 rpm it stops. Subsequently, we see the HFTO in bursts rather than being steady at a lower level. At 125 seconds, for example, we see a single burst of HFTO with the amplitude increase by an order of magnitude, then drop as quickly. This entire process takes around 0.04 seconds. Over this period the bit rotated about 30° and the outer cutters moved about 40 mm.

At lower speed, the HFTO is steady and the resonance continuous. At higher speeds, however, the HFTO is not sustainable. It is triggered and the amplitude grows very rapidly. However, it is also attenuated as quickly.

There is some very significant complexity in the bit-cutter-rock interaction; understanding this will be key to characterizing the drivers behind HFTO.
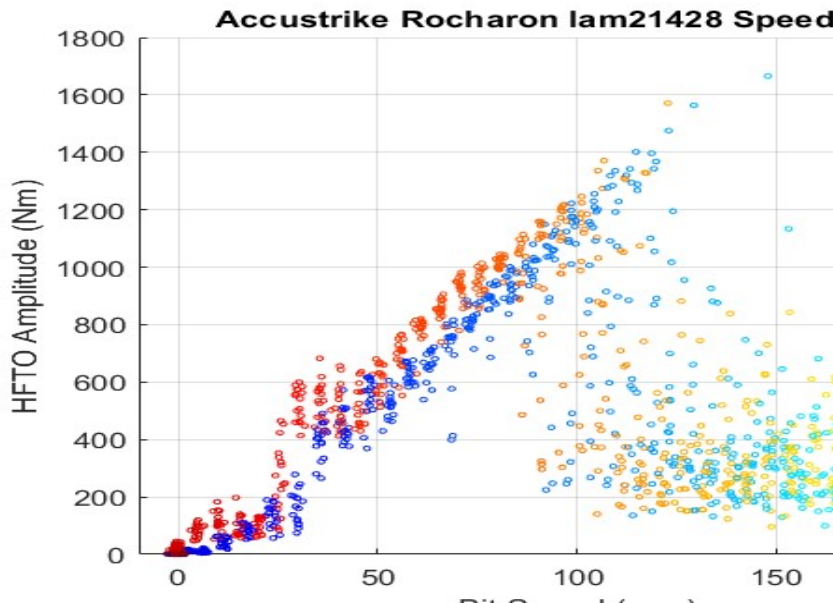

Fig. 6—HFTO amplitude plotted against collar speed for cycled speed test. Amplitude calculated from an fft with a window of 0.1 second.
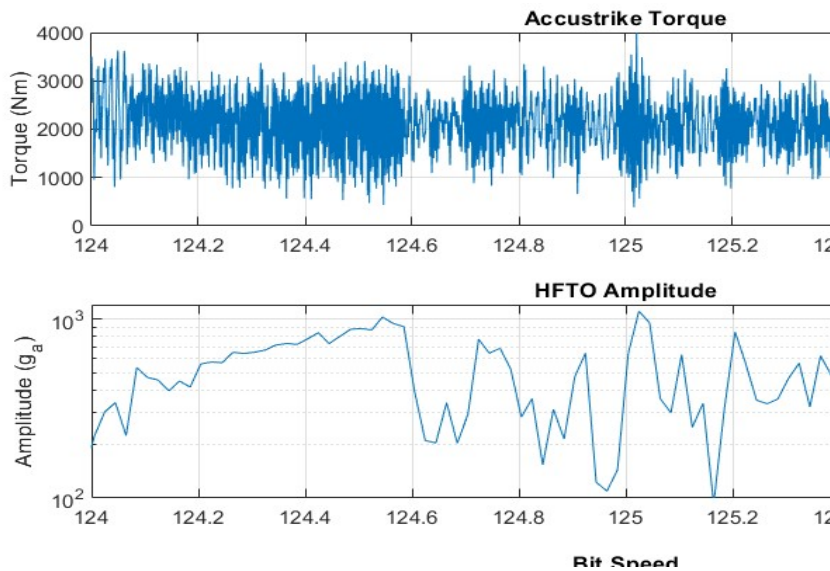

Fig. 7—Drilling torque time series together with HFTO amplitude from a 0.016-second window fft and instantaneous collar speed.

CONCLUSIONS

HFTO is one of the more damaging dysfunctions we encounter in our regular drilling operations. Although there has been much analysis of the resultant mechanical damage as well as dynamics data, an understanding of the fundamental drivers has eluded the industry. Notably, the impact of collar speed, where HFTO is significant at moderate speeds but mitigated at both low and high rotation rates, has been identified but never explained.

To characterize these drivers, we built a new HFTO experiment using the torsional mass spring resonance model. This has enabled a new level of testing where we can enable and disable HFTO as well as make precise experimental tests separating out the key drilling parameters.

We have shown that HFTO is not driven by broadband drilling noise but rather resonance at the bit-cutter-rock contact.

We have reproduced the speed effect in the laboratory environment. At low speeds, the amplitude of the HFTO will increase with rotation rate, the dysfunction increasing as energy is put into the system. Up to this threshold rate, the vibration is stable and sustained; higher than this rate, and the dysfunction becomes unstable. Bursts of HFTO will form and grow in amplitude very rapidly (milliseconds) but these will cease, as quickly. Typically, these bursts will be sustained for a few tens of degrees of rotation.

ACKNOWLEDGMENTS

REFERENCES

Johnson, A., Balka, M. S., Bhoite, S. et al. 2023. Mitigation of Drilling Dysfunction: Data Analysis and Physical Modelling Shine a New Light on HFTO. Paper presented at the SPE/IADC International Drilling Conference and Exhibition, Stavanger, Norway, 7–9 March. SPE-212500-MS. https://doi.org/10.2118/212500-MS.

Kueck, A., Everhard, E., Xu, H. et al. 2023. Qualifying Bit Influence on High-Frequency Torsional Oscillations Based on Full-Scale Laboratory Experiments. Paper presented at the SPE/IADC International Drilling Conference and Exhibition, Stavanger, Norway, 7–9 March. SPE-212566-MS. https://doi.org/10.2118/212566-MS.

Pastusek, P. E., Sullivan, E., and Harris, T. M. 2007. Development and Utilization of a Bit Based Data Acquisition System in Hard Rock PDC Applications. Pape r presented at the SPE/IADC Drilling Conference, Amsterdam, The Netherlands, 20–22 February. SPE-105017-MS. https://doi.org/10.2118/105017-MS.

Prentis, J. M. 1980. *Dynamics of Mechanical Systems*, 2nd edition, Halsted Press, ISBN: 0-85312-158-3.

Tipples, R., Keshiyev, S., Sheikhrezaei, K. et al. 2021. Bit Design Methodology to Mitigate High-Frequency Torsional Oscillation. Paper presented at the SPE Annual Technical Conference and Exhibition, Abu Dhabi, UAE, 21–23 September. SPE-206353-MS. https://doi.org/10.2118/206353-MS.

RESPONSIBILITY NOTICE

Dynamic data-driven application systems and drilling

B. Shayak – University of Maryland (USA)
S. Chanana – University of Maryland (USA)
B. Balachandran – University of Maryland (USA)

Dynamic data-driven application systems and drilling

B Shayak [1], S. Chanana [1], and B. Balachandran [1]*

[1] Department of Mechanical Engineering, University of Maryland, College Park, Maryland – 20742, USA

* Corresponding author. balab@umd.edu

Abstract: Dynamic data-driven application systems (DDDAS) is a data-driven paradigm through which experimentally measured data can be assimilated with simulation data to provide an accurate estimation of the system behavior. In this work, the authors demonstrate how this paradigm can be applied to study the dynamics of a drill string.

Keywords: DDDAS, data assimilation, simulation data, experimental data, drilling

INTRODUCTION

DDDAS was introduced by Darema (2004) and now this data-driven paradigm occupies a certain niche in data-driven approaches. It is especially useful when the ab initio (physics-based) modeling of a system is difficult to do or prohibitively expensive to solve. In the authors' group, the DDDAS paradigm has used to study aeroelastic responses of an unmanned vehicle (Zhao *et al*., 2019, 2021) and robot leg interactions with granular media (Wang *et al*., 2024). In the present work, this approach is demonstrated in the context of drilling dynamics.

METHODOLOGY

The basic methodology, which has been used in the authors' group to develop an input-output relationship, is illustrated in Figure 1. In the context of drilling, the system design parameters can correspond to the drill-string geometry and the operational conditions such as the input drive speed at the top of a drill string. The drill bit speed and weight on the drill bit could constitute the system behavior quantities of interest.
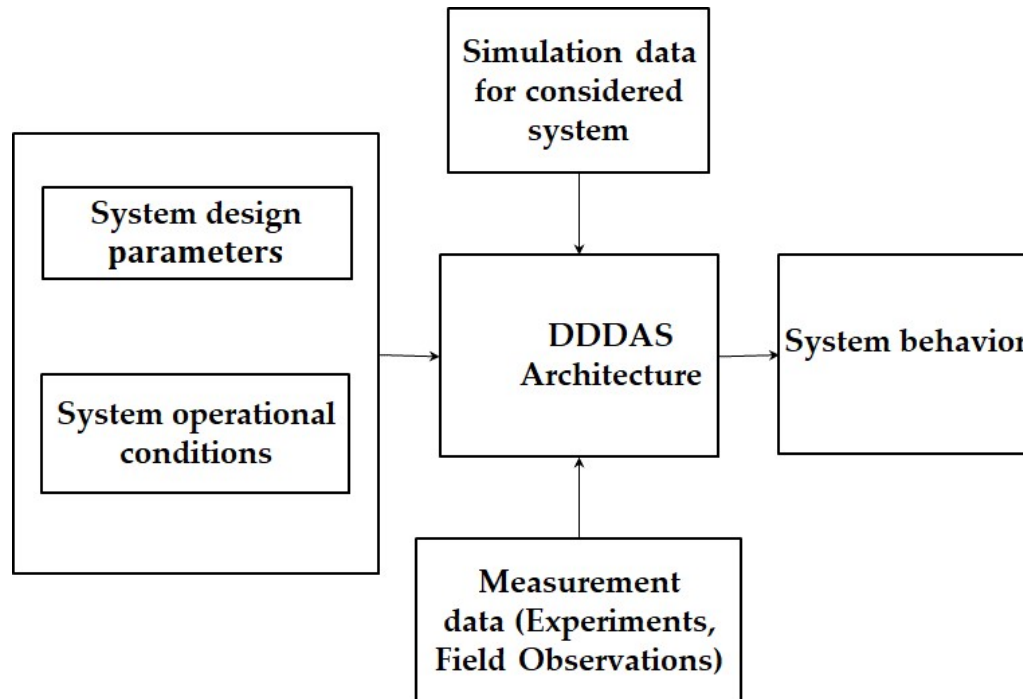

Figure 1 – Assimilation of simulation and experimental data to develop an input-output relationship.

The DDDAS approach is based on an integration of dimension reduction (Sequentially Truncated Higher Order Singular Value Decomposition), surrogate modeling for interpolation (Gaussian Process), and data assimilation techniques (Reduced Order Particle Filter). This three-step approach has been used in the authors' group for unmanned aerial vehicle (Zhao *et al*., 2019, 2021) and robotics applications (Wang *et al*., 2024).

To generate the simulation data, the model used by Lobo *et al.* (2020) is used. For experimental data, the simulation data with the addition of Gaussian noise is considered as synthetic data.

CONCLUDING REMARKS

The outcome of the DDDAS studies will be presented at the meeting and discussed along with the challenges encountered in using experimental data particular to a drilling experiment.

REFERENCES

Darema, F., 2004, "Dynamic data driven applications systems: A new paradigm for application simulations and measurements", in: M. Bubak, G. D. van Albada, P. M. A. Sloot and J. Dongarra (Eds.), *Computational Science - ICCS 2004, Lecture Notes in Computer Science*. Springer Verlag Heidelberg, Germany, pp. 662–669. https://doi.org/10.1007/978-3-540-24688-6_86.

Lobo, D. M., Ritto, T. G., Castello, D. A., and de Souza, M. L. M., 2020, "On the Calibration of drill string models based on hysteresis cycles data", *International Journal of Mechanical Sciences* 177, #105578.

Wang, G., Zhao, X., Azarm, S., and Balachandran, B., 2024, "Data-Driven prediction of dynamic interactions between robotic appendage and granular material," in preparation for submission.

Zhao, X., Azarm, S., and Balachandran, B., 2021, " Online data-driven prediction of spatio-temporal system behavior using high-fidelity simulations and sparse sensor measurements," *ASME Journal of Mechanical Design*, Vol. 143(2).

Zhao, X., Kebbie-Anthony, A., Azarm, S., and Balachandran, B., 2019, "Dynamic multi-step-ahead prediction with simulation data and sensor measurements," *AIAA Journal* 57 (6), pp. 2270-2279..

A Machine Learning approach to classify drilling operations data as a support tool for detection of dynamic drilling dysfunctions

João V. B. dos Santos – Radix (Brazil)
Leone B. Florindo – Radix (Brazil)
Letícia T. Vechi – Radix (Brazil)
Gregory S. Payette – ExxonMobil (USA)

A Machine Learning approach to classify drilling operations data as a support tool for detection of dynamic drilling dysfunctions

João V. B. dos Santos[1]**, Leone B. Florindo**[1]**, Letícia T. Vechi**[1] **and Gregory S. Payette**[2]

[1] Radix Engenharia e Desenvolvimento de Software. Rua do Passeio, 38 - torre 2, 14º andar - Centro, 20021-290, Rio de Janeiro - RJ, Brasil

[2] ExxonMobil Technology and Engineering Company. Houston, Texas, USA.

Abstract: During the drilling of wells, surface sensors serve as essential tools for collecting valuable data pertaining to the well construction process. However, the interpretation of this data presents significant challenges, owing to the intricate and dynamic nature of the drilling processes. There are a multitude of operational steps involved in the drilling process. Proper classification of these steps is essential for implementing automated control systems and to effectively identify and mitigate dynamic dysfunctions such as stuck pipes, kicks, unexpected lithological transitions, severe mechanical vibrations, and bit wear. This research aims to design a specialized machine learning classifier with supervised learning techniques to identify drilling operational procedures. Leveraging surface drilling data collected from eighteen wells, the methodology involves data preprocessing, precise class definition, and detailed labeling procedures. Through a rigorous training process that was arrived at via experimentation and refinement utilizing 5-fold cross-validation, the study yielded a model of notable performance, achieving a high F1 score and accuracy rate. The developed classifier has been instrumental in providing an effective means of processing data, enabling its use by downstream analyses and physics-based algorithms. These algorithms generate indicators and early warnings of potentially hazardous events during drilling operations. The significance of these findings extends beyond the statistical performance metrics presented for the current research work and highlights the potential to apply similar machine learning-based methodologies within the drilling industry to improve safety, streamline processes, and drive performance gains.

Keywords: Drilling, Operations in Drilling, Rig State, Machine Learning Classifier, Labeling

INTRODUCTION

The extraction of oil and gas relies on mechanical structures, such as drilling platforms and drillship, to access the deep layers of the subsurface. Controlling complex and nonlinear drilling processes under continuously changing geological conditions can meet the growing demands for efficiency and safety in automation systems. The surface sensors integrated into drilling platforms provide valuable information about the ongoing process, but often the data collected during the drilling process lacks an organized and easily interpretative structure. One of the major challenges of data analysis and real-time implementation is that, during the drilling phase, a series of procedures are carried out, including tripping in and out, reaming, rotary drilling, slide drilling, and various others. Properly classifying these operations is essential to enabling the applicability of automatic control systems that use modern approaches such as Machine Learning (ML) modeling.

The primary objective of this study is to develop a classifier for drilling operations using supervised ML techniques. Subsequently, an empirical investigation was conducted to assess its efficacy in a case study aimed at refining the computation of physics-based indicators, including Mechanical Specific Energy (MSE), with the main objective of enabling early-signs detection of hazardous events during drilling operations. For this purpose, data from common surface sensors, including Weight on Bit (WOB), Hook Load (HL), and Revolutions Per Minute (RPM), were utilized. Given the supervised learning approach, various methods for labeling data within predefined operation classes were explored to train the model.

Considering the time-series nature of drilling data, different moving window sizes were evaluated alongside Feature Selection, Hyperparameter Tuning, and Cross-Validation Techniques to optimize the model based on F1-Score and Accuracy metrics. The resulting classification model accurately identifies each step of the drilling process using surface sensor data, offering valuable insights for drilling optimization and the development of physics-based and AI models. This precise operations classification is crucial for understanding event sequences and identifying issues during specific operations, underscoring its importance for diverse research applications.

METHODOLOGY AND DEVELOPMENT

In this study, our focus was on developing a classifier for drilling operations that can be used to identify anomalous drilling behavior and operational issues. The intent behind this work is to enable enhanced operational efficiencies by accurately identifying and leveraging operational states. The resulting classifier is envisioned to serve as a valuable tool for future data-driven analyses and workflows that require precise identification of drilling operations. Our methodology

follows a systematic approach outlined in the accompanying flowchart (see Figure 1), comprising the following key stages: Data Acquisition, Preprocessing, Modeling, Optimization, and Implementation.
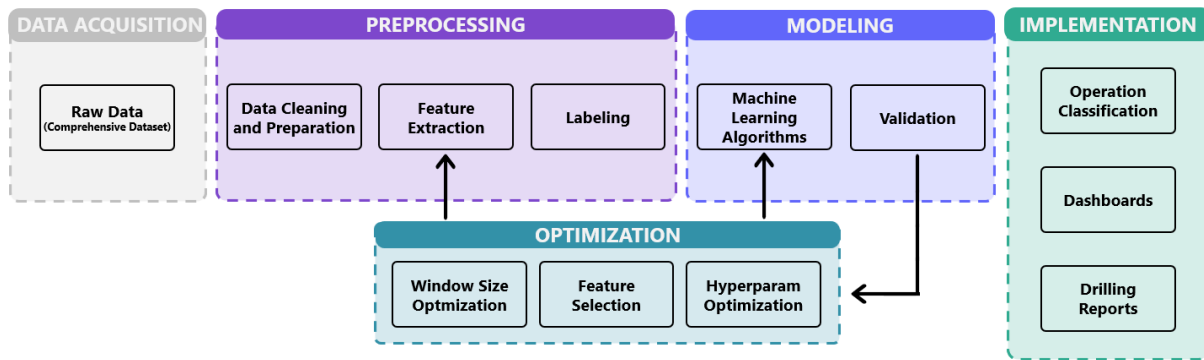

Figure 1 – Overall flowchart from classifier solution.

Data Acquisition

The primary data used for the current modeling effort consists of time-series sensor data pertaining to drilling activies for 18 historical unconventional wells. Our dataset includes data for the entire operational duration of each of these wells (i.e., includes data from surface hole spudding to reaching total depth of the production hole section). Primarily, the raw data consists of measurements from surface sensors obtained through the Wellsite Information Transfer Standard Markup Language (WITSML). The complete list of extracted variables is available in Table 1. All data points are recorded at a frequency of one second, providing a high-resolution temporal view of drilling operations.

Table 1 – Variables received for model development

Variable	Unit	Variable	Unit	Variable	Unit
Azimuth (AZ)	dega	Hole Depth (DEPT)	ft	Differential Pressure (DIFP)	psi
Convertible Torque (CTOR)	kft.lbf	Hook Load (HL)	klbf	Inclination (INCL)	dega
Flow (FLOW)	%	Rotary Speed (RPM)	rpm	Weight on Bit (WOB)	klbf
Rate of Penetration (ROP)	ft/h	Standpipe Pressure (SPP)	psi	Total Pump Output (TPO)	USGal/min
Bit Depth (BDEP)	ft	Block Height (BHT)	ft		

Preprocessing

The preprocessing stage plays a pivotal role in this study as it involves preparing the data for model development. Initially, the available data undergoes a comprehensive quality assessment, addressing issues such as missing or null values, data freezing, frequency evaluation, and outlier removal. Additionally, insights from tabulated data highlighting operational problems aid in data refinement.

Following the initial data quality assessment, the focus shifts to data preparation for modeling, encompassing feature extraction and labeling. With data sampled at one-second intervals, fluctuations challenge classification tasks. To mitigate this, a moving window is applied as a noise reduction filter, enhancing temporal data dependency and classification accuracy, as recommended by Ben *et al.* (2019) and Tripathi *et al.* (2021). The moving window technique, coupled with various statistical calculations such as mean, median, standard deviation, and interquartile range (IQR), constitutes a crucial point for feature extraction (Yin *et al.*, 2020; Bilal *et al.*, 2011). An important consideration in implementing this technique is the selection of the window size, a parameter that requires iterative optimization. The iterative nature of this process underscores the need for a comprehensive and iterative solution to achieve optimal results (Yin *et al.*, 2018). The dataset was refined and prepared for subsequent modeling stages by integrating these preprocessing techniques.

As the classifier is based on a supervised learning method, we need to have the data labeled. This data absence is common in such scenarios, prompting researchers to devise solutions. One pragmatic yet time-intensive approach involves formulating a business rule to label the data corresponding to specific operations. In this regard, identifying key operations pertinent to the problem at hand and assessing variable behavior and correlations with the listed operations becomes crucial (Coley, 2019). For the current study, the data classification was based on common drilling operations. Leveraging the physical understanding of each operation enabled the development of a labeling rule as described in Table 2 (Coley, 2019; Curina *et al.*, 2021).

Despite the efforts, occasional misclassifications were observed, prompting the need for a filter to correct short classifications in the output function. Additionally, manual adjustments were necessary to enhance classifier performance,

Table 2 – Business rules for labeling the data

	In Slips	Rotary Drilling	Slide Drilling	Static	Rotation	Trip In	Trip Out	Ream Down	Backream	Circulate
HL	↓	-	-	-	-	-	-	-	-	-
BDEP	-	↑	↑	-	-	↑	↓	↑	↓	-
DEPT	-	↑	↑	-	-	-	-	-	-	-
DEPT - BDEP	>0	0	0	>0	>0	>0	>0	>0	>0	≥ 0
RPM	0	>0	0	0	>0	0	0	>0	>0	-
ROP	0	>0	>0	0	0	0	0	0	0	0
TPO	-	>0	>0	0	0	-	-	>0	>0	>0

including the creation of a "No Monitoring" class representing periods with no operations, crafted entirely through manual intervention.

These corrections underscore the limitations of relying solely on a classification rule, as it may not adequately capture data variability. Hence, utilizing a supervised learning model proves more effective in classifying operations accurately. This intricate and exhaustive process involved numerous stages and validations, culminating in the beginning of the classifier modeling process.

Modeling

For the baseline model, the Random Forest algorithm, acclaimed by Coley (2019) for its superior performance, was employed. Following Coley's recommendations, the variables exhibiting the highest correlation with the problem at hand are identified, along with, insights from Curina *et al.* (2021), and Yin *et al.* (2018) that suggest the significance of other variables in describing relevant information, we arrive at the input variables for the baseline model (Table 3).

Table 3 – First set of input variables

Inputs				
BHT Median	HL Median	ROP Median	RPM Median	CTOR Median
SPP Median	WOB Median	TPO Median	DEPT - BDEP	BDEP Derivative

Notably, the median of variables is chosen due to its lower noise and fluctuations, ensuring a more stable input. One of the variables to be used is the difference between the well depth and the drill bit depth, as well as the first derivative of the drill bit position. With the primary definitions nearing completion, the next step is to divide the data into training (80% of data) and testing (20% of data) sets that best suit the classifier.

Although the Random Forest algorithm was initially selected as the baseline model, we seek to evaluate the performance of other models. In our analyses, we compared the performance of Random Forest (RF), Extreme Gradient Boost (XGB), Multi-Layer Perceptron (MLP), and Naive Bayes (NB) algorithms. Those models with diverse principles and default parameters were assessed to provide a comprehensive comparison. Ultimately, the objective is to identify a high-performing model that seamlessly meets the required demands. This process is iterative, and iterations will continue until an optimized result is achieved.

Validation of all models was conducted using accuracy and F1 score metrics. Additionally, the selection of the algorithm will take into account an evaluation of the generated file size, which is essential for dashboard implementation, ensuring seamless allocation and application.

Optimization

The primary objective of optimization is to define the key parameters of the modeling process and thereby achieve an optimized classifier. Initially, we focus on determining the optimal size of the sliding window. Based on empirical evaluations, we begin with a window size of 10 points, but through iterative analyses, we refine this parameter to find the ideal window size. This evaluation relies heavily on classifier metrics, weighing accuracy against execution time.

The other two techniques employed in this phase are commonly utilized in machine learning model development. Firstly, feature selection, while not extensively explored in this study, plays a vital role in identifying the optimal set of input variables for a model. In this work, we prioritize leveraging recommendations from existing literature to guide our feature selection process. Additionally, hyperparameter tuning involves searching for combinations of parameters within the chosen algorithm to enhance the final classifier's performance. Once the best-performing algorithm is selected, a systematic exploration of its parameter space will be conducted to maximize classification performance.

Implementation

In the implementation phase, the primary focus is on developing a centralized hub to integrate and unify solutions that utilize the classification model for drilling operations. The output of the model is critical for conducting further analyses

of common issues in the drilling process. By automating this evaluation, we aim to create a system that assists in the study of anomalies related to drilling operations. For this paper, we conducted an evaluation of the classifier for calculating the Mechanical Specific Energy (MSE), following the formulation suggested by Dupriest *et al.* (2023).

To facilitate this, a dashboard will be developed to present key information to operators and stakeholders. This dashboard will provide real-time insights and facilitate informed decision-making by showcasing vital data points and trends identified by the classifier. The classification of operations is essential before any subsequent analysis, ensuring that the data is accurately segmented and that the insights derived are relevant and actionable. By implementing this centralized system, we will enhance the overall efficiency and reliability of the drilling process, providing a robust tool for monitoring, analysis, and continuous improvement in operational performance.

RESULTS AND DISCUSSION

Based on the preliminary choices for initiating the modeling process, we proceeded with a cross-validation analysis among the wells to determine the optimal training and testing sets, adhering to the 80-20 split. Our initial assumptions included the use of the Random Forest algorithm with default parameters, a sliding window size of 10 points, and the input variables listed in Table 3.

Following these parameters, we conducted a 5-fold cross-validation, ensuring that each well was included in the validation set at least once. This approach yielded an average accuracy of 90.16% ± 3.5% and an F1 score of 0.83 ± 0.048. These results indicate a slight instability in the model's performance depending on the specific wells used for training and testing, but overall, the model demonstrates good performance for a baseline. From this analysis, we determined the optimal data distribution, achieving the best results with an accuracy of 94.32% and an F1 score of 0.905, using wells 1, 3, 4, 6, 7, 9, 10, 12, 14, 16, and 18 for training and 8, 11, and 15 for validation.

As presented earlier, our initial analyses utilized the Random Forest algorithm, based on its proven effectiveness in the literature. However, given the unique challenges posed by unconventional wells, it was imperative to ensure that we were employing the most efficient model. To this end, we conducted comprehensive comparisons among algorithms with different operational principles. We focused our analysis on several key metrics: Accuracy (acc), F1 score, processing time, and the size of the generated file. The file size, in particular, is a critical parameter as it facilitates smoother implementation in production environments alongside the dashboard.

The results of these comparisons, detailed in Table 4, reveal notable insights. For instance, the MLP model utilized the StandardScaler during the analysis. Among the evaluated models, the RF, XGB, and MLP algorithms demonstrated similar performance metrics. However, the RF model produced a significantly larger file compared to the other two, leading to its exclusion from further consideration.

Table 4 – Metrics for different classification algorithms

	F1 Score										F1 Avg	Acc	Time [min]
	Backream	Circulate	In Slips	Ream Down	Rotary Drilling	Rotation	Slide Drilling	Static	Trip In	Trip Out			
RF	0.801	0.922	0.976	0.909	0.972	0.879	0.966	0.898	0.837	0.889	0.905	94.31%	89.35
NB	0.268	0.421	0.044	0.628	0.954	0.275	0.932	0.287	0.031	0.087	0.393	55.43%	0.58
XGB	0.823	0.930	0.976	0.926	0.9682	0.842	0.951	0.898	0.858	0.894	0.907	94.36%	12.31
MLP	0.742	0.893	0.959	0.903	0.962	0.729	0.935	0.869	0.777	0.878	0.865	92.03%	117.95

When we examined the XGB and MLP models, we found that their primary differences lay in their individual performance in classifying specific operations. For our final application, it is crucial to achieve robust performance in the classification of drilling and in slips operations. Consequently, we determined that the XGB model would be the most suitable for further analysis. Tree-based models like XGB offer the additional advantage of being less susceptible to overfitting, which further supports our choice.

Following the initial results, we proceeded with the analysis to determine the optimal window size for the final model. This analysis utilized XGBoost with default parameters and the dataset defined during cross-validation. We evaluated window sizes of 5, 10, 20, 30, 40, 50 and 60 points to assess the model's accuracy and execution time. The findings of this analysis are depicted in Figure 2. After analyzing the results, it becomes evident that a window size of 30 points is optimal. This window size strikes a balance between high performance and low processing time, ensuring efficient and accurate monitoring of drilling operations.

With the window size defined, we set out to evaluate the impact of the corrections made on the output of the developed rule-based classification. Despite thorough efforts to physically describe each operation, the rule-based method still showed classification errors, because of that, we transitioned to a machine learning model. Manual corrections and filtering were applied to the rule-based classifier's outputs, correcting approximately 3% of the data.

This highlights the discrepancies and improvements made by the manual corrections and filtering process. Although the rule-based classifier benefited from these adjustments, some errors still necessitate further refinement to reduce the need for manual intervention. We anticipate that the classifier's performance will improve with continued development.
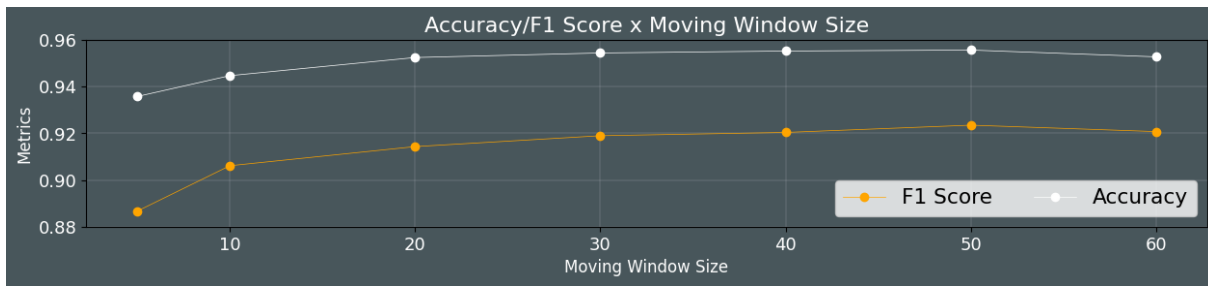
Figure 2 – Variation of Accuracy and F1 Score using different window sizes

To enhance the model's performance, the hyperparameters of the chosen algorithm were tuned. During this stage of parameter evaluations, we conducted random assessments within a defined workspace, based on empirical knowledge. Based on our extensive analyses and evaluations, we have established the final model metrics, as in Table 5, by changing the parameters *n_estimators* and *learning_rate* to 25 and 0.2, respectively.

Table 5 – Machine Learning Classifier Model Result

F1 Score										F1 Avg	Acc
Backream	Circulate	In Slips	Ream Down	Rotary Drilling	Rotation	Slide Drilling	Static	Trip In	Trip Out		
0.881	0.935	0.986	0.948	0.991	0.914	0.983	0.943	0.877	0.901	0.936	96.35%

Upon identifying the final model, we conducted a performance evaluation to ensure its effectiveness in the desired drilling scenarios. It is crucial to note that relying solely on the developed business rule for classification, instead of the machine learning model, was impractical. The business rule, as depicted in Figure 3, exhibits susceptibility to classification errors, necessitating corrections before it can be used to train ML models.
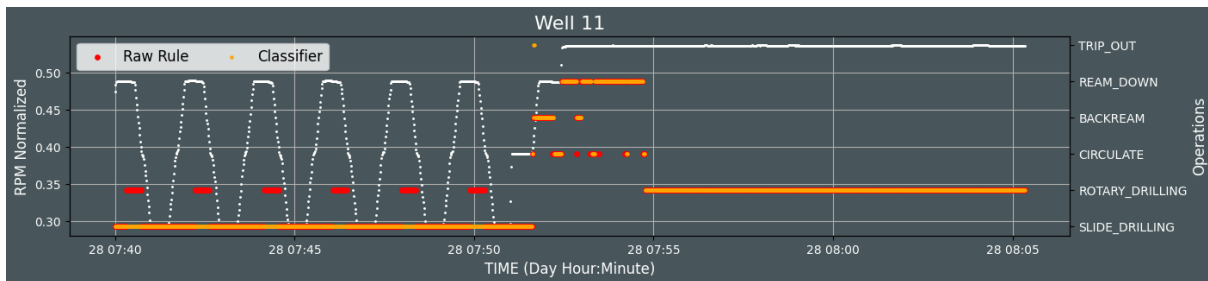

Figure 3 – Comparison between the rule and the classifier

The primary issue, highlighted in Figure 3, is the misclassification of Slide Drilling as Rotary Drilling. These small yet significant errors justify the necessity of the ML classifier, which correctly identifies operations as expected. Such inaccuracies in the business rule can escalate and impact other problem-solving solutions that depend on accurate classification. For instance, when identifying lithology, the calculation of Mechanical Specific Energy (MSE) is often used. Misclassifications can lead to errors in MSE calculations, as shown in Figure 4. Therefore, having the most accurate classification results is imperative to avoid misinterpretations.

Ensuring the accuracy of training data is crucial for developing effective supervised learning classification models. Heuristic rules, while useful for initial classifications, can lead to significant errors due to unexpected data variations or inherent issues. Training models on manually corrected data prevents these errors, allowing the model to learn from reliable examples. Unlike rigid rule-based systems, machine learning models, such as decision trees, develop their own structured rules from the input data. This dynamic learning allows the model to handle small data variations more effectively, leading to better performance. By learning and adapting to data behaviors, machine learning models offer superior robustness and reliability, making them valuable for complex classification tasks.

Moreover, this example underscores the broader utility of the drilling operations classifier. Accurate operation identification is fundamental, not only for immediate application but also for ensuring the reliability of subsequent analyses and decisions based on this data.
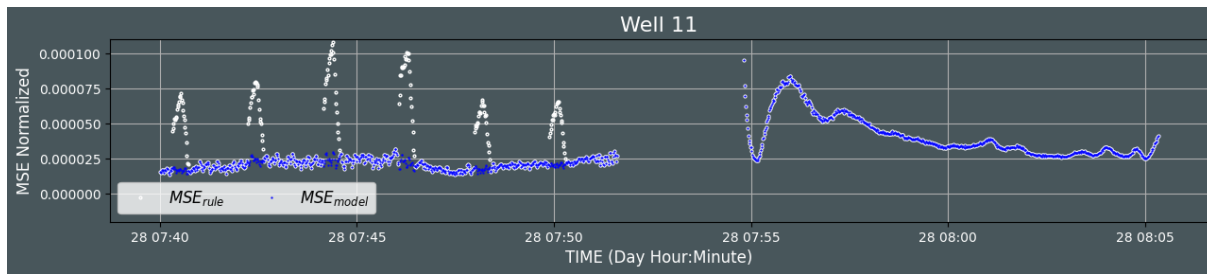
Figure 4 – Comparison between the MSE output with the classifier rule and model

CONCLUDING REMARKS

After the experiments, the developed model achieved preliminary results of a 0.936 F1 score and 96.35% accuracy, values considered relevant for solving the prediction problem of various drilling operations. In our case study, we were able to employ the results from the developed operations classifier to improve the computation of physics-based quantities such as Mechanical Specific Energy. This is pertinent because robust operational classification is foundational to the implementation of similar analysis methodologies that might seek to differentiate between normal drilling conditions and hazardous events.

As we look to the future, we plan to further optimize the current model by conducting a more comprehensive feature selection process, as well as new rounds of hyperparameter tuning and sliding window size evaluations. We also plan to investigate to what extent the model generalizes to datasets that are fundamentally different from the one considered in this investigation. In the current study we have applied the methodology to the analysis 18 unconventional wells that share a number of common features. Additional investigations into usability and generalizability are warranted to determine to what extent additional model training is warranted when well programs change.

The results presented in this study demonstrate promise for the application of supervised ML techniques to the analysis and interpretation of drilling data. However, as emphasized in this study, the construction of effective ML models is possible when model building is underpinned by robust preliminary data processing routines that include preprocessing, data integration, class definition, and precise labeling.

ACKNOWLEDGMENTS

REFERENCES

Ben, Y., James, C. and Cao, D., 2019. "Development and application of a real-time drilling state classification algorithm with machine learning". In *Unconventional Resources Technology Conference, Denver, Colorado, 22-24 July 2019*. Unconventional Resources Technology Conference (URTeC), pp. 3053–3066.

Bilal, E., Arghad, A., Rudolf, K. and Gerhard, T., 2011. "A statistical feature-based approach for operations recognition in drilling time series." *International Journal of Computer Information and Industrial Management Applications*, Vol. 3.

Coley, C., 2019. "Building a rig state classifier using supervised machine learning to support invisible lost time analysis". In *SPE/IADC Drilling Conference and Exhibition*. SPE, p. D011S005R003.

Curina, F., Abdo, E., Rouhi, A. and Mitu, V., 2021. "Rig state identification and equipment optimization using machine learning models". In *Offshore Mediterranean Conference and Exhibition*. OMC, pp. OMC–2021.

Dupriest, F., Lai, S., Behounek, M., Pastusek, P., Cutts, C., Best, B., Cook, B., Bassarath, W., Collins, J., Kamyab, M. *et al.*, 2023. "Standardization of mechanical specific energy equations and nomenclature". *SPE Drilling & Completion*, Vol. 38, No. 01, pp. 73–89.

Tripathi, A.M., DuttaBaruah, R. and Subbiah, S., 2021. "Oil well drilling activities recognition using a hierarchical classifier". *Journal of Petroleum Science and Engineering*, Vol. 196, p. 107883.

Yin, Q., Yang, J., Hou, X., Tyagi, M., Zhou, X., Cao, B., Sun, T., Li, L. and Xu, D., 2020. "Drilling performance improvement in offshore batch wells based on rig state classification using machine learning". *Journal of Petroleum Science and Engineering*, Vol. 192, p. 107306.

Yin, Q., Yang, J., Zhou, B., Jiang, M., Chen, X., Fu, C., Yan, L., Li, L., Li, Y. and Liu, Z., 2018. "Improve the drilling operations efficiency by the big data mining of real-time logging". In *SPE/IADC Middle East Drilling Technology Conference and Exhibition*. SPE, p. D021S009R003.

RESPONSIBILITY NOTICE

The authors are the only ones responsible for the printed material included in this paper.

Comparing Open-Source Drill String Models

Dongyoung Yoon – University of Texas (USA)
Elmir Hamidov – University of Tulsa (USA)
Lance Endres – CNPC (USA)
Eduardo Gildin – Texas A&M (USA)
Paul Pastusek – Consultant (USA)
Roman Shor – Texas A&M (USA)

Comparing Open-Source Drill String Models

Dongyoung Yoon[1]**, Elmir Hamidov**[2]**, Lance Endres**[3]**, Eduardo Gildin**[4]**, Paul Pastusek**[5]**, Roman Shor**[4]

[1] University of Texas, 2515 Speedway, Austin, TX 78712

[2] University of Tulsa, 800 S Tucker Dr, Tulsa, OK 74104

[3] CNPC USA, 2901 Wilcrest Rd, Houston, TX 77042

[4] Texas A&M, 400 Bizzell St, College Station, TX 77843

[5] Consultant, 10 Candle Pine Pl., The Woodlands, TX 77381

Abstract: Two open-source drillstring models were evaluated on a series of test cases. The first is the distributed, torsional model of Aarsnes and Shor. The second is the lumped-mass, coupled axial-torsional model of Dixit, et al. These models were compared using specially developed test cases that varied in complexity, aiding in debugging differences in the results. Although the models' mathematical derivations were very different, the results showed strong alignment in predicting stick-slip behavior and frequency. In cases of slight variation, access to multiple models and source code allowed a means to locate the origins of the discrepancies. The project served as a pilot study for using open-source software in drilling dynamics, demonstrating its advantages for model improvement, debugging, and accelerated learning.

Keywords: Drill string models, Torsional dynamics, Open-source, Model comparison, Test cases

INTRODUCTION

The field of drilling operations has seen significant advancements over the decades, driven by the increasing complexity of drilling environments and the evolving need for more sophisticated simulation models. The foundational work by Bailey and Finnie (1960) set a new ground in understanding the interactions between drill bits and rock, setting the stage for subsequent studies on drillstring dynamics and operational efficiencies.

Building upon early insights, Dareing and Livesay (1968) explored the dynamic effects of drillstrings under load, providing essential knowledge on the mechanical behaviors that affect drilling performance. The phenomenological models developed by Detournay and Defourny (1992) offered a deeper understanding of the drilling mechanisms of drag bits, enhancing the predictability of drilling outcomes under varied geological conditions.

In response to operational challenges, researchers like Kalsi *et al.* (1987) utilized Finite Element Methods to analyze the transient dynamics of drillstrings, particularly under jarring operations, shedding light on the critical responses of drill systems to sudden operational changes. Also, there were significant contributions from Elliott and Hutchinson (2015), who examined the role of control systems in managing torsional vibrations, thereby improving the operational stability and efficiency of drilling systems.

The integration of computational technologies into drilling operations was marked by significant advancements in the 2000s. Kamel and Yigit (2014) discussed the impact of real-time data acquisition on drilling decisions, highlighting the growing importance of data-driven strategies in managing complex drilling operations. Parallel to this, Butlin and Langley (2015) and Cayeux *et al.* (2020) developed advanced models that simulated drillstring behaviors in highly deviated wells, addressing the challenges posed by extended-reach drilling.

The dynamic nature of drillstrings, particularly during tripping operations, was further explored by Miska *et al.* (2015), who introduced an improved soft string model that incorporated the actual motion of the drillstring, enhancing the accuracy of force predictions and operational strategies. This line of research was complemented by Liu and Gao (2017), who focused on the interactions between drillstrings and geological formations, aiming to optimize drillstring designs to mitigate stick-slip oscillations effectively.

Recent comparative studies, such as those by Mirhaj and Aadnoy (2016), have underscored the importance of choosing between soft-string and stiff-string torque and drag models based on specific operational contexts, particularly for wells with complex trajectories. This highlights the ongoing need to refine modeling techniques to better reflect the actual conditions encountered during drilling.

The industry has seen 60 years of model development. The modern era of drilling dynamics modeling began in the early 90's with the development of several models (Jansen (1993), Heisig (1993), Ma *et al.* (1995), Langeveld (1992), Hanson and Hansen (1995)), some of which led directly or indirectly to commercialized models that are still in use. These models have seen over 30 years of development. While they have demonstrated their value, they have yet to reach the accuracy of methods such as finite element analysis, computational fluid dynamics, and molecular dynamics used in other
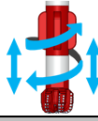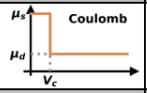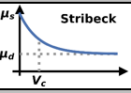
Figure 1: A summary of key points of the two models that were compared.

industries. Several issues hinder the accuracy of drilling dynamics models, with one significant factor being the approach used in their development. Early FEA models such as NASTRAN from NASA and Structural Analysis Program from Berkeley were made widely available. Additionally, the mathematical foundations of these models are published. In contrast, the petroleum industry is fragmented into individual entities that have each re-implemented the models and little is published on the inner workings of the models.

In recent years, a movement has begun to be more transparent in the development of models (Pastusek *et al.* (2019)). This effort has been organized into the *Open-Source Drilling Community* (*OSDC*). A primary motivation for the current work was to serve as a pilot project utilizing open-source models in a collaborative environment. The project's objectives were to review the existing open-source models, establish test cases for comparing drillstring models, document the procedures and findings, and evaluate the models to assess their features and performance.

MODELS

A review of drilling dynamics models available through the *OSDC* led to the selection of two models for further comparison. These are the Aarsnes-Shor (A-S) torsional dynamics model (Aarsnes and Shor (2017)) and the Dixit coupled axial-torsional model (Dixit *et al.* (2021)).[1] Each model is described below and a comparison is provided in Figure 1. Key assumptions of both models are the following:

- A soft string model (lateral bending moments and displacement are ignored, entire string in contact with the borehole)
- The bit-rock interaction is simplified
- Viscous damping is included
- Cuttings must be manually accounted for as additional uniform friction along the borehole
- Cased and open hole sections have the same friction factor

Aarsnes and Shor Model

Aarsnes and Shor developed a distributed model for torsional dynamics of drillstrings. The derivation and solution approach involved solving the governing equations for angular velocity and torque using the finite difference method (Figure 2). The drillstring and borehole friction is a Coulomb model that allows for a non-zero critical velocity for transitioning between static and dynamic friction.

It can be used for both vertical and inclined wells and can incorporate BHA components. The model assumes the bit is off-bottom, therefore, the bit-rock interaction is not considered. However, an input to the model allows for a torque to be applied at the end of the drillstring. Tool joint effects are not directly included and must be accounted for manually.

Dixit Model

The Dixit model is a lumped mass and spring system for axial-torsional dynamics of drillstrings. The approach was to discretize the string, write the resulting system of equations, and solve the governing equations using a Runge-Kutta-Fehlberg method. The drillstring and borehole friction is a Stribeck type friction model (Cayeux *et al.* (2020)) and buoyancy effects of the drilling fluid are included. The axial and torsional degrees of freedom are coupled through the friction terms. There is no coupling from material properties or inertia terms.

It is designed to simulate the dynamics of a drillstring under various drilling and tripping conditions for both vertical and inclined wells. The bit-rock interaction model is based on depth-of-cut and calculated by tracking the bit-depth

---

[1]For purposes of discussion, we will define *drillstring model* (or simply *model*) to mean the entire simulation software. A drillstring model can contain other sub-models such as a top drive model, drillstring-borehole friction model (or simply *friction model*), a bit model, et cetera. Sub-models will always be referred to by a specific name.
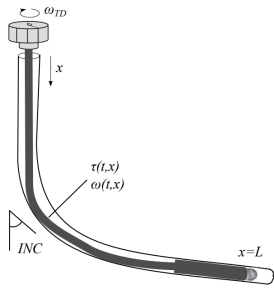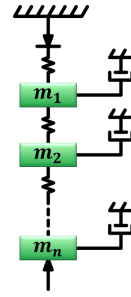
Figure 2: Schematic of the Aarsnes-Shor model.

Figure 3: Schematic of the Dixit model.

Table 1: Scenarios of the defined test cases. FF stands for *friction factor* (the coefficient of friction).

Test Case	Well Type	Static FF	Dynamic FF	Viscous Damping	BHA	On Bottom
Test case 1	Vertical	0	0	0	N	N
Test case 2a	Deviated (60°)	0.5	0.5	0	N	N
Test case 2b	Deviated (60°)	0.5	0.25	0	N	N
Test case 3	Vertical	0	0	0	Y	N
Test case 4a	Deviated (60°)	0.5	0.5	0	Y	N
Test case 4b	Deviated (60°)	0.5	0.25	0	Y	N

relative to hole-depth. Tool joints effects can be included by providing the information as input.

TEST CASES

To compare the models, a series of test cases were developed. These cases were specially designed for model comparison; they incrementally increase in complexity to isolate different parameters and allow debugging of observed differences. Test case 1 is the simplest and removes the effects of BHA components (mass, stiffness changes), friction factors, and bit-rock interaction. It is simple enough to be checked analytically. This allows for a baseline check of the models and debugging of the input. The other test cases are designed to incrementally add in new features. By doing so, differences can be attributed to a single source. The viscous damping is neglected for the simplicity of the tests in this study and should be examined in future studies. The tests were conducted by assuming the top drive velocity is increased from an initial 0 *RPM* to 40 *RPM* at 1 second. The velocity is maintained for the remainder of the simulation. A top drive control algorithm (e.g. "soft torque") was not used.

In total, six test cases are presented. Test cases 1 and 3 encompass scenarios involving vertical wells, with the distinction being the presence or absence of BHA components. Similarly, test cases 2 and 4 are deviated well scenarios with a 60° inclination angle. Test cases 2 and 4 differ by the presence or absence of BHA components. In addition, to analyze the effect of frictional factors, test cases 2 and 4 are further divided into *a* and *b* subcases (2a, 2b, 4a, 4b). All the current test cases are for off-bottom scenarios. Table 1 summarizes the scenarios for each test case. Table 2 summarizes the parameters and BHAs used for the test cases.

RESULTS AND FINDINGS

In the comparison of torsional vibration between the A-S and Dixit models, both models demonstrated a remarkable correlation. The frequency analysis, as detailed in Table 3, shows minimal discrepancies in their results, with percentage differences mainly within the 3% to 4% range across various test cases. The responses of the bit velocity, as seen in Figure 4a, both show stick-slip at a large scale. When the slip phase is examined in detail, as seen in Figure 5a, a secondary vibration frequency is seen. This highlights the precision of both models in capturing the critical dynamics of torsional modes under simulated conditions.

Close examination of the results revealed some differences between the models. The frequency differences were small but accumulated over time (see Figure 4a). When the stick phase of the models was compared (Figure 5b) differences in bit velocity was observed. The Dixit model exhibited movement of the bit whereas the A-S model did not. These variations prompted a revision of the A-S model to incorporate the Stribeck friction model used by the Dixit model. Doing so provided a means to investigate the sources of differences.

When the two versions of the A-S model, one with Coulomb friction and one with Stribeck friction, were compared

Table 2: Input parameters for the test cases.

Parameter	Value (imperial units)	Value (metric units)	Description	Note
ρ	$490.6\ lb/ft^3$	$7850\ kg/m^3$	Drill pipe density	
G_{DP}	$1.67{\cdot}10^9\ lbf/ft^2$	$7.99{\cdot}10^{10}\ Pa$	Shear modulus	
OD_{DP}	$5.88\ in$	$0.15\ m$	Drill pipe outer diameter	
ID_{DP}	$5.00\ in$	$0.127\ m$	Drill pipe inner diameter	
OD_{HWDP}	$4.50\ in$	$0.1143\ m$	HWDP outer diameter	Only test cases with BHA
ID_{HWDP}	$2.50\ in$	$0.0635\ m$	HWDP inner diameter	Only test cases with BHA
L_{HWDP}	$60\ ft$	$18.30\ m$	Length of HWDP	Only test cases with BHA
OD_{DC}	$6.00\ in$	$0.1524\ m$	Drill collars outer diameter	Only test cases with BHA
ID_{DC}	$2.00\ in$	$0.0508\ m$	Drill collars inner diameter	Only test cases with BHA
L_{DC}	$270\ ft$	$82.30\ m$	Length of drill collars	Only test cases with BHA
w_c	$10\ RPM$	$10\ RPM$	Friction critical velocity	
θ	$60°$	$60°$	Inclination	Deviated test cases only
KOP	$4921.3\ ft$	$1500\ m$	Kick off point	Deviated test cases only
EOB	$6889.8\ ft$	$2100\ m$	End of bend	Deviated test cases only
$BD_{vertical}$	$5905.5\ ft$	$1800\ m$	Bit depth	Vertical test cases only
$BD_{deviated}$	$8202.1\ ft$	$2500\ m$	Bit depth	Deviated test cases only

Table 3: Comparison of model results. Despite very different derivations, the models demonstrate very similar results with torsional vibration frequency differences of four percent or less. The bit velocities are largely within a few percent. In test case 4b the maximum bit velocity was significantly different, but this was during the initial slip phase and the response difference was damped out over time. Simulation times were measured on a computer with Intel® Core™ i7-8650U CPU and 16GB RAM.

Test Case	Torsional Freq (Hz)			Maximum Bit Vel (RPM)			Simulation Time (s)		
	A-S	Dixit	% Diff	A-S	Dixit	% Diff	A-S	Dixit	% Diff
1	0.44	0.43	**3.0**	79	81	**2.5**	36	106	**98.6**
2a	0.28	0.27	**4.0**	78	79	**1.3**	25	117	**129.6**
2b	0.28	0.27	**4.0**	106	115	**8.1**	25	116	**129.0**
3	0.42	0.41	**2.9**	80	81	**1.2**	36	104	**97.1**
4a	0.27	0.26	**3.0**	78	79	**1.3**	32	231	**151.3**
4b	0.27	0.26	**3.0**	116	96	**18.9**	32	231	**151.3**
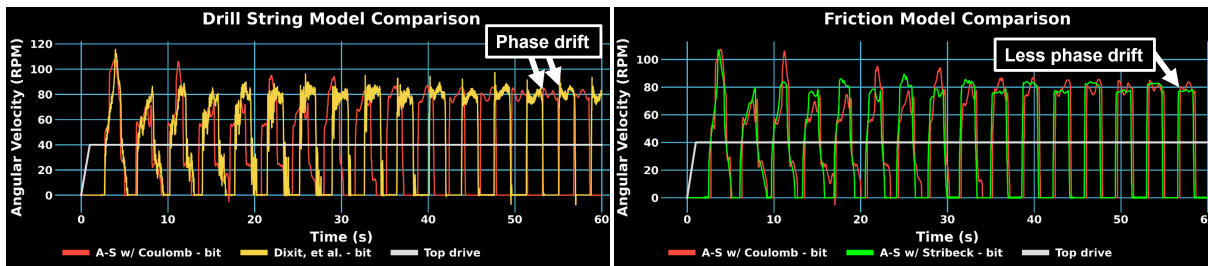
(a) The original A-S with Coulomb friction is compared to the Dixit model. While the difference in the stick-slip frequency is small, it accumulates over several cycles and results in the signals being out of phase.

(b) The A-S model was modified to use Stribeck friction and compared to the original A-S model that uses Coulomb friction. The phase drift was much smaller.

Figure 4: Phase drift comparison between Dixit and A-S models. The results are from test case 2B. By comparing multiple models and using different friction models, it can be shown that the friction model does not contribute significantly to differences in the torsional frequency. Other factors of the model formulation contribute to the majority of the stick-slip frequency variations.
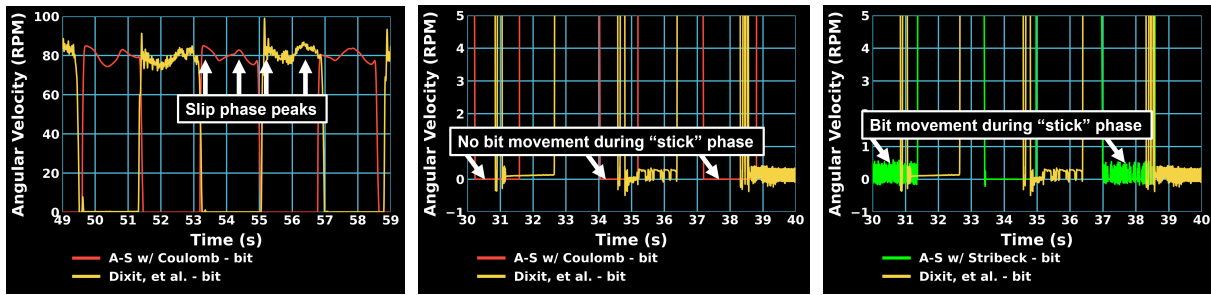
(a) Slip phase comparison of the A-S model with Coulomb friction and Dixit model.

(b) Stick phase comparison of the A-S model with Coulomb friction and the Dixit model.

(c) Stick phase comparison of the A-S model with Stribeck friction model and the Dixit model.

Figure 5: Comparison between the Dixit and the A-S models in the slip and stick phases (test case 2B). In (a) it is seen that while the Dixit models exhibits more noise in the slip phase, both model capture similar behavior such as a secondary vibration frequency. In (b) it is seen that when Coulomb friction is used in the A-S model, the bit rotary speed is zero in the stick phase. When Stribeck friction is used in the A-S model, as shown in (c), the bit shows small vibrations in the stick phase. These movements resemble the ones in the Dixit model, which also uses Stribeck friction.

(Figure 4b) it was found that the phase drift was nearly eliminated.[2] By comparing this result to Figure 4a it can be concluded that the friction model is an insignificant source of stick-slip frequency variation. Other factors of the model such as the equation derivation, discretization, and computational methodologies play a more important role.

When the modified A-S model (the version using Stribeck friction) was examined (Figure 5c) it was found to demonstrate similar bit movement as the Dixit model in the stick phase. This alignment demonstrates that the previous lack of bit movement in the A-S model during the stick phase (Figure 5b) was primarily due to its friction model assumptions rather than other factors.

For future studies, it would be beneficial to further explore these differences. Detailed sensitivity analyses could help isolate the impact of each model parameter, changes in the BHA, and on-bottom vs. off-bottom on the observed behaviors. Such analyses would enhance the robustness and reliability of predictive models used in drilling. Understanding these differences is crucial, as they could impact the predictive accuracy and operational reliability of the models in real-world drilling scenarios.

Discussion

Although the two models were derived and formulated using completely different methods, they produced remarkably similar results. This verification provides users with confidence in the accuracy of the models.

Each model demonstrated unique strengths and weaknesses. The A-S model had shorter run times (see Table 3), whereas the Dixit model was more generalized. The Dixit model can accommodate an arbitrary number of BHA components added and accounts for tool joints. In contrast, the current incarnation of the A-S model requires manually accounting for the tool joints and averaging the properties (e.g. moment of inertia) of the BHA components. However, inspection by the authors suggests these differences could be reduced; it seems probable that the computational efficiency of the Dixit model could be improved and the A-S model could be generalized.

CONCLUDING REMARKS

Perspective

Drilling dynamics models have proved to be useful tools in prewell design and postwell analysis. However, there remain a number of issues. Progress towards improvements of predictive ability has been slow and there is conflicting information in the literature. While many entities desire to have the models, building them is a difficult and resource intensive proposition. Understanding and proper use of the models also requires specialized knowledge and training. Currently, the models provide good qualitative results, but accurate quantitative results require some form of calibration to data.

The industry is changing. Automation efforts are underway in earnest. New opportunities such as geothermal are price sensitive and require de-risking of wells. To achieve these goals, better models will be required. Moreover, the rate of enhancement will need to be increased to meet the expected timelines associated with the industry's objectives.

To speed development, it is proposed that the *methods* used to create, improve, and use the models need to change.

---

[2]This indicates the stick-slip frequencies were closely matched.

Open-source software has proven itself as a cost-effective tool for rapid development and innovation. It also fosters collaboration and knowledge sharing. Combined, these properties of open-source could speed innovation while lowering costs.

The *OSDC* originated in 2018 to encourage public release of source code and validation sets. Several models have been released but they had not previously been utilized in a systematic manner. This project served as a pilot project to demonstrate the benefits and viability of using open-source models and industry collaboration. From this perspective it proved successful; learning, development, and findings were accelerated. However, it was an ad hoc, volunteer-based initiative. What is needed is a more structured approach. The *Wells of the Future* initiative at Texas A&M seeks to formalize and manage the work of the *OSDC* and should serve to generate more projects using open-source models.

Summary

Two open-source soft string models, one from Aarsnes and Shor and one from Dixit, et al, were evaluated. Although the two models were built on different assumptions and mathematical foundations, the results aligned well. Both models exhibited similar responses in the velocity of the bit, comparable amplitude and frequency of vibrations, and a similar response during stick-slip events.

Having multiple models and access to the source code allowed for interrogating the models to determine sources of differences in the results. It was discovered that the choice of the friction model (Coulomb or Stribeck) was insignificant to the stick-slip frequencies, but it was an important factor influencing bit behavior in the stick phase.

In comparing the features of the models, it was found that the Aarsnes and Shor model solves problems more quickly, whereas the Dixit model is easier to adapt to new features. As such, each model will have use cases it is best suited for.

This comparative study of open-source drillstring models demonstrates the feasibility of using open-source software for drilling dynamics. The results emphasize the potential for collaborative development and the necessity for further improvements to enhance model accuracy and reliability.

ACKNOWLEDGMENTS

REFERENCES

Aarsnes, U.J. and Shor, R., 2017. "Torsional vibrations with bit off bottom: Modeling, characterization and field data validation". *Journal of Petroleum Science and Engineering*, Vol. 163. doi:10.1016/j.petrol.2017.11.024.

Bailey, J.J. and Finnie, I., 1960. "An Analytical Study of Drill-String Vibration". *Journal of Engineering for Industry*, Vol. 82, No. 2, pp. 122–127. ISSN 0022-0817. doi:10.1115/1.3663017.

Butlin, T. and Langley, R., 2015. "An efficient model of drillstring dynamics". *Journal of Sound and Vibration*, Vol. 356, pp. 100–123. ISSN 0022-460X. doi:10.1016/j.jsv.2015.06.033.

Cayeux, E., Ambrus, A., Øy, L., Helleland, A., Brundtland, S.T. and Nevøy, H., 2020. "Analysis of torsional stick-slip situations observed with downhole high-frequency magnetometer data". In *SPE/IADC Drilling Conference and Exhibition*. Vol. Day 1 Tue, March 03, 2020. doi:10.2118/199678-MS.

Dareing, D.W. and Livesay, B.J., 1968. "Longitudinal and Angular Drill-String Vibrations With Damping". *Journal of Engineering for Industry*, Vol. 90, No. 4, pp. 671–679. ISSN 0022-0817. doi:10.1115/1.3604707.

Detournay, E. and Defourny, P., 1992. "A phenomenological model for the drilling action of drag bits". *Int J Rock Mech Min Sci & Geomech*, Vol. 29, No. 1, pp. 13–23. ISSN 0148-9062. doi:10.1016/0148-9062(92)91041-3.

Dixit, R., Manna, A., Pastusek, P. and Payette, G., 2021. *ExxonMobil Drillstring Dynamics Simulator*. ExxonMobil, 22777 Springwoods Village Pkwy Spring TX 77389.

Elliott, A.S. and Hutchinson, M., 2015. "Fully-Coupled Nonlinear 3-D Time-Domain Simulation of Drilling Dysfunctions Using a Multi-Body Dynamics Approach". Vol. Day 3 Thu, March 19, 2015 of *SPE/IADC Drilling Conference and Exhibition*. doi:10.2118/173154-MS.

Hanson, J.M. and Hansen, W.R., 1995. "Dynamics modeling of PDC bits". In *IADC/SPE Drilling Conference*. IADC/SPE Drilling Conference, Amsterdam, pp. 589–604.

Heisig, G., 1993. *On the Static and Dynamic Behavior of Drill Strings in Spatially Curved Boreholes*. Ph.D. thesis, Technical University Braunschweig.

Jansen, J., 1993. *Nonlinear Dynamics of Oilwell Drillstrings*. Ph.D. thesis, Delft University.

Kalsi, M.S., Wang, J.K. and Chandra, U., 1987. "Transient Dynamic Analysis of the Drillstring Under Jarring Operations by the FEM". *SPE Drilling Engineering*, Vol. 2, No. 01, pp. 47–55. ISSN 0885-9744. doi:10.2118/13446-PA.

Kamel, J.M. and Yigit, A.S., 2014. "Modeling and analysis of stick-slip and bit bounce in oil well drillstrings equipped with drag bits". *Journal of Sound and Vibration*, Vol. 333, No. 25, pp. 6885–6899. ISSN 0022-460X. doi:10.1016/j.jsv.2014.08.001.

Langeveld, C.J., 1992. "PDC bit dynamics". In *IADC/SPE Drilling Conference*. International Association of Drilling Contractors/Society of Petroleum Engineers, New Orleans, LA, pp. 227–241. doi:10.2118/23867-MS.

Liu, Y. and Gao, D., 2017. "A nonlinear dynamic model for characterizing downhole motions of drill-string in a deviated well". *Journal of Natural Gas Science and Engineering*, Vol. 38, pp. 466–474. ISSN 1875-5100. doi:10.1016/j.jngse.2017.01.006.

Ma, D., Zhou, D. and Deng, R., 1995. "The computer simulation of the interaction between roller bit and rock". In *International Meeting on Petroleum Engineering*. Society of Petroleum Engineers, Beijing, Vol. 1, pp. 309–319.

Mirhaj, S. A., K.E. and Aadnoy, B.S., 2016. "Torque and Drag Modeling; Soft-string versus Stiff-string Models". Vol. Day 3 Thu, January 28, 2016 of *SPE/IADC Middle East Drilling Technology Conference and Exhibition*. doi:10.2118/178197-MS.

Miska, S., Zamanipour, Z., Merlo, A. and Porche, M., 2015. "Dynamic soft string model and its practical application". In *SPE/IADC Drilling Conference and Exhibition*. Society of Petroleum Engineers, Stavanger, Norway, Vol. Day 3 Thu, March 19, 2015. doi:10.2118/173084-MS.

Pastusek, P., Payette, G., Shor, R., Cayeux, E., Aarsnes, U.J., Hedengren, J., Menand, S., Macpherson, J., Gandikota, R., Behounek, M., Harmer, R., Detournay, E., Illerhaus, R. and Liu, Y., 2019. "Creating open source models, test cases, and data for oilfield drilling challenges". In *SPE/IADC Drilling Conference and Exhibition*. Vol. Day 3 Thu, March 07, 2019. doi:10.2118/194082-MS.

RESPONSIBILITY NOTICE

The authors are solely responsible for the printed material included in this paper.

Web-based system for drill string analysis with data-driven and numeric models

L. P. Gouveia – Federal University of Alagoas (Brazil)
F. A. V. Binas – Federal University of Alagoas (Brazil)
D. V. G. Ferreira – Federal University of Alagoas (Brazil)
A. S. R. Barboza – Federal University of Alagoas (Brazil)
E. T. Lima Junior – Federal University of Alagoas (Brazil)
J. P. L. Santos – Federal University of Alagoas (Brazil)
J. R. B. Moura Filho – Petrobras (Brazil)

Web-based system for drill string analysis with data-driven and numeric models

Gouveia, L. P.[1], Binas, F. A. V.[1], Ferreira, D. V. G.[1], Barboza, A. S. R.[1], Lima Junior, E. T.[1], Santos, J. P. L.[1], Moura Filho, J. R. B.[2]

[1] Federal University of Alagoas, Av. Lourival Melo Mota, S/n - Tabuleiro do Martins, Maceió – AL

[2] Petrobras, Av. Horácio Macedo, 950 - Cidade Universitária, Rio de Janeiro - RJ

Abstract: This work presents the web-based solution CAESAR, devoted to drill string analysis in different operational scenarios, like bottom hole drilling, reaming, and coring. Numerical models are applied to estimate contact forces, buckling, fatigue, vibration, and bit-rock interaction, indicating safe operational limits. In parallel, by leveraging data of previous operations, usually collected from mud logs, the user can easily interact with drilling performance indicators. Machine learning algorithms are also applied to this data to accurately predict the rate of penetration (ROP). The integration of the numerical models and the data-driven techniques provide an important overview of the drill string structural integrity and performance, aiming for optimal operation. In the user interface, a detailed multi-component Bottom-Hole-Assembly (BHA) can be configured to simulate actual drilling conditions more accurately. In summary, CAESAR provides a collaborative environment for drilling design, meeting normative requirements, and ensuring data conformity, robustness and agility.

Keywords: digital transformation, drill string integrity, machine learning, ROP prediction,

INTRODUCTION

The analysis of the drill string is essential for the efficient construction of oil and gas wells. It is necessary to prevent equipment failures and ensure a viable rate of penetration (ROP). Drilling simulators enable sophisticated analyses, anticipating possible operational problems and avoiding its occurrence. However, it is necessary to integrate the results from various specialized software, often operated by different professionals, into a single drilling program. In this context, it is essential that the information on the drill string equipment, lithology, and operations be compatible in all analyses, avoiding inaccurate or even erroneous conclusions. Digital transformation applied to this scenario contributes to the governance of the process, bringing agility and greater reliability to decision-making in drilling design.

The drill string is the equipment responsible for extending the depth of the oil well. It consists of tubes and other components with mechanical and data transmission functions, often sensitive to shocks caused by excessive vibrations. Depending on the demand, specialized components such as downhole motors, reamers, perforating guns, protectors, and beaters are used to provide additional necessary functionalities. During well construction, the drill string is subject to combined loads and conditions that can induce element failure or reduce efficiency. These forces can be distributed over the entire length or localized due to the presence of special components or changes in inclination at certain points in the well trajectory.

Pastusek et al. (2019) review the literature and point several studies devoted to better represent drill string behavior by different approaches - drill string dynamics, drill hydraulics, drill-rock interaction, directional control, data analysis, among others. The authors describe the initiative to create an open-source repository for drilling analysis, aiming to improve the learning rate of the community in pursuit of drilling automation.

This work presents strategies and computational tools for drill string analysis and design, consolidating them in a web-based system called CAESAR. Models from the literature are implemented in this system, both for mechanical analysis, as well as data-driven analysis and lessons learned from offset wells. Results from other applications are also imported and structured into the solution, which is hosted in a collaborative well design environment, developed and maintained by Petrobras and partners. The proposal aims to allow increasingly sophisticated simulators to be incorporated into future CAESAR versions leveraging its extensibility. The development includes stages of modeling validation, mockup elaboration, back-end and front-end implementations, homologation tests, and production version deploys. Results of cases in the web tool are presented to illustrate its robustness and the benefits for the analysis and design of drilling programs.

WEB-BASED WELL PROJECT ENVIRONMENT

Petrobras developed a collaborative web environment, called PoçoWEB, to enhance the practice of oil well projects, particularly in terms of accessing the most up-to-date well data in a single, audited repository. Those responsible for the various projects required for the construction of an oil well can access and gather their inputs, as well as publish their results and reports. In this environment, the various applications can exchange information with one another. Therefore, data entered in one application does not need to be re-entered in others; it can simply be imported. It not only optimizes

the time spent filling in the inputs but also ensures data conformity. Within the context of this collaborative environment, many applications have already been developed (Araújo et al. 2020), including CAESAR.

Figure 1 presents the architecture of CAESAR and how it communicates with PoçoWEB. The use of HTTPS (Hypertext Transfer Protocol Secure) is significant for ensuring secure communication between different components. The Back-End Python Container is responsible for processing engineering models and managing data. It communicates with databases and with the front-end. The PostgreSQL is a relational database management system (RDBMS) used for storing structured data. The Redis is an in-memory data structure store, often used to efficiently manage queues of simulations. The Oracle is another RDBMS, commonly used for large-scale enterprise applications. The Front-End Web Container handles user interactions and serves the web interface, through which users interact with the application. Finally, the Ingress Component handles network traffic management and routing. It ensures requests reach the appropriate components.
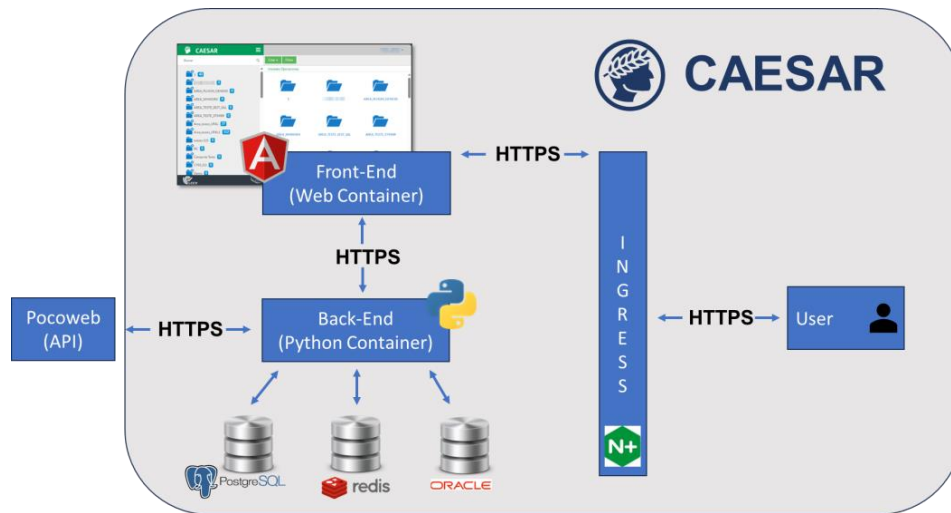

Figure 1 – CAESAR architecture.

Therefore, drilling engineering implementations are developed on the back-end in Python, which makes the work of programmer engineers easier. The rest of the services are maintained by specialized programmers. The entire team that develops initially deploy their code in a homologation version for testing by specialist engineers. After sufficient rounds of revisions, a production version can be released to the end user. Below are the engineering modules that make up the back-end in CAESAR. The methodologies applied are explained, examples of use are presented, and proposals for future improvements are made for each module.

ENGINEERING MODULES

An essential part of drill string analysis is simulating the effects to which this element is subjected during drilling. The concept of structural instability and its relationship with structural equilibrium is addressed. The calculation of forces, such as axial force, torque, bending moment, and stresses, is conducted using a stiff-string torque and drag model and a Finite Element Method (FEM) approach. The main vibration modes (stick-slip, bit-bounce, backward whirl) and their consequences for operations like reaming and coring are presented. A model of analysis is also implemented that considers the interaction between the bit and rock, providing a methodology for quantifying the severity of vibrations. Fatigue is among the main causes of failure in drill strings. Its effect is linked to material properties and stress conditions. Therefore, a model for quantifying fatigue life consumption in drill strings using S-N curves and the cumulative damage rule has been implemented. Finally, ROP prediction is addressed with classical analytical methods and machine learning approaches, aiming the future integration of numerical models, lessons learned from offset wells, and actual drilling data.

Drill String Modelling

The torque and drag model utilizes equilibrium equations for pipes subjected to axial and shear forces. A force continuity is applied at the connection between elements, allowing the calculation to proceed to the other elements. Therefore, the calculation flow starts from one end of the column, where the forces are known. On the other hand, the solution process by FEM involves solving a system of linear equations. In other words, in this method, the displacements of the nodes of the column discretization are all obtained simultaneously. The drill string is described as a linear structure composed of bars. The adoption of FEM allows for the solution of equilibrium equations for the bar elements, in addition to being essential in obtaining the consistent mass matrix and the theoretical damping matrix. The contact points are estimated by setting hinge supports when the radial displacement crosses the cased wall or the open hole wall (Figure 2).

The model iterates until no more contact points are found. In the user interface, a detailed multi-component Bottom-Hole-Assembly (BHA) can be configured to simulate actual drilling conditions accurately.
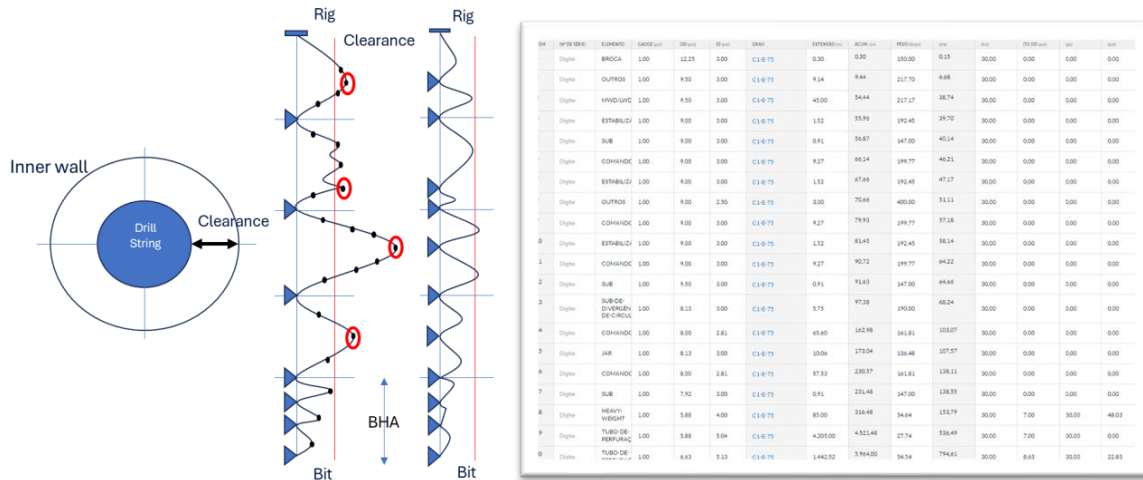

Figure 2 – FEM approach for the drill string modelling.

Reaming

The reaming operation involves drilling a region of the well that has already been drilled, but with a tool of larger diameter than previously used. This operation can be applied both in a pilot well and simultaneously with drilling. In the Reaming While Drilling (RWD) operation, the reamer is positioned above the bit so that it can cut the well walls, increasing the diameter while the bit penetrates the rock formation. If not properly designed, such operations can lead to problems such as low ROP, severe vibration, and premature damage to bottom-hole tools. In this module, the mathematical model proposed by Servaes et al. (2016) was used, which utilizes the following input data: bit and reamer diameters, friction coefficients of the bit and reamer, rock layer resistance, depth of the rock section, and total weight on the system. Applying this methodology provides weight and torque on the bit and reamer, total system torque, ROP, and drilling duration. The computational method applies an iterative process, where each iteration compares the total system weight to the lithological layers to be drilled. It is natural that at certain depths, the bit-reamer assembly transitions between rock formations with different characteristics, causing changes in the drilling stage due to variations in the rock resistance in contact with the tools.

As a result, the quantification and visualization of the weight distribution (see Figure 3) and torque on the bit-reamer assembly are provided. It is observed that the weight values exhibit a behavior directly proportional to the variations in rock resistance. Regarding the obtained ROP values, there is a clear tendency for reduction as rock resistance increases. Thus, a better understanding of the bit-reamer assembly behavior in RWD drilling is obtained, highlighting the importance of analyzing transition zones between rock formations.
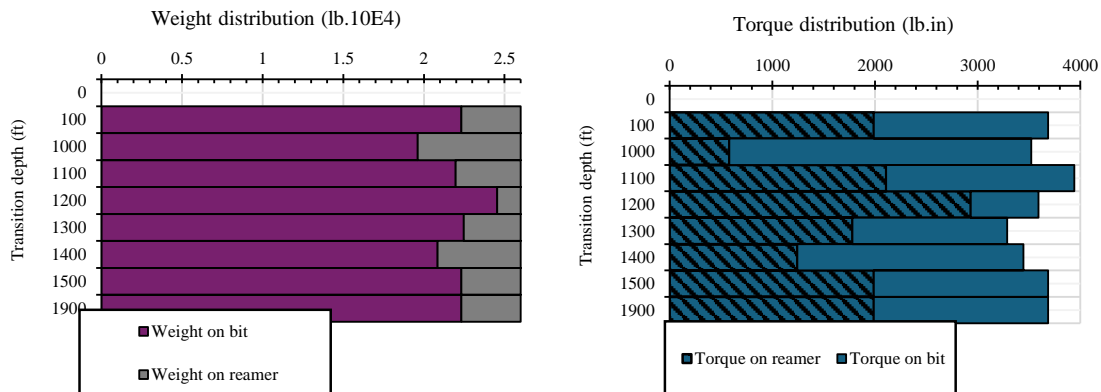

Figure 3 – Bit-reamer weight and torque distributions.

Bit-Rock Interaction

This module focuses on the analysis of torsional vibrations, which in their most severe form are known as stick-slip and can cause damage to the drill string, premature wear of the structure and the bit, as well as a reduction in ROP. Therefore, a cutting model developed for polycrystalline diamond compact (PDC) bits is incorporated into the dynamic analysis with the objective of identifying the operational parameter limits that reduce the likelihood of severe vibrations occurring. To consider the rock cutting process, a model compatible with single cutter tests is adopted (Figure 4). This approach is essential for defining the strategy for simulating self-excited vibrations since its compatibility with these tests excludes the effects of torque decay with angular velocity. Consequently, the drill bit-rock interaction relationships are addressed according to the methodology proposed by Detournay and Defourny (1992) and Detournay et al. (2008). This interaction provides a unique model where the weight on the bit and the torque are divided into their decoupled cutting and friction components. Thus, the criteria characterizing stick-slip, associated with the momentary stoppage of the bit, are defined. Finally, in a dimensionless manner, a three-step solution strategy is adopted concerning the surface boundary condition, a two-degree-of-freedom drill string model, and the bit-rock interaction.
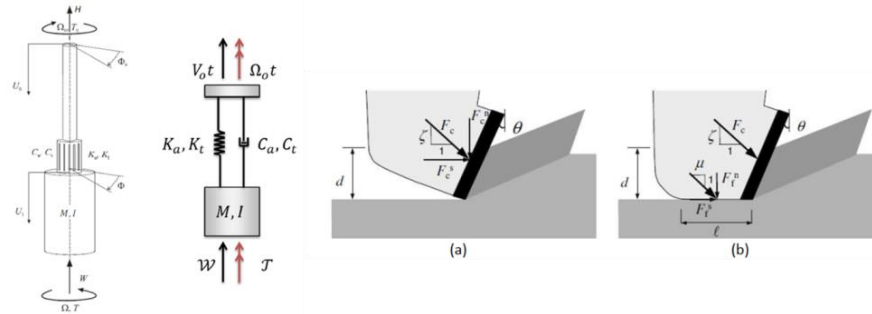

Figure 4 – Bit-rock interaction modelling (NANDAKUMA and WIERCIGROCH, 2013; HOFFMANN, 2006).

The model allows identifying the severity of torsional vibrations considering the parameters weight on bit (WOB) and rotation per minute (RPM) (see Figure 5). The model also enables the detection of bit-bounce. This accelerates the decision-making process for defining operational parameters, aiming for drilling without the presence of vibrations.
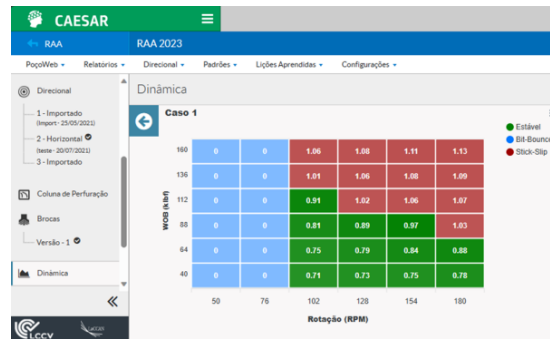

Figure 5 – Results view of the bit-rock interaction module.

Fatigue

Drill strings are subject to fluctuating stresses and deformations, which can lead to a permanent structural change and result in fatigue failure. The methodology employed for fatigue life analysis of a drill string follows this order: i) Calculation of forces, such as axial force, torque, and bending moment, and stresses along the string; ii) Use of SN curves to quantify the number of alternating stress cycles needed to cause fatigue failure; iii) Application of Miner's Rule for calculating accumulated damage, also known as the linear damage rule, where the damage factor represents the proportion of the structure's useful life consumed.

As a result, the cumulative fatigue life graph can be seen in an illustrative example in Figure 6. Eleven operations are considered, with drilling operations 3, 4, 5, and 7 being the main contributors to structural damage since they occur in regions with greater curvature. However, the fatigue life consumption does not reach alarming values, reaching only 3.72%. This allows us to conclude that this element can still withstand approximately 26 more operations similar to the one performed, assuming the structure fails when the damage reaches a unit value. This information can support decision-making in a project, such as changing the trajectory, selecting new drill string components, aiming to reduce fatigue damage to the drill string.
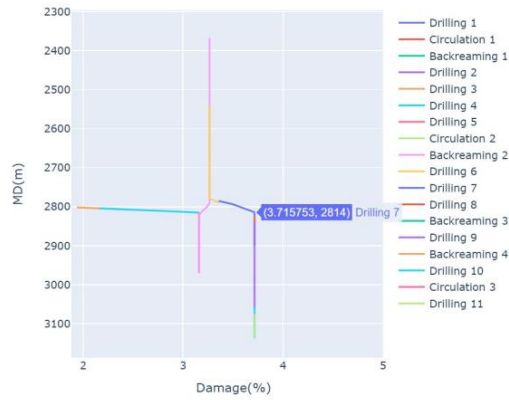
Figure 6 – Results view of the fatigue module.

Other studies aimed at improving the module have been conducted. In this context, FEM is applied for fatigue analysis in connections by quantifying the Stress Amplification Factor (SAF) using the software ABAQUS. To achieve the objective, the problem-solving process in ABAQUS was divided into three stages: pre-processing, processing, and post-processing. In the first stage, a coupling and a pin, components of the 7-5/8 REG connection, were modeled using four-node axisymmetric elements with reduced integration (CAX4R). Additionally, the initial interference fit, the contact between surfaces, the internal pressure, the tensile stress, and the movement constraints were defined. After creating the model, generating the mesh, and defining the boundary conditions, the simulation processing is executed. Finally, in the post-processing stage, the results are analyzed through graphical visualization and output variables. The simulation results allow visualization of the problem, predicting the regions with the highest stress concentration where potential failures in the threaded connection may occur.

ROP Prediction

The rate of penetration (ROP) is the main indicator considered in drilling efficiency studies. An appropriate estimate of the ROP helps determining the drilling time of a phase, in addition to allowing the simulation of scenarios ahead of the drilling, which provides an operational window for controlling the drilling parameters. A better interpretation of the ROP in a specific section enables a more detailed understanding of the drilling process in the region and aids in the planning of future wells. The retroanalysis of historical drilling data seeks to establish a basis to answer questions like those mentioned, contribute to the understanding of the drill string behavior, and indicate performance improvements. It can be stated that the main objective in the study of ROP is drilling optimization, as it indeed relates the ROP to cost reduction by minimizing drilling time.
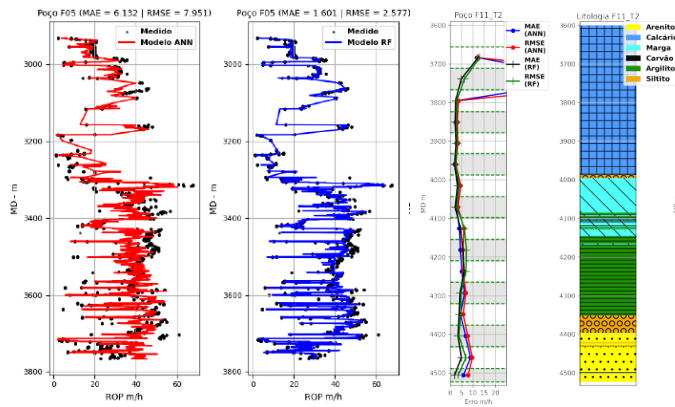
Figure 7 – Results of ROP prediction methods for retro analysis and real time forecasting.

Traditionally, models for predicting ROP are developed to correlate various influential drilling parameters, such as RPM and WOB (Ferro et al., 2023). Generally, analytical techniques based on empirical relationships or statistical regression models are employed. The applicability of these models generally depends on certain restrictions, such as the type of bit used. However, once a representative ROP model is defined, it is possible to use it to understand more deeply the relationship between ROP and the most relevant influencing variables and, mainly, to use them in optimization studies. Modern techniques that employ machine learning are also used for predicting ROP and consequently for drilling optimization, where in this case, analytical models are also generally used as performance references. The applications are in the context of a project with analysis of historical data, aiming to recommend equipment of greater efficiency; as

well as in real-time monitoring, when performance can be predicted and changes in operational parameters can be indicated, aiming at greater efficiency (Figure 7).

The integration of numerical models with machine learning techniques can enable the development of a robust drilling digital twin. Initially, it is necessary to have compliance of input data so that the simulations are closer to the actual condition of the operation. Modeling should then be performed periodically in order to monitor safety and opportunities for performance improvement. Finally, the proposal is that the results support a quick decision making process ensuring safety and efficiency.
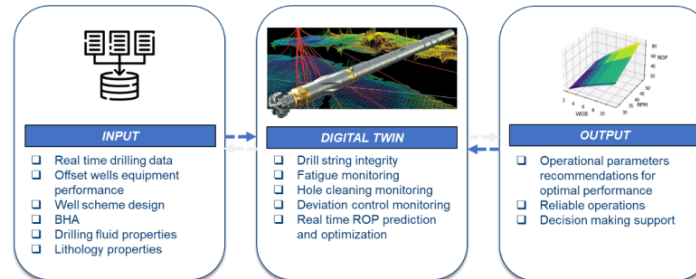

Figure 8 – Digital Twin proposal of the drilling operation.

CONCLUDING REMARKS

This work presented the CAESAR web tool that aims to bring integration of drill string analysis in the design stage. It contains engineering modules that import information from other computational applications (trajectory, lithology, casing scheme, equipment, etc.) and generate reports and structured information for other applications on the PoçoWEB environment. The tool is in constant evolution, with new versions being periodically released, so that new stages of the drilling program are being incorporated to achieve an operation increasingly practical, agile, and reliable.

ACKNOWLEDGMENTS

REFERENCES

Araújo, J. P. N., Gouveia, L. P., Silva, T. B., Lima Junior, E. T., Santos, J. P. L., Lira, W. W. M., Anjos, J. L. R., Oliveira, F. L., Gonçalves, C. and Ferreira, M. V. D., 2020, "Automated Oil Well Casing Design on a Collaborative Web Environment", Proceedings of Rio Oil & Gas 2020, n. 139, Rio de Janeiro, Brazil.

Detournay, E. and Defourny, P., 1992, "A Phenomenological Model for the Drilling Action of Drag Bits", International Journal of Rock Mechanics and Mining Sciences & Geomechanics Abstracts, Vol. 29, pp. 13-23.

Detournay, E., Richard, T. and Shepherd, M., 2008, "Drilling Response of Drag Bits: Theory and Experiment", International Journal of Rock Mechanics and Mining Sciences, Vol. 45, pp. 1347-1360.

Ferro, A. P. A., Barboza, A. S. R., Gouveia, L. P., 2023, "Performance Analysis of Random Forest and Bourgoyne & Young Models in Rate of Penetration Prediction". Proceedings of ENAHPE 2023 – Encontro Nacional de Construção de Poços de Petróleo e Gás. Matinhos – PR.

Hoffmann, O. J.-M. Drilling Induced Vibration Apparatus. Ph.D. dissertation, University of Minnesota. Minneapolis, Minnesota, USA. 2006.

Pastusek, P., Payette, G., Shor, R., Cayeux, E., Aarsnes, U. J., Hedengren, J., Menand, S., Macpherson, J., Gandikota, R., Behounek, M., Harmer, R., Detournay, E., Illerhaus, R. and Liu, Y., 2019, "Creating Open Source Models, Test Cases, and Data for Oilfield Drilling Challenges" Proceedings of the SPE/IADC International Drilling Conference and Exhibition, The Hague, The Netherlands.

Nandakumar, K.; Wiercigroch, M. "Stability analysis of a state dependent delayed, coupled two dof model of drill-string vibration". Journal of Sound and Vibration, 2013.

Servaes, L., Hardin Jr, J. R., Mancini, S., Lauret, E. and Chen, S., 2016, "Reamer and Bit Interaction Model System and Method. US Patent 9,518,450.

Valença, J. P. V., Binas, F. A. V., Ferreira, D. V., Lima, E. T., Barboza, A. S., Riente, A. F. "Fatigue Analysis of Drill String Using Goodman and Sooderberg SN Curves". Paper presented at the Offshore Technology Conference Brasil, Rio de Janeiro, Brazil, October 2023. OTC-32866-MS. https://doi.org/10.4043/32866-MS

RESPONSIBILITY NOTICE

Model-Based Drilling Performance Analysis of a Downhole Regulator

Arviandy G. Aribowo – Eindhoven University of Technology (Netherlands)
Ulf Jakob F. Aarsnes – Norwegian Research Centre (Norway)
Kaidong Chen – Eindhoven University of Technology (Netherlands)
Emmanuel Detournay – University of Minnesota (USA)
Nathan van de Wouw – Eindhoven University of Technology (Netherlands)

Model-Based Drilling Performance Analysis of a Downhole Regulator

Arviandy G. Aribowo[1]**, Ulf Jakob F. Aarsnes**[2]**, Kaidong Chen**[1]**, Emmanuel Detournay**[3]**, and Nathan van de Wouw**[1]

[1] Department of Mechanical Engineering, Eindhoven University of Technology, the Netherlands

[2] NORCE Norwegian Research Centre, Oslo, Norway

[3] Department of Civil, Environmental and Geo-Engineering, University of Minnesota, U.S.A.

Abstract: This work presents a model-based investigation of the effect of a downhole passive regulator (AST) on the performance of a rotary drilling system. In this work, the drill-pipe is represented as a continuum model in the form of partial differential equations (PDEs), capturing all axial and torsional dynamic modes. The bottom-hole-assembly (BHA) is described by a discrete model governed by ordinary differential equations (ODEs) and the evolution of the rock surface under the bit is characterized by a PDE. These sub-systems are assembled and form a coupled PDE-ODE-PDE system model, including a non-smooth bit-rock interaction model. We perform simulation-based studies on the proposed model for cases without and with the AST and analyze the drilling performance in terms of the nonlinear behavior of both drilling systems, particularly in terms of rate-of-penetration (ROP) and drilling efficiency. These numerical studies show that the use of the AST regulator can assist to improve the drilling performance. The latter observation is robust within a realistic parametric space of the drilling operations, the drill-string, and the rock formations.

Keywords: Drilling performance, AST, Distributed parameter (infinite-dimensional) systems, Non-smooth mechanics.

INTRODUCTION

In earlier works (Vromen *et al.*, 2019; Wildemans *et al.*, 2019; Aribowo *et al.*, 2023), it has been observed that the AST can have a positive effect on ROP when studied in low-order, lumped-parameter models. These study results are in line with the field observation. Given the findings, we intend to reveal whether the distributed (infinite-dimensional) model response of the drill-string with the AST is still possessing the same tendency (in terms of increasing drilling performance) as observed in the lumped-parameter (lower-dimensional) models.

In this work, first, we derive the set-valued PDE-ODE-PDE models of the coupled axial-torsional dynamics of rotary drilling systems without and with the AST (here referred to as the benchmark (BM) and AST distributed models, respectively) by employing the distributed-parameter modeling approach presented by (Aarsnes and Aamo, 2016; Aarsnes and van de Wouw, 2018, 2019). Moreover, we consider the (set-valued) bit-rock interface law developed by (Detournay *et al.*, 2008; Aribowo *et al.*, 2022) for the case of homogeneous rock properties and the PDE-based evolution of the depth-of-cut in (Gupta and Wahi, 2016) is used for the interface law. Secondly, we compare the steady-state responses of both models to investigate the impact of the AST on the distributed dynamics and on drilling performance. Finally, a robustness study on the AST design parameters (the stiffness and the lead angle of the helical spline) is performed under the variation of the drill-string length, the physical properties of rock formations (soft vs hard rocks), and the operational drilling parameters.

DISTRIBUTED PARAMETER MODELS OF DRILLING SYSTEMS WITHOUT AND WITH AST

This section details the coupled PDE-ODE-PDE system dynamics for the BM and AST models as depicted in Figure 1 (left for the BM model and right for the AST model). The drill-string system in both models is divided into two main parts, namely the drill-pipe (upper part) and BHA (lower part). The upper part mainly represents the long-slender structure of the drill-pipe and the rig imposing the operational drilling parameters (here also referred as the drill-pipe model). The lower part represents for the BHA (i.e., drill-collar, stabilizers, and other downhole components such as the AST) and the drill-bit with the bit-rock interface law (here also referred as the BHA model).

First, we present the distributed-parameter model developed for the drill-pipe part of both BM and AST models. Second, we describe the lumped-parameter models for the BHA parts of both models for a drilling scenario in vertical wellbore with homogeneous rock formation - see the zoomed parts in Figures 1.

The distributed model of the drill-pipe (the upper part of drill-string)

Following earlier works (Germay *et al.*, 2009; Aarsnes and van de Wouw, 2019), the dynamics of the drill-pipe for both BM and AST models in Figure 1 are modeled in terms of wave equations. Hereto, two sets of (first-order linear hyperbolic) PDEs of the axial and torsional dynamics of the drill-pipes in both models are considered as follows.
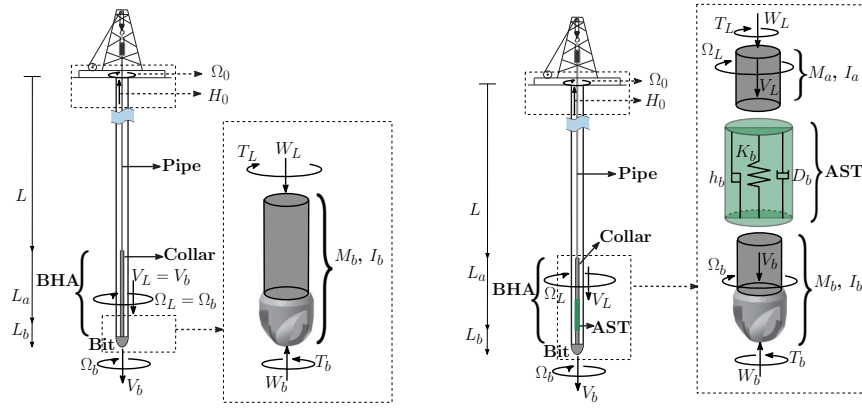
Figure 1 – Schematic overview of the BM model (left) and the AST model (right) in a vertical well-bore. The zoomed schematics are the lower part of the drill-string (BHA), including the drill-bit, for both models.

The PDEs for the axial dynamics of the upper part are given by

$$\frac{\partial W(t,x)}{\partial t} + AE\frac{\partial V(t,x)}{\partial x} = 0, \tag{1}$$

$$A\rho\frac{\partial V(t,x)}{\partial t} + \frac{\partial W(t,x)}{\partial x} = -k_a\rho AV(t,x), \tag{2}$$

where the variable $U(t,x)$ is the axial displacement such that the axial velocity is given by $\frac{\partial U(t,x)}{\partial t} = V(t,x)$. The drill-pipe parameters for the axial dynamics consider the cross-sectional area of the drill-pipe element A and the Young's modulus E. The parameter ρ is the pipe mass density and the damping coefficient k_a represents the effect of viscous dissipation (shear stresses, structural damping) in the axial direction.

The PDEs for the torsional dynamics of the upper part can then be written as follows:

$$\frac{\partial T(t,x)}{\partial t} + JG\frac{\partial \Omega(t,x)}{\partial x} = 0, \tag{3}$$

$$J\rho\frac{\partial \Omega(t,x)}{\partial t} + \frac{\partial T(t,x)}{\partial x} = -k_t\rho J\Omega(t,x). \tag{4}$$

The variable $\Phi(t,x)$ is the angular displacement in the string such that the angular velocity is given by $\frac{\partial \Phi(t,x)}{\partial t} = \Omega(t,x)$. The drill-pipe parameters for the torsional dynamics consider the polar moment J and the shear modulus G. The damping coefficient k_t represents the combined effect of the shear stress and structural damping in the torsional direction.

The top boundary conditions for the PDEs in Eqs. (1) - (2) and Eqs. (3) - (4) are given by the following kinematic equalities: $W(t,x=0) = -H_0$ and $\Omega(t,x=0) = \Omega_0$, with the hookload H_0 applied by the hoisting system and the top angular velocity Ω_0 imposed by the rotary table system of the drilling rig at surface. Moreover, at the bottom of the drill-pipe (i.e., at the rigid interface with the BHA at the depth $x = L$; see Figure 1), the kinematic boundary conditions are given by

$$V(t,x=L) = V_L, \tag{5}$$

$$\Omega(t,x=L) = \Omega_L, \tag{6}$$

where the velocities V_L and Ω_L are, respectively, the axial and torsional velocities at the interface of the drill-pipe and BHA at the coordinate $x = L$.

The lumped-parameter model of the BHA (the lower part of drill-string)

In this section, firstly, we summarize the bit-rock interface law in (Detournay *et al.*, 2008; Aribowo *et al.*, 2022) and the evolution of the rock cutting in (Gupta and Wahi, 2016). Secondly, the lumped-parameter models for the BHA parts of both BM and AST models, as a coupled system with the interface law (Wildemans *et al.*, 2019; Aribowo *et al.*, 2023), are presented.

Bit-rock interface law

The bit-rock interaction is essentially composed of two fundamental processes, namely the frictional contact at the interface of the bit wearflat and rock surface and the rock cutting process. Total contributions of each component in
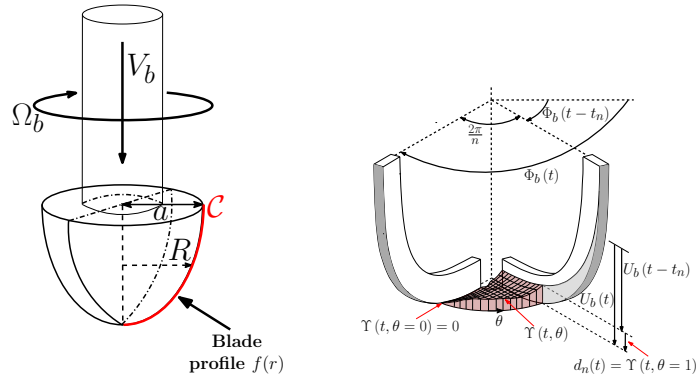
Figure 2 – The bit profile (left) and the depth-of-cut evolution in the bit-rock interaction (right).

the bit-rock interaction into the weight and torque acting on the bit, respectively, are as follows: $W_b = W_f + W_c$ and $T_b = T_f + T_c$. The subscripts f and c are used for the frictional and the cutting components of the interaction, respectively, while the subscript b denotes the variable at the bit. The bit velocities for the axial and torsional directions are denoted by V_b and Ω_b, respectively.

The weight-on-bit (WOB) and torque-on-bit (TOB) due to the frictional contact between the bit and rock are given, respectively, by the following inclusions on velocity level:

$$W_f \in n\,\sigma\,a\,\ell_n\,g\,(V_b)\,, \tag{7}$$

$$T_f \in \frac{1}{2}\mu\,a\,\xi\,W_f\,\mathrm{Sign}\,(\Omega_b)\,, \tag{8}$$

with σ the normal contact stress, ℓ_n the wearflat length, a the bit radius, n the number of the bit blades, μ the friction coefficient, and

$$g\,(V_b) := \frac{1}{2}\,(1+\mathrm{Sign}\,(V_b))\ \text{ with }\ \mathrm{Sign}\,(y) := \begin{cases} 1 & y > 0 \\ [-1,1] & y = 0 \\ -1 & y < 0 \end{cases}. \tag{9}$$

The bit-design parameter representing the orientation and the distribution of the wearflat is expressed as

$$\xi := 2\int_0^1 r\sqrt{(f'(r))^2 + 1}\,\mathrm{d}r \tag{10}$$

with a (dimensionless) bit profile function $f(\cdot)$. In Figure 2 (left), a radial coordinate R on the bit is considered as the radial distance of a point located along the curve of the blade profile $\mathscr{C}$ from the bit axis of symmetry (i.e., $0 \le R \le a$). Here the bit profile is considered as a parabolic function, i.e., $f(r) = a_z r^2$ for a positive constant a_z and a dimensionless bit radius $r = R/a$ with $0 \le r \le 1$.

The WOB and TOB due to the cutting process are given, respectively, by

$$W_c = a\,\zeta^*\,\varepsilon\,d\,, \tag{11}$$

$$T_c = \frac{1}{2}a^2\varepsilon d \tag{12}$$

with ε the intrinsic specific energy of the rock and d the total depth-of-cut. The bit-design parameter representing the orientation of the cutting force is represented by $\zeta^* = \zeta\,\vartheta_\zeta$ with a positive constant ζ and

$$\vartheta_\zeta := \int_0^1 \frac{1}{\sqrt{(f'(r))^2 + 1}}\,\mathrm{d}r. \tag{13}$$

The evolution of the rock cutting process (with a single bit blade) can be described by the following transport equation (Gupta and Wahi, 2016):

$$\frac{\partial \Upsilon(t,\theta)}{\partial t} + \Omega_b(t)\frac{n}{2\pi}\frac{\partial \Upsilon(t,\theta)}{\partial \theta} = V_b(t) \tag{14}$$
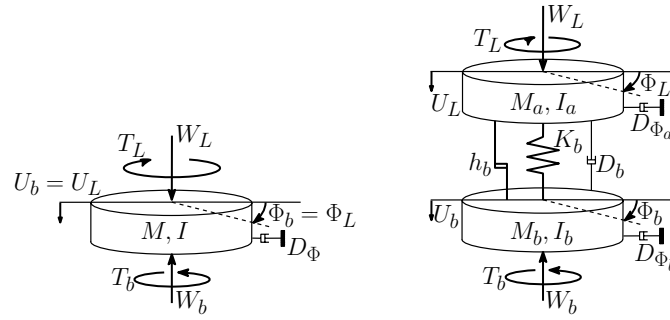
Figure 3 – The lumped-parameter models of the BHA (lower) parts, including the drill-bit, of drill-string systems for the BM model (left) and the AST model (right).

with its evolution state variable $\Upsilon(t,\theta)$ that represents the depth of *uncut* rock at the angular position θ relative to the axial bit position at time t, see Figure 2. The angular position $\theta \in [0,1]$ is the (normalized) angle between an arbitrary surface point on the rock (at a blade) and the reference (next) blade, i.e., initiated at $\theta = 1$ and at $\theta = 0$ after a rock cutting evolution. Herein, the following boundary condition holds: $\Upsilon(t,\theta = 0) = 0$. The depth-of-cut (DOC) produced by a single blade of the drill-bit is then given by $d_n(t) = \Upsilon(t,\theta = 1)$. Subsequently, the total depth-of-cut produced by all n identical blades is obtained as follows: $d = nd_n(t)$.

The lumped-parameter models of the BHA dynamics

The BHA (lower) parts of the drill-string dynamics are modeled as the lumped-parameter models depicted in Figure 3 for the BM model (in left) and for the AST model (in right). These lumped-parameter models of each drill-string system are later to be coupled with the PDEs in Eqs. (1) - (2) and Eqs. (3) - (4) for both axial and torsional dynamics, respectively, of the drill-pipe. We write the equations-of-motion (EOMs) of both lumped-parameter models for the BHA parts into the following generic form:

$$\mathbf{M}\ddot{\mathbf{q}} - \mathbf{H}(t,\mathbf{q},\dot{\mathbf{q}}) = \mathbf{W}\lambda, \tag{15}$$

with the mass matrix $\mathbf{M}$, the generalized smooth forces column $\mathbf{H}$, the non-smooth forces column λ and the associated force direction matrix $\mathbf{W}$. The generalized coordinate vector is denoted by $\mathbf{q}$.

In the BM model, the BHA is essentially represented by a lumped section including the drill-bit and the bit-rock interface law as its bottom boundary conditions. The generalized coordinates $\mathbf{q}$ of the BHA part in the BM model are given by $\mathbf{q} = \begin{bmatrix} U_b & \Phi_b \end{bmatrix}^\top$ where the axial and torsional displacements at the bit are denoted by U_b and Φ_b, respectively. Note that we use the notation $V_b = \dot{U}_b$ and $\Omega_b = \dot{\Phi}_b$ for the bit axial and torsional velocities, respectively. Herein, the matrices of the EOMs in Eq. (15) for the BHA dynamics of the BM model in Figure 3 (left) are given by

$$\mathbf{M} = \begin{bmatrix} M & 0 \\ 0 & I \end{bmatrix}, \tag{16}$$

$$\mathbf{H} = \begin{bmatrix} W_L + W_g - W_c \\ T_L - T_c - D_\phi \Omega_b \end{bmatrix}, \tag{17}$$

$$\mathbf{W} = \begin{bmatrix} 1 & 0 \\ 0 & 1 \end{bmatrix}, \tag{18}$$

$$\lambda = \begin{bmatrix} \lambda_a & \lambda_t \end{bmatrix}^\top, \tag{19}$$

with M the total mass of the BHA, I the total inertia, and D_ϕ the torsional damping coefficient representing the viscous friction terms along the BHA. Herein, $W_g = Mg$ is the total BHA weight and g is the gravitational acceleration. The force $\lambda_a = -W_f$ and the torque $\lambda_t = -T_f$ abide by the inclusions in Eqs. (7) and (8), respectively. The force W_L and the torque T_L are the interaction forces acting at the interface between the drill-pipe and BHA parts of the drill-string system. The cutting component of the bit-rock interaction follows Eqs. (11) - (12) for the weight W_c and the torque T_c, respectively.

Following the schematic of the BHA (lower) part for the BM model in Figure 3 (left), the axial and torsional displacements for the bottom side of the drill-pipe part are denoted by U_L and Φ_L, respectively. As the drill-pipe and BHA parts of the drill-string system are rigidly interconnected at the interface located at the spatial coordinate $x = L$, this condition implies that the following kinematic relations at the interface hold: $U_L = U_b$ and $\Phi_L = \Phi_b$. On velocity level, this kinematic condition also implies the boundary conditions for the PDEs of the drill-pipe in Eqs. (5) – (6) as follows: $V(t, x = L) = V_b$ and $\Omega(t, x = L) = \Omega_b$. In addition, the interaction forces at the interface are also coupled with the state variables of the

drill-pipe distributed model as follows:

$$W(t, x = L) = W_L, \tag{20}$$

$$T(t, x = L) = T_L. \tag{21}$$

In the AST model, the lumped model of the BHA part is divided into two lumped sections, which are connected by the AST. The bit-rock interface law acts as the bottom boundary condition of the lumped section below the AST – where the drill-bit is mounted. The generalized coordinates $\mathbf{q}$ of the BHA part in the AST model are given by $\mathbf{q} = \begin{bmatrix} U_L & U_b & \Phi_b \end{bmatrix}^\top$. The axial and torsional displacements for the lumped BHA section above the AST are U_L and Φ_L, respectively, see Figure 3 (right). Note that we also use the notations $V_L = \dot{U}_L$ and $\Omega_L = \dot{\Phi}_L$ for the velocities of this lumped section above the AST. The matrices of the EOMs in Eq. (15) for the BHA dynamics of the AST model in Figure 3 (right) are given by

$$\mathbf{M} = \begin{bmatrix} M_a + \frac{I_a}{\alpha^2} & -\frac{I_a}{\alpha^2} & \frac{I_a}{\alpha} \\ -\frac{I_a}{\alpha^2} & M_b + \frac{I_a}{\alpha^2} & -\frac{I_a}{\alpha} \\ \frac{I_a}{\alpha} & -\frac{I_a}{\alpha} & I_a + I_b \end{bmatrix}, \tag{22}$$

$$\mathbf{H} = \begin{bmatrix} -D_b(V_L - V_b) - K_b(U_L - U_b) + W_L + W_{ag} + \frac{1}{\alpha}\left(T_L - D_{\phi_a}\Omega_L\right) \\ D_b(V_L - V_b) + K_b(U_L - U_b) + W_{bg} - W_c + \frac{1}{\alpha}\left(D_{\phi_a}\Omega_L - T_L\right) \\ T_L - T_c - D_{\phi_a}\Omega_L - D_{\phi_b}\Omega_b \end{bmatrix}, \tag{23}$$

$$\mathbf{W} = \begin{bmatrix} 0 & 0 \\ 1 & 0 \\ 0 & 1 \end{bmatrix}, \tag{24}$$

$$\lambda = \begin{bmatrix} \lambda_a & \lambda_t \end{bmatrix}^\top. \tag{25}$$

The mass M_a and the inertia I_a lump the BHA section above the AST, and the torsional damping coefficient D_{ϕ_a} is the viscous terms for this BHA section. In addition, the mass M_b and the inertia I_b are for the lumped section below the AST, with the torsional damping coefficient D_{ϕ_b} as the viscous terms along this section. The weights $W_{ag} = M_a g$ and $W_{bg} = M_b g$ are the weights for the BHA sections above and below the AST, respectively.

The AST consists of an internal spring with a stiffness K_b, a structural damping D_b, and a (holonomic) kinematic constraint (due to the helical spline in the AST) that couples the axial and torsional kinematics of the BHA. This constraint is accounted as follows (written on velocity level):

$$(V_L - V_b) = \frac{p_{sp}}{2\pi r_{sp}}\left(r_{sp}\Omega_L - r_{sp}\Omega_b\right), \tag{26}$$

or alternatively on position level as follows:

$$h_b(\mathbf{q}) := \alpha\left(\Phi_L - \Phi_b\right) - (U_L - U_b) = 0, \quad \text{with } \alpha = \frac{p_{sp}}{2\pi}, \, p_{sp} = 2\pi r_{sp}\tan\beta. \tag{27}$$

The lead p_{sp} is a function of the lead angle β and radius r_{sp} of the spline. Based on the BHA schematic for the AST model in Figure 3 (right), the lumped BHA section above the AST is set to be kinematically connected to the bottom side of the drill-pipe at the interface located at the spatial coordinate $x = L$. This implies the following boundary conditions of the drill-pipe in Eqs. (5) – (6) (on velocity level): $V(t, x = L) = V_L$ and $\Omega(t, x = L) = \Omega_L$. Besides, the interaction forces at the interface between the bottom side of the drill-pipe and the lumped BHA section above the AST are also coupled with the state variables of the drill-pipe distributed model and exactly following Eqs. (20) – (21).

Now, we have presented the set-valued PDE-ODE-PDE model for both the BM and AST models – that couples the distributed model of the drill-pipe part and the lumped model of the BHA part. The numerical scheme to solve this type of set-valued infinite-dimensional model is detailed in (Aribowo *et al.*, 2024). In the following section, we will provide illustrative numerical examples based this model for investigating the impact of the AST on the drilling performance, including the robustness study on the AST design parameters.

NUMERICAL SIMULATION RESULTS

In this section, we present the simulation results of the BM and AST models. In particular, we focus on the following aspects:

1. Comparison of the steady-state and the time-averaged responses of BM and AST models to evaluate drilling performance under variation of the drilling operational parameters,
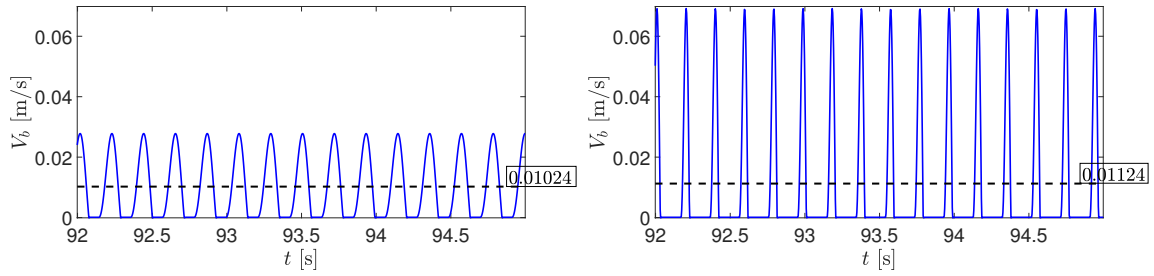
Figure 4 – Bit velocity, V_b, response of the BM model (left) and the AST model (right) with hookload $H_0 = 56.6$ kN and top-drive angular velocity $\Omega_0 = 60$ rpm.
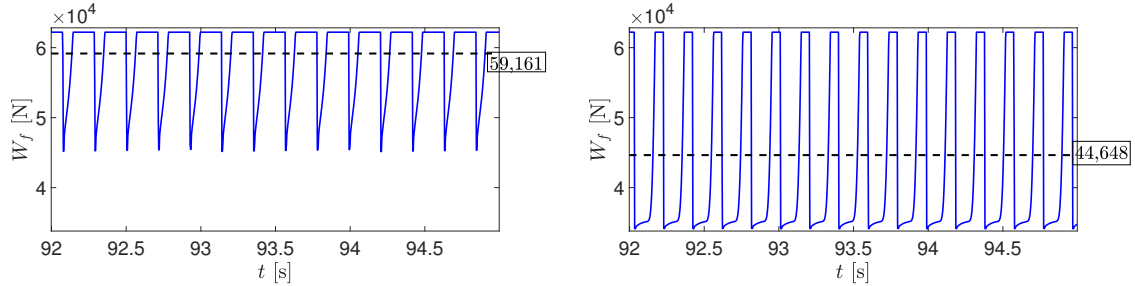

Figure 5 – The evolution of contact forces at the bit for the BM model (left) and the AST model (right) with hookload $H_0 = 56.6$ kN and top-drive angular velocity $\Omega_0 = 60$ rpm.

2. Robustness of the drilling performance of the AST when changing the spring stiffness and the lead angle of its helical spline and varying the drilling operational conditions, drill-string parameters, and rock formation characteristics.

For the numerical simulations, we consider the system parameters used in the earlier works in (Wildemans *et al.*, 2019; Aarsnes and van de Wouw, 2019; Zhang and Detournay, 2022; Aribowo *et al.*, 2023) and the optimal design parameters of the AST obtained in (Aribowo *et al.*, 2024).

Effect of the AST on drilling performance

Figure 4 depicts the steady-state responses of the axial velocities at the bit for the BM model (on left side) and the AST model (on right side) for hookload $H_0 = 56.6$ kN and top-drive angular velocity $\Omega_0 = 60$ rpm. The black dashed lines in the responses show the averaged magnitudes of the velocities for both BM and AST models. In general, the steady-state responses of both the BM and AST models exhibit axial and torsional limit-cycles, with a stick-slip in the axial dynamics. This limit cycling behavior is induced by the fact that the nominal (constant angular and axial velocities) solution is unstable. These periodic responses are dominated by lower dynamic modes of the axial and torsional dynamics in both models.

Furthermore, Figure 4 shows that the presence of the AST increases the ROP. The peak values of the axial bit velocity response in the AST model are up to three times the peak values of the axial vibrations in the BM model and also the average ROP increases (black dashed lines). These findings suggest that stronger axial vibrations are induced due to the presence of AST and these result in higher ROP. As a remark, these results are inline with the conclusions presented in the earlier works in (Vromen *et al.*, 2019; Wildemans *et al.*, 2019; Aribowo *et al.*, 2023) on low-order lumped-parameter models.

Figure 5 shows the comparison of the contact force responses between the BM and AST models (see Eq. (19) or Eq. (25)). The black dashed lines in both responses show the averaged magnitudes of the contact forces for both BM and AST models. First, this comparison shows that the stronger axial vibrations induced by the AST result in a lower averaged contact force at the bit (in Eq. (7)) for the AST model. As indicated in Figure 5, the averaged magnitude of the contact force for the AST model shows about 25% reduction compared to the BM model. This effect arises because the AST leads to longer axial sticking periods (see Figure 4), during which that axial contact force W_f can be lower than its maximum value (which is always attained during axial slip periods); see the set-valued force law for W_f in Eq. (7). Second, the average decrease of the contact force in the bit-rock interaction shows that in the AST model more force (and torque) is used for the rock cutting process (i.e., producing more DOC) while less frictional dissipation at the bit-rock interface (wearflat) takes place.
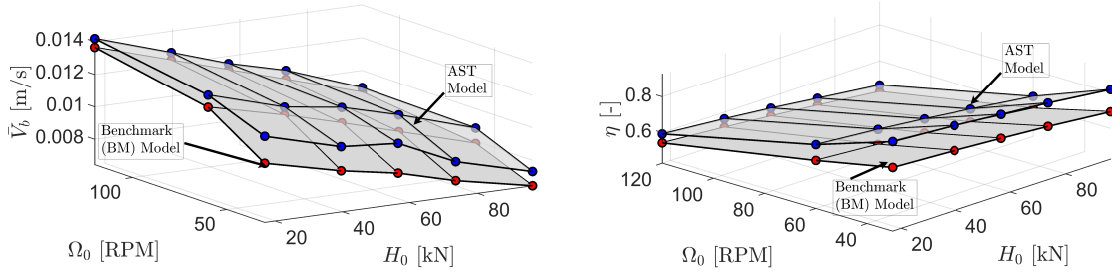
Figure 6 – The comparison of averaged rate-of-penetrations (ROP; left) and drilling efficiency (right) for the BM and AST models for $H_0 \in \{16.9, 39.6, 56.6, 73.6, 96.2\}$ **kN and** $\Omega_0 \in \{30, 60, 120\}$ **rpm.**
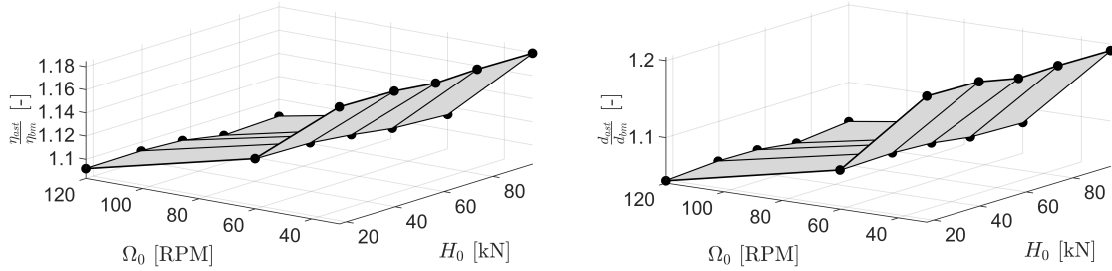

Figure 7 – The gain ratios of drilling efficiency (left) and depth-of-cut (right) of the AST model relative to the BM model for $H_0 \in \{16.9, 39.6, 56.6, 73.6, 96.2\}$ **kN and** $\Omega_0 \in \{30, 60, 120\}$ **rpm.**

Comparison of drilling performance under the variation of drilling operational parameters

The influence of the AST on drilling performance becomes even more apparent when comparing the averaged axial bit velocity (ROP) and drilling efficiency of the BM (red-dots) and AST (blue-dots) models, as depicted in Figure 6. In these plots, a comparative analysis is conducted under drilling operational parameter variations: hookload $H_0 \in \{16.9, 39.6, 56.6, 73.6, 96.2\}$ kN and top angular velocity $\Omega_0 \in \{30, 60, 120\}$ rpm. Note that the applied weight on the drill-string increases as the hookload decreases; see Figure 1. The hookload acts as a control parameter for drilling performance in the axial direction, i.e., we expect an increase of ROP when decreasing the hookload.

The average drilling efficiency is expressed as the ratio between the average TOB used in the rock cutting process T_c and the total of the average TOB (which includes the torque lost due to the frictional dissipation T_f):

$$\eta = \frac{\langle T_c \rangle}{\langle T_c \rangle + \langle T_f \rangle}, \tag{28}$$

where $\langle T_c \rangle$ and $\langle T_f \rangle$ are the average values of the (periodic) steady-state solutions of TOB from the cutting and frictional components in the bit-rock interaction, respectively.

From Figure 6, first, the left plot shows that the average ROP in the AST model consistently outperforms the ROP in the BM model over the employed ranges of drilling operational conditions. Second, the right plot supports the result established in the left plot by visualizing that the rock cutting process in the AST model is more energy-efficient than in the BM model and thus results in higher ROP.

Moreover, the average ROP increases in both BM and AST models with decreasing hookload H_0 and increasing top angular velocity Ω_0. A decrease in hookload H_0, under a prescribed contact top angular velocity Ω_0, results in increasing drilling efficiencies. However, increasing top angular velocity Ω_0 leads to slightly decreasing drilling efficiencies for both BM and AST models. This indicates that less energy is used in rock cutting process.

Figure 7 shows the gains in terms of drilling efficiency (left) and depth-of-cut (right) of the AST model relative to these types of quantities obtained from the BM model (i.e., $\frac{\eta_{ast}}{\eta_{bm}}$ and $\frac{d_{ast}}{d_{bm}}$, respectively) for the same ranges of operational drilling conditions. In this way, the essential benefits of using the AST to improve drilling performance are clearly seen, i.e., positive gain in drilling efficiency with the AST up to 18% (in the left plot) and positive gain in depth-of-cut with the AST up to 20% (in the right plot).

Figure 8 compares the contact force ratios of the BM and AST models under the same drilling operational variations,
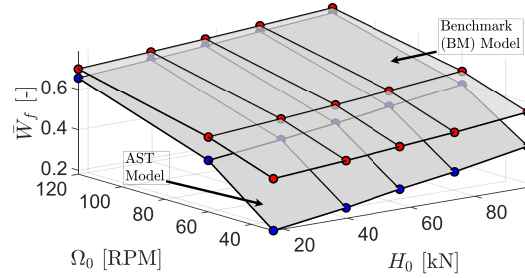
Figure 8 – The comparison of averaged contact force ratio at the bit wearflat for the BM and AST models for $H_0 \in \{16.9, 39.6, 56.6, 73.6, 96.2\}$ **kN and** $\Omega_0 \in \{30, 60, 120\}$ **rpm.**

where this contact force ratio is given by

$$\bar{W}_f = \frac{\langle W_f \rangle}{\langle W_c \rangle + \langle W_f \rangle}. \tag{29}$$

The quantities $\langle W_c \rangle$ and $\langle W_f \rangle$ are the averaged values of WOB from the cutting and frictional components of the bit-rock interface law in steady-state region, respectively. This figure shows the consistency of the reduction of the contact force at the bit in the AST model compared to that in the BM model.

In a qualitative sense, the above observations are in line with those in (Vromen *et al.*, 2019; Wildemans *et al.*, 2019; Aribowo *et al.*, 2023) on the basis of low-order lumped-parameter models. We care to stress that it has been observed in (Liu *et al.*, 2014; Aarsnes and van de Wouw, 2019) that the stability properties (of the nominal constant velocity solutions) are essentially different for the infinite-dimensional and low-order BM models. However, for practically relevant operational conditions, instability generally arises, which results in steady-state limit cycling behavior that is dominated by relatively low-frequency behavior. This explains why, at least in a qualitative sense, the same ROP improvement is observed in both types of models.

Robustness analysis on the performance-based design of the AST parameters

In (Aribowo *et al.*, 2024), the design parameters for optimal performance of the AST (namely the optimal spring stiffness K_b^{opt} and the optimal lead angle β_{ast}^{opt}) are obtained under the variations of drill-string length and rock formation characteristics (i.e., the normal contact stress σ and the intrinsic specific energy ε of the rock). These optimal design parameters give the highest drilling efficiency under such parametric variations of drill-string and rock formation for a nominal set of hookload H_0 and top-drive angular velocity Ω_0. In this section, the robustness of the AST model with these optimally tuned design parameters is analyzed under parametric variations of drilling operational conditions, drill-string, and rock formation parameters, and its performance is compared to the performances of the AST model with the standard (existing) design parameters and the BM model.

Figure 9 shows the comparison of the average drilling efficiencies (as a ratio relative to the drilling efficiency of the BM model) based on the steady-state responses of the standard AST model ($K_b = 1522.5 \frac{\text{kN}}{\text{m}}$ and $\beta_{ast} = 45$ deg) and the tuned AST model (with $K_b^{opt} = 1979.2 \frac{\text{kN}}{\text{m}}$ and $\beta_{ast}^{opt} = 30$ deg). Figure 10 shows the comparison of the average depths-of-cut (also as a ratio relative to the depth-of-cut of the BM model) obtained from the same AST models responses. These comparisons are conducted under the variations of the drill-string parameter (the drill-pipe length): $L \in \{700, 1000, 1500\}$ m and the rock parameters: $\varepsilon = \sigma \in \{60, 72, 90, 120\}$ MPa and with the parametric sets of drilling operational conditions above.

First, these two comparisons show that the tuned AST design consistently gives higher drilling efficiency and a superior cutting process (reflected in the depth-of-cut) than the standard AST model. Relative to the efficiency and the DOC obtained from the BM model (without the AST), the tuned AST model can gain in average efficiency and DOC up to 18% and 20%, respectively, depending on the drilling operational parameters being employed. The standard AST model gains up to 12% in average efficiency and 15% in average DOC with the same operational conditions. Second, these results also show the robustness of the tuned and standard design parameters of the AST over the parametric spaces of drilling operational conditions, rock and drill-string physical characteristics.

CONCLUDING REMARKS

The main conclusions from this study are drawn as follows:

- The AST induces increased axial vibrations on the bit, which lowers wearflat loading and the frictional losses at the bit. This mechanism leads to a lower (friction-induced) thermal loading on the bit, potentially beneficial for bit life.

- Drilling performance (in terms of ROP and drilling efficiency) is improved by including the AST. This is due to a
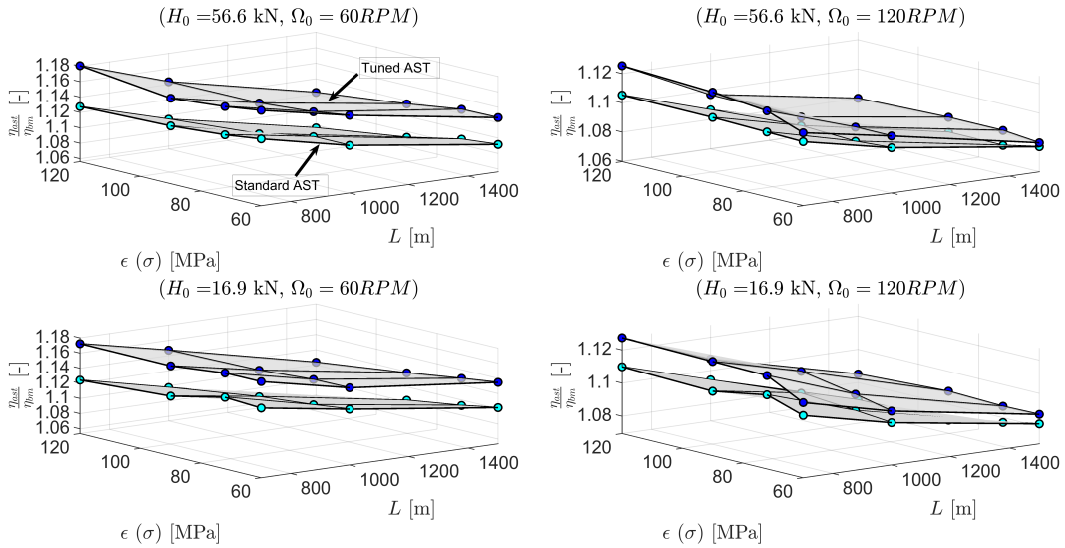
Figure 9 – Drilling efficiency ratios (relative to the drilling efficiency of the BM model) for the AST models with the standard design parameters ($K_b = 1522.5\,\frac{kN}{m}$ and $\beta_{ast} = 45$ deg) and with the optimally tuned design parameters ($K_b^{opt} = 1979.2\,\frac{kN}{m}$ and $\beta_{ast}^{opt} = 30$ deg), for the drill-pipe length $L \in \{700, 1000, 1500\}$ m and the rock parameters: $\varepsilon = \sigma \in \{60, 72, 90, 120\}$ MPa and under: 1) $H_0 = 56.6$ kN and $\Omega_0 = 60$ rpm (top-left), 2) $H_0 = 56.6$ kN and $\Omega_0 = 120$ rpm (top-right), 3) $H_0 = 16.9$ kN and $\Omega_0 = 60$ rpm (bottom-left), 4) $H_0 = 16.9$ kN and $\Omega_0 = 120$ rpm (bottom-right).

Figure 10 – Averaged depth-of-cut (DOC) ratios (relative to the DOC of the BM model) for the AST models with the standard design parameters ($K_b = 1522.5\,\frac{kN}{m}$ and $\beta_{ast} = 45$ deg) and with the optimally tuned design parameters ($K_b^{opt} = 1979.2\,\frac{kN}{m}$ and $\beta_{ast}^{opt} = 30$ deg), for the drill-pipe length $L \in \{700, 1000, 1500\}$ m and the rock parameters: $\varepsilon = \sigma \in \{60, 72, 90, 120\}$ MPa and under: 1) $H_0 = 56.6$ kN and $\Omega_0 = 60$ rpm (top-left), 2) $H_0 = 56.6$ kN and $\Omega_0 = 120$ rpm (top-right), 3) $H_0 = 16.9$ kN and $\Omega_0 = 60$ rpm (bottom-left), 4) $H_0 = 16.9$ kN and $\Omega_0 = 120$ rpm (bottom-right).

reduction in the average (frictional) contact force at the bit resulting in a higher cutting force (improvement on the rock cutting efficiency).

- The limit cycling behavior is dominated by the lower-frequency modes. This explains the consistency of the observations regarding the effect of the AST on drilling performance between lumped- in (Vromen *et al.*, 2019; Wildemans *et al.*, 2019; Aribowo *et al.*, 2023) and distributed-parameter models in this paper.

- From the robustness analysis, it is observed that both the standard AST and an optimally tuned AST design can robustly improve drilling efficiency for a wide range of drill-string parameters, rock formation characteristics, and operational conditions.

ACKNOWLEDGMENTS

REFERENCES

Aarsnes, U.J.F. and Aamo, O.M., 2016. "Linear stability analysis of self-excited vibrations in drilling using an infinite dimensional model". *Journal of Sound and Vibration*, Vol. 360, pp. 239–259. URL `https://doi.org/10.1016/j.jsv.2015.09.017`.

Aarsnes, U.J.F. and van de Wouw, N., 2018. "Dynamics of a distributed drill string system: Characteristic parameters and stability maps". *Journal of Sound and Vibration*, Vol. 417, pp. 376–412. URL `https://doi.org/10.1016/j.jsv.2017.12.002`.

Aarsnes, U.J.F. and van de Wouw, N., 2019. "Axial and torsional self-excited vibrations of a distributed drill-string". *Journal of Sound and Vibration*, Vol. 444, pp. 127–151. URL `https://doi.org/10.1016/j.jsv.2018.12.028`.

Aribowo, A.G., Aarsnes, U.J.F., Chen, K., Detournay, E. and van de Wouw, N., 2024. "Analysis of a downhole passive regulator in drilling: a distributed parameter modeling approach". *to be submitted*.

Aribowo, A.G., Wildemans, R., Detournay, E. and van de Wouw, N., 2022. "Drag bit/rock interface laws for the transition between two layers". *International Journal of Rock Mechanics and Mining Sciences*, Vol. 150, p. 104980. ISSN 1365-1609. doi:10.1016/j.ijrmms.2021.104980. URL `https://doi.org/10.1016/j.ijrmms.2021.104980`.

Aribowo, A.G., Wildemans, R., Detournay, E. and van de Wouw, N., 2023. "Dynamic analysis of a downhole regulator for drilling in interbedded formations". *SPE Journal*, Vol. 28, No. 4, pp. 1611–1635. URL `https://doi.org/10.2118/214310-PA`. SPE-214310-PA.

Detournay, E., Richard, T. and Shepherd, M., 2008. "Drilling response of drag bits: Theory and experiment". *International Journal of Rock Mechanics and Mining Sciences*, Vol. 45, No. 8, pp. 1347–1360. ISSN 1365-1609. URL `https://doi.org/10.1016/j.ijrmms.2008.01.010`.

Germay, C., Denoël, V. and Detournay, E., 2009. "Multiple mode analysis of the self-excited vibrations of rotary drilling systems". *Journal of Sound and Vibration*, Vol. 325, No. 1-2, pp. 362–381. URL `https://doi.org/10.1016/j.jsv.2009.03.017`.

Gupta, S. and Wahi, P., 2016. "Global axial-torsional dynamics during rotary drilling". *Journal of Sound and Vibration*, Vol. 375, pp. 332–352. URL `https://doi.org/10.1016/j.jsv.2016.04.021`.

Liu, X., Vlajic, N., Long, X., Meng, G. and Balachandran, B., 2014. "State-dependent delay influenced drill-string oscillations and stability analysis". *ASME Journal of Vibration and Acoustics*, Vol. 136, No. 5, p. 051008 (9 pages). URL `https://doi.org/10.1115/1.4027958`.

Vromen, T., Detournay, E., Nijmeijer, H. and van de Wouw, N., 2019. "Dynamics of drilling systems with an antistall tool: Effect on rate of penetration and mechanical specific energy". *SPE Journal*, Vol. 24, No. 05. URL `https://doi.org/10.2118/194487-PA`.

Wildemans, R., Aribowo, A.G., Detournay, E. and van de Wouw, N., 2019. "Modelling and dynamic analysis of an anti-stall tool in a drilling system including spatial friction". *Nonlinear Dynamics*, Vol. 98, No. 4, pp. 2631–2650. URL `https://doi.org/10.1007/s11071-019-05075-6`.

Zhang, H. and Detournay, E., 2022. "A high-dimensional model to study the self-excited oscillations of rotary drilling systems". *Communications in Nonlinear Science and Numerical Simulation*, Vol. 112, p. 106549. ISSN 1007-5704. doi:https://doi.org/10.1016/j.cnsns.2022.106549. URL `https://www.sciencedirect.com/science/article/pii/S1007570422001666`.

RESPONSIBILITY NOTICE

On the Robustness of Deep Drilling Control Techniques

Ricardo P. Féres – University of São Paulo, São Carlos (Brazil)
Hélio J. Cruz Neto – University of São Paulo, São Carlos (Brazil)
Pedro A.P. Magalhães – University of São Paulo, São Carlos (Brazil)
Marcelo A. Trindade – University of São Paulo, São Carlos (Brazil)

On the Robustness of Deep Drilling Control Techniques

Ricardo P. Féres[1], **Hélio J. Cruz Neto**[1], **Pedro A.P. Magalhães**[1], **and Marcelo A. Trindade**[1]

[1] São Carlos School of Engineering, University of São Paulo, Department of Mechanical Engineering, Av. Trabalhador São-Carlense, 400, São Carlos, SP, 13566-590, Brazil

Abstract: Torsional vibrations due to stick-slip may lead to large variations in deep drilling angular velocities causing a large number of failures in the drilling process. Previous works have shown that standard linear proportional-integral (PI) control laws may be ineffective in controling stick-slip. In the last decade, different control techniques have been proposed to mitigate the stick-slip occurrence, such as the techniques commercially known as SoftTorque, SoftSpeed and ZTorque. While some of them are still heavily based on the PI strategy, but introduce interesting ways of setting the corresponding control gains, others require measurement and/or estimation of additional outputs in order to improve the control performance. Current results with other more complex techniques, usually requiring additional outputs, such as the OSOF strategy, for instance, indicate that it should indeed be possible to improve both drilling performance and robustness by including few well selected additional outputs. Nevertheless, there is still no published studies on the robustness analyses of these more modern drilling control techniques, while such drilling systems operate under strongly uncertain bit-rock nonlinear interaction. To assess their robustness, it is proposed to consider uncertain parameters for the bit-rock interaction model. This is done using a stochastic model for the bit-rock interaction torque which combined to Monte Carlo simulations then leads to stochastic results for the angular velocity response, when subjected to each control strategy. Statistical analyses of the results are used to assess and compare the performance of these drilling control strategies from a robustness perspective.

Keywords: Drilling control techniques, stick-slip, torsional vibrations, robustness analysis, uncertainty quantification

INTRODUCTION

A successful oil-well drilling process generally involves the opening of a borehole in selected rock formations as quickly and safely as possible. This is done using a rotating drill-bit driven by an actuated rotary table at the surface that provides torque to the drill-bit through a so-called drillstring. Since oil wells can reach a few kilometers and drillstring are made of pipes with diameters within tens of centimeters, the drillstring can be a very slender structure and, thus, very flexible in torsion and bending leading to potential torsional and lateral vibrations. The drill-bit is part of the Bottom-Hole Assembly (BHA) to which a drive torque is applied (transmitted through the drillstring). It is also subjected to a reaction torque induced by the interaction between drill-bit and rock formation (Spanos *et al.*, 2003).

Drillstring vibrations are among the main causes of inefficiency, malfunctioning and failure in oil-well drilling process (Schlumberger Ltd., 2006). For instance, torsional vibrations induced by stick-slip phenomenon may twist drillstrings by several turns during drilling process which may cause failure in one or more drill pipes connections and/or sections. When untwisting, an extra torque is transmitted to the drill-bit inducing much higher angular velocities, leading to potential mechanical failure of the drill-bit. This dynamic behavior has been observed in field measurements and presents itself as self-excited stable periodic low-frequency oscillations of the effective drilling angular velocity (Placido *et al.*, 2002). These stick-slip oscillations may be reduced by either reducing the weight-on-bit (WOB) or increasing the target angular velocity (Spanos *et al.*, 2003). The latter, however, is normally avoided since it may induce lateral (bending) vibrations that lead to other drilling failure modes. Therefore, when oscillations are observed for the angular velocity at the drive table, the strategy generally considered in field operations is to reduce the WOB. For that, the hook-load applied to the top assembly is usually increased. However, this action reduces the drilling performance in terms of rate of penetration, since this rate is almost linearly proportional to drill-bit angular velocity and weight-on-bit (Tucker and Wang, 1999).

In the last decades, several techniques were proposed to control (reduce) the torsional vibrations in oil-well drilling operations (Saldivar *et al.*, 2016), such as proportional-integral (PI) control (Monteiro and Trindade, 2017), PI control combined with WOB variation (Navarro-López and Suárez, 2004; Monteiro and Trindade, 2017), SoftSpeed (Kyllingstad and Nessjoen, 2009), torque feedback techniques such as SoftTorque (Tucker and Wang, 1999; Runia *et al.*, 2013) and ZTorque (Dwars, 2015; Kyllingstad, 2017; Aarsnes *et al.*, 2018; Auriol *et al.*, 2022). The PI control has the advantage of already being implemented in most real drilling rigs. Modern techniques such as SoftTorque, SoftSpeed and ZTorque have been increasingly installed and tested in operation with relative success, although with a potential increase in drilling costs and still requiring additional studies to evaluate their robustness. Other complex techniques may be effective but may also require significant modifications in well established practices and equipments.

Recently, it was shown that the stick-slip phenomenon induced by drilling process may be reduced by using properly designed PI control parameters (control gains) (Monteiro and Trindade, 2017). However, the dynamic nonlinear behavior combined to an uncertain bit-rock interaction torque may undermine the predicted drilling performance. Thus, in order

to, at least, predict the potential performance reduction due to variabilities or uncertainties in the drilling process, a non-deterministic approach may be necessary (Trindade, 2020). To assess the robustness of such control strategies, one possible approach is to consider uncertain parameters for the bit-rock interaction model. This can be done using a stochastic model for the bit-rock interaction torque which combined to Monte Carlo simulations then leads to stochastic results for the angular velocity response, when subjected to each control strategy. Statistical analyses of the results could help assessing and comparing the performance of these drilling control strategies also from a robustness perspective.

DRILLING SYSTEM MODEL

The torsional dynamics of the drilling system is represented in a simplified way considering three main components: the rotary table, the bottom hole assembly (BHA) and the drillstring. The BHA contains the stabilizers, drill-collars and drill-bit and, for modeling purposes, is represented as a rigid body. The hypothesis of rigid body is also assumed for the rotary table. The drillstring is modeled as a circular shaft using the fundamental torsional-deformation assumptions. Additionally, the material is considered linear elastic with constant properties. The following properties were considered: for the drillstring, mass density 8010 kg/m^3, shear modulus 79.6 GPa, length 3000 m, inner radius 0.0543 m, outer radius 0.0635 m, for the BHA effective rotary inertia 394 kg m^2 and for the drive table effective rotary inertia 500 kg m^2.

The drillstring is modeled using finite elements in terms of the nodal angular displacements of the drillstring. The effective damping of the system, due to interaction between the drillstring and drilling mud and other dissipation sources, is modeled using a damping matrix defined a posteriori to provide reasonable damping levels. Using these assumptions, the equations of motion are written using a state space representation

$$\dot{\mathbf{x}} = \mathbf{A}\mathbf{x} + \mathbf{B}_t T_t + \mathbf{B}_b T_b, \tag{1}$$

in which $\mathbf{x}$ is the vector of state variables, $\mathbf{A}$ the state matrix composed of mass, damping and stiffness properties of the system, T_t and T_b are the torques applied to the drilling system by the control system at the drive table and by the rock formation at the drill-bit, respectively, and $\mathbf{B}_t$ and $\mathbf{B}_b$ are their corresponding vectors of input distributions.

The bit-rock interaction torque T_b is modeled using Karnopp's model with an exponential decaying friction term

$$T_b = \begin{cases} T, & \text{for } |\omega_b| \leq \delta \text{ and } |T| \leq a_2 N_b, \\ a_2 N_b sgn(T), & \text{for } |\omega_b| \leq \delta \text{ and } |T| > a_2 N_b, \\ \left[a_1 + (a_2 - a_1)e^{-\beta|\omega_b|} \right] N_b sgn(\omega_b), & \text{for } |\omega_b| > \delta \end{cases} \tag{2}$$

in which the values a_1 and a_2 are called dynamic and static friction coefficients, respectively, β is a positive exponential friction coefficient, T is the torque transmitted by the drillstring to the bit, N_b is the normal force applied to the bit and ω_b is the bit angular speed. The parameters for the dry friction model were taken from (Monteiro and Trindade, 2017): $a_1 = 0.026$ m, $a_2 = 0.085$ m, $\beta = 0.098$, $\delta = 10^{-4}$ rad/s, for a WOB of 140 kN.

CONTROL STRATEGIES

The control torque T_t has the primary objective of inducing a prescribed target angular velocity ω_r at the rotary table and, consequently, in the drillstring and drill-bit. There are many strategies for that, but most of them are based on the standard proportional-integral (PI) feedback of the measured angular velocity at the drive table. Modern techniques consider the measurement of additional quantities in order to improve the control performance.

PI controller

The standard and most common angular velocity control strategy is based on a PI controller defined as

$$T_t = K_p(\omega_r - \omega_t) + K_i(\omega_r t - \theta_t). \tag{3}$$

Thus, the control torque T_t only depends on the measured angular velocity at the drive table ω_t. Nevertheless, due to the drillstring low torsional stiffness and bit-rock interaction torque, the application of such a control strategy with any pair of control gains K_p and K_i does not guarantee a constant angular velocity, neither at top drive nor at drill-bit.

Stiff controller. The objective of the so-called stiff controller strategy is to prioritize the maintenance of the angular velocity of the rotary table at a reference value. To achieve this, it is necessary to use high values of control gains K_p and K_i, but this leads to negative consequences on the drill-bit velocity. According to (Aarsnes *et al.*, 2018), it is possible to determine the control gain values of a stiff controller by taking into consideration known top drive and drillstring characteristics with the following expression

$$K_p = 100\zeta_p, \quad K_i = 5J_d, \tag{4}$$

where ζ_p is the characteristic line impedance of the drill pipes and is given as $J_p\sqrt{\rho G_p}$, in which the index p refers to the drill pipe, and J_d is the effective top drive inertia.

SoftSpeed controller. The so-called SoftSpeed controller (Kyllingstad and Nessjoen, 2009) considers a 'smarter' choice of the control gains to reduce the torsional waves at the top rotary system. The objective of the SoftSpeed controller is to reduce the reflection coefficient of the top rotary system at a given target frequency, usually the frequency of observed stick-slip oscillations. This leads to

$$K_p = \zeta_p/m, \quad K_i = J_d \omega_{ss}^2, \tag{5}$$

in which m is a normalized mobility factor less than 1 and ω_{ss} is the frequency of stick-slip oscillations. Notice that, while m is a free design parameter, ω_{ss} is usually either estimated from previous experience or identified from measured angular velocity oscillations in the occurrence of stick-slip.

Optimized PI controller. Another strategy is to use an optimization procedure combined with a selected performance criteria, such as the average deviation of angular velocity compared to the target value, to determine potentially good solutions for the control gains K_p and K_i. This was proposed using either nominal or robust performance criteria in (Monteiro and Trindade, 2017; Trindade, 2020). In both cases, however, a set of numerical simulations is required leading to high computational cost depending on the dynamic model and operating conditions considered.

PI controller augmented by torque feedback

Two recent control techniques introduce the idea of using a potential measurement of the torque applied by the drillstring to the rotary table in order to further reduce the reflection coefficient proposed in the SoftSpeed controller. The main idea is to filter out particular frequency components of the control torque based on observed stick-slip frequencies.

SoftTorque. The SoftTorque technique (Tucker and Wang, 1999; Runia *et al.*, 2013) consists of deducing the predicted effect of a reflected torque from the tracking error in a PI controller, such that

$$T_t = K_p(\omega_r - \omega_t - hT_f) + K_i(\omega_r t - \theta_t - hT_c/f_c) \text{ with } T_f = T_{contact} - T_c, \tag{6}$$

where h is an additional control gain and f_c is a cutoff frequency. The torque T_c is obtained from a first-order low-pass filter based on the measured torque $T_{contact}$ that is applied by the drillstring to the drive table,

$$\dot{T}_c = -f_c T_c + f_c T_{contact}. \tag{7}$$

ZTorque. The ZTorque technique (Aarsnes *et al.*, 2018) also adds a high-pass filter to the measured torque $T_{contact}$, leading to a second-order band-pass filter to compute the PI tracking error, such that in the Laplace domain,

$$T_t = (K_p + K_i/s)e_{PI}, \text{ with } e_{PI} = \omega_r - \omega_t - Z\frac{s}{(s+1/t_{hp})(1+t_{lp}s)}T_{contact}, \tag{8}$$

in which $Z = 1/\zeta_p$ and t_{hp} and t_{lp} are the low-pass and high-pass time constants to be determined for a given frequency range where the reflection should be reduced, usually containing the stick-slip frequency.

Optimal output feedback controller

To design techniques based on the optimal control theory, it is necessary to transform the original tracking problem into a stabilization problem. For that, the state variables are redefined, extracting the components of the original state variables after stabilization $\mathbf{x}_{eq}$, in which the entire drillstring is deformed but rotating with a constant target angular velocity. Then, the applied control torque T_t is also decomposed into a feedback component u, to suppress vibrations, and a constant feedforward component $\tilde{u}$, inducing $\mathbf{x}_{eq}$, such that $T_t = \tilde{u} + u$. The constant parameters $\mathbf{x}_{eq}$ and $\tilde{u}$ are computed for a given target angular velocity ω_r from $\mathbf{A}\mathbf{x}_{eq} + \mathbf{B}_t\tilde{u} + \mathbf{B}_b T_b(\omega_r) = \mathbf{0}$. Then, the equations of motion are rewritten in terms of a new set of state variables, such that

$$\dot{\xi} = \mathbf{A}\xi + \mathbf{B}_t u + \mathbf{B}_b q(\omega_d) = \mathbf{g}(\xi, u), \text{ with } \xi = \begin{bmatrix} \xi_d \\ \xi_v \end{bmatrix} = \begin{bmatrix} \bar{\eta} - \bar{\eta}_{eq} \\ \dot{\eta} - \dot{\eta}_{eq} \end{bmatrix} = \mathbf{x} - \mathbf{x}_{eq}, \tag{9}$$

where η is the vector of modal displacements and $\bar{\eta}$ is obtained by excluding the modal displacements corresponding to the rigid body modes from η. The desired operating point has been shifted to the origin, ω_d is the difference between drill bit and target velocities, $\omega_d = \omega_b - \omega_r = \phi^\mathsf{T}(L)\xi_v$, and $q(\omega_d)$ is a translated interaction torque $q(\omega_d) = T_b(\phi^\mathsf{T}(L)\xi_v + \omega_r) - T_b(\omega_r)$.

To ensure that, at the equilibrium, the drillstring rotates with the desired angular velocity, even under unknown and varying bit-rock interaction conditions, and, thus, that $\tilde{u} = T_b(\omega_r)$ holds, (9) is augmented with the error integral, to avoid any steady-state error, $\dot{\sigma} = e = \omega_t - \omega_r = \phi^\mathsf{T}(0)\xi_v$, yielding the augmented system

$$\dot{\zeta} = \begin{bmatrix} \dot{\sigma} \\ \dot{\xi} \end{bmatrix} = \begin{bmatrix} \phi^\mathsf{T}(0)\xi_v \\ \mathbf{A}\xi + \mathbf{B}_t u + \mathbf{B}_b q(\omega_d) \end{bmatrix} = \mathbf{A}_n\zeta + \mathbf{B}_{tn}u + \mathbf{B}_{bn}q(\omega_d) = \mathbf{h}(\zeta, u). \tag{10}$$

The idea of adding σ as a state is to use it for feedback, such that u, and consequently ξ, become a function of σ. This is a standard procedure in control theory known as integral action that guarantees regulation in the presence of uncertainties if the closed-loop system is structurally stable (Khalil, 2015). Then, the output feedback control law is written as

$$u = -\mathbf{KC}(\boldsymbol{\alpha})\zeta \tag{11}$$

where $\boldsymbol{\alpha}$ defines the positions along the drillstring were feedback sensors are considered. Previous results have shown that very satisfactory results can be obtained by using only two sensors, one at the drive table and another sufficiently distant from the table. Here, it is assumed that the distance between the second sensor and the drive table could be up to 10% of the total drillstring length. Then, a feedback of the steady-state error, the relative angular displacement between the two sensors, and the angular velocity at the two sensors is considered, leading to

$$\mathbf{C}(\boldsymbol{\alpha}) = \begin{bmatrix} 1 & 0 & 0 & 0 \\ 0 & \bar{\phi}(\alpha_1) - \bar{\phi}(\alpha_2) & 0 & 0 \\ 0 & 0 & \phi(\alpha_1) & \phi(\alpha_2) \end{bmatrix}^{\mathsf{T}}. \tag{12}$$

Optimal Static Output Feedback (OSOF). The optimal static output feedback (OSOF) is based on the linear quadratic regulator (LQR), but with the constraint of using only measured signals for feedback (Levine and Athans, 1970). Recently, a new optimization was proposed based on the minimization of the ratio between the cost functions of the OSOF and LQR controllers, which is independent of measurement and excitation locations (Cruz Neto and Trindade, 2019, 2023). The technique ends up consisting of finding the initial condition that maximizes this ratio, which is the solution of the generalized eigenvalue problem involving matrices P_o and P_l, solutions of the algebraic Riccati equations of OSOF and LQR problems, for given $\mathbf{Q}$ and $\mathbf{R}$ LQR weighting matrices.

In the present case, the matrix $\mathbf{Q}$ is adopted such that $\mathbf{x}^{\mathsf{T}}\mathbf{Q}\mathbf{x}$ is the system total energy with an additional weighting factor (q_i) for the error integral. The constant q_i is chosen such that, when applying the OSOF controller, the average deviation from the drill-bit target angular velocity (criterion proposed in (Monteiro and Trindade, 2017)) is minimized

$$J = \frac{1}{\Delta t} \int_0^{\Delta t} \frac{|\omega_b - \omega_r|}{\omega_r} \, \mathrm{d}t. \tag{13}$$

Negative Damping Based Controller (NDBC). For a target angular velocity ω_r sufficiently greater than zero, q is a smooth function of ω_d, and the qualitative behavior of the solutions of (9) in a neighborhood of the origin can be determined by a linear approximation at this point, leading to

$$\dot{\xi} = \mathbf{A}_l \xi, \tag{14}$$

in which, $\mathbf{A}_l$ is the matrix of first order partial derivatives of $\mathbf{g}$ with respect to ξ, evaluated at the origin

$$\mathbf{A}_l = \left.\frac{\partial \mathbf{g}}{\partial \xi}\right|_{\xi=0} = \begin{bmatrix} \mathbf{0} & \bar{\mathbf{I}} \\ -\bar{\Lambda} & -[\mathbf{D} + n_d \boldsymbol{\phi}(L)\boldsymbol{\phi}^{\mathsf{T}}(L)] \end{bmatrix}, \text{ with } n_d = \left.\frac{\mathrm{d}q}{\mathrm{d}\omega_d}\right|_{\omega_d=0} = -\beta(a_2 - a_1)e^{-\beta\omega_r} WOB. \tag{15}$$

Thus, the reaction torque applied to the bit is locally equivalent to a viscous damper with a negative damping coefficient n_d, yielding the observed instability in field operations (Brett, 1992; Mihajlović *et al.*, 2004; Saldivar *et al.*, 2013). Thus, a potential goal for a controller would be to render the operating point asymptotically stable. Envisioning a more robust controller, it is proposed to find the control gains that maximize the value of the negative damping coefficient for which the operating point is asymptotically stable,

$$\min_{\mathbf{K}} \gamma, \text{ with } Z = \{n_d \in \mathbb{R}_- \mid \nu(\mathbf{A}_{cl}(\mathbf{K}, n_d)) > 0\}, \text{ and } \mathbf{A}_{cl}(\mathbf{K}, n_d) = \mathbf{A}_l(n_d) - \mathbf{B}_{tn}\mathbf{KC}. \tag{16}$$

UNCERTAINTY QUANTIFICATION AND ROBUSTNESS ANALYSES

Next, it is desirable to assess how bit-rock interaction parametric uncertainties affect the control performance of the studied system. For that, two important parameters, namely a_1 and $\delta a = a_2 - a_1$ from (2), that characterize the torque due to the interaction between drill-bit and rock formation are considered stochastic. Hence, a stochastic model is constructed for these parameters based on potentially known information on their variability. Here, it is assumed that their nominal values are $a_1 = 0.026$ m and $\delta a = 0.059$ m and they follow a Gamma probability distribution function with relative dispersion of 10%. This stochastic model guarantees positive only values for a_1 and δa and, thus, values of a_2 larger than a_1 which is expected in realistic conditions. The stochastic model is then used to produce a number of samples N for the parameters and, for each sample pair, a Monte Carlo simulation is performed using the previously presented model. This leads to N responses of the system for which a statistic analysis may be performed. It is then possible to compute the mean responses, standard deviations, confidence intervals, and so on.

It should be noticed that different control strategies lead to diverse nominal results and, thus, nominal performance, but they also have distinct design methodologies and parameters. Therefore, their strict comparison must be taken with care. Besides, for the sake of brevity, here, the performances of different control strategies are compared only through the predicted responses of the drill-bit angular velocities, for a given drilling condition (defined by a target angular velocity of 100 rpm and a target WOB of 140 kN) and under prescribed uncertainty of the bit-rock interaction model parameters, a_1 and a_2. Distinct drilling conditions and/or uncertainties may lead to different comparative results and conclusions.

Of particular interest are the nominal responses, that is, for nominal bit-rock interaction model parameters, and their 95% confidence interval. A given control strategy may perform well nominally but poorly when uncertainties are considered. This is the case for a standard PI control, as shown in Figure 1a. Although, through optimization, control gains were computed so that the stick-slip oscillations are controlled in the nominal response, the confidence intervals indicate these control gains may lead to permanent (non-controlled) stick-slip oscillations.

Optimal output feedback controllers, OSOF and NDBC, are able to control stick-slip oscillations even under uncertainties considered (Figures 1b and 1c). The nominal response of OSOF seems a bit better than that of NDBC since it presents a smaller overshoot (maximum angular velocity). However, confidence intervals indicate that NDBC leads to faster exit from the stick condition and stabilization and should be considered more appropriate from a robustness standpoint. Preliminary results for the modern techniques SoftSpeed, SoftTorque and ZTorque also indicate that, nominally, it is possible to mitigate stick-slip oscillations, as shown in Figures 1d, 1e and 1f. Nevertheless, since the control parameters were designed aiming at improving the nominal response, both SoftSpeed and SoftTorque perform poorly when subject to the considered uncertainties. As for the ZTorque, despite a long initial stick phase duration, which is usually expected for this controller, it presents a pretty robust performance (Figure 1f). It is expected, however, that both nominal performance and robustness of these techniques could be further improved by fine tuning the control parameters. This is currently part of ongoing research.
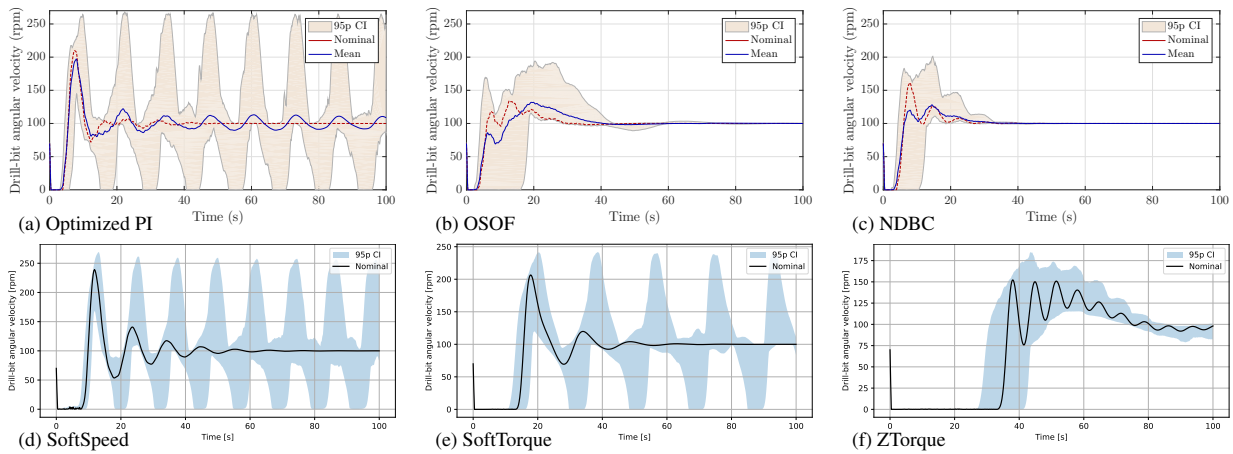
Figure 1 – Comparison between nominal, mean and confidence intervals of time responses of drill-bit angular velocity obtained for the studied control techniques.

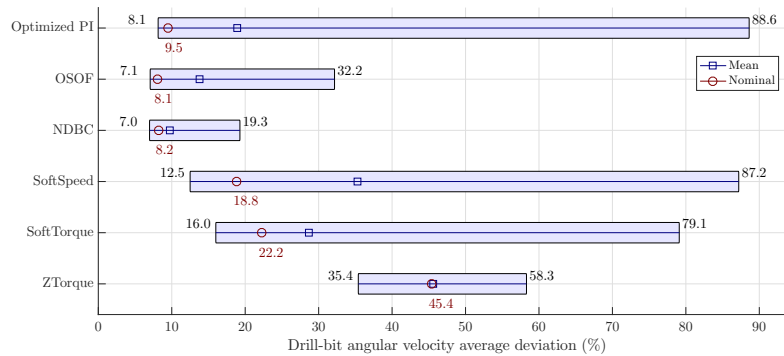**Figure 2 – Comparison between nominal, mean and confidence intervals of drill-bit angular velocity average deviations obtained for the studied control techniques.**

Since it is not necessarily easy to compare time responses, the use of a more compact metric could be interesting, such as the average deviation of drill-bit angular velocity, as defined in (13). Thus, for each sample and control strategy, it was

computed and used to evaluate their nominal and mean values and their confidence intervals. The results, shown in Figure 2, confirm that OSOF is indeed marginally better than NDBC, nominally. Also, the optimized PI is nominally nearly as well performing as OSOF and NDBC. The confidence intervals, however, indicate that the drill-bit angular velocity average deviation can be quite high for PI (consequence of non-controlled stick-slip oscillations) and that NDBC is substantially more robust than OSOF, reducing the worse deviation from 32.2% to 19.3%. Both SoftSpeed and SoftTorque perform similarly to the optimized PI, in terms of robustness, but with worse nominal and mean deviation values. From the average deviation standpoint, the ZTorque controller is indeed more robust that the latter two but with high deviation values (between 35.4% and 58.3%). Note, however, that this is substantially affected by a long initial stick phase duration.

CONCLUDING REMARKS

Robustness analyses of standard and modern drilling control techniques, such PI, SoftSpeed, SoftTorque, ZTorque, OSOF and NDBC, under uncertain bit-rock nonlinear interaction were performed through Monte Carlo simulations. Results indicate, as expected, that a controller designed to maximize performance under parametric deviations such as NDBC provides a more robust performance. Nevertheless, it is suggested that the other strategies could be more robust if their parameters accounted for a pre-defined set of uncertainties. Therefore, based on the present findings, future research shall be directed to methodologies that allow designing the many free control parameters of these distinct strategies aiming at providing a more robust performance.

ACKNOWLEDGMENTS

REFERENCES

Aarsnes, U., di Meglio, F. and Shor, R., 2018. "Benchmarking of industrial stick-slip mitigation controllers". *IFAC PaperOnLine*, Vol. 51, No. 8, pp. 233–238.

Auriol, J., Boussaada, I., Shor, R., Mounier, H. and Niculescu, S.I., 2022. "Comparing advanced control strategies to eliminate stick-slip oscillations in drillstrings". *IEEE Access*, Vol. 10, pp. 10949–10969. doi:10.1109/access.2022.3144644.

Brett, J., 1992. "The genesis of torsional drillstring vibrations". *SPE Drilling Engineering*, Vol. 7, No. 3, p. 168 – 174.

Cruz Neto, H.J. and Trindade, M.A., 2019. "On the noncollocated control of structures with optimal static output feedback: Initial conditions dependence, sensors placement, and sensitivity analysis". *Structural Control and Health Monitoring*, Vol. 26, No. 10, p. e2407.

Cruz Neto, H.J. and Trindade, M.A., 2023. "Control of drill string torsional vibrations using optimal static output feedback". *Control Engineering Practice*, Vol. 130, p. 105366.

Dwars, S., 2015. "Recent advances in soft torque rotary systems". In *SPE/IADC Drilling Conference and Exhibition*. SPE, London, England, UK. doi:10.2118/173037-ms.

Khalil, H., 2015. *Nonlinear Control*. Pearson, New York.

Kyllingstad, A. and Nessjoen, P., 2009. "A new stick-slip prevention system". In *SPE/IADC Drilling Conference*. SPE, Amsterdam, The Netherlands, p. 119660.

Kyllingstad, A., 2017. "A comparison of stick-slip mitigation tools". In *SPE/IADC Drilling Conference*. SPE, The Hague, The Netherlands. doi: 10.2118/184658-ms.

Levine, W. and Athans, M., 1970. "On the determination of the optimal constant output feedback gains for linear multivariable systems". *IEEE Transactions on Automatic Control*, Vol. 15, No. 1, pp. 44–48.

Mihajlović, N., Van Veggel, A., Van De Wouw, N. and Nijmeijer, H., 2004. "Analysis of friction-induced limit cycling in an experimental drill-string system". *Journal of Dynamic Systems, Measurement and Control, Transactions of the ASME*, Vol. 126, No. 4, p. 709 – 720.

Monteiro, H.L.S. and Trindade, M.A., 2017. "Performance analysis of proportional-integral feedback control for the reduction of stick-slip-induced torsional vibrations in oil well drillstrings". *Journal of Sound and Vibration*, Vol. 398, pp. 28–38.

Navarro-López, E. and Suárez, R., 2004. "Practical approach to modeling and controlling stick-slip oscillations in oilwell drillstring". In *Proceedings of the 2004 IEEE International Conference on Control Applications*. Taipei, Taiwan, pp. 1454–1460.

Placido, J., Santos, H. and Galeano, Y., 2002. "Drillstring vibration and wellbore instability". *Journal of Energy Resources Technology*, Vol. 124, pp. 217–222.

Runia, D., Dwars, S. and Stulemeijer, I., 2013. "A brief history of the shell "soft torque rotary system" and some recent case studies". In *SPE/IADC Drilling Conference*. Amsterdam, The Netherlands.

Saldivar, B., Mondié, S., Loiseau, J.J. and Rasvan, V., 2013. "Suppressing axial-torsional coupled vibrations in drillstrings". *Control Engineering and Applied Informatics*, Vol. 15, No. 1, pp. 3–10.

Saldivar, B., Mondié, S., Niculescu, S.I., Mounier, H. and Boussaada, I., 2016. "A control oriented guided tour in oilwell drilling vibration modeling". *Annual Reviews in Control*, Vol. 42, pp. 100–113. doi:10.1016/j.arcontrol.2016.09.002.

Schlumberger Ltd., 2006. "Shock and vibration in the drilling environment, tutorial video, 8min20s,". Http://www.slb.com/services/drilling.aspx.

Spanos, P., Chevallier, A., Politis, N. and Payne, M., 2003. "Oil and gas well drilling: A vibrations perspective". *The Shock and Vibration Digest*, Vol. 35, No. 2, pp. 85–103. doi:10.1177/0583102403035002564.

Trindade, M.A., 2020. "Robust evaluation of stability regions of oil-well drilling systems with uncertain bit-rock nonlinear interaction". *Journal of Sound and Vibration*, Vol. 483, p. 115481. doi:10.1016/j.jsv.2020.115481.

Tucker, R. and Wang, C., 1999. "On the effective control of torsional vibrations in drilling systems". *Journal of Sound and Vibration*, Vol. 224, No. 1, pp. 101–122.

RESPONSIBILITY NOTICE

Stick slip vibrations in drilling: modeling, estimation, avoidance

Jean Auriol – Université Paris-Saclay (France)
Nasser Kazemi – Université du Québec à Monréal (Canada)

Stick slip vibrations in drilling: modeling, estimation, avoidance

Jean Auriol[1] **and Nasser Kazemi**[2]

[1] Université Paris-Saclay, CNRS, CentraleSupélec, L2S, Gif-sur-Yvette, France.

[2] Université du Qubéc à Montréal, Department of Earth and Atmospheric Sciences, Montreal, Canada.

Abstract: This writeup presents a field-validated torsional model for the drill string dynamics and different algorithms for estimating the friction factors along the drill string and bottom hole rotational velocity. These friction terms characterize the interaction between the drill pipe and the wellbore walls (Coulomb source terms) within the curving wellbore. This information is essential to designing the next generation of stick-slip mitigation controllers, developing real-time wellbore monitoring tools, and enabling effective toolface control for directional drilling.

Keywords: drill-string vibrations, stick-slip, observer design, transformers

INTRODUCTION

Extraction of resources at depths greater than a few hundred meters in the earth's subsurface (oil, gas, minerals, and thermal energy) necessitates the drilling of long slender boreholes (from the surface to the subsurface target) that may induce deviated well paths with extensive horizontal sections (Sveinbjornsson and Thorhallsson, 2014; Wei *et al.*, 2022). Advanced drilling control strategies are essential for designing such complex wells, as undesirable vibrations can occur during transient off-bottom phases. Notably, torsional oscillations, which cause damage and reduce the rate of penetration, must be mitigated. This phenomenon, known as *stick-slip*, results from significant friction between the drill string and the borehole (Aarsnes *et al.*, 2018). To prevent such oscillations, advanced control approaches have been developed, incorporating the underlying distributed dynamics into controller design (Auriol *et al.*, 2022a). These control strategies have demonstrated faster convergence to a reference trajectory compared to state-of-the-art controllers while preventing stick-slip oscillations. They are based on the field-validated model presented in (Aarsnes and Shor, 2018) that accurately describes the evolution of angular velocity and torque $(\omega(t,x), \tau(t,x))$ along the drilling device using coupled hyperbolic Partial Differential Equations (PDEs). However, implementing such control laws requires knowledge of the distributed state along the drill string. In the field, available measurements are mainly surface data, such as surface RPM or motor torque. Additionally, these methods require all system parameters, particularly subsurface physical properties, to be known (Auriol *et al.*, 2019, 2021).

In this abstract, we present the high-fidelity model introduced by Aarsnes and Shor (2018) to describe torsional oscillations in the drilling device. We then show how this model can be used to design appropriate near real-time state observers. In particular, we present an adaptive observer (adjusted from (Aarsnes *et al.*, 2019)) and an innovative *dual architecture of physics-informed transformer-based neural networks* (Vaswani *et al.*, 2017). Indeed, recent advances have shown that deep neural networks can be used to learn distributed dynamics from measurements (Lu *et al.*, 2021). Finally, we briefly show how these estimations can be used to control the downhole behavior of the drill string while avoiding undesired oscillations.

TORSIONAL DYNAMICS OF THE DRILL STRING

This section introduces a hyperbolic PDEs model incorporating distributed friction terms to describe the torsional motion of drill string dynamics. The proposed high-fidelity model, detailed in (Aarsnes and Shor, 2018), has been validated against field data. Its computational simplicity makes it suitable for control and estimation applications. We assume that the torsional motion of the drill string is the dominating dynamic behavior (i.e., there is no distributed axial dynamics). Moreover, the effects of along-string cuttings distribution on the friction is assumed to be homogeneous and the transition from static to dynamic Coulomb friction is a jump, i.e., the Stribeck curve is assumed negligible. Finally, the bit is also assumed to be off-bottom, meaning there is no bit-rock interaction, which occurs during transient phases when the bit is not in contact with the rock, such as when adding a new pipe section to the drilling system or when removing the drill string from the borehole to address a failure. For $(t,x) \in [0,T] \times [0,L]$ (where $T > 0$ is the chosen time window and $L > 0$ is the length of the drilling device), we denote $\omega(t,x)$ the angular velocity and $\tau(t,x)$ the torque at any point of the drill string. The states satisfy the following equations

$$\frac{\partial \tau(t,x)}{\partial t} + JG \frac{\partial \omega(t,x)}{\partial x} = 0, \qquad J\rho \frac{\partial \omega(t,x)}{\partial t} + \frac{\partial \tau(t,x)}{\partial x} = \mathscr{S}(t,x), \qquad (1)$$

where J is the polar moment for inertia, G is the shear modulus, and ρ is the mass density, averaged for a drill string section and supposedly known. The source terms $\mathscr{S}$ is due to frictional contact with the borehole. It verifies

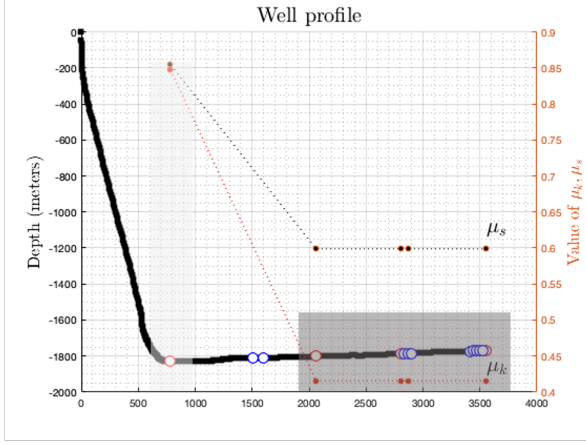$$\mathscr{S}(t,x) = -k_t \rho J \omega(t,x) - \mathscr{F}(t,x), \qquad (2)$$

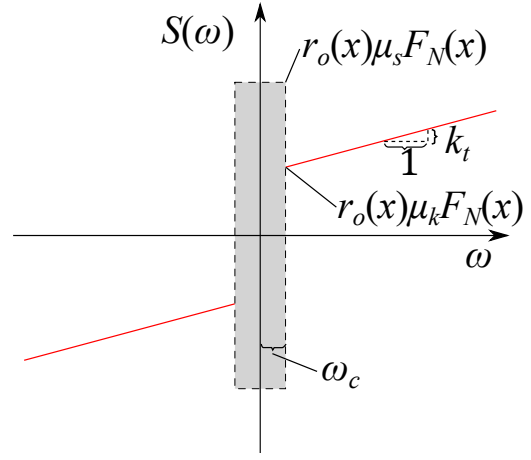Figure 1: Schematic indicating the distributed drill string lying in deviated bore-hole.

Figure 2: Friction source term $S(\omega,x)$. The red curve indicates the dynamic torque as a function of angular velocity.

where the damping constant k_t is the viscous shear stress and $\mathcal{F}$ is a differential inclusion that corresponds to the Coulomb friction between the drill string and the borehole, also known as the side force:

$$\begin{cases} \mathcal{F}(t,x) = \text{sign}(\omega(t,x))F_k(x), & |\omega(t,x)| > \omega_c, \\ \mathcal{F}(t,x) \in \pm r_o(x)\mu_s F_N(x), & |\omega(t,x)| \leqslant \omega_c, \end{cases} \quad (3)$$

where the function $\mathcal{F}(\omega) = -\frac{\partial \tau(t,x)}{\partial x} \in \pm r_o(x)\mu_s F_N(x)$ is the differential inclusion. The functions $F_k(x) \doteq r_o(x)\mu_k F_N(x)$ (resp. $F_s(x) \doteq r_o(x)\mu_s F_N(x)$) corresponds to the dynamic (resp. static) Coulomb torque. The expression of the normal force acting between the drill string and the borehole wall $F_N(x)$ depends on the well geometry (Sheppard *et al.*, 1987). While the outer drill string radius $r_o(x)$ is known, the static and kinetic friction coefficients (μ_s, μ_k) and the angular velocity threshold ω_c are not. At the surface level, the top drive is actuated by an electrical motor that imparts torque to the drill string. The evolution of the angular velocity at the surface level and the downhole torque follows

$$\frac{d}{dt}\omega(t,0) = \frac{1}{I_{TD}}(\tau_m(t) - \tau(t,0)), \quad \tau(t,L) = 0 \quad (4)$$

where I_{TD} corresponds to the top-drive inertia and τ_m to the motor torque. We denote $\omega_0(t) = \omega(t,0)$ the top-drive angular velocity. The motor torque corresponds to the control input and may be expressed as a PI feedback (Åström and Murray, 2010): i.e. $\tau_m = k_p(\omega_{SP} - \omega_{t,0}) + k\int_0^t(\omega_{SP}(\xi) - \omega_{t,0}(\xi))d\xi$, where ω_{SP} is a desired reference set-point, k_p is a proportional gain and k an integral gain. It can also be defined through more advanced control strategies (as shown in (Aarsnes *et al.*, 2018; Auriol *et al.*, 2022a)). However, such advanced mitigation laws require knowledge of the entire distributed angular state. In the field, we typically have access only to the top-drive angular velocity and the motor torque $(\omega(t,0), \tau_m(t))$ measured with a frequency of $1Hz$. Therefore, it is necessary to reconstruct the entire state from these measurements, as proposed in (Aarsnes *et al.*, 2019). Reconstructing the state may also require knowledge of unknown physical parameters, such as static and kinetic friction coefficients. In the following, we denote $Y = (P, \{(\omega(t,0), \tau_m(t))_{i\in[1,N]}\}) \in \mathcal{Y} = \mathbb{R}^{N_p} \times \mathbb{R}^{2\times N}$ an input data containing a set of N_p known physical parameters (depth of bit L, collar and pipes mechanical properties) concatenated in the vector P and N sequential pairs of surface measurements.

STATE ESTIMATION

The design of the next generation of stick-slip mitigation controllers requires reliable estimations of the state and friction parameters. More precisely, our objective is twofold: Estimate the physical parameters (μ_s, μ_k) and the distributed state $(\omega(t,x), \tau(t,x))$ from the surface data. In this section, we present different methods (adjusted from Auriol *et al.* (2022b)) to estimate all (or part) of the friction parameters.

First approach: Adaptive observer

The first approach we propose is adapted from the adaptive state observer introduced in (Aarsnes *et al.*, 2019). This observer integrates measurements from physical sensors, particularly the top-drive angular velocity ω_0, with the proposed system dynamics model. It provides reliable estimates of the torque and RPM states as well as the side forces friction parameters when the bit is off-bottom (Aarsnes *et al.*, 2019). Here, we summarize the main ideas of this observer. Denote

with the $\hat{\cdot}$ superscript the estimated states and $e(t) = \hat{\omega}_0(t) - \omega_0(t)$ the measured estimation error of the top-drive angular velocity. The observer equations given in (Aarsnes *et al.*, 2019) correspond to a copy of the original dynamics expressed in the Riemann coordinates, to which are added output correction terms. The Riemann invariants are the states corresponding to a transformation of the system which has a diagonalized transport matrix. We define them as $\alpha = \omega + \frac{1}{J\sqrt{G\rho}}\tau$ and $\beta = \omega - \frac{1}{J\sqrt{G\rho}}\tau$. The observer equations read as follows

$$\dot{\hat{\omega}}_0 = a_0\left(\hat{\beta}_p(t,0) - \hat{\omega}_0\right) + \frac{1}{I_{TD}}\tau_m - p_0 e(t), \tag{5}$$

$$\frac{\partial\hat{\alpha}}{\partial t}(t,x) + c_t\frac{\partial\hat{\alpha}}{\partial x}(t,x) = \hat{\mathscr{S}}(t,x) - p_\alpha(t,x)e(t), \qquad \frac{\partial\hat{\beta}}{\partial t}(t,x) - c_t\frac{\partial\hat{\beta}}{\partial x}(t,x) = \hat{\mathscr{S}}(t,x) - p_\beta(t,x)e(t), \tag{6}$$

where $c_t = \sqrt{\frac{G}{\rho}}$. The source term in each section is computed from the estimated states and friction factors $\hat{\mathscr{S}}(t,x) = k_t(\hat{\alpha}(t,x) + \hat{\beta}(t,x)) + \frac{1}{J\rho}\hat{\mathscr{F}}(t,x)$ where $\hat{\mathscr{F}}$ has an expression identical to (3), the different variables being replaced by their estimates. The different boundary conditions are now expressed as $\hat{\alpha}(t,0) = 2\hat{\omega}_0(t) - \hat{\beta}(t,0) - P_0 e(t)$, $\hat{\beta}(t,L) = \hat{\alpha}(t,L)$, and the estimates of the friction factor are updated according to

$$\dot{\hat{\mu}}_s(t) = \begin{cases} -l_s e(t), & |\min_x \hat{\omega}(t,x)| \leqslant \omega_c, \\ 0, & |\min_x \hat{\omega}(t,x)| > \omega_c, \end{cases} \quad \dot{\hat{\mu}}_k(t) = \begin{cases} 0, & |\min_x \hat{\omega}(t,x)| \leqslant \omega_c, \\ l_k e(t), & |\min_x \hat{\omega}(t,x)| > \omega_c, \end{cases} \tag{7}$$

Finally, we use a saturation to improve the robustness of the approach: $\hat{\mu}_s = \max(\hat{\mu}_s, \hat{\mu}_k)$. The different constants and observer gains $a_0, p_\alpha, p_\beta, p_0, p_1, P_0, P_1, l_s, l_k$ can be found in (Aarsnes *et al.*, 2019). As shown in (Aarsnes *et al.*, 2019), the convergence is guaranteed in the absence of friction term. Moreover, the proposed procedure is robust to uncertainties and delays and provides correct estimations of μ_k and μ_s when tested in simulations and against field data. However, it requires the knowledge of ω_c, and there is no proof of convergence for the adaptive part.

Second approach: transformer-based dual architecture network

We now present a learning methodology based on a *dual architecture*, originally introduced in Redaud *et al.* (2024). A first transformer-based neural network (using Y as input) estimates the physical parameters (μ_s, μ_k). We opted for transformers (Vaswani *et al.*, 2017) instead of recurrent neural networks to enhance speed and reduce the computational cost of training. The estimated physical parameters (μ_s, μ_k) and the input Y are then fed into a second transformer-based neural network, which aims to provide the distributed state $(\omega(t,x), \tau(t,x))$. Following (Raissi *et al.*, 2019; Sun *et al.*, 2021), we incorporate physical laws into the training loss functions to improve the performance of the estimation algorithms. The output of the first network is required to compute loss functions. Both networks are trained simultaneously using an extensive simulated training dataset. The proposed network is schematically illustrated in Figure 5.

Estimation of physical parameters

The first neural network aims at estimating the physical parameters $M = (\mu_k, \mu_s) \in \mathbb{R}^2$. It is a transformer (Vaswani *et al.*, 2017) characterized by trainable parameters θ, and denoted $T_\theta(.)$. It aggregates the sequence of inputs $Y \in \mathbb{R}^{N_p+2N_t}$ and gives as an output $\hat{M} \in \mathbb{R}^2$. We obtain θ by minimizing the L_2- loss function $\mathscr{L}_{L_2}(\theta) = \frac{1}{N_b}\sum_{i=1}^{N_b}\|M - T_\theta(Y)\|_2^2$.

Estimation of the distributed state

Inspired by (Lu *et al.*, 2021), we tackle the second objective using a two-branch architecture. Denote $\mathscr{X} = [0,L]$ as the spatial domain and $\mathscr{T} = [0,T]$ as the temporal domain where the state is defined. We aim to select the most appropriate state representation concerning physical constraints using sets of discrete inputs Y. Therefore, we approximate

$$S: \begin{array}{ccc} \mathscr{Y} & \longrightarrow & \mathscr{C}^\infty(\mathscr{T}\times\mathscr{X}, \mathbb{R}^2) \\ Y & \mapsto & S_{Y,\Theta}(\cdot,\cdot) \end{array},$$

where $\mathscr{C}^\infty$ is the set of infinitely differentiable functions from $\mathscr{T}\times\mathscr{X}$ to $\mathbb{R}^2$ (the regularity could be leveraged). This defines a class of parametric functions $S_{Y,\Theta}$, which we use for approximating the real states $(\omega(t,x), \tau(t,x))$. The corresponding approximations is denoted as $(\hat{\omega}(t,x), \hat{\tau}(t,x))$. In our design, the first branch of the proposed architecture relies on a transformer encoder to aggregate the input sequences Y augmented with $\hat{M}$. This produces an abstract representation of the system when combined with an abstract representation of the requested coordinates. Inspired by Fourier Neural Operators (Li *et al.*, 2021), this abstract representation is then used to output the intensity, frequency, and phase of the Fourier decomposition representing the distributed state $X(t,x) \doteq (\omega(t,x), \tau(t,x))$ along the drill string. The second branch constructs the spatiotemporal grid mesh $(t,x) \in \mathscr{T}\times\mathscr{X}$, where the estimation is evaluated.

Physic-informed neural networks

Following (Sun *et al.*, 2021; Wang *et al.*, 2021), we define the composite loss $\mathscr{L}(\Theta) = \mathscr{L}_{\mathscr{D}}(\Theta) + \mathscr{L}_{\text{PDE}}(\Theta) + \mathscr{L}_{\text{BC}}(\Theta)$. The term $\mathscr{L}_{\mathscr{D}}$ is the usual error term when training a neural network on a dataset. It corresponds to the

state estimation residual in the squared L_2-norm. The term $\mathscr{L}_{\text{PDE}}$ ensures that (1) is satisfied. Finally, the last term $\mathscr{L}_{\text{BC}}$ guarantees that the solution meets the boundary condition. More precisely, we have

$$\mathscr{L}_{\mathscr{D}}(\Theta) = \frac{1}{N_x}\frac{1}{N_t}\frac{1}{N_b}\sum_{i=1}^{N_b}\sum_{j=1}^{N_x}\sum_{k=1}^{N_t}\|X(t_k,x_j) - S_{Y,\Theta}(t_k,x_j)\|_2^2,$$

$$\mathscr{L}_{\text{PDE}}(\Theta) = \frac{1}{N_x}\frac{1}{N_t}\frac{1}{N_b}\sum_{i=1}^{N_b}\sum_{j=1}^{N_x}\sum_{k=1}^{N_t}\|\mathscr{O}(f_{Y,\Theta}(t_k,x_j))\|_2^2, \quad \mathscr{L}_{\text{BC}}(\Theta) = \frac{1}{N_t}\frac{1}{N_b}\sum_{i=1}^{N_b}\sum_{k=1}^{N_t}\|\mathscr{B}(S_{Y,\Theta}(t_k))\|_2^2 + |\hat{\tau}(t_k,L)|^2,$$

with $\mathscr{B}(S_{Y,\Theta}(t)) = \frac{\partial\hat{\omega}}{\partial t}(t,0) - \frac{1}{I_{TD}}(\tau_m(t) - \hat{\tau}(t,0))$ and $\mathscr{O}(S_{Y,\Theta}(t,x)) = \begin{pmatrix} \frac{\partial\hat{\tau}}{\partial t}(t,x) + JG\frac{\partial\hat{\omega}}{\partial x}(t,x) \\ \frac{\partial\hat{\tau}}{\partial x}(t,x) + J\rho\frac{\partial\hat{\omega}}{\partial t}(t,x) - \mathscr{S}(\hat{\omega},x) \end{pmatrix}$. This machine-learning approach is reliable and easy to implement. It consists of a fast algorithm (once properly trained) that provides good estimations of the friction parameters and the state. The data and physics-driven losses add *a priori* knowledge of the underlying dynamics (1)-(4) during training. However, the proposed approach requires thousands of training points and may lack generalizability as it depends on the model and the initial condition of the system.

CONTROLLER DESIGN

During the drilling process, the operator usually wants to control the downhole behavior of the drill string and optimize the Rate Of Penetration (ROP) while avoiding undesired oscillations. More precisely, the main control objective is to regulate the downhole angular velocity at the start-up of a drilling operation (e.g., after a connection) to avoid entering a stick-slip limit cycle. Most of the controllers applied in industrial applications correspond to high-gain PI control laws, such as the SoftSpeed and SoftTorque approaches. These approaches are easy to implement and analyze since the gains are tuned to obtain a certain reduction in the proximal reflection coefficient over a limited frequency range. However, they may present several fundamental limitations, such as possible poor inherent robustness margins (which can be overcome using impedance matching controllers such as ZTorque (Dwars, 2015)) or the generation of significant oscillations when changing the set-points. Advanced control methods have been proposed in (Auriol *et al.*, 2022a), leading to better performance but requiring real-time estimation. Below, we summarize the main ideas behind the approaches proposed in (Auriol *et al.*, 2022a) and detail their corresponding requirements, limitations, and performance. In these control strategies, the effect of the friction terms is seen as a distributed source term $d(t)$ that needs to be compensated.

1. **ZTorque and feed-forward controller.** A feedforward controller that can be seamlessly integrated with standard industry ZTorque impedance matching feedback controllers without affecting the closed-loop behavior has been proposed in (Aarsnes *et al.*, 2018). This control law adheres to the 3DOF controller architecture (Åström and Murray, 2010), as it has three components: a feedback term, a feedforward term (leveraging the model's differential flatness), and a disturbance cancellation term. This approach is a state-of-the-art controller and requires the knowledge of top-drive torque and estimation of the disturbance term. The feedforward component and disturbance compensation term reduce residual oscillations but may induce overshoots and long convergence times.

2. **Multiplicity Induced Dominancy Controller.** This approach involves analyzing the transfer function between the downhole velocity and the actuator. This transfer function represents a time-delay system for which we can design a control law that ensures the placement of the dominant root in the complex plane, thereby guaranteeing the stability of the closed-loop system. This approach requires the estimation of downhole velocity and disturbance terms. It is robust with respect to parameter uncertainties and exhibits slight overshoot and oscillations with a low computational effort. However, it may be sensitive to noise.

3. **Recursive dynamics interconnection framework.** This procedure is well-suited for multi-sectional drilling devices. For each section, we find the virtual input that stabilizes the section and guarantees that the output converges towards the virtual input of the next subsystem. The virtual input of the last subsystem (downhole ODE) is chosen to guarantee the tracking of the reference signal. It requires a reliable estimation of the disturbance term and predictions of the states. As it consists of a direct compensation of the disturbance term, it can guarantee a fast convergence without residual oscillations at the cost of an instantaneous high-control effort. All in all, it is a complex control algorithm with an extensive computational cost.

EXPERIMENTAL SETTING

In this section, we illustrate the performance of the proposed transformer-based observer and of the ZTorque and feedforward controller with simulations.

Generation of dataset and Training parameters

To train and validate our estimation algorithm, we generate a wide dataset following the numerical scheme presented in (Aarsnes and Shor, 2018). To obtain representative data, we use the real well geometry (J1), illustrated in Figure 1.
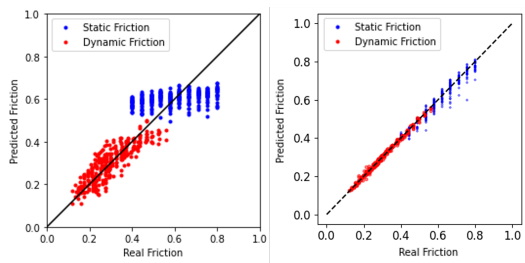
Figure 3: Estimation of (μ_k, μ_s) using (Auriol *et al.*, 2022b) (left) and the transformer approach (right).
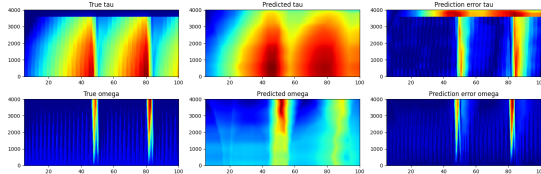

Figure 4: Example of a prediction for a sample of the validation set after training.

We generated 1000 sequences of 100s of 20Hz surface measurements (motor torque and surface angular velocity), for $L \in [2500, 4000]$m, $\mu_s \in [0.2, 0.8]$, $\mu_k \in [0.06, 0.72]$. The reference trajectory is constant (60 RPM with slope). The implemented control input is ZTorque with a feed-forward component. The dataset is split $80\% - 20\%$ as training and validation datasets. To obtain the parameters (θ, Θ) minimizing the losses $\mathscr{L}_{L_2}(\theta), \mathscr{L}(\Theta)$, we use AdamW (Loshchilov and Hutter, 2017) with an initial learning rate of 10^{-3}. The training is done on 100 epochs, with a batch size $N_b = 16$. We use automatic differentiation techniques (Baydin *et al.*, 2015) to compute the derivatives.

Simulation results

Both networks are trained simultaneously on a comprehensive dataset of simulated data based on the proposed well geometry. The trained neural networks' performance is then evaluated using a separate validation dataset, as detailed in (Auriol *et al.*, 2022b). We compare these results with the estimations obtained from the convolutional neural network-based approach presented in (Auriol *et al.*, 2022b). The friction coefficients were estimated on the validation dataset with an average relative error of $\delta(\mu_k) = 2.3\%$ (resp. $\delta(\mu_s) = 3.3\%$) and a standard deviation of $5.2e^{-3}$(resp. $1.8e^{-2}$) after 2500 steps. As illustrated in Figure 3, our proposed method outperformed the existing estimation methods presented in (Auriol *et al.*, 2022b), as the standard deviation is reduced, and the average estimated value is closer to the true value.

We also obtained promising results for the state estimation with an average absolute error of 2.3 on 200 validation examples. We have plotted in Figure 4 the obtained estimation for τ and ω and compared them with their real values. We used color plots to picture these 2D data (red corresponding to higher values, the horizontal axis being time, and the vertical axis being the curvilinear abscissa). As expected, the solutions predicted by the proposed networks are consistent with the physics. Finally, we illustrate in Figure 6 how this observer can be combined with the ZTorque feedback controller with a flatness trajectory planning feed-forward component to stabilize the system around different set-points. In the considered scenario, the lowest part of the drilling device (collar and BHA) is almost horizontal, and the stationary drill string is initially kept in place by the Coulomb friction until enough torque is built up to overcome it. The different physical parameters can be found in Auriol *et al.* (2022a).

CONCLUSIONS

We presented a field-validated torsional model for drill string dynamics. We then introduced two algorithms to estimate the friction factors along the drill string, providing an estimate of the bottom hole rotational velocity. These observers were then used to design the next generation of stick-slip mitigation controllers. Future improvements include reducing the numerical complexity of the different control strategies and a better online adaptive estimation of the disturbance term. The current architecture for the machine learning observer includes hyperparameters that can be optimized to enhance performance, e.g., by balancing the empirical loss of model predictions, model complexity, and physical loss.

REFERENCES

Aarsnes, U.J.F., Auriol, J., Di Meglio, F. and Shor, R., 2019. "Estimating friction factors while drilling". *Journal of Petroleum Science and Engineering*, Vol. 179, pp. 80–91.

Aarsnes, U.J.F., Di Meglio, F. and Shor, R.J., 2018. "Avoiding stick slip vibrations in drilling through startup trajectory design". *Journal of Process Control*, Vol. 70, pp. 24–35.

Aarsnes, U.J.F. and Shor, R.J., 2018. "Torsional vibrations with bit off bottom: Modeling, characterization and field data validation". *Journal of Petroleum Science and Engineering*, Vol. 163, pp. 712–721.

Åström, K.J. and Murray, R.M., 2010. *Feedback systems: an introduction for scientists and engineers*. Princeton university press, 2nd edition. ISBN 9780691135762.

Auriol, J., Boussaada, I., Shor, R.J., Mounier, H. and Niculescu, S.I., 2022a. "Comparing advanced control strategies to eliminate stick-slip oscillations in drillstrings". *IEEE access*, Vol. 10, pp. 10949–10969. ISSN 2169-3536.
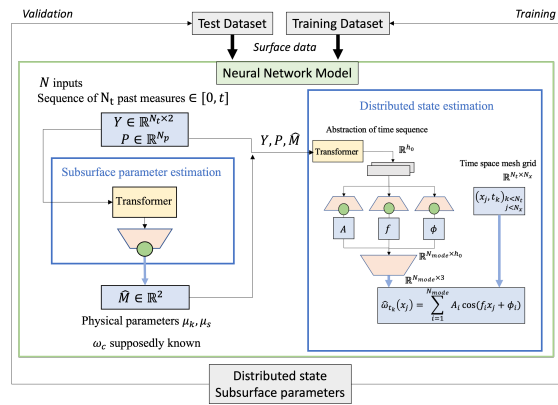
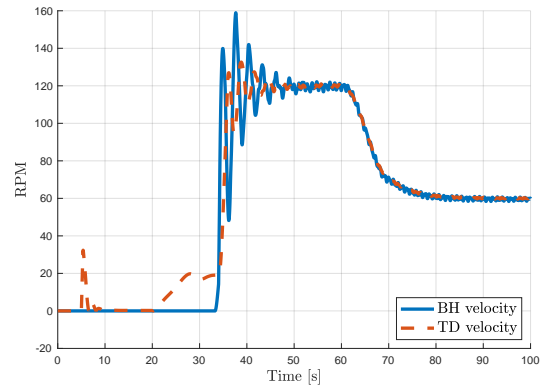Figure 5: Detailed view of the neural network architecture.

Figure 6: Response to velocity set-point changes using a ZTorque feedback controller with a flatness trajectory planning feed-forward component (depth=1800m).

Auriol, J., Shor, R., Niculescu, S.I. and Kazemi, N., 2022b. "Estimating drill string friction with model-based and data-driven methods". In *2022 American Control Conference (ACC)*. pp. 3464–3469.

Auriol, J., Kazemi, N. and Niculescu, S.I., 2021. "Sensing and computational frameworks for improving drill-string dynamics estimation". *Mechanical Systems and Signal Processing*, Vol. 160, p. 107836.

Auriol, J., Kazemi, N., Shor, R.J., Innanen, K.A. and Gates, I.D., 2019. "A sensing and computational framework for estimating the seismic velocities of rocks interacting with the drill bit". *IEEE Transactions on geoscience and remote sensing*, Vol. 58, No. 5, pp. 3178–3189.

Baydin, A., Pearlmutter, B., Radul, A. and Siskind, J.M., 2015. "Automatic differentiation in machine learning: a survey".

Dwars, S., 2015. "Recent Advances in Soft Torque Rotary Systems". In *Proceedings of 2015 SPE/IADC Drilling Conference*. March, pp. 17–19.

Li, Z., Kovachki, N., Azizzadenesheli, K., Liu, B., Bhattacharya, K. and Stuart, A., 2021. "Fourier neural operators for parametric partial differential equations". p. 16.

Loshchilov, I. and Hutter, F., 2017. "Decoupled weight decay regularization". doi:10.48550/ARXIV.1711.05101.

Lu, L., Jin, P. and Karniadakis, G.E., 2021. "DeepONet: Learning nonlinear operators for identifying differential equations based on the universal approximation theorem of operators". *Nature Machine Intelligence*, Vol. 3, No. 3, pp. 218–229.

Raissi, M., Perdikaris, P. and Karniadakis, G.E., 2019. "Physics-informed neural networks: A deep learning framework for solving forward and inverse problems involving nonlinear partial differential equations". *Journal of Computational physics*, Vol. 378, pp. 686–707.

Redaud, J., Darrin, M., Kazemi, N. and Auriol, J., 2024. "Physics-informed dual architecture neural networks for enhanced estimation of drilling dynamics". In *IGARSS, IEEE International Geoscience and Remote Sensing Symposium*. Vol. to appear.

Sheppard, M.C., Wick, C. and Burgess, T., 1987. "Designing Well Paths To Reduce Drag and Torque". *SPE Drilling Engineering*, Vol. 2, pp. 344–350.

Sun, J., Innanen, K.A. and Huang, C., 2021. "Physics-guided deep learning for seismic inversion with hybrid training and uncertainty analysis". *GEOPHYSICS*, Vol. 86, No. 3, pp. R303–R317.

Sveinbjornsson, B.M. and Thorhallsson, S., 2014. "Drilling performance, injectivity and productivity of geothermal wells". *Geothermics*, Vol. 50, pp. 76–84.

Vaswani, A., Shazeer, N., Parmar, N., Uszkoreit, J., Jones, L., Gomez, A.N., Kaiser, L. and Polosukhin, I., 2017. "Attention is all you need". doi:10.48550/ARXIV.1706.03762.

Wang, S., Wang, H. and Perdikaris, P., 2021. "Learning the solution operator of parametric partial differential equations with physics-informed DeepONets". *Science Advances*, Vol. 7, No. 40, p. 8605.

Wei, C., Mao, L., Yao, C. and Yu, G., 2022. "Heat transfer investigation between wellbore and formation in U-shaped geothermal wells with long horizontal section". *Renewable energy*, Vol. 195, pp. 972–989. ISSN 0960-1481.

Examples of Downhole Tools Lateral Dynamics Modeling in Frequency and Time Domains

Mohamed Mahjoub – Helmerich & Payne (France)
Khac-Long Nguyen – Helmerich & Payn (France)
Ngoc-Ha Dao – Helmerich & Payn (France)
Stéphane Menand – Helmerich & Payne (USA)

Examples of Downhole Tools Lateral Dynamics Modeling in Frequency and Time Domains

Mohamed Mahjoub [1], Khac-Long Nguyen [1], Ngoc-Ha Dao [1], and Stéphane Menand [2]

[1] Helmerich & Payne, Villeurbanne, France

[2] Helmerich & Payne, Houston, TX, USA

Abstract: Understanding and mitigating lateral drill string vibration is a long-standing challenge not only because of its consequences on drilling performance and downhole equipment lifetime, but also because of its complexity in terms of modeling. The bottom hole assembly (BHA) lateral dynamics is highly nonlinear namely due to the string-wellbore contact and friction forces. The presence of special tools in the BHA with custom geometries and materials makes the modeling even more complex. In this work, we focus on three examples of tools and how their detailed characteristics can affect the BHA vibration. First, the rotor/stator relative motion in mud motors is analyzed in terms of mass imbalance and excitation frequency. Second, the importance of stabilizers' detailed geometry is shown. Namely, the effect of blade count, spirality, and width on contact forces and acceleration levels is presented. Finally, the dampening capabilities of some tools with special non-elastic materials is investigated. To do that, we rely on two types of modelling: a linearized frequency-domain analysis in the form of a forced vibration approach, and a more complex nonlinear time-domain analysis. The first type allows to get fast answers, which can be practical for BHA design comparisons and optimization, whereas the second type allows to get a more in-depth picture of BHA dynamics but at the cost of computation time. The use of both models offers a complimentary combination for understanding and mitigation.

Keywords: modeling, dynamics, downhole tools, drill string

INTRODUCTION

During the drilling process, the drill string can vibrate in the axial, torsional, and lateral directions due to the various external loads, like string-wellbore contact and friction, string-fluid interaction, and bit-rock cutting forces, the choice of the operating parameters, namely weight on bit (WOB), surface rotation speed, and flow rate, and the design of the drill string itself, including the bottom hole assemble (BHA), the size of drill pipes, and the choice of the drill bit. Depending on the operating parameters and the current rock formation engaged by the bit, these three directions of vibration can occur separately or simultaneously and can be strongly coupled or with a dominant direction. Also, depending on the nature of vibration, low or high frequency, the drill string's length, and the level of tortuosity in the well trajectory, some downhole dysfunctions or suboptimal drilling conditions may or may not be detected from the real-time surface measurements. Namely, lateral vibrations occurring at the BHA are likely to be dissipated by the contact and friction forces along the drill string and become difficult to measure directly at surface. Modeling and numerical simulations of this type of dynamics can be an interesting tool to better understand the origin of vibrations and attempt to mitigate them, either by finding optimal operating parameters or improving the BHA design.

The modeling of lateral dynamics is generally focused on the BHA part where shocks on sensitive and costly downhole tools is the most critical. It involves the complexity of nonlinear external lateral loads, especially the contact and friction forces, and the design particularities of some downhole tools like mud motors, stabilizers, and dampening tools. The most complete modeling approach consists in solving the nonlinear dynamics equation of motion in the time-domain (see for example Heisig and Neubert 2000, Mahjoub et al. 2020, and Wilson and Noynaert 2016). With this method, different scenarios can be tested with variable inputs and different sources of excitations allowing to mimic the reality. This requires however an intense workload to calibrate the different model unknown parameters (like friction coefficients) and, depending on the simulation complexity, long computation time.

The use of forced vibration computations represents an interesting and computationally efficient approach to study the lateral BHA vibrations (see Bailey et al. 2010 and Nguyen et al. 2022). This requires the identification of the main sources of excitations and their frequency in relation to the surface, motor, and bit rotation speeds (see for instance Besaisow & Payne 1988 and Harvey and Wassell 1991). The magnitude of these excitation can be related to the WOB for example in the case of cutting forces due the bit-rock interaction, or to a mass imbalance due to the internal geometry of downhole tools like mud motors.

In the first section of this paper, the dynamics equation of motion of the drill string is recalled both in time and frequency domains. In the second section, three examples of downhole tools' impacts on BHA vibration are examined: (i) a detailed description of the contact forces at spiral bladed stabilizers; (ii) the mud motor mass imbalance due to rotor/stator relative motion; and (iii) an example of downhole dampening tool effect with different placements in the BHA. Finally, the last section is dedicated to concluding remarks.

DRILL STRING DYNAMICS EQUATIONS IN TIME AND FREQUENCY DOMAINS

Time-domain formulation

Using the finite element method, the drill string can be discretized into a series of beam elements with two nodes each. In the general 3D case, each node is characterized by three displacements (1 axial and 2 lateral) and 3 rotations (1 torsional and 2 bending). These 6 degrees of freedom (DOFs) can be called generalized displacements for convenience to avoid distinguishing between displacements and rotations. After writing the equation of motion of each element, and assembling the adjacent elements based on their common nodes, the drill string equation of motion can be written in the following matrix form:

$$\boldsymbol{M}\ddot{\vec{X}} + \boldsymbol{C}\dot{\vec{X}} + \boldsymbol{K}\vec{X} = \vec{F}\left(t, \vec{X}, \dot{\vec{X}}\right) \tag{1}$$

where $\boldsymbol{M}$, $\boldsymbol{C}$, and $\boldsymbol{K}$ are respectively the mass, damping, and stiffness matrices, $\vec{X}$ is the vector of the generalized displacements of all the nodes of the drill string, and $\vec{F}$ is the vector of generalized external forces (forces and moments) acting on the drill string. This englobes constant forces, like gravity, and time dependent forces, like contact and friction forces and bit-rock interaction forces.

Frequency-domain formulation

Solving Eq. (1) in the time-domain can provide interesting results by numerically mimicking different scenarios, where the different inputs (rotation speed, weight on bit, …) can change with time. This yields however to computationally challenging simulation that require important computing power and time. An alternative is switch to a simpler resolution in the frequency domain by removing the nonlinearities of the original equation, namely that of the external contact and friction forces. This can be achieved by computing the Jacobian matrix of these forces around an initial state $\left\{t_0, \vec{X}_0, \dot{\vec{X}}_0\right\}$ leading to the following linear forced vibration formulation:

$$\boldsymbol{M}\ddot{\vec{X}} + \left(\boldsymbol{C} - \frac{\partial \vec{F}\left(t, \vec{X}, \dot{\vec{X}}\right)}{\partial \dot{\vec{X}}}\bigg|_{t_0, \vec{X}_0, \dot{\vec{X}}_0}\right)\boldsymbol{C}\dot{\vec{X}} + \left(\boldsymbol{K} - \frac{\partial \vec{F}\left(t, \vec{X}, \dot{\vec{X}}\right)}{\partial \vec{X}}\bigg|_{t_0, \vec{X}_0, \dot{\vec{X}}_0}\right)\vec{X} = \vec{F}_e \sin(\omega_e t) \tag{2}$$

In this equation, the second member consists of a harmonic force with a magnitude $\vec{F}_e$ and pulsation ω_e. This equation can be solved then for different configurations where the harmonic force can be varied to examine different sources of excitations, like BHA or mud motor mass imbalances or cutting process forces. The excitation pulsation ω_e is generally related to the surface rotation speed, allowing to investigate the stability of BHAs in a range of operating rotation speeds.

Another simpler option also commonly used in the industry to analyze lateral vibrations is to assume dynamic nodes at the stabilizers and sleeves and to cut the BHA at a certain effective length. Compared to Eq. (2), the Jacobian matrices are not considered, but the total DOFs of the system is reduced by blocking the lateral displacements of the nodes.

APPLICATION TO EXAMPLES OF DOWNHOLE TOOLS

Spiral bladed stabilizer

Most of the stabilizers used in drilling are made of spiral blades, with distinction in terms of number, length, width, and spirality of blades that change from one manufacturer to another and from one application to another. The helical shape of the spiral blades is characterized by the spirality corresponding to the inverse of the helix pitch. We note that zero spirality corresponds to straight blades. We can also define the spiral angle as the rotation of one blade along the blade length:

$$\text{Spiral angle} = \text{Spirality} \times \text{Blade length} = \frac{\text{Blade length}}{\text{Pitch}} \tag{5}$$

The spirality is related to the wrap angle presented in API Specification 7-1. The wrap angle is the total angular extent of full blade diameter, summed across all blades. It can be expressed via the blade characteristics as:

$$\text{Wrap angle} = \text{Number of blades} \times \left(\frac{\text{Blade width}}{\text{Blade radius}} + \text{Spiral angle}\right) \tag{6}$$

The model used to analyze the performance of these stabilizers is introduced in the work of Nguyen et al. 2023. Distributed contact forces between the stabilizer and the wellbore are modeled to study the influence of the design characteristics on lateral vibrations. For a given cross-section of the bladed zone of a stabilizer (see Figure 1a), two situations are possible: the first situation (Figure 1b) corresponds to the case where only one blade is in contact with the wellbore; and the second situation (Figure 1c) corresponds to the case where the edges of two consecutive blades can be in contact.

In the first situation, the radial displacement vector $\vec{r}$ of the stabilizer's center falls within a blade width. The normal contact force $\vec{F}_{cn}$, friction force $\vec{F}_{ct}$ and torque $\vec{T}$ can then be defined by

$$\vec{F}_{cn} = f_{cr}\vec{e}_r, \quad \vec{F}_{ct} = \mu_t f_{cr}\vec{e}_t, \quad \vec{T} = R_b\vec{e}_r \wedge (\vec{F}_{cn} + \vec{F}_{ct}) \tag{7}$$

where f_{cr} is the normal contact force magnitude, R_b and R_w denote, respectively, the stabilizer and well radii, $\vec{e}_r = \vec{r}/\|\vec{r}\|$ and $\vec{e}_t = \vec{e}_z \times \vec{e}_r$ are respectively the radial and tangential directions based on the stabilizer's radial displacement, and μ_t is the tangential friction.

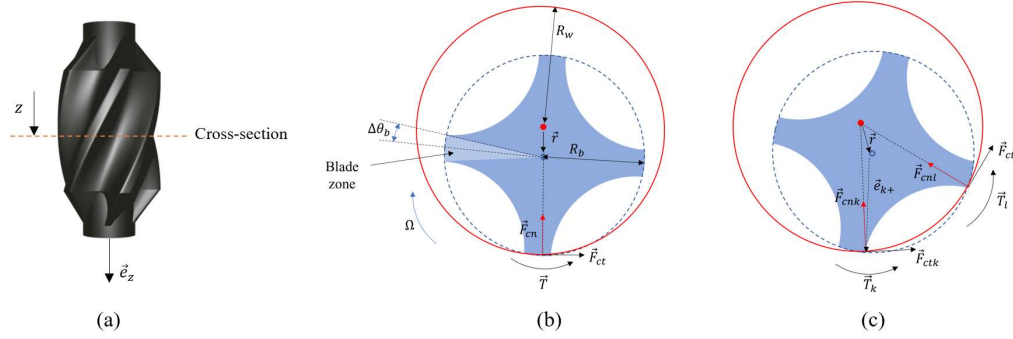(a)   (b)   (c)

Figure 1 – Schematic representation of the two possible contact configurations at a cross-section of the bladed stabilizer. (a) Axial position of the cross-section, (b) One blade in contact with the wellbore, (c) Two consecutive blades in contact with the wellbore.

For the second situation, two consecutive blades k and l can be in contact with the wellbore. The total contact forces and torque applied to the stabilizer are then the sum of those applied to each blade. For the blade k, the displacement of its edge is given by:

$$\vec{r}_k = \vec{r} + R_b\vec{e}_{k+}, \quad \vec{e}_{k+} = [\cos(\theta_{bk} + \Delta\theta_b), \sin(\theta_{bk} + \Delta\theta_b), 0]^T \tag{8}$$

where $\Delta\theta_b$ is the angle corresponding to the blade width, θ_{bk} is the blade angle position in the cross-section plane defined by $\theta_{bk} = \theta_{zk} + (k-1)\frac{2\pi}{N} + \xi z$, with θ_{zk} being the rotation angle of this blade around the axial direction $\vec{e}_z$, N the blade number, z the axial position of the cross-section in the stabilizer's bladed zone, and ξ is blade spirality. Like the first situation, the normal contact force, friction, and torque at the edge of the blade k can be written as follows:

$$\vec{F}_{cnk} = f_{cr,k}\vec{e}_k, \quad \vec{F}_{ctk} = \mu_t f_{cr,k}\vec{e}_t, \quad \vec{T}_k = R_b\vec{e}_{k+} \wedge (\vec{F}_{cnk} + \vec{F}_{ctk}) \tag{9}$$

where $f_{cr,k}$ is the corresponding normal contact force magnitude, $\vec{e}_k = \vec{r}_k/\|\vec{r}_k\|$.

To showcase the importance of the stabilizer geometry on vibration, an example of a 5-bladed 12 7/32 in. stabilizer placed in a placed in 12 ¼ in. horizontal wellbore is considered. As shown in Figure 2, different levels of spirality are considered, from straight geometry (0 spirality angle) to an extreme (nonrealistic) case with 360° spirality angle.

Spiral angle(°)	0	36	72	144	360
Wrap angle(°)	164	344	524	884	1965
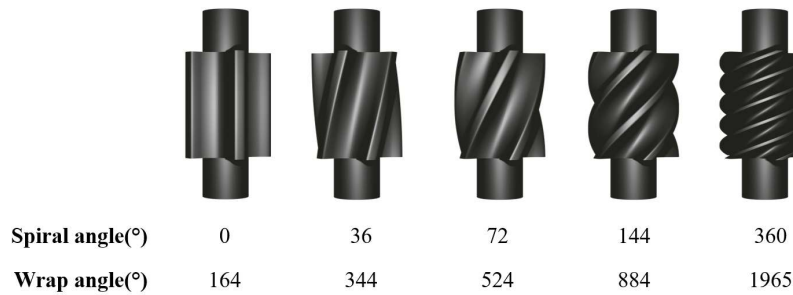
Figure 2 – 3D schematic representation of bladed stabilizers with different spiral angles.

Figure 3 shows the rotation speed at the end of the stabilizer, the total contact force, and the lateral acceleration. As expected, higher spirality angles contribute to a smoother rolling between the string and wellbore and therefore produce less vibration. Figure 4 represents time-depth heatmaps of the contact forces on the stabilizer blades. It shows the

intermittent and chaotic nature of the contacts for the case of straight blades, compared to the cases with spiral blades where the contact patterns are periodic and more predictable. For a higher spirality, the total contact force is better distributed along the stabilizer. This ensures a smoother transition of contact forces between blades and leads to reduced lateral accelerations.
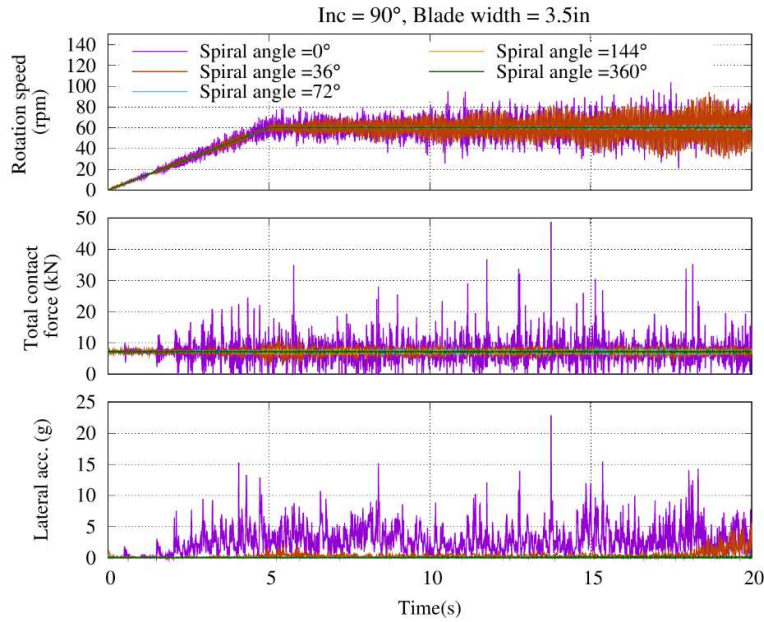

Figure 3 – Comparison of bottom rotation speed, total contact force, and mid-point acceleration for different spiral angles.
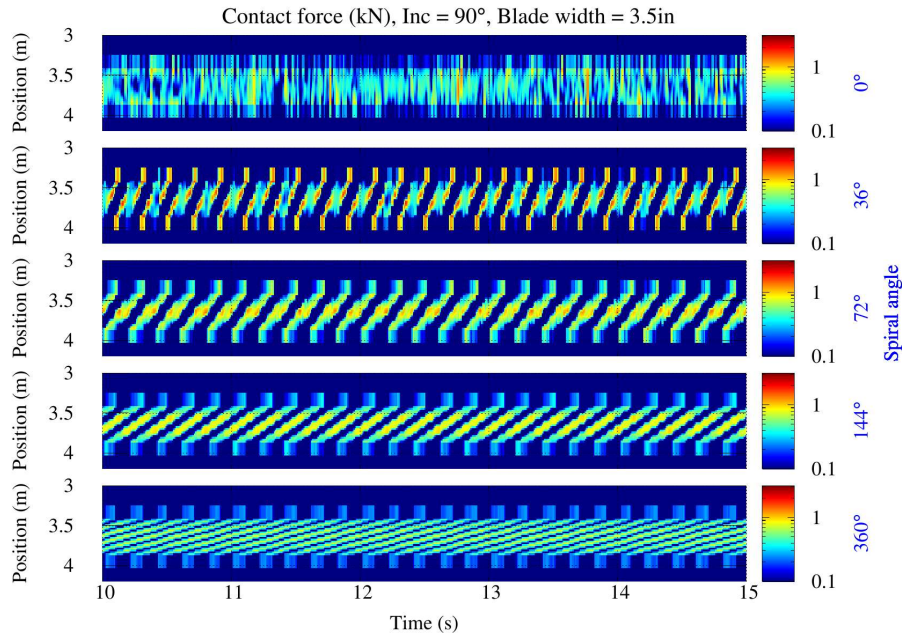
Figure 4 – Time-depth heatmaps of contact force and lateral acceleration for different blade spiral angles.

Mud motor rotor/stator motion

Mud motors are usually composed of an internal part called rotor and an external part called stator. The cross-section of both parts has a hypocycloid shape with N lobes for the rotor and $N + 1$ lobes for the stator (see Figure 5). By design, at each section, the rotation of the rotor is eccentric with respect to the stator center. This eccentricity can be deduced from the hypocycloid geometry (see for example Nguyen et al. 2014 and 2017, Samuel et al. 2021, and Harvey and

Wassell 1991) and is generally provided by the mud motor manufacturer in his specification sheet. It yields a mass imbalance at each section with the following speed:

$$\Omega_{imbalance} = N\Omega_{rotor} - \Omega_{stator} \tag{3}$$

where the stator speed Ω_{stator} is the speed above the mud motor in the BHA, and Ω_{rotor} is the additional speed provided by the motor itself, i.e., a point below the mud motor rotates at the total speed $\Omega_{stator} + \Omega_{rotor}$. This mass imbalance speed comes also from the rotor and stator geometry. As illustrated in Figure 5 (middle), as a rotor lobe rotates from a stator lobe to the following, the center of the rotor makes a full rotation in the opposite direction. This means that the relative rotation of the rotor center with respect to the stator is $-N$ times the rotation of the rotor. From this imbalance forces, the eccentricity, and the linear mass of the motor m, we can compute a mass imbalance linear force magnitude as follows:

$$F_{imbalance} = me\Omega_{imbalance}^2 \tag{4}$$

In addition to these geometrical relations in a cross-section, the mud motor is designed with a helical shape along the mud motor axis (see Figure 5, right). This makes the eccentricity orientation changes with the distance along the mud motor. The number of helical revolutions of the motor is commonly called "number of stages" and can be a whole or real number.
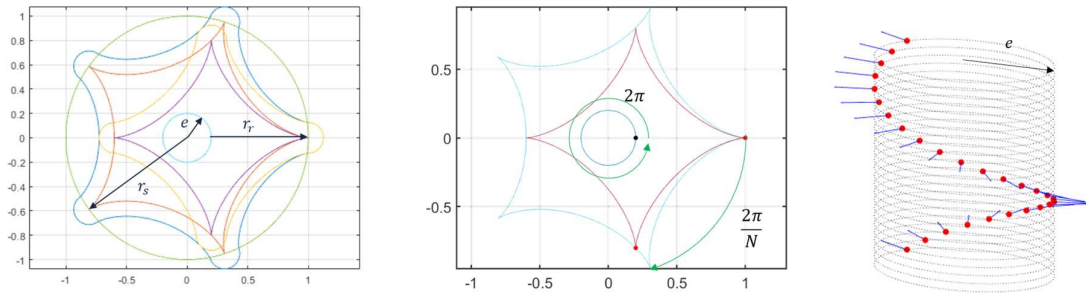

Figure 5 – Illustration of the relative motion between the rotor and stator at a cross-section of a mud motor.

To illustrate the effect of the mud motor geometry on the BHA vibration a forced vibration computation is conducted on the BHA shown in Figure 6. The rotor has 4 lobes, and the rotation speeds are assumed to be $\Omega_{rotor} = \Omega_{stator} = 60$ rpm, leading to an imbalance speed of 180 rpm. Figure 7 shows the BHA vibration strain energy, normalized by the theoretical case with straight geometry (0 stages), as a function of the motor number of stages. The straight case with 0 stages is only a theoretical reference with the worst-case scenario where the mass imbalance forces of all the cross-sections are aligned. In a general case with a positive number of stages, the imbalance forces do not act on the same direction which tends reduce the overall effect of the mass imbalance. This is particularly the case when the number of stages is a whole number (1, 2, 3, …). In this situation, the sum of the imbalance forces is zero, but as they are not located in the same position, their overall effect does not cancel out, but yields generally less vibration. This can explain the local minimums around the whole number of stages in Figure 7. The general tendency of strain energy is to decrease with the number of stages, which can be explained by the fact that eccentricities with opposite directions tends to get closer as the number of helix steps increases within the same length. The result might vary if we would, for instance, fix the helix pitch and change the motor length as we increase the number of stages.
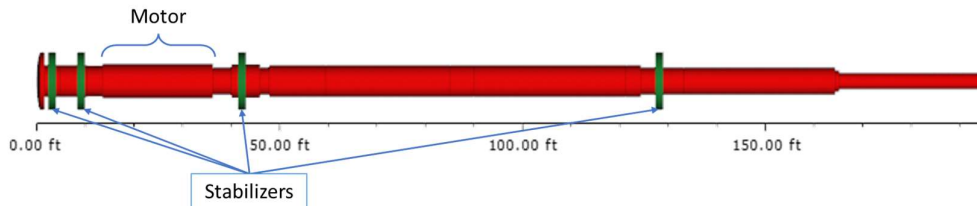

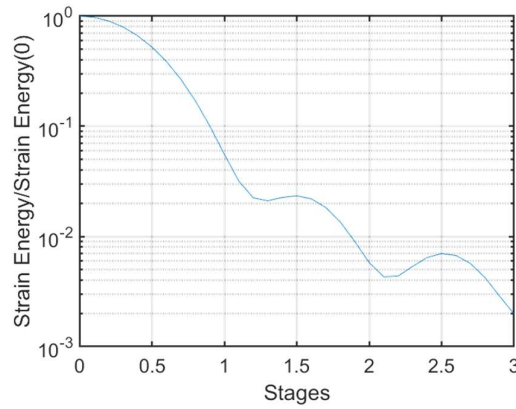**Figure 6 – Example of BHA with a mud motor.**

Figure 7 – Normalized vibration strain energy of the BHA as function of the number of stages of the mud motor.

Dampening tool

Many dampening tools are available in the industry with different mechanisms and different applications. We focus here on two design aspects that are present in some tools: a local change of stiffness, generally a reduction compared to a steel pipe with the same dimensions; and a change of material with viscous properties that produces an internal dampening effect. To model that, we consider two parameters acting on the bending degree of freedom: a rigidity reduction and a damping coefficient. To analyze the effect of these parameters, the BHA in Figure 6 is employed with the assumption that dampening tools are potentially present in the positions showed in Figure 8. In these computations, the stabilizers are assumed to be dynamic nodes. The simulations are conducted with the parameters in Table 1. Only an excitation at the bit is considered here with the magnitude related to the WOB and the pulsation related to the bit rotation speed (surface + motor rotation speed) with a coefficient (frequency multiplier).

Table 1 – Simulation parameters used to study the effect of dampening tools.

Property	Value
Surface rotation speed (rpm)	30-180
Motor rotation speed (rpm)	120
Mud weight (ppg)	10
Well inclination (deg)	45
WOB (klbf)	30
Bit excitation force magnitude / WOB (%)	10
Bit excitation force frequency multiplier	1
Tool 1 & 2 rigidity reduction (%)	80
Tool 1 & 2 damping coefficient (N.m/(rad/s))	1E+5

Figure 8 shows the mode shapes corresponding to the natural frequencies in the range of interest. In fact, as the excitation comes from the bit, the critical surface rotation speeds correspond to the natural frequencies (expressed with the units of a rotation speed) minus the motor rotation speed. Here, Mode 3 correspond to a critical surface rotation speed of 64 rpm and Mode 4 to 162 rpm. We can see that the two mode shapes are different around Tools 1 and 2 meaning that different responses are to be expected from them in the forced vibration computations.
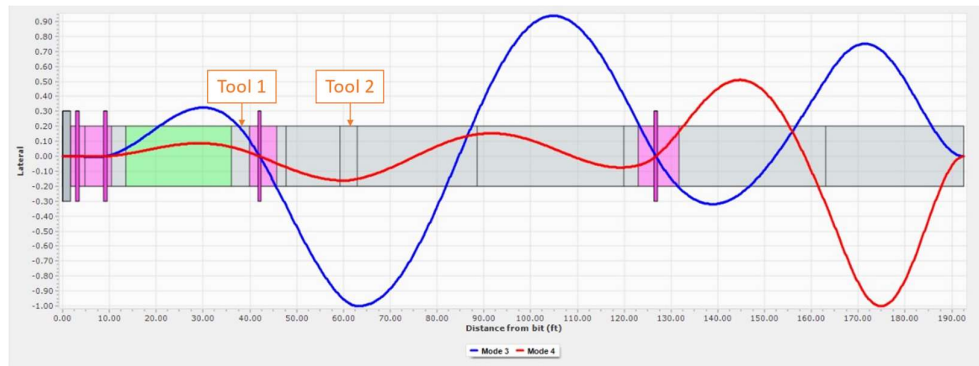
Figure 8 – BHA mode shapes #3 and #4.

Figure 9 shows the effect on the BHA lateral strain energy when using the rigidity reduction and bending damping with either Tool 1 or Tool 2. First, the reference red curve shows the case with no change in the rigidity or addition of damping from both tools. The spikes on this curve correspond to Modes 3 and 4 shown in the previous figure. Between these two spikes, in the range 80-150 rpm, the BHA seems resilient to the applied excitation as the strain energy is low. The application of only a rigidity reduction yields a shift to the left of natural frequencies, where Tool 1 seems to have more effect on Mode 3 and Tool 2 an effect on both modes. Adding the damping reduces the severity of the strain energy spikes with, again, Tool 1 having more effect on Mode 3, and Tool 2 an effect on both modes. This shows that the placement of this type of dampening tools is crucial to get the best vibration mitigation results.
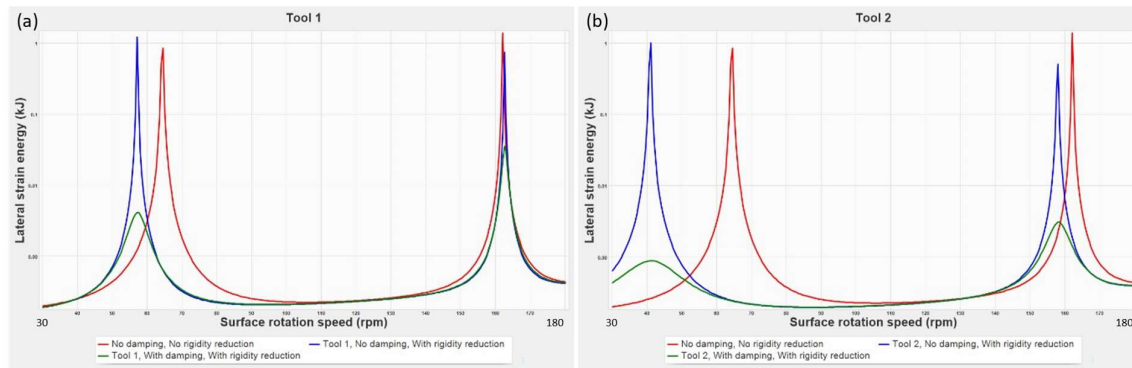

Figure 9 – Effect of rigidity reduction and damping with (a) Tool 1 and (b) Tool 2.

CONCLUDING REMARKS

This paper showcases the importance of using modeling tools to better understand the complex lateral dynamics especially in the presence of special downhole tools in the BHA. The first example of downhole tool is the spiral bladed stabilizers. It is modeled in time domain with a detailed description of contact and friction forces on the stabilizer blades. The simulations allow to show how the spirality of this tool helps a smooth transition of contact forces from one blade to the other with minimal lateral vibrations. The following two downhole tool examples are analyzed in frequency domain. The mud motor internal geometry involving the relative motion of the rotor with respect to the stator is utilized to compute the mass imbalance at each cross-section of the motor. The computations show then the impact of the motor's number of stages on the BHA's overall lateral vibration. The last example shows how some downhole dampening tools might be modeled in a forced vibration framework, by accounting for two characteristics: rigidity reduction and damping coefficient. The simulations show how each of these parameters affects the BHA vibration and how the placement of the tool is key to minimize the vibration level.

REFERENCES

ANSI/API. (2011). *Specification for Rotary Drill Stem Elements.* ANSI/API SPECIFICATION 7-1, ADDENDUM 3.

Bailey, J. R., & Remmert, S. M. (2010). Managing Drilling Vibrations Through BHA Design Optimization. *SPE Drilling & Completion, 25*(04), 458–471.

Besaisow, A. A., & Payne, M. L. (1988). A Study of Excitation Mechanisms and Resonances Inducing Bottomhole-Assembly Vibrations. *SPE Drilling Engineering, 3*, 93–101. doi:10.2118/15560-PA

Harvey, P., & Wassell, M. (1991). The Design of Steerable BHA's To Minimize the Adverse Effects of Motor Imbalance and Drilling Forces. *SPE Annual Technical Conference and Exhibition.* Dallas, Texas: Society of Petroleum Engineers.

Heisig, G., & Neubert, M. (2000). Lateral Drillstring Vibrations in Extended-Reach Wells. *IADC/SPE Drilling Conference, SPE-59235-MS.* New Orleans, Louisiana. doi:https://doi.org/10.2118/59235-MS

Mahjoub, M., Nguyen, K.-L., Menand, S., Tran, Q.-T., Andrianoely, M.-A., Manin, L., . . . Isbell, M. (2020). Dynamics Vibration Prediction and Comparison with Downhole Data Measurements in Unconventional Wells. *IADC/SPE International Drilling Conference and Exhibition.* Galveston, Texas, USA: Society of Petroleum Engineers. doi:10.2118/199571-MS

Nguyen, K.-L., Mahjoub, M., Dao, N.-H., & Menand, S. (2022). Application of a Forced Vibration Modeling Approach to Better Quantify the Role of Downhole Vibrations and Excitation Tools. *IADC/SPE International Drilling Conference and Exhibition.* Galveston, Texas, USA: Society of Petroleum Engineering. doi:10.2118/208698-MS

Nguyen, K.-L., Mahjoub, M., Dao, N.-H., & Menand, S. (2023). Detailed Dynamics Modeling Helps to Assess the Effect of Stabilizer Design on Drill String Vibrations. *SPE/IADC International Drilling Conference and Exhibition.* Stavanger, Norway: Society of Petroleum Engineers. doi:10.2118/212549-MS

Nguyen, T. C., Bui, K. D., Al-Safran, E., & Saasen, A. (2017). Theoretical Modeling of Positive Displacement Motor Performance. *AADE National Technical Conference and Exhibition.* Houston, Texas: AADE.

Nguyen, T., Al-Safran, E., Saasen, A., & Nes, O.-M. (2014). Modeling the design and performance of progressing cavity pump using 3-D vector approach. *Journal of Petroleum Science and Engineering*, 180-186.

Samuel, R., Baldenko, F., & Baldenko, D. (2021). Mud Motor PDM Dynamics: An Analytical Model. *SPE Annual Technical Conference and Exhibition.* Dubai, UAE: Society of Petroleum Engineers.

Wilson, J. K., & Noynaert, S. F. (2016). A New Damping Model for Nonlinear Drillstring Dynamics: Understanding the Effects of Rotation, Eccentricity, and Confined Fluid Flow and Their Impact on Unconventional Drillstring Design. *IADC/SPE Drilling Conference and Exhibition.* Fort Worth, Texas, USA: Society of Petroleum Engineering. doi:10.2118/178817-MS

RESPONSIBILITY NOTICE

Nonlinear Modeling of Three-Dimensional Borehole Propagation

He Zhang – Halliburton (Singapore)
Ketan Bhaidasna – Halliburton (USA)

Nonlinear Modeling of Three-Dimensional Borehole Propagation

He Zhang[1], and Ketan Bhaidasna[2]

[1] Haliiburton, SG, 639940, Singapore

[2] Haliiburton, Houston, TX, 77032, USA

Abstract: This paper extends the groundwork laid by a first-principle three-dimensional (3D) borehole propagation model proposed by Perneder (2013) through incorporating nonlinearities arising from stabilizer contacts with a circular borehole in 3D space and accounting for bit tilt saturation at the bit-rock interface. An innovative iterative algorithm is introduced to tackle the challenges posed by nonlinear 3D contacts and bit tilt saturation. Recognizing the existence of a quasi-stationary solution when the dynamics of borehole propagation are stable, we employ an assumption of quasi-uniform curvature to transform the high-fidelity model into a simplified model. Notably, the simulation results between the high-fidelity and simplified models reveal minimal differences. However, the computational efficiency of solving the simplified model significantly surpasses that of the high-fidelity model, rendering it viable for integration into optimization framework for model calibration and borehole trajectory control in real time.

Keywords: Borehole propagation; Contact nonlinearity; Iterative algorithm; Directional Drilling.

INTRODUCTION

The continuous decline in conventional natural oil and gas resources has driven the expansion of directional drilling, which involves the creation of complex, curved boreholes to access previously unreachable reservoirs. Advances in downhole drilling tools allow directional drillers to actively steer the borehole trajectory using point- or push-the-bit rotary steerable systems (RSS). However, field observations have revealed that these directional drilling technologies can lead to borehole oscillations at high curvatures, resulting in borehole rippling in two-dimensional (2D) and spiraling in three-dimensional (3D) spaces (Pastusek and Brackin, 2003). These oscillations significantly reduce drilling efficiency and complicate subsequent casing insertion. Field tests and simulations have demonstrated that optimizing bit design and increasing weight-on-bit (WOB) can mitigate borehole oscillations (Pastusek and Brackin, 2003).

A more pressing issue in directional drilling is the deviation of the drilled trajectory from the well plan due to uncertainties in rock formation and downhole drilling conditions. This deviation results in low borehole quality due to undesirable borehole (micro-) tortuosity and imprecise borehole placement, leading to reduced reservoir drainage. Model predictive control (MPC) methods have been applied in directional drilling to track the well plan by providing steering commands while satisfying constraints on states and control inputs (Demirer *et al.*, 2019). Several field case studies have demonstrated the potential of MPC to achieve autonomous drilling with high borehole quality and accurate borehole placement (Demirer *et al.*, 2019). However, previous MPC approaches primarily relied on data-driven models governing borehole propagation (BHP), overlooking the underlying physics of BHP. This oversight means that these models lack insights into the effects of bottom-hole assembly (BHA) design, rock formation, bit design, and drilling parameters (i.e., WOB and RSS actuating force) on BHP.

The dynamics of BHP within 3D space and the root cause of borehole spiraling/rippling have been extensively analyzed by Perneder (2013) through an advanced model. The mathematical formulation of the BHP model yields a set of delay differential equations (DDEs) where the state variables are the inclination and the azimuth of the borehole. Analysis of the simulation results revealed that borehole spiraling occurs when the system of the DDEs is unstable. Conversely, the stable DDE system yields a quasi-stationary solution characterized by a slow variation of the borehole curvature, implying that the borehole curvature can be treated as uniform at the scale of the BHA length. One limitation of this model lies in its inability to simulate steady-state borehole spiraling, as it does not incorporate essential nonlinearities.

The two aspects of nonlinearity in the BHP model are bit tilt saturation and contact nonlinearity. Shakib *et al.* (2019), considered both nonlinearities in their 2D BHP model governing the evolution of borehole inclination. In this model, the 2D contact and bit tilt saturation were formulated as linear complementarity problems (LCP). For a 3D BHP model, the 3D contact between the stabilizers and the circular borehole wall violates the linear relationship between the contact forces and the gap variables. Derksen (2021) formulated the 3D contact problem as a nonlinear complementarity problem, which was solved using a proximal point approach. However, bit tilt saturation is not included in their 3D BHP model.

This manuscript extends the 3D BHP model in (Perneder, 2013; Derksen, 2021) by incorporating both contact nonlinearity and bit tilt saturation. A novel iterative algorithm is proposed to address the unilateral nature of both nonlinearities simultaneously. The accuracy of the algorithm was verified by comparison with published results from a 2D BHP model, and the validity of the 3D BHP model was confirmed against field measurement data. The current study focuses on the quasi-stationary solution of the BHP model, assuming uniform curvature to simplify the set of DDEs into a system

of ordinary differential equations (ODEs). Simulation results from both DDEs and ODEs are compared to validate the uniform-curvature assumption for the quasi-stationary solution of the 3D BHP model. The benefit of simulating ODEs lies in their high computational efficiency, making the simplified BHP model suitable for integration into an optimization framework for real-time model calibration and MPC control.

MATHEMATICAL MODEL

The 3D BHP model in (Perneder, 2013; Derksen, 2021) has been extended to incorporate the realistic BHA used in the directional drilling with a push-the-bit RSS. A notable distinction between the realistic BHA and the simplified BHA in (Perneder, 2013; Derksen, 2021) is that the realistic BHA comprises components with varying material properties and cross-sectional areas. The detailed description of the realistic BHA model is provided in (Xu *et al.*, 2024). For simplicity, this section presents the final analytical expressions for the 3D BHP model, which are obtained by following the derivation in Derksen (2021) with the aid of a symbolic toolbox in MATLAB.

High-Fidelity BHP Model

The high-fidelity BHP model is formulated in terms of a set of dimensionless DDEs governing the evolution of the bit inclination θ_0 and azimuth ϕ_0, as well as average borehole inclinations $\langle\Theta\rangle_{(k)}$ and azimuths $\langle\Phi\rangle_{(k)}$ over the $k-$th BHA segment between the $(k-1)-$th and $k-$th stabilizers

$$\begin{pmatrix} \frac{d\phi_0}{d\xi}\sin\theta_0 \\ \frac{d\theta_0}{d\xi} \end{pmatrix} = \frac{1}{\chi\Pi}\begin{bmatrix} \sum_{k=1}^{n-1}\hat{\alpha}_k\hat{F}_{k,3} + \sum_{k=1}^n\hat{\beta}_k\left(\langle\Phi\rangle_{(k)} - \phi_0\right)\sin\left(\langle\Theta\rangle_{(1)}\right) + \hat{\gamma}\hat{F}_{r,3} \\ \sum_{k=1}^{n-1}\hat{\alpha}_k\hat{F}_{k,2} + \sum_{k=1}^n\hat{\beta}_k\left(\langle\Theta\rangle_{(k)} - \theta_0\right) + \hat{\gamma}\hat{F}_{r,2} + \hat{\zeta}\hat{w}\sin\langle\Theta\rangle_{(1)} \end{bmatrix}, \tag{1}$$

$$\frac{d\langle\Theta\rangle_{(k)}}{d\xi} = \frac{\Theta_{k-1} - \Theta_k}{\lambda_k}, \qquad \frac{d\langle\Phi\rangle_{(k)}}{d\xi} = \frac{\Phi_{k-1} - \Phi_k}{\lambda_k}, \; k=1,2,...,n, \tag{2}$$

where n stands for the number of stabilizers, ξ signifies the dimensionless borehole depth, Π represents the scaled WOB, χ denotes the angular steering resistance; $\hat{\alpha}_k$, $\hat{\beta}_k$, $\hat{\gamma}$, $\hat{\zeta}$ are constant coefficients dependent on the realistic BHA configurations [1]; $\hat{F}_{k,j}$, $j=2$, 3 denotes the contact force at the $k-$th stabilizer, $F_{r,j}$, $j=2$, 3 represents the scaled RSS actuating force, $\hat{w}$ stands for the scaled BHA weight per unit length; Θ_k (Φ_k) represents the borehole inclination (azimuth) at the $k-$th stabilizers, λ_k is the dimensionless length of the $k-$th BHA segment. Throughout this paper, the subscript 0 denotes variables at the bit, while subscript 2 (or 3) signifies variables in the inclination (or pseudo-azimuth) plane. The borehole inclination Θ_0 and azimuth Φ_0 are related to the bit inclination θ_0 and azimuth ϕ_0 in terms of the output equations

$$\Theta_0 = \theta_0 - \psi_2, \; \Phi_0\sin\langle\Theta\rangle_{(1)} = \phi_0\sin\langle\Theta\rangle_{(1)} - \psi_3, \tag{3}$$

where ψ_2 and ψ_3 denote the bit tilt angles. Integrating the set of DDEs necessitates information of the contact forces and bit tilt angles, which are determined by a system of algebraic equations describing the displacement $\delta_{i,j}$, $j=2$, 3 of the $i-$th stabilizer in (4) and the bit-rock interface law in (5)

$$\begin{bmatrix} \delta_{i,2} \\ \delta_{i,3} \end{bmatrix} = \begin{bmatrix} \sum_{k=1}^{n-1}\alpha_{k,i}\hat{F}_{k,2} + \sum_{k=1}^n\beta_{k,i}\left(\langle\Theta\rangle_{(k)} - \theta_0\right) + \gamma_i\hat{F}_{r,2} + \zeta_i\hat{w}\sin\langle\Theta\rangle_{(1)} \\ \sum_{k=1}^{n-1}\alpha_{k,i}\hat{F}_{k,3} + \sum_{k=1}^n\beta_{k,i}\left(\langle\Phi\rangle_{(k)} - \phi_0\right)\sin\left(\langle\Theta\rangle_{(1)}\right) + \gamma_i\hat{F}_{r,3} \end{bmatrix}, \quad i=1,2,...,n-1, \tag{4}$$

$$\begin{pmatrix} \cos\varpi & \sin\varpi \\ -\sin\varpi & \cos\varpi \end{pmatrix}\left(\eta\Pi\begin{pmatrix} \psi_2 \\ \psi_3 \end{pmatrix} - \begin{pmatrix} \hat{F}_{s,2} \\ \hat{F}_{s,3} \end{pmatrix}\right) = \begin{bmatrix} \sum_{k=1}^{n-1}\tilde{\alpha}_k\hat{F}_{k,2} + \sum_{k=1}^n\tilde{\beta}_k\left(\langle\Theta\rangle_{(k)} - \theta_0\right) + \tilde{\gamma}\hat{F}_{r,2} + \tilde{\zeta}\hat{w}\sin\langle\Theta\rangle_{(1)} \\ \sum_{k=1}^{n-1}\tilde{\alpha}_k\hat{F}_{k,3} + \sum_{k=1}^n\tilde{\beta}_k\left(\langle\Phi\rangle_{(k)} - \phi_0\right)\sin\left(\langle\Theta\rangle_{(1)}\right) + \tilde{\gamma}\hat{F}_{r,3} \end{bmatrix}, \tag{5}$$

where $\alpha_{k,i}$, $\tilde{\alpha}_k$, $\beta_{k,i}$, $\tilde{\beta}_k$, γ_i, $\tilde{\gamma}$, $\zeta_i, \tilde{\zeta}$ are constant coefficients dependent on the realistic BHA configurations (refer to footnote 1); ϖ denotes the bit walk angle, η stands for the lateral steering resistance; $\hat{F}_{s,2(3)}$ represents the saturation force corresponding to the bit tilt saturation. The delay nature of this model arises from the delayed influence of the borehole geometry on the stabilizers, which must conform to the existing borehole.

Contact Nonlinearity

The contact forces $\hat{F}_{i,j}$ and the displacement $\delta_{i,j}$ $(i=1,2,n-1;j=2,3)$ for $i-$th stabilizer must comply with Signorini's law, expressed as

---

[1]Symbolic toolbox is employed to derive these constant coefficients for a realistic BHA using the method of sections, as described in (Shakib *et al.*, 2019; Xu *et al.*, 2024)

$$\hat{F}_i \geqslant 0, \quad g_i \geqslant 0, \quad \hat{F}_i g_i = 0, \quad i = 1, 2, ..., n-1 \tag{6}$$

where $\hat{F}_i = \sqrt{\hat{F}_{i,2}^2 + \hat{F}_{i,3}^2}$ represents the resultant contact force, $g_i = \delta_i^* - \delta_i$ denotes the gap between the stabilizer and the borehole wall, $\delta_i = \sqrt{\delta_{i,2}^2 + \delta_{i,3}^2}$ signifies the resultant stabilizer displacement, and δ_i^* is the clearance. The unilateral nature of the contact dictates that the orientation of $\hat{F}_i$ must be opposite to that of δ_i (Derksen, 2021).

Bit Tilt Saturation

When the bit tilt reaches saturation, the bit side force becomes set-valued. Saturation of the bit tilts implies that $\left|\psi_{2(3)}\right| \leq \psi^*$, where ψ^* is the saturation boundary. The unilateral nature of bit tilt saturation can be expressed in terms of the following constraints

$$\begin{cases} \hat{F}_{s,2(3)} = 0, & \left|\psi_{2(3)}\right| < \psi^* \\ \hat{F}_{s,2(3)} > 0, & \psi_{2(3)} = -\psi^* \\ \hat{F}_{s,2(3)} < 0, & \psi_{2(3)} = \psi^* \end{cases} \tag{7}$$

Iterative Algorithm

For a realistic BHA with n stabilizers, solving the high-fidelity BHP model in (1) - (3) relies on computing the contact force and bit tilt angles. These can be obtained by solving a system of $2n$ algebraic equations given in (4) - (5). However, there exist a total of $4n$ unknown variables: the displacements ($\delta_{i,2}$ and $\delta_{i,3}$) and contact forces ($\hat{F}_{i,2}$ and $\hat{F}_{i,3}$) at the $i-$th stabilizer ($i = 1, 2, ..., n-1$), the bit tilt angles ψ_2 and ψ_3, and the saturation forces $\hat{F}_{s,2}$ and $\hat{F}_{s,3}$.

The unilateral nature of the contact in (6) and bit tilt saturation in (7) provides $2n$ constraints. It is worth noting that the contact forces and stabilizer displacements form conjugate pairs. During contact, the displacements are known while the corresponding contact forces are unknown, and vice versa when the contact is absent. Similarly, bit tilts and saturation forces also form conjugate pairs. Consequently, the $2n$ unilateral constraints can be converted into a system of $2n$ equations if the contact configurations (including locations and orientations) and the occurrence of bit tilt saturation are known.

Figure (1) illustrates the flow chart of an iterative algorithm for identifying the contact configuration. In cases with multiple stabilizers in contact with the borehole wall, this algorithm aims to identify one contact point in each iteration. This is achieved by selecting the stabilizer that extends furthest beyond the borehole wall. The index j of the identified stabilizer in contact is then added to a contact list J. Displacement constraints are applied to the contact points in J to compute the corresponding contact forces using (4) and (5). For stabilizers not in the contact list J, zero contact forces are assigned. Subsequently, the directions of these contact forces and displacements are compared to ensure compliance with the unilateral contact condition. If a violation is detected at contact point j, it is removed from J, and the calculation is repeated. Otherwise, the algorithm proceeds to the next iteration.

The iteration begins with the assumption that $\hat{F}_{i,2} = 0$, $\hat{F}_{i,3} = 0$, $\hat{F}_{s,2} = 0$, and $\hat{F}_{s,3} = 0$. It contunites until the displacements of all stabilizers remain within the borehole, and the unilateral contact conditions are satisfied for all contact points. After the iteration terminates, the values ψ_2, ψ_3 are compared with ψ^* to ascertain if bit tilts have reached saturation. If saturation is detected, the algorithm incorporates the bit tilt saturation to calculate the corresponding saturation force.

During the simulation, the Euler-forward finite difference technique discretizes the differential operations in (1) and (2). The iterative algorithm is used to solve the contact forces and bit tilt at each depth step. The output equation (3) yields the borehole inclinationa and azimuth with respect to the increasing borehole depth.

Simplified BHP Model

The stability of the high-fidelity BHP model depends on the value of the key dimensionless group $\eta\Pi$. The model is stable when $\eta\Pi > \eta\Pi^*$ and unstable otherwise, where $\eta\Pi^*$ is a critical value obtained from linear stability analysis (Shakib *et al.*, 2019). When the BHP model is stable, a quasi-stationary solution exists, characterized by the slow variation of the borehole curvature. In this regime, the borehole curvature can be assumed to be uniform over the length of the BHA, leading to the following geometric relations

$$\langle\Theta\rangle_{(k)} - \theta_0 = -\psi_2 + \frac{\kappa_\Theta}{2}(\lambda_i - 2s_i), \quad \left(\langle\Phi\rangle_{(k)} - \phi_0\right)\sin\langle\Theta\rangle_{(1)} = -\psi_3 + \frac{\kappa_\Phi \sin\langle\Theta\rangle_{(1)}}{2}(\lambda_i - 2s_i) \tag{8}$$

where κ_Θ and κ_Φ represent the build rate and turn rate, respectively; $s_i = \sum_{k=0}^{i} \lambda_k$ is the distance between the $i-$th stabilizer and the bit. Another consequence of the uniform curvature assumption is that the bit tilts ψ_2 and ψ_3 remain constant over the BHA length, leading to
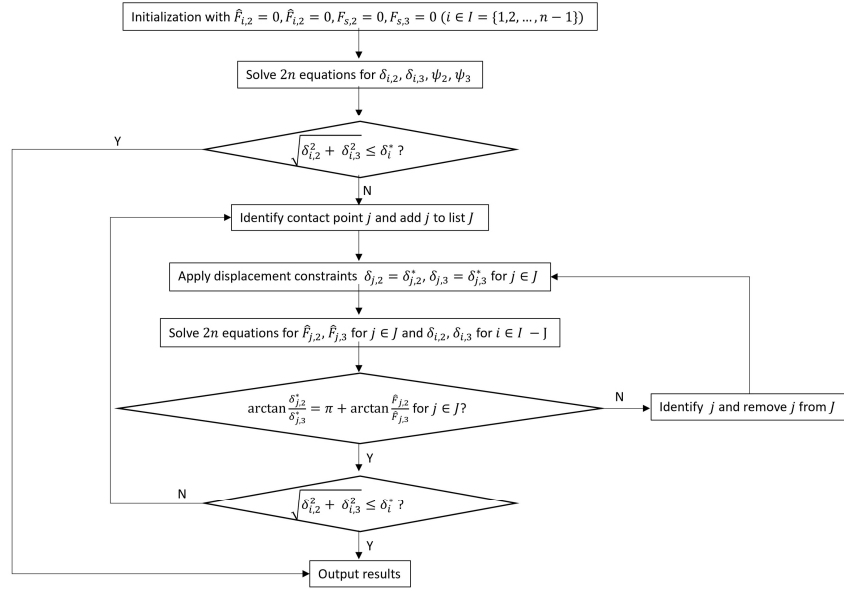
Figure 1: Flow chart of an iterative algorithm to address contact nonlinearity.

$$\frac{\mathrm{d}\theta_0}{\mathrm{d}\xi} = \frac{\mathrm{d}\Theta_0}{\mathrm{d}\xi} = \kappa_\Theta, \quad \frac{\mathrm{d}\phi_0}{\mathrm{d}\xi} = \frac{\mathrm{d}\Phi_0}{\mathrm{d}\xi} = \kappa_\Phi. \tag{9}$$

Noting that $\theta_0 \approx \langle\Theta\rangle_{(1)}$ and substituting (8) and (9) into both sides of (1), we can derive expressions for κ_Θ and κ_Φ as follows

$$\begin{bmatrix} \kappa_\Theta \\ \kappa_\Phi \sin\langle\Theta\rangle_{(1)} \end{bmatrix} = \begin{bmatrix} \sum_{k=1}^{n-1} \hat{a}_k \hat{F}_{k,2} + \hat{b}\hat{F}_{r,2} + \hat{c}\hat{w}\sin\langle\Theta\rangle_{(1)} + \hat{d}\psi_2 \\ \sum_{k=1}^{n-1} \hat{a}_k \hat{F}_{k,2} + \hat{b}\hat{F}_{r,3} + \hat{d}\psi_3 \end{bmatrix} \tag{10}$$

Substituting (8) into (4) and (5) yields

$$\begin{bmatrix} \delta_{i,2} \\ \delta_{i,3} \end{bmatrix} = \begin{bmatrix} \sum_{k=1}^{n-1} a_{k,i} \hat{F}_{k,2} + b_i \hat{F}_{r,2} + c_i \hat{w}\sin\langle\Theta\rangle_{(1)} + d_i\psi_2 + e_i\kappa_\Theta \\ \sum_{k=1}^{n-1} a_{k,i} \hat{F}_{k,3} + c_i \hat{F}_{r,3} + d_i\psi_3 + e_i\kappa_\Phi\sin\langle\Theta\rangle_{(1)} \end{bmatrix}, \quad i = 1,2,...,n-1, \tag{11}$$

$$\begin{pmatrix} \cos\varpi & \sin\varpi \\ -\sin\varpi & \cos\varpi \end{pmatrix} \left(\eta\Pi \begin{pmatrix} \psi_2 \\ \psi_3 \end{pmatrix} - \begin{pmatrix} \hat{F}_{s,2} \\ \hat{F}_{s,3} \end{pmatrix} \right) = \begin{bmatrix} \sum_{k=1}^{n-1} \tilde{a}_k \hat{F}_{k,2} + \tilde{b}\hat{F}_{r,2} + \tilde{c}\hat{w}\sin\langle\Theta\rangle_{(1)} + \tilde{d}\psi_2 + \tilde{e}\kappa_\Theta \\ \sum_{k=1}^{n-1} \tilde{a}_k \hat{F}_{k,3} + \tilde{b}\hat{F}_{r,3} + \tilde{d}\psi_2 + \tilde{e}\kappa_\Phi\sin\langle\Theta\rangle_{(1)} \end{bmatrix}, \tag{12}$$

where $a_{k,i}$, $\tilde{a}_k$, $\hat{a}_k$, b_i, $\hat{b}$, $\tilde{b}$, c_i, $\tilde{c}$, $\hat{c}$, $d_i, \tilde{d}$, $\hat{d}, e_i$, $\tilde{e}$ $(k, i = 1,2,...,n-1)$ are constant coefficients (refer to footnote 1). Employing the geometric relation (8) removes the states $\langle\Theta\rangle_{(k)}$ and $\langle\Phi\rangle_{(k)}$ in the high-fidelity model, which converts the system of DDEs (1) - (2) into a system of ODEs (10).

For the simplified BHP mode, there are a total of $2n+2$ algebraic equations in (10) - (12), which involve $4n+2$ unknowns. These unknowns comprisie stabilizer displacements ($\delta_{i,2}$ and $\delta_{i,3}$) and contact forces ($\tilde{F}_{i,2}$ and $\tilde{F}_{i,3}$) at the $i-$th stabilizer ($i = 1,2,...,n-1$), bit tilts (ψ_2 and ψ_3), saturation force ($\tilde{F}_{s,2}$ and $\tilde{F}_{s,3}$), and curvatures (κ_Θ and κ_Φ). Recognizing the $2n$ constraints arising from the unilateral nature of the contact and bit tilt saturation, we utilize an iterative algorithm to solve the $4n+2$ unknowns. Upon termination of the iteration, we obtain κ_Θ and κ_Φ, which are subsequently utilized in the system of ODEs (9) to propagate the borehole inclination and azimuth with respect to the increasing borehole depth.

SIMULATION RESULTS

Validation

Accuracy of the Iterative Algorithm

In (Shakib *et al.*, 2019), contact nonlinearity and bit tilt saturation are incorporated into a 2D BHP model by formulating a LCP. The accuracy of the proposed iterative algorithm is validated by comparing its simulation results with those obtained using the LCP. Figures 2a and 2b display the simulation results for a realistic BHA with seventeen stabilizers, as

described in (Xu *et al.*, 2024). The small value of $\eta\Pi$ results in slight borehole rippling in Fig. 2a, while Fig. 2b illustrates a steady-state borehole evolution with a gradual change in borehole curvature. In both cases, the iterative algorithm and the LCP yield identical results. The computation time are 20.68s and 29.75s for the LCP and the iterative algorithm, respectively.
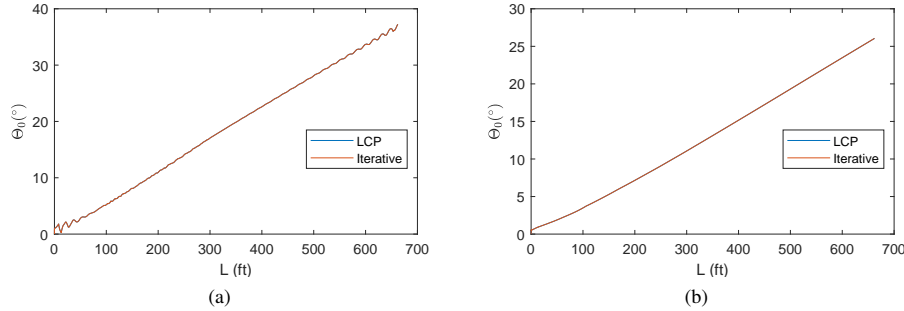

Figure 2: Simulation results of a 2D BHP model with: (a) $\eta\Pi = 0.0491$ and (b) $\eta\Pi = 0.327$.

Validation of the 3D High-Fidelity BHP Model with Field Data

The validity of the 3D high-fidelity BHP model and the iterative algorithm is further verified by comparing the simulation results with field survey data. The first two subplots in Fig. 3 illustrate the simulation results and the survey data for borehole inclination and azimuth, respectively. The field RSS actuating force (shown in the third and fourth subplots in Fig. 3) and filtered WOB (depicted the fifth plot in Fig. 3) corresponding to the survey data are used as inputs for the simulation. To minimize the discrepancy between the simulation results and field survey data, the model parameters, such as lateral steering resistance η and walk angle ϖ, can be calibrated. In the simulation, two sets of values are chosen: $\eta = 35$, $\varpi = 10°$ for the first half and $\eta = 70$, $\varpi = 0°$ for the second half of the entire borehole length. The satisfactory agreement between the simulation results and survey data, particularly for the inclination, validates the effectiveness of the 3D BHP model. Discontinuities in the simulated inclination and azimuth are arise from changes in the contact configuration between the stabilizers and the borehole wall. These discontinuities lead to fluctuations in subsequent simulation results, which decay quickly as the BHP model is stable. Borehole spiraling would occur if the model were unstable for given values of $\eta\Pi$,

Comparison between High-Fidelity and Simplified 3D BHP Models

The simulation results depicted in Fig. 3 reveal a gradual evolution of curvatures under varying RSS actuating force and WOB, providing justification for employing the simplified BHP model. Figures 4a and 4b showcase the comparison between the high-fidelity and simplified models for inclination and azimuth, respectively, with $\eta = 35$ and $\varpi = 10°$. It
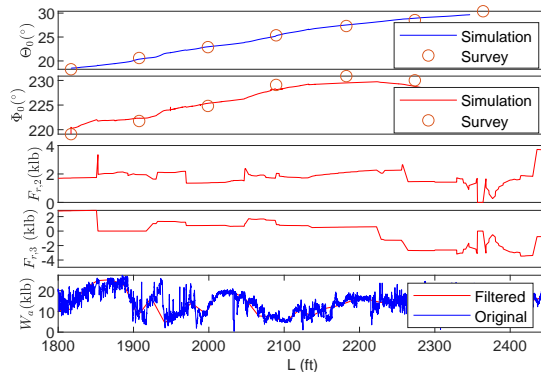

Figure 3: Comparison between simulation results from the 3D high-fidelity BHP model and field survey data using field RSS actuating force and WOB.

is evident that the simulation results obtained using the simplified model closely align with those from the high-fidelity model. Notably, the simplified model yields smoother results compared to its high-fidelity counterpart. Furthermore, the formulation of the simplified model as a set of first-order ODEs ensures stability, allowing it to be solved with arbitrary depth steps [2]. Consequently, the computational time for simulating the simplified model is significantly reduced compared to that for the high-fidelity model. In this case, the simplified model requires merely 0.32 seconds, while the high-fidelity model takes 40.88 seconds. The remarkable computational efficiency of the simplified model makes it suitable for integration into optimization frameworks for real-time model calibration (such as η and ϖ) and borehole trajectory control using the MPC approach.
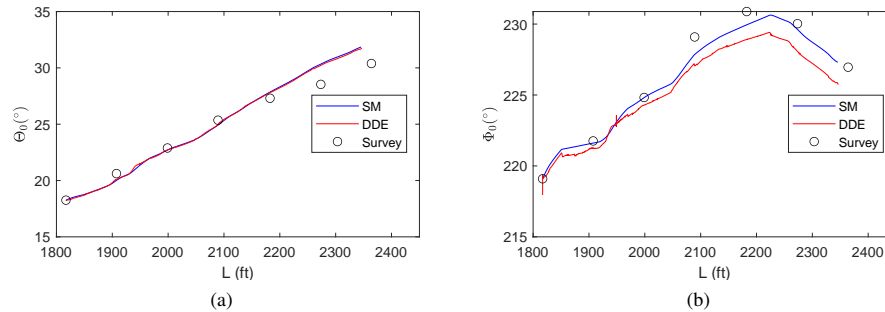

Figure 4: Comparison of simulation results between high-fidelity and simplified models for: (a) inclination and (b) azimuth.

CONCLUDING REMARKS

This paper extends an existing 3D BHP model to incorporate both contact nonlinearity and bit tilt saturation. An innovative algorithm is proposed to address these nonlinearities simultaneously. The accuracy of this algorithm is verified against the LCP using a 2D BHP model. Remarkably, the computational efficiency of the iterative algorithm is comparable to that of the LCP. Recognizing the infrequent change in contact configuration for stable solutions, the iterative algorithm can be further enhanced. By substituting the contact configuration obtained in the last depth step into the current one, the number of iterations required can be reduced. The validity of the 3D high-fidelity BHP model and its simplified counterpart, based on the uniform curvature assumption, is confirmed through comparison with field survey data. Notably, the computational efficiency of the simplified BHP model surpasses that of the high-fidelity model by two orders of magnitude. This efficiency enables the integration of the simplified model into optimization frameworks for real-time model calibration and borehole trajectory control using the MPC approach.

REFERENCES

Demirer, N., Zalluhoglu, U., Marck, J., Gharib, H. and Darbe, R., 2019. "A model predictive control method for autonomous directional drilling". In *SPE Annual Technical Conference and Exhibition?* SPE, p. D022S077R002.

Derksen, H., 2021. "Nonlinear modeling for dynamical analysis of 3d directional drilling processes".

Pastusek, P. and Brackin, V., 2003. "A model for borehole oscillations". In *SPE Annual Technical Conference and Exhibition?* SPE, pp. SPE–84448.

Perneder, L., 2013. *A three-dimensional mathematical model of directional drilling*. Ph.D. thesis, University of Minnesota.

Shakib, M., Detournay, E. and van de Wouw, N., 2019. "Nonlinear dynamic modeling and analysis of borehole propagation for directional drilling". *International Journal of Non-Linear Mechanics*, Vol. 113, pp. 178–201.

Xu, J., Demirer, N., Pho, V., Tian, K., Zhang, H., Bhaidasna, K., Darbe, R. and Chen, D., 2024. "Advancing real-time drilling trajectory prediction with an efficient nonlinear dde model and online parameter estimation". *Geoenergy Science and Engineering*, Vol. 238, p. 212829.

RESPONSIBILITY NOTICE

The authors are the only responsible for the printed material included in this paper.

---

[2]In practice, the depth step should be less than the interval where the WOB and RSS actuating force remain constant.

Distributed drilling system analysis: a time-delay system approach

Shabnam Tashakori, Mohammad – Shiraz University of Technology
(Iran)
Mohammad A. Faghihi – KTH Royal Institute of Technology (Sweden)

Distributed drilling system analysis: a time-delay system approach

Shabnam Tashakori[1], and Mohammad Amin Faghihi[2]

[1] Department of Mechanical Engineering, Shiraz University of Technology, Iran

[2] Department of Civil and Architectural Engineering, KTH Royal Institute of Technology, Sweden

Abstract: Self-excited axial-torsional vibrations in drilling are one of the main causes of the reduction of drilling efficiency, system failure, and rig downtime. Different approaches have been employed to model the complex coupled dynamics of the drilling system, among which models based on time-delay systems approach strike a favorable balance between modeling accuracy and complexity of simulation, analysis, and control. In this approach, the equations of motion are represented in terms of Delay Differential Equations (DDE) with constant time-delays related to the wave travel time along the drill-string. The bit-rock interaction is responsible for the coupling between the axial and torsional dynamics of the drilling system. To deal with the multiple regenerative effects in the bit-rock interaction, which is a consequence of bit-bounce in the case of severe axial vibrations, or bit reverse rotation, three approaches are investigated. In the first approach, named the State-Dependent Delay (SDD) model, the depth of cut is obtained by solving an implicit delay algebraic equation with a state-dependent time-delay, induced by the cutting process at the bit. In the second and third approaches, the cut surface profile is determined in order to estimate the depth of cut. In the second model, the profile of the cut surface is obtained by solving a nonlinear Partial Differential Equation (PDE). Therefore, the model is named the PDE pattern evolution model. Whereas, in the third approach, named the algebraic pattern evolution model, the well-bottom depth function is formulated through algebraic equations rather than PDEs, which enables capturing the discontinuities in the rock surface depth function, as well as reducing the computational burden. The efficacy of the distributed modeling of the drilling system in terms of DDEs with three strategies for the bit-rock interaction will be discussed and compared. Furthermore, a discussion on the control of models derived from the time-delay systems approach will be presented.

Keywords: drilling vibrations, time-delay system approach, multiple regenerative effect

INTRODUCTION

A variety of approaches have been employed to model the dynamics of the drill-string: (i) lumped-parameter models Richard *et al.* (2007); Navarro-López (2009); Liu *et al.* (2017); Huang *et al.* (2018), (ii) finite element models Depouhon and Detournay (2014); Fernandes *et al.* (2018); Feng *et al.* (2019); Priest *et al.* (2021), (iii) distributed parameter models Bresch-Pietri and Krstic (2014); Aarsnes and van de Wouw (2018, 2019), and (iv) Neutral-type Time-Delay (NTD) models Tashakori *et al.* (2020, 2021); Faghihi *et al.* (2022, 2023, 2024). NTD models are obtained directly from the distributed parameter models when the damping effects are disregarded along the drill-string. Compared to lumped-parameter models, the distributed elastic nature of the drilling system (as a platform for propagating waves) is taken into consideration in the NTD model which enables studying the infinite-dimensional dynamics of the system. Furthermore, more analysis and control strategies are available in the literature for models formulated by Delay Differential Equations (DDEs) in comparison with models in terms of Partial Differential Equations (PDEs) Krstic (2009).

to model the bit–rock interaction in drilling systems, several approaches have been presented. The interaction between the Poly-crystalline Diamond Compact (PDC) bit and the formation is decomposed to cutting- and frictional contact-induced forces in Detournay and Defourny (1992). Cutting forces are functions of the depth of cut, depending on the current and the previous drill-bit axial position. This dependency is called the regenerative cutting effect Liu *et al.* (2014b), which is known as the root cause of self-excited vibrations and instability in the drill-string.

To capture the depth of cut, Richard *et al.* (2007) proposed an implicit algebraic delay equation, which introduces a state-dependent delay to the equations of motion. This state-dependent delay model has been exploited to study the roots of unwanted oscillations in Germay *et al.* (2009); Liu *et al.* (2013); Depouhon and Detournay (2014); Liu *et al.* (2014c); Besselink *et al.* (2015); Aarsnes and van de Wouw (2018); Zheng *et al.* (2020); Tashakori *et al.* (2020). However, this model loses its validity in the case of severe self-excited vibrations, where the contact between the cutting blades and the formation might be lost. This can occur during (i) bit-bounce or (ii) bit reverse rotation. Later, in Liu *et al.* (2014a), this bit-rock interaction model was modified to account for bit-bouncing. However, as the depth of cut calculation was still valid just in the case when the bit cuts the formation, the problem was not fully taken into account. The modification of the state-dependent delay model was presented in Liu *et al.* (2020) by assessing the bit penetration in multiple previous rotations rather than only one previous rotation to account for multiple regenerative effects. Therein, the instantaneous depth of cut is characterized by the current and multiple preceding positions of the blade, which incorporates several state-dependent time-delays (rather than one) to the dynamics. However, the bit reverse rotation is disregarded and only the multiple regenerative effects caused by the bit-bounce are considered in this research. In an alternative approach, proposed

in Wahi and Chatterjee (2008); Gupta and Wahi (2016), regenerative axial dynamics is incorporated through a functional description of the cut surface profile instead of an implicit delay equation. Therein, the evolution of the cut surface is governed by a PDE, where its boundary conditions capture multiple regeneration in the event of bit-bounce. However, this PDE model cannot capture nonsmooth and discontinuous cut patterns, which is the case when (i) the torsional stick and the bit-bounce occur simultaneously, and (ii) the bit rotates in the reverse direction. In the third approach, presented in Faghihi *et al.* (2024), the cut surface depth function is formulated by algebraic equations rather than PDEs, which enables capturing the discontinuous cut pattern. It is, hence, valid in the presence of multiple regenerative effects both in the cases of bit bouncing and bit reverse rotation.

DISTRIBUTED DRILL-STRING MODEL

The drill-string is modeled as a continuous shaft under torsional torques and a continuous rod under axial forces with constant material and geometric properties, and negligible damping effects. Consequently, the drill-string torsional and axial dynamics are governed by the wave equations as follows Bresch-Pietri and Krstic (2014); Saldivar *et al.* (2014); Aarsnes and van de Wouw (2018):

$$\frac{\partial^2 \Phi}{\partial x^2}(x,t) = c_t^2 \frac{\partial^2 \Phi}{\partial t^2}(x,t), \tag{1a}$$

$$\frac{\partial^2 U}{\partial x^2}(x,t) = c_a^2 \frac{\partial^2 U}{\partial t^2}(x,t), \tag{1b}$$

where $\Phi(x,t)$ and $U(x,t)$ are, respectively, the angular and axial displacements along the drill-string which are functions of time t, and the distance from the top extremity x, ranging from 0 at the top to L at the Bottom Hole Assembly (BHA) with L the length of the drill-string. The wave constants c_t and c_a are the wave constants given by:

$$c_t = \sqrt{\frac{\rho}{G}}, \quad c_a = \sqrt{\frac{\rho}{E}}, \tag{2}$$

with ρ, G, and E, respectively, the density, the shear modulus, and the Young modulus of the string.

Top-drive dynamics

The torsional and axial top-drive dynamics are given by Faghihi *et al.* (2024):

$$GJ\Phi_r'(t) = J_r\ddot{\Phi}_r(t) + b_t\dot{\Phi}_r(t) - T_r(t), \tag{3a}$$

$$EAU_r'(t) = M_r\ddot{U}_r(t) + b_a\dot{U}_r(t) - W_r(t), \tag{3b}$$

where Φ_r and U_r are the angular and axial velocities at the top-drive, i.e.,

$$\Phi_r(t) := \Phi(0,t), \quad U_r(t) := U(0,t), \tag{4}$$

with the derivatives defined as follows:

$$q_r'(t) := \frac{\partial q}{\partial x}(0,t), \quad \dot{q}_r(t) := \frac{\partial q}{\partial t}(0,t), \quad q \in \{\Phi, U\}. \tag{5}$$

In Eq. (3), A and J are the cross-sectional area and the polar moment of area of the string, and J_r and M_r are the top-drive moment of inertia and mass, respectively. Damping coefficients between the top-drive and the fixed housing are shown as b_t and b_a with subscripts t and a for torsional and axial directions, respectively. $T_r(t)$ and $W_r(t)$ are the motor torque, and the hook force.

BHA dynamics

The torsional and axial BHA dynamics are given by Tashakori *et al.* (2020, 2021):

$$GJ\Phi_b'(t) = J_b\ddot{\Phi}_b(t) - T_b(t), \tag{6a}$$

$$EAU_b'(t) = M_b\ddot{U}_b(t) - W_b(t), \tag{6b}$$

where Φ_b and U_b are the angular and axial displacements of the BHA, defined as follows:

$$\Phi_b(t) := \Phi(L,t), \quad U_b(t) := U(L,t), \tag{7}$$

with

$$q_b'(t) := \frac{\partial q}{\partial x}(L,t), \quad \dot{q}_b(t) := \frac{\partial q}{\partial t}(L,t), \quad q \in \{\Phi, U\}. \tag{8}$$

The BHA moment of inertia and mass are, respectively, shown by J_b and M_b, with $T_b(t)$ and $W_b(t)$ the Torque On Bit (TOB) and the Weight On Bit (WOB).

Time-delay model

As Eqs. (1a) and (1b) are wave equations, d'Alambert solution can be employed to obtain $\Phi(x,t)$ and $U(x,t)$ in terms of Riemann variables, as follows:

$$\Phi(x,t) = \eta_t(t + c_t x) + \xi_t(t - c_t x), \tag{9a}$$

$$U(x,t) = \eta_a(t + c_a x) + \xi_a(t - c_a x), \tag{9b}$$

where Rimemann variables η_i and ξ_i, $i \in \{a, t\}$, represent the up- and down-traveling waves, with subscripts a and t for axial and torsional dynamics. The following relations between the top- and bottom-side variables can be concluded from Eq. (9) (Interested readers may refer to Tashakori *et al.* (2020); Faghihi *et al.* (2024) for more detail):

$$\frac{1}{2}\dot{\Phi}_r(t) + \frac{1}{2c_t}\Phi'_r(t) = \frac{1}{2}\dot{\Phi}_b(t - \tau_t) + \frac{1}{2c_t}\Phi'_b(t - \tau_t), \tag{10a}$$

$$\frac{1}{2}\dot{\Phi}_r(t) - \frac{1}{2c_t}\Phi'_r(t) = \frac{1}{2}\dot{\Phi}_b(t + \tau_t) - \frac{1}{2c_t}\Phi'_b(t + \tau_t), \tag{10b}$$

for torsional dynamics, and

$$\frac{1}{2}\dot{U}_r(t) + \frac{1}{2c_a}U'_r(t) = \frac{1}{2}\dot{U}_b(t - \tau_a) + \frac{1}{2c_a}U'_b(t - \tau_a), \tag{11a}$$

$$\frac{1}{2}\dot{U}_r(t) - \frac{1}{2c_a}U'_r(t) = \frac{1}{2}\dot{U}_b(t + \tau_a) - \frac{1}{2c_a}U'_b(t + \tau_a), \tag{11b}$$

for axial dynamics. The time-delays τ_t and τ_a are the travel time of the torsional and axial waves along the drill-string, given as follows:

$$\tau_t = c_t L, \quad \tau_a = c_a L. \tag{12}$$

Shifting the time by $-2\tau_t$ in Eq. (10b) and then summing it up with Eq. (10a) lead to the following relation in which Φ'_b is omitted:

$$\Phi'_r(t) - \Phi'_r(t - 2\tau_t) = -c_t\left(\dot{\Phi}_r(t) + \dot{\Phi}_r(t - 2\tau_t) - 2\dot{\Phi}_b(t - \tau_t)\right). \tag{13}$$

Following the same approach for omitting Φ'_r gives:

$$\Phi'_b(t) - \Phi'_b(t - 2\tau_t) = c_t\left(\dot{\Phi}_b(t) + \dot{\Phi}_b(t - 2\tau_t) - 2\dot{\Phi}_r(t - \tau_t)\right). \tag{14}$$

By substituting Φ' from the top- and down-side boundary conditions, Eqs. (3a) and (6a), into Eqs. (13) and (14), the torsional dynamics is formulated through the following Neutral-type DDEs (NDDEs):

$$\ddot{\Phi}_r(t) - \ddot{\Phi}_r(t - 2\tau_t) = -\frac{1}{J_r}(GJc_t + b_t)\dot{\Phi}_r(t) - \frac{1}{J_r}(GJc_t - b_t)\dot{\Phi}_r(t - 2\tau_t) + \frac{2GJc_t}{J_r}\dot{\Phi}_b(t - \tau_t)$$
$$+ \frac{1}{J_r}\left(T_r(t) - T_r(t - 2\tau_t)\right), \tag{15a}$$

$$\ddot{\Phi}_b(t) - \ddot{\Phi}_b(t - 2\tau_t) = \frac{GJc_t}{J_b}\left(\dot{\Phi}_b(t) + \dot{\Phi}_b(t - 2\tau_t) - 2\dot{\Phi}_r(t - \tau_t)\right) + \frac{1}{J_b}\left(T_b(t) - T_b(t - 2\tau_t)\right). \tag{15b}$$

Similarly, from Eq. (11) and boundary conditions in Eqs. (3b) and (6b), the axial dynamics is governed by NDDEs as follows:

$$\ddot{U}_r(t) - \ddot{U}_r(t - 2\tau_a) = -\frac{1}{M_r}(EAc_a + b_a)\dot{U}_r(t) - \frac{1}{M_r}(EAc_a - b_a)\dot{U}_r(t - 2\tau_a) + \frac{2EAc_a}{M_r}\dot{U}_b(t - \tau_a)$$
$$+ \frac{1}{M_r}\left(W_r(t) - W_r(t - 2\tau_a)\right), \tag{16a}$$

$$\ddot{U}_b(t) - \ddot{U}_b(t - 2\tau_a) = \frac{EAc_a}{M_b}\left(\dot{U}_b(t) + \dot{U}_b(t - 2\tau_a) - 2\dot{U}_r(t - \tau_a)\right) + \frac{1}{M_b}\left(W_b(t) - W_b(t - 2\tau_a)\right). \tag{16b}$$

Equations (15) and (16) give the NTD model for the coupled axial-torsional dynamics of the drilling system, using which the top-side and BHA torsional displacements (Φ_r and Φ_b), as well as, the axial displacements (U_r and U_b) can be obtained. The coupling between these two dynamics takes place in the bit-rock interaction, T_b and W_b, as presented in the next section. Note that all the time delays involved in these NDDEs are constant.

Compared to previous time-delay model proposed in Tashakori *et al.* (2020), the inertia of the top-drive is taken into account. Note that, therein, the approach presented cannot directly be employed for the inclusion of top-drive inertia as it would need taking derivatives of the WOB and TOB which may be discontinuous and not differentiable. An alternative formulation was then proposed in Faghihi *et al.* (2024) in terms of Delay Differential Algebraic Equations (DDAEs) in the presence of top-drive dynamics. The approach presented in this article is identical to the one presented in Faghihi *et al.* (2024) but the final model is governed in a more compact form, i.e., NDDEs rather than DDAEs, without loss of generality.
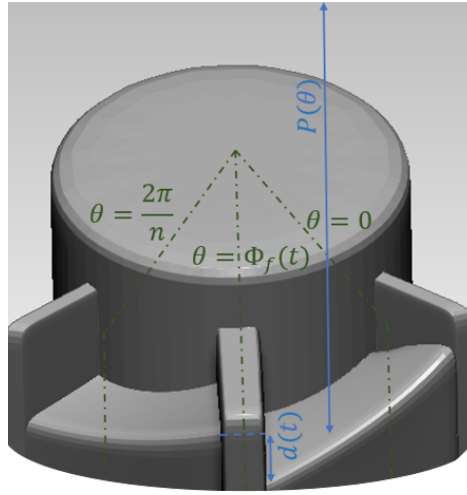
Figure 1 – Schematic of the cutting blades and the cut pattern Faghihi *et al.* (2024).

BIT-ROCK INTERACTION

The torque and weight on bit, $T_b(t)$ and $W_b(t)$ in Eqs. (15b) and (16b), can be decomposed into the cutting and frictional components, denoted with c and f subscripts as follows Detournay and Defourny (1992); Richard *et al.* (2007):

$$T_b(t) = T_c(t) + T_f(t), \tag{17a}$$
$$W_b(t) = W_c(t) + W_f(t), \tag{17b}$$

with

$$T_c(t) = \frac{1}{2}n\varepsilon a^2 d(t), \tag{18a}$$

$$T_f(t) = \frac{1}{2}\mu\gamma a^2 \sigma l, \tag{18b}$$

$$W_c(t) = n\varepsilon a\zeta d(t), \tag{18c}$$
$$W_f(t) = \sigma al, \tag{18d}$$

where n is the number of the cutting blades, ε is the rock intrinsic specific energy required to disintegrate a unit volume of the rock, a is the bit radius, μ is the friction coefficient between the blades and the formation, γ is the bit geometry number, σ is the maximum contact stress at the wear-flat rock interface, l is the length of the drill-bit wear-flat, ζ is the cutter face inclination number, and $d(t)$ is the depth of cut.

The bit-rock interaction model in (18) is modified as follows to account for bit-bouncing and bit reverse rotation Liu *et al.* (2014a); Tashakori *et al.* (2020):

$$T_c(t) = \frac{1}{2}\varepsilon a^2 \mathbf{R}(nd(t))\,\mathbf{H}\left(\dot{\Phi}_b(t)\right), \tag{19a}$$

$$T_f(t) = \frac{1}{2}\mu\gamma a^2 \sigma l\,\mathbf{Sign}\left(\dot{\Phi}_b(t)\right)\mathbf{H}(d(t))\,\mathbf{H}\left(\dot{U}_b(t)\right), \tag{19b}$$

$$W_c(t) = \varepsilon a\zeta\mathbf{R}(nd(t))\,\mathbf{H}\left(\dot{\Phi}_b(t)\right), \tag{19c}$$
$$W_f(t) = \sigma al\mathbf{H}(d(t))\,\mathbf{H}\left(\dot{U}_b(t)\right), \tag{19d}$$

with $\mathbf{R}(.)$, $\mathbf{H}(.)$, and $\mathbf{Sign}(.)$, the Ramp, Heaviside, and Sign functions, respectively. Equations (19) describe that when the depth of cut is negative, both the cutting and frictional components of TOB and WOB vanish because the bit is off bottom and there is no contact between the bit and the formation. Similarly, the frictional components are zero when the bit axial velocity is negative since the bit is not in contact with the well bottom but may still be in contact with the rock if the depth of cut is positive (so the cutting components would not be necessarily zero). Moreover, when the bit rotates contrariwise, the cutting components are zero because the rock had been cut before.

State-Dependent Delay (SDD) model

The thickness of the rock layer that the cutting blades face is called the depth of cut, shown by $d(t)$, which can also be considered as the difference between the well surface position in the front and the back side of the blade, see Fig. 1. The
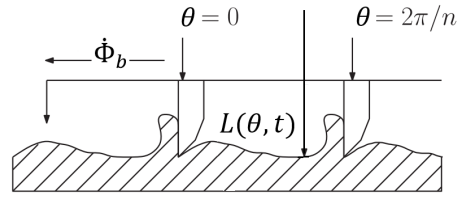
Figure 2 – Planar illustration of the cut pattern Gupta and Wahi (2016).

depth of cut is hence defined by the following delayed equation Richard *et al.* (2007):

$$d(t) = U_b(t) - U_b(t - \tau_n(t)),$$ (20)

where τ_n is obtained from:

$$\Phi_b(t) - \Phi_b(t - \tau_n(t)) = \frac{2\pi}{n}.$$ (21)

Equation (21) shows that τ_n is a state-dependent time-delay since it is dependent on the state Φ_b.

The point is that Eq. (20) is valid when the cutting process is uninterrupted. When the drill-bit rotates without cutting the formation, the depth of cut is no longer determined by the position of the current blade and one preceding blade, but instead influenced by the position of several preceding blades. Then, the right-hand side of Eq. (21) may be an integer multiple of $\frac{2\pi}{n}$ rather than $\frac{2\pi}{n}$. Therefore, even employing Eqs. (19) instead of (18) does not remedy this issue in the case of multiple regenerative effects as the depth of cut is not being obtained correctly.

Complex State-dependent delay model

In order to capture multiple regenerative effects, the relations for determining the depth of cut $\big($Eqs. (20) and (21)$\big)$ are modified as follows Liu *et al.* (2020):

$$d(t) = min_{i=1}^{N_r}\big(U_b(t) - U_b(t - \tau_i)\big),$$ (22)

with

$$\Phi_b(t) - \Phi_b(t - \tau_i(t)) = i\frac{2\pi}{n}, \quad i = 1,2,3,...N_r,$$ (23)

where N_r is set as the maximum number of regeneration. Indeed, by checking the penetration of several preceding blades and finding the one with the maximum penetration, the depth of cut is obtained. However, this approach needs a higher burden of calculation compared to the other approaches according to the conservative number N_r. Moreover, reverse rotation is not taken into account since only the penetration of the preceding blades is checked, and not the succeeding blades, which may be determinative in the case of reverse rotation.

PDE pattern evolution model

In this model, in order to determine the depth of cut, the rock surface depth is defined in a cylindrical coordinate attached to the bit. Considering a material point at an angular location $\theta \in [0, \frac{2\pi}{n})$ on the cut surface, rotating by an angular velocity of $-\dot{\Phi}_b(t)$ in the aforementioned coordinate. Accordingly, at the time $t + dt$, with the infinitesimal value dt, the material point is at the azimuth angle $\theta - \dot{\Phi}_b(t)dt$ in the bit coordinate (see Fig. 2). Defining $L(\theta, t)$ as the rock surface depth function at the azimuth angle θ and time t with

$$L\big(\theta - \dot{\Phi}_b(t)dt, t + dt\big) = L(\theta, t),$$ (24)

leads to

$$\frac{\partial L}{\partial t} = \dot{\Phi}_b(t)\frac{\partial L}{\partial \theta}.$$ (25)

In Gupta and Wahi (2016), this PDE pattern evolution model is compared with the State-Dependent Delay (SDD) model, by employing a lumped parameter model, governed by Ordinary Differential Equations (ODE). Therein, the time evolution of the bit axial and torsional motions is presented for two cases: (a) stable regime, and (b) unstable regime. It is demonstrated that both PDE and SDD models predict the same behavior when the dynamics is stable. However, in the unstable regime, the SDD model diverges.

However, there is still another side to this story. The first-order PDE (25) needs one boundary condition, which is imposed by the cutting process at the leading blade, i.e.,

$$L(\frac{2\pi}{n}, t) = max\big(U_b(t), L(0, t)\big),$$ (26)

which eventually leads to the calculation of the depth of cut, as follows:

$$d(t) = max\Big(U_b(t) - L(0,t), 0\Big). \tag{27}$$

The *max* function in Eq. (26) indicates that the well surface depth is designated by the cutting blades only if the bit is penetrated to the rock, i.e., $U_b(t)$ is greater than the rock surface at that point $L(0,t)$. This is the key point that enables this model to capture the multiple regenerative effects. However, if the bit angular velocity $\dot{\Phi}_b(t)$ becomes negative, Eq. (25) becomes unstable and diverges in numerical simulation. Assume that the domain $[0, \frac{2\pi}{n})$ is discretized by m nodes with equal distances. Subsequently, $L(\theta, t)$ is approximated with m univariate functions $L_i(t)$, $i \in \{1, 2, .., m\}$, where $L_i(t)$ represents $L(\frac{i-1}{m-1}\frac{2\pi}{n}, t)$. The boundary condition is $L_m(t) = max\Big(U_b(t), L_1(t)\Big)$. Noting that the boundary condition is given at the endpoint m, the discretized form of Eq. (25) is defined as follows:

$$\dot{L}_i(t) = \dot{\Phi}_b(t)\frac{L_{i+1}(t) - L_i(t)}{\Delta\theta}, \quad i = 1, 2, ..., m-1, \tag{28}$$

where $\Delta\theta = \frac{2\pi/n}{m-1}$ is the angular distance between two adjacent nodes. The dynamics (28) has one eigenvalue of degree $m-1$ which is equal to $-\frac{\dot{\Phi}_b(t)}{\Delta\theta}$. Consequently, if $\dot{\Phi}_b(t)$ becomes negative in some intervals, the formulated system (28) becomes unstable with the growth rate $-\frac{\dot{\Phi}_b(t)}{\Delta\theta}$. The notable point is that this growth rate increases when the number of nodes increases (decreasing $\Delta\theta$). This issue is addressed in the approach presented in the next section.

Algebraic pattern evolution model

In the following, a modified model, proposed in Faghihi *et al.* (2024), is introduced to obtain the depth of cut which enables capturing the multiple regenerative effects in both bit-bounce and reverse rotation cases. Herein, similar to the previous model, a function representing the rock surface depth is established to determine the depth of cut. However, the employed cylindrical coordinate for defining the rock surface depth function is stuck to the ground, and not rotating with the drill-bit, as shown in Fig. 1. Hence, unlike the previous model, the azimuth positions of the cutting blades are not constant; they are functions of the bit rotation angle. If the drill-bit axial position surpasses the rock surface depth at the corresponding azimuth angles, it means that the blades have penetrated the rock. Accordingly, the difference between the axial position of the bit and the rock surface depth (at the corresponding azimuth angle) results in the depth of cut. Subsequently, the rock surface depth value at this azimuth angle updates and becomes equal to the bit axial position. On the other hand, if the bit axial position does not exceed the rock surface depth at the corresponding azimuth angle, the rock surface depth function is not modified.

Since the axial positions of all blades are equal, the cutting chip thickness is the same for all n blades. Consider the blade which is located in the first sector, between $\theta = 0$ and $\theta = \frac{2\pi}{n}$, at time t. The azimuth position of this blade, $\Phi_f(t)$, is given by:

$$\Phi_f(t) = Rem(\Phi_b(t), \frac{2\pi}{n}), \tag{29}$$

where $Rem(.)$ denotes the remainder of division. By defining $P(\theta, t)$ as the rock surface depth function, the following algebraic relation governs the time evolution of $P(\theta, t)$:

$$P\big(\Phi_f(t), t\big) = \begin{cases} max\Big(U_b(t), \lim_{\varepsilon \to 0^+} P\big(\Phi_f(t), t - \varepsilon\big)\Big) & \dot{\Phi}_b > 0, \\ \lim_{\varepsilon \to 0^+} P\big(\Phi_f(t), t - \varepsilon\big) & \dot{\Phi}_b \le 0. \end{cases} \tag{30}$$

Equation (30) indicates that the evolution of the rock surface function only occurs at the bit azimuth position $\Phi_f(t)$. Moreover, there are two necessary conditions for such evolution to take place; (i) $U_b(t)$ is greater than $P\big(\Phi_f(t)\big)$, indicating that the bit is penetrated to the rock surface, and (ii) $\dot{\Phi}_b(t) > 0$, indicating that the bit is rotating in the cutting direction. Otherwise, the rock surface function remains unchanged according to the fact that the cutting is not in progress. Then, the depth of cut is determined by:

$$d(t) = max\Big(U_b(t) - \lim_{\varepsilon \to 0^+} P\big(\Phi_f(t) + \varepsilon, t\big), 0\Big). \tag{31}$$

It is important to note that in this algebraic model, the formulation does not use a differential framework (unlike the PDE model Gupta and Wahi (2016)), which makes the model capable of capturing non-differentiable and discontinuous rock surface depth functions. The bit axial motion in the torsional stick phase or bit reverse rotation may cause such discontinuities. For more insight, see Fig. 3. In Fig. 3(a), the bit is stuck torsionally. However, the bit is oscillating in the axial direction and bounces. Consequently, the depth of cut decreases until the bit can cut the formation (see Fig. 3(b)) and overcome the stick phase, as shown in Fig. 3(c). Moreover, Fig. 4 illustrates the discontinuity in the rock surface pattern when reverse rotation occurs. In Fig. 4(a), first, the bit stops rotating, and then, as illustrated in Fig. 4(b), it rotates in the opposite direction, leaving a discontinuity at the last point that was cut.
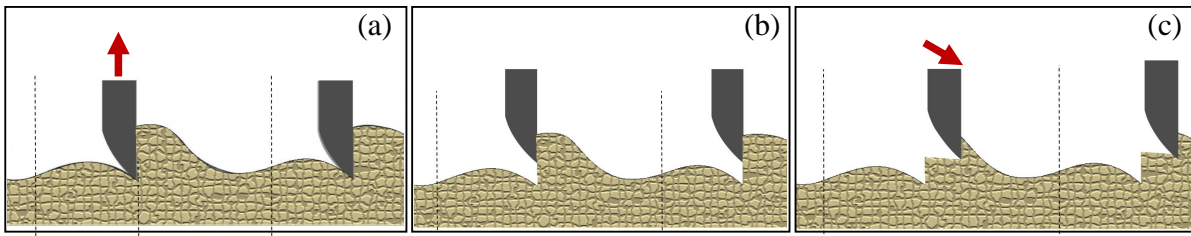
Figure 3 – A planar representation of the cut pattern when the bit (a) is stuck rotationally but bounces, (b) decreases the the depth of cut , (c) and finally overcomes the rotational stick phase and continues rotating Faghihi *et al.* (2024).
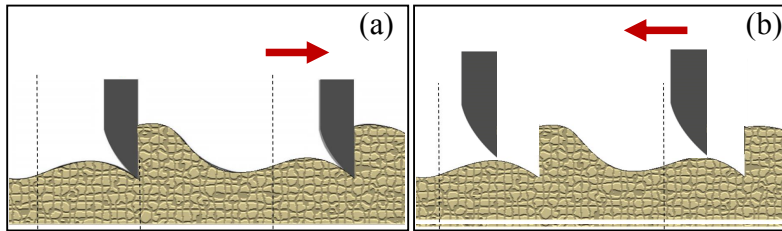

Figure 4 – A planar representation of the cut pattern when the bit (a) angular velocity becomes zero, (b) an then rotates in the reverse direction.

A comparison between the simulation results of the SDD model presented in Tashakori *et al.* (2020) and the proposed algebraic pattern evolution model is depicted in Fig. 5. The considered nominal operation velocities are $\Omega_0 = 60rpm$ and $V_0 = 5m/h$, and the formation specific energy ε equals $60MPa$. It is observed that the velocities are almost positive and neither bit-bounce nor reverse rotation occurs. Thus, there is no multiple-regenerative effect, and the results from both models are almost the same.

Let us consider a more extreme case regarding undesirable oscillations. The simulation result for a case with the parameters $\Omega_0 = 60rpm$, $V_0 = 20m/h$, and $\varepsilon = 200MPa$ is illustrated in Fig. 6. It is observed that the bit-bounce occurs frequently, resulting in a notable difference between results. It should be noted that the results of the PDE model Gupta and Wahi (2016) diverge in these scenarios, due to discontinuities in the cut pattern, and are therefore not shown in these figures. Figure 7 shows the cut surface pattern at different times $t_1 < t_2 < t_3 < t_4 < t_5 < t_6 < t_7 < t_8 < t$. The dashed blades correspond to the previous cutting blades. The discontinuities in the cut pattern arise from the occurrence of the bit-bounce during the torsional stick phase.

DISCUSSION ON CONTROL DESIGN

The model introduced in this paper to study the distributed axial-torsional vibrations of the drilling system is governed by neutral-type delay differential equations. On one hand, a wider range of stability analysis and control synthesis methods are available for such systems compared to (distributed) PDE models Krstic (2009). On the other hand, the control problem is still more complicated compared to lumped parameter models since employing classical control design approaches are either not applicable or need special treatment due to the infinite-dimensional nature of the system Michiels and Niculescu (2007). Additionally, control design strategies proposed for time-delay systems are mostly for linear problems. Therefore, available articles on the control of the time-delay-based drilling models studies a relatively small domain around the nominal state values in which the dynamics can be considered linear. It is noteworthy to mention that in this (linear) domain, all the three bit-rock interaction models, introduced in this article, will be identical, since the main difference between those models arises in nonlinear behaviors known as multiple regenerative effects.

In the equations of motion, Eqs. (15) and (16), the control inputs are delayed. These constant time-delays are induced by the finite wave propagation speed along the drill-string, causing a delay in the input affecting down-hole variables. The control design for such systems is more challenging. One approach to address the problem of input delays consists of designing a state-predictor which allows to compensate for the input delays. However, most of these predictor design methodologies are model-based. Hence, the prediction-based controller is not robust to model uncertainties and disturbances. However, of course a more accurate model, like the one presented in this paper with time-delay systems approach in combination with an algebraic cut pattern evolution model can relax this issue to some extent.
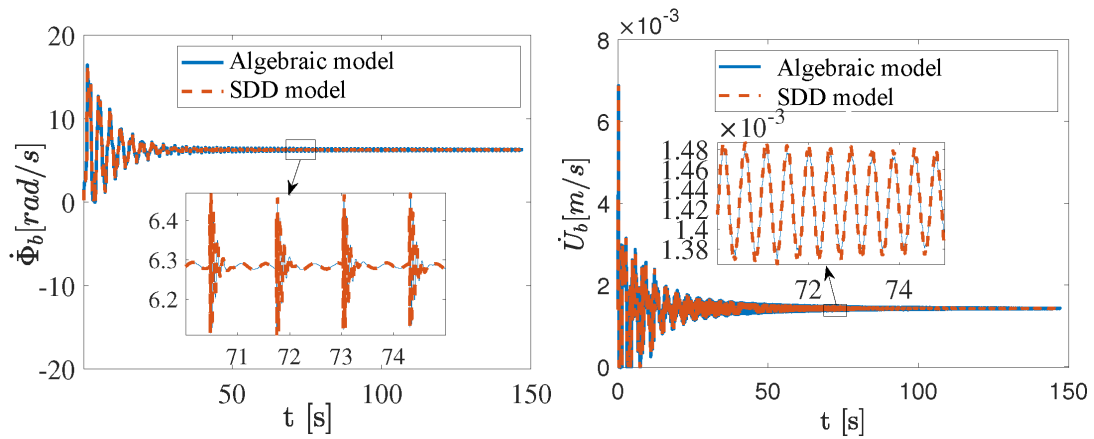
Figure 5 – Simulation results of the Algebraic model and the SDD model for the case with $V0 = 20\text{m/h}$, $\Omega_0 = 60\text{rpm}$, **and** $\varepsilon = 60\text{MPa}$ **Faghihi *et al.* (2024).**
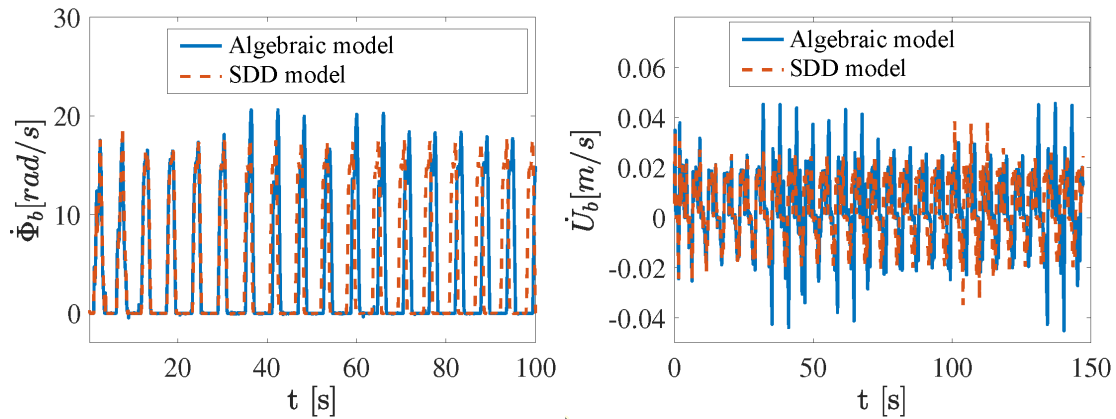

Figure 6 – Simulation results of the Algebraic model and the SDD model for the case with $V0 = 20\text{m/h}$, $\Omega_0 = 60\text{rpm}$, **and** $\varepsilon = 200\text{MPa}$ **Faghihi *et al.* (2024).**

CONCLUDING REMARKS

This article presented a distributed model for studying the coupled axial-torsional dynamics of the drilling system with the time-delay systems approach. Compared to previous time-delay models presented for the drill-string, the top-drive inertia is taken into consideration, and the equations of motion are in terms of neutral-type delay differential equations. Furthermore, three bit-rock interaction models, considering both frictional and cutting components at the bit has been introduced. The main difference between these models, named state-dependent delay (SDD) model, PDE pattern evolution, and algebraic pattern evolution model, are on the depth of cut calculation. It is discussed why the SDD model (even the proposed modified versions) cannot effectively account for multiple regenerative effects. Furthermore, it is shown that the PDE pattern evolution model that had been proposed to compensate for the shortcomings of SDD model, also fails at special cases. However, the most recent approach (algebraic pattern evolution model) circumvent determining a state-dependent delay or solving a PDE, which are generally computationally expensive. Moreover, it can captures multiple regenerative effects as well as special cases that lead to nonsmooth and discontinuous cut pattern.

REFERENCES

Aarsnes, U.J.F. and van de Wouw, N., 2018. "Dynamics of a distributed drill string system: Characteristic parameters and stability maps". *Journal of Sound and Vibration*, Vol. 417, pp. 376–412.

Aarsnes, U.J.F. and van de Wouw, N., 2019. "Axial and torsional self-excited vibrations of a distributed drill-string". *Journal of Sound and Vibration*, Vol. 444, pp. 127–151.

Besselink, B., Vromen, T., Kremers, N. and Van De Wouw, N., 2015. "Analysis and control of stick-slip oscillations in drilling systems". *IEEE transactions on control systems technology*, Vol. 24, No. 5, pp. 1582–1593.
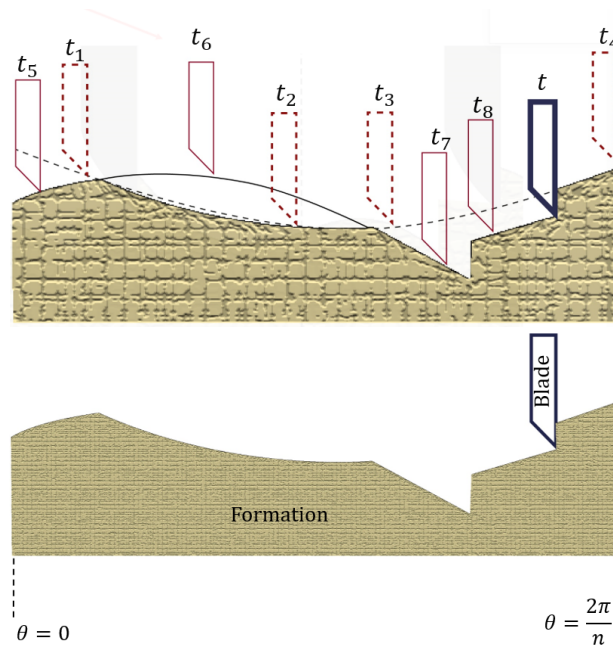
Figure 7 – The rock surface pattern and the blade trajectory with the schematic of the blade . The nominal operating speeds are $V0 = 20$m/h, $\Omega_0 = 60$rpm**, with the rock intrinsic energy** $\varepsilon = 200$MPa **Faghihi** *et al.* **(2024).**

Bresch-Pietri, D. and Krstic, M., 2014. "Adaptive output feedback for oil drilling stick-slip instability modeled by wave pde with anti-damped dynamic boundary". In *2014 American Control Conference*. IEEE, pp. 386–391.

Depouhon, A. and Detournay, E., 2014. "Instability regimes and self-excited vibrations in deep drilling systems". *Journal of Sound and Vibration*, Vol. 333, No. 7, pp. 2019–2039.

Detournay, E. and Defourny, P., 1992. "A phenomenological model for the drilling action of drag bits". In *International journal of rock mechanics and mining sciences & geomechanics abstracts*. Elsevier, Vol. 29, pp. 13–23.

Faghihi, M.A., Mohammadi, H., Yazdi, E.A., Eghtesad, M. and Tashakori, S., 2024. "Distributed model for the drill-string system with multiple regenerative effects in the bit-rock interaction". *Journal of Sound and Vibration*, Vol. 571, p. 118120.

Faghihi, M.A., Tashakori, S., Yazdi, E.A., Eghtesad, M. and van de Wouw, N., 2022. "Suppression of axial-torsional vibrations of a distributed drilling system by the eigenvector contradiction method". *IFAC-PapersOnLine*, Vol. 55, No. 36, pp. 109–114.

Faghihi, M.A., Tashakori, S., Yazdi, E.A., Mohammadi, H., Eghtesad, M. and van de Wouw, N., 2023. "Control of axial–torsional dynamics of a distributed drilling system". *IEEE Transactions on Control Systems Technology*.

Feng, T., Bakshi, S., Gu, Q. and Chen, D., 2019. "A finite element modeling framework for planar curved beam dynamics considering nonlinearities and contacts". *Journal of Computational and Nonlinear Dynamics*, Vol. 14, No. 8, p. 081003.

Fernandes, M.G., Fonseca, E.M. and Natal, R.M., 2018. "Three-dimensional dynamic finite element and experimental models for drilling processes". *Proceedings of the Institution of Mechanical Engineers, Part L: Journal of Materials: Design and Applications*, Vol. 232, No. 1, pp. 35–43.

Germay, C., Denoël, V. and Detournay, E., 2009. "Multiple mode analysis of the self-excited vibrations of rotary drilling systems". *Journal of Sound and Vibration*, Vol. 325, No. 1-2, pp. 362–381.

Gupta, S.K. and Wahi, P., 2016. "Global axial–torsional dynamics during rotary drilling". *Journal of Sound and Vibration*, Vol. 375, pp. 332–352.

Huang, Z., Xie, D., Xie, B., Zhang, W., Zhang, F. and He, L., 2018. "Investigation of pdc bit failure base on stick-slip vibration analysis of drilling string system plus drill bit". *Journal of Sound and Vibration*, Vol. 417, pp. 97–109.

Krstic, M., 2009. "Delay compensation for nonlinear, adaptive, and pde systems".

Liu, X., Long, X., Zheng, X., Meng, G. and Balachandran, B., 2020. "Spatial-temporal dynamics of a drill string with complex time-delay effects: bit bounce and stick-slip oscillations". *International Journal of Mechanical Sciences*, Vol. 170, p. 105338.

Liu, X., Vlajic, N., Long, X., Meng, G. and Balachandran, B., 2013. "Nonlinear motions of a flexible rotor with a drill bit: stick-slip and delay effects". *Nonlinear Dynamics*, Vol. 72, No. 1, pp. 61–77.

Liu, X., Vlajic, N., Long, X., Meng, G. and Balachandran, B., 2014a. "Coupled axial-torsional dynamics in rotary drilling with state-dependent delay: stability and control". *Nonlinear Dynamics*, Vol. 78, pp. 1891–1906.

Liu, X., Vlajic, N., Long, X., Meng, G. and Balachandran, B., 2014b. "Multiple regenerative effects in cutting process and nonlinear oscillations". *International Journal of Dynamics and Control*, Vol. 2, No. 1, pp. 86–101.

Liu, X., Vlajic, N., Long, X., Meng, G. and Balachandran, B., 2014c. "State-dependent delay influenced drill-string oscillations and stability analysis". *Journal of Vibration and Acoustics*, Vol. 136, No. 5.

Liu, Y., Paez Chavez, J., De Sa, R. and Walker, S., 2017. "Numerical and experimental studies of stick–slip oscillations in drill-strings". *Nonlinear dynamics*, Vol. 90, No. 4, pp. 2959–2978.

Michiels, W. and Niculescu, S.I., 2007. *Stability and stabilization of time-delay systems: an eigenvalue-based approach*. SIAM.

Navarro-López, E.M., 2009. "An alternative characterization of bit-sticking phenomena in a multi-degree-of-freedom controlled drillstring". *Nonlinear Analysis: Real World Applications*, Vol. 10, No. 5, pp. 3162–3174.

Priest, J., Ghadbeigi, H., Avar-Soberanis, S. and Gerardis, S., 2021. "3d finite element modelling of drilling: The effect of modelling method". *CIRP Journal of Manufacturing Science and Technology*, Vol. 35, pp. 158–168.

Richard, T., Germay, C. and Detournay, E., 2007. "A simplified model to explore the root cause of stick–slip vibrations in drilling systems with drag bits". *Journal of sound and vibration*, Vol. 305, No. 3, pp. 432–456.

Saldivar, B., Knüppel, T., Woittennek, F., Boussaada, I., Mounier, H. and Niculescu, S.I., 2014. "Flatness-based control of torsional-axial coupled drilling vibrations". *IFAC Proceedings Volumes*, Vol. 47, No. 3, pp. 7324–7329.

Tashakori, S., Vossoughi, G., Zohoor, H. and van de Wouw, N., 2021. "Prediction-based control for mitigation of axial–torsional vibrations in a distributed drill-string system". *IEEE Transactions on Control Systems Technology*, Vol. 30, No. 1, pp. 277–293.

Tashakori, S., Vossoughi, G., Zohoor, H. and Yazdi, E.A., 2020. "Modification of the infinite-dimensional neutral-type time-delay dynamic model for the coupled axial–torsional vibrations in drill strings with a drag bit". *Journal of Computational and Nonlinear Dynamics*, Vol. 15, No. 8.

Wahi, P. and Chatterjee, A., 2008. "Self-interrupted regenerative metal cutting in turning". *International Journal of Non-Linear Mechanics*, Vol. 43, No. 2, pp. 111–123.

Zheng, X., Agarwal, V., Liu, X. and Balachandran, B., 2020. "Nonlinear instabilities and control of drill-string stick-slip vibrations with consideration of state-dependent delay". *Journal of Sound and Vibration*, Vol. 473, p. 115235.

RESPONSIBILITY NOTICE

The authors are the only responsible for the printed material included in this paper.

List of participants

Adriano Passos – Petrobras (Brazil)

   `https://www.linkedin.com/in/adriano-passos/`

Aliel Riente – Petrobras (Brazil)

   `https://www.linkedin.com/in/aliel-riente-6ab520a0/`

Aline Barboza – UFAL/LCCV (Brazil)

   `http://lattes.cnpq.br/4857672279132119`

Allan Albuquerque – Halliburton (Brazil)

   `https://www.linkedin.com/in/allannogueira/`

Antonio Ferreira Junior – Petrobras (Infotec Brazil)

   `https://www.linkedin.com/in/eng-antonio-ferreira/`

Ashley Johnson – SLB (UK)

   `https://www.linkedin.com/in/ashley-johnson-67194a165/`

Balakumar Balachandran – University of Maryland (USA)

   `https://enme.umd.edu/clark/faculty/508/Balakumar-Balachandran`

Beatriz Caldas – UFRJ (Brazil)

`http://lattes.cnpq.br/3874264202181754`

Daniel Breno Menezes – Petrobras (Brazil)

`https://www.linkedin.com/in/daniel-guerra-7696291`

Daniel Castello – UFRJ (Brazil)

`http://lattes.cnpq.br/9561665589595461`

Diego Vasconcelos – (UFAL/LCCV (Brazil)

`https://www.linkedin.com/in/diego-de-vasconcelos-gon%C3%`
`A7alves-ferreira-72b7b5b8/`

Emmanuel Detournay – University of Minnesota (USA)

`https://cse.umn.edu/cege/detournay-emmanuel`

Farley Vilaca – GA Drilling (Brazil)

`https://www.linkedin.com/in/farley-vilaca-3b6b8918/`

Fernando Castro Pinto – UFRJ (Brazil)

`http://lattes.cnpq.br/5018072793043957`

Fernando Laroca – Petrobras (Brazil)

`https://www.linkedin.com/in/fernando-laroca-67038b33/`

Gabriel Thurler – UFRJ (Brazil)

`http://lattes.cnpq.br/0309265858266109`

Gregory Payette – ExxonMobil (USA)

`https://www.linkedin.com/in/greg-payette-5429461b1/`

Guilherme Britto – Petrobras (Brazil)

    https://www.linkedin.com/in/guilherme-britto-7a739457/

He Zhang – Halliburton (Singapore)

    https://www.linkedin.com/in/he-zhang-84159a196/?originalSubdomain=
    sg

Jean Auriol – CNRS, Université Paris-Saclay (France)

    https://l2s.centralesupelec.fr/u/auriol-jean/

João Victor B. dos Santos – Radix (Brazil)

    https://www.linkedin.com/in/joao-victor-bsantos/?originalSubdomain=
    br

José Ricardo Brígido – Petrobras (Brazil)

    https://www.linkedin.com/in/jos%C3%A9-ricardo-br%C3%ADgido-a1020933/

Kaidong Chen – Eindhoven University of Technology (Netherlands)

    https://www.tue.nl/en/research/researchers/kaidong-chen/

Lance Endres – CNPC (USA)

    https://www.linkedin.com/in/lanceaendres/

Letícia Tavares Vechi – Radix (Brazil)

    https://www.linkedin.com/in/let%C3%ADcia-vechi-93104b172/

Lucas Gouveia – UFAL/LCCV (Brazil)

    http://lattes.cnpq.br/7723601707648620

Lucas Kort – UFRJ (Brazil)

   `http://lattes.cnpq.br/5558221635756668`

Lucas Melick – UFRJ (Brazil)

   `http://lattes.cnpq.br/8958348842995189`

Luiz Bez – UFRJ (Brazil)

   `http://lattes.cnpq.br/9187994737243322`

Marcelo Savi – UFRJ (Brazil)

   `http://lattes.cnpq.br/1224532648969159`

Marcelo Trindade USP-Sâo Carlos (Brazil)

   `http://lattes.cnpq.br/0419443097971251`

Matus Gajdos – GA Drilling (Slovakia)

   `https://www.linkedin.com/in/matus-gajdos-00b13426/`

Michael Souza – UFRJ (Brazil)

   `http://lattes.cnpq.br/9154912926116839`

Mohamed Mahjoub – Helmerich & Payne (France)

   `https://www.linkedin.com/in/mohamed-mahjoub/en?originalSubdomain=`
`fr`

Nathan van de Wouw – Eindhoven University of Technology
(Netherlands)

   `https://www.tue.nl/en/research/researchers/nathan-van-de-wouw`

Ricardo Féres USP-São Carlos (Brazil)

http://lattes.cnpq.br/5337189963291420

Ricardo Halfeld – GA Drilling (Brazil)

https://www.linkedin.com/in/ricardohalfeld/

Rodrigo Tobisawa – Petrobras (Brazil)

https://www.linkedin.com/in/rodrigo-yugi-ikuta-tobisawa-a93544101/

Roman J. Shor – Texas A&M University (USA)

https://engineering.tamu.edu/petroleum/profiles/shor-roman.html

Romulo Aguiar – SLB (Brazil)

https://www.linkedin.com/in/romulo-aguiar-b273811b/

Sandro Valente – UFRJ (Brazil)

http://lattes.cnpq.br/4183287961709825

Shabnam Tashakori – Shiraz University of Technology (Iran)

https://en.sutech.ac.ir/mae/faculty-members/profile/?user=true&userid=My9lT2Jka240ZUhwdWIvcksyeklVZz09

Silvia Corbani – UFRJ (Brazil)

http://lattes.cnpq.br/6675220344808708

Thiago Ritto – UFRJ (Brazil)

http://lattes.cnpq.br/8907423644221097

Tiago Paulino – UFRJ (Brazil)

> http://lattes.cnpq.br/1996059844733426

Yuri Moralles – UFRJ (Brazil)

> http://lattes.cnpq.br/4272171995174595